Imperial College London

Baseline-Free Structural Health Monitoring for Aeronautical Structures Under In-Service Conditions

---

By

Yuhang Pan

Thesis submitted in part fulfilment of the requirements for the degree of Doctor of Philosophy of Imperial College London

Department of Aeronautics
Faculty of Engineering
Imperial College London
February 2025

Declaration of Originality

I hereby declare that all the work and material presented in this thesis is composed and reported as my own. All information and data obtained from external sources are properly acknowledged and cited in text with the full list of references given in the final bibliography section.

Yuhang Pan

31 January , 2025

Copyright Declaration

The copyright of this thesis rests with the author. Unless otherwise indicated, its contents are licensed under a Creative Commons Attribution-Non Commercial 4.0 International Licence (CC BY-NC).

Under this licence, you may copy and redistribute the material in any medium or format. You may also create and distribute modified versions of the work. This is on the condition that: you credit the author and do not use it, or any derivative works, for a commercial purpose.

When reusing or sharing this work, ensure you make the licence terms clear to others by naming the licence and linking to the licence text. Where a work has been adapted, you should indicate that the work has been changed and describe those changes.

Please seek permission from the copyright holder for uses of this work that are not included in this licence or permitted under UK Copyright Law.

Acknowledgments

First and foremost, I would like to express my deepest gratitude to my supervisor, Professor Zahra Sharif Khodaei. Her unwavering support and encouragement have been instrumental in pushing me to reach my fullest potential. Beyond her guidance, she has been an inspiring role model in academia, someone I will always admire and strive to emulate.

I also extend my heartfelt thanks to my co-supervisor, Professor Ferri Aliabadi, for his kind support and encouragement throughout my PhD journey. It has been a privilege to learn from his academic vision and life wisdom, lessons that will benefit me for years to come. His insightful guidance and countless fruitful discussions have been a constant source of inspiration.

I would like to express my heartfelt gratitude to Dr. Sina Asadi and Dr. Francisco Rodrigues for their invaluable support during my experiments and for their unwavering encouragement during challenging times, which gave me the strength to persevere. This thesis would not have been possible without the companionship and support of my colleagues and friends. I am deeply grateful to Ilias, Dong, Massimiliano, Jiangang, Fatih, Samet, Amin, Tongrui, Chi Hin, Haolin, Fanzeng, Wongon, Ali, Aldy, Valentin, Tafara, Hongmin, Haomiao and Guangxiao. I have learned so much from all of you, and your friendship has made this journey far more rewarding. I would also like to thank the technicians and staff at the Department of Aeronautics, especially Keith, Joseph, Gary, Jon, and Franco, for their assistance with my experiments.

A special thanks goes to Feifei and Yingwu, whose companionship made my journeys truly unforgettable and brought joy beyond the demands of research. I am also deeply grateful to my fitness and sports coaches: Martin, my gym trainer; Adrian, my running and swimming coach; Josephine, my yoga instructor; and Francisco, my squash coach. Your guidance and support not only kept me active but also added vitality and balance to my life in London, offering much-needed moments of respite and connection outside my academic pursuits.

I would also like to acknowledge my dearest friends Mengke, Ganlin, Zhengyuan, Shiwei, and Qiqi. Every stage of life brings lifelong friends, and I am deeply thankful for your unwavering support and companionship during challenging times. In addition, I am profoundly grateful to those who offered me support during difficult times, both financially and emotionally: Professor Aimin Yang and Guanchen Zhou, Dr Di Zhang, Xueyong, Fanbei, Dr Shulei Yang, Wei Liang, Fang Gao, Yajuan Qiao, Yue Tian, Zhendong, Chong Li, and Haipeng. Your kindness and generosity have been a true lifeline, and I will never forget the impact you have had on my life.

To my dearest partner and the love of my life, Tianjiao Li, thank you for your boundless patience, unconditional love, and steadfast support. You have been my rock through every milestone, and I am excited to continue building our future together.

Most importantly, I want to express my heartfelt gratitude to my family: my father Jianjun, my mother Yanxiu, my sister Jiejing, my two adorable nephews Panyue and Panfeng, as well as my grandparents and aunt. Without your unwavering support and constant encouragement, I would not have made it this far. I love you all more than words can express.

Abstract

This PhD research has developed innovative methodologies for Structural Health Monitoring (SHM), addressing key challenges in damage detection, and damage growth prediction under varying environmental and operational conditions. By integrating vibration- and guided-wave based methods and leveraging the multifunctionality of PZT transducers, the research enhances SHM systems' sensitivity to minor damage, independence from baseline data, and resilience to temperature variations.

A hybrid SHM approach combining guided wave and vibration-based techniques is proposed to improve the performance of damage detection and localization, utilizing their complementary strengths for monitoring complex structures with greater accuracy and robustness. Building upon this foundation, a novel vibration-based SHM method is introduced, utilizing transmissibility functions (TFs) as temperature-insensitive features for damage detection. This approach represents a more advanced level of fusion by employing piezoelectric transducers (PZTs) for modal analysis, enabling reliable detection performance across diverse materials and environmental conditions.

Furthermore, a comprehensive comparative analysis of linear and nonlinear guided wave methods, alongside vibration-based techniques, underscores their respective strengths and limitations in monitoring progressive damage. This analysis also provides critical validation for the proposed hybrid approach, demonstrating its effectiveness in addressing the challenges of damage detection under varying conditions.

Finally, an innovative baseline-free framework is also presented for in-service crack detection and growth prediction. Using passive PZT transducers and advanced analytics, this approach enables early damage detection and precise crack quantification without baseline data, significantly enhancing in-service SHM applications.

The contribution of this research to the advancement of SHM technologies by addressing key challenges about environmental variation, baseline dependency, and real-time monitoring.

Contents

1 Introduction **1**

1.1 Background 1

1.2 Aims and objectives 6

1.3 Thesis Outline 8

1.4 Thesis Contribution 10

2 Fundamental Concepts and Theoretical Background **12**

2.1 Introduction 12

2.2 Ultrasonic-guided wave based SHM 12

2.2.1 Ultrasonic guided wave based SHM 13

2.2.2 Nonlinear ultrasonic guided wave-based SHM 19

2.3 Vibration-based SHM 23

2.3.1 FRF for vibration analysis 23

2.3.2 Modal Parameters-Based SHM 26

2.4 Auxiliary techniques 29

2.4.1 Electro-mechanical Impedance for Integrity assessment of piezoelectric transducers 30

2.4.2 Fatigue Life Analysis 31

2.4.3 Machine learning development for SHM 34

2.5 Summary 38

3 A hybrid method based on vibration and guided waves for damage detection and localization **39**

3.1 Introduction . . . 39
3.2 Experimental Set-up . . . 40
3.3 Hybrid Methodology . . . 41
3.3.1 Feature Extraction . . . 41
3.3.2 Model Development . . . 44
3.3.3 Model Evaluation and Validation . . . 45
3.4 Results and Discussion . . . 46
3.4.1 Damage Detection . . . 46
3.4.2 Damage Localization . . . 48
3.5 Summary . . . 50

4 A robust hybrid method for damage detection under varying environmental conditions 52

4.1 Introduction . . . 53
4.2 Experimental Setup . . . 56
4.2.1 Test specimens . . . 56
4.2.2 Sensor integration . . . 57
4.2.3 Experimental setup . . . 57
4.3 Damage detection methods . . . 60
4.3.1 Data acquisition . . . 61
4.3.2 Feature extraction . . . 62
4.3.3 Decision making: outlier analysis . . . 64
4.3.4 Performance analysis . . . 65
4.4 Damage detection results . . . 65
4.4.1 Temperature and damage effects on TFs . . . 66
4.4.2 Detection results . . . 68
4.4.3 Uncertainty quantification . . . 71
4.5 Summary . . . 74

5 Progressive damage detection under varying temperatures: linear versus nonlinear ultrasonic guided waves and vibration-based methods 76

5.1 Introduction . . . 76

5.2 Experimental Setup . . . 80

5.2.1 Tensile test . . . 80

5.2.2 Fatigue experiment setup . . . 81

5.2.3 The signal measurement . . . 82

5.3 Methodology for the crack detection . . . 83

5.3.1 ToF-based DI for linear methods . . . 83

5.3.2 Second harmonic-based DI for nonlinear methods . . . 85

5.3.3 FRF-based DI for Vibration methods . . . 87

5.4 Results and discussion . . . 88

5.4.1 Temperature and crack effect on the features . . . 88

5.4.2 Crack propagation result . . . 93

5.4.3 Crack detection results . . . 93

5.5 Conclusion . . . 97

6 Baseline-free methods for online fatigue crack monitoring 100

6.1 Introduction . . . 100

6.2 Experimental Setup . . . 101

6.2.1 Fatigue test . . . 101

6.2.2 Data acquisition system . . . 102

6.3 Methodology . . . 103

6.3.1 Higher harmonic generation . . . 103

6.3.2 Early Warning for Fatigue Life Assessment . . . 105

6.4 Results and discussion . . . 106

6.4.1 Feature extraction . . . 106

6.4.2 The FCG results . . . 108

6.4.3 Crack detection results . . . 110

6.4.4 Crack growth modelling results . . . 114

6.4.5 Uncertainty quantification . . . 116
6.5 Summary . . . 122

7 In-service baseline-free method for fatigue crack monitoring 124
7.1 Introduction . . . 124
7.2 Experimental setup . . . 126
7.3 Methodology . . . 128
7.3.1 In-service automated crack detection based on higher harmonic analysis . . . 128
7.3.2 The crack growth model based on LSTM . . . 133
7.4 Results and discussion . . . 140
7.4.1 Fatigue growth behaviour . . . 140
7.4.2 Automatic crack detection based on the DPL method . . . 140
7.4.3 Robustness analysis of the DPL method on the crack detection . . . 143
7.4.4 Crack growth result . . . 148
7.5 Summary . . . 151

8 Conclusions and Future Work 153
8.1 Conclusions . . . 153
8.2 Future Work . . . 156

Bibliography 158

List of Figures

1.1 Different types of sensors used in SHM. 5

1.2 The principles of the passive sensing and active sensing [1]. 6

2.1 The symmetric and anti-symmetric Lamb modes. 15

2.2 Dispersion curves of (a) phase velocity and (b) group velocity for Aluminum-5152 with 2 mm thickness. 17

2.3 The specimens with (a) PZT piezoelectric Ceramic Disc and (b) DuraAct patch transducers. 17

2.4 Distortion in the waveform during propagation by nonlinear elasticity and higher harmonic generation. 19

2.5 (a) SinePhase Impedance analyser with measurement setup and User interface, (b) Real and imaginary parts of the impedance of a DuraAct transducer being attached to the Aluminum. 31

2.6 Common fatigue failure zones for Airbus A300 [2]. 32

2.7 Stages of fatigue crack growth (FCG) based on the fatigue crack propagation model [3]. 33

2.8 Development history of machine learning categorized into infancy, upsurge, and booming periods, highlighting major models and breakthroughs. 35

2.9 The difference between supervised and unsupervised learning [4]. 37

3.1 The hybrid system based on vibration and guided wave for damage detection and localization. 41

3.2 Roadmap of damage detection and localization based on the hybrid method. 42

3.3 FRF obtained from pristine and damaged condition with frequency range: (a) 5-2000Hz, (b) 500-2000Hz 43
3.4 The eigenvalue and the cumulative percentage obtained from PCA: (a) All points, (b) First thirty-five points. 43
3.5 The developed model for damage detection and localization. 44
3.6 Damage index 1 obtained under different conditions: (a) Pristine state, (b) Damage state. 47
3.7 Damage detection results obtained from: (a) equation (3.1), (b) equation (3.2), (c) equation (3.3). 48
3.8 Damage detection results obtained by the vibration-based method: (a) Features used in the vibration method. (b) Detection results obtained by the neural pattern. 48
3.9 Damage localization results obtained by: (a) vibration-based method, (b) guided wave-based method-DI2. 49
3.10 (a) Damage localization results obtained by the combined method. (b) The average MND and minimum MND obtained by the different methods. 50

4.1 Schematic diagram of the experimental setup. 57
4.2 Schematic diagram of the experimental setup. 58
4.3 Different experimental conditions. (a) The definition of the damage size, (b) Damage with different sizes on the plates, and (c) Damage positions inside and outside the sensor area. 59
4.4 The framework of the proposed damage detection methodology. 60
4.5 The process of feature extraction. 62
4.6 TF of M1 obtained by sensors 2 and 3 under different conditions.(a) The effect of different temperatures(20°C, 30°C, 40°C, 50°C and 60°C, from bottom to top respectively) on TF and (b) the effect of damage sizes (D_s= 0.28%, 0.56%, 0.84%, 1.12%, 1.40%, from bottom to top respectively) on TF. 66

4.7 TF of M2 obtained by sensors 2 and 3 under different conditions. (a) The effect of different temperatures(20°C, 30°C, 40°C, 50°C and 60°C, from bottom to top respectively) on TF and (b) the effect of damage sizes (D_s= 0.28%, 0.56%, 0.84%, 1.12%, 1.40%, from bottom to top respectively) on TF. 67

4.8 TF of M3 obtained by sensors 2 and 3 under different conditions. (a) The effect of different temperatures(20°C, 30°C, 40°C, 50°C and 60°C, from bottom to top respectively) on TF and (b) the effect of damage sizes (D_s= 0.28%, 0.56%, 0.84%, 1.12%, 1.40%, from bottom to top respectively) on TF. 68

4.9 Results of M1 obtained by different conditions: (a) Damage index obtained by M1 at different temperatures when damage size =1.4%, (b) Damage index obtained by M1 at different temperatures when damage size =0.28%, (c) *Accuracy* obtained by actuator PZT1 and Specimen M1, (d) $F1-score$ obtained by actuator PZT1 and Specimen M1. 69

4.10 Results of M2 obtained by different conditions: (a) Damage index obtained by M2 at different temperatures when damage size =1.4%, (b) Damage index obtained by M2 at different temperatures when damage size =0.28%, (c) *Accuracy* obtained by actuator PZT1 and Specimen M2, (d) $F1-score$ obtained by actuator PZT1 and Specimen M2. 70

4.11 Results of M3 obtained by different conditions: (a) Damage index obtained by M3 at different temperatures when damage size =1.4%, (b) Damage index obtained by M3 at the same temperature when damage size =0.28%, (c) *Accuracy* obtained by actuator PZT1 and Specimen M3, (d) $F1-score$ obtained by actuator PZT1 and Specimen M3. 71

4.12 The configuration of different actuator locations. 72

4.13 *Accuracy* and $F1-Score$ results for M1 (a, d), M2 (b, e), and M3 (c, f) Using PZT2 as Actuator. 73

5.1 The experimental platform for the tensile test, a) tensile test setup, b) stress and strain curve and c) the geometry of the coupon. 81

5.2 The experiment setup and facilities: (a) the fatigue experiment setup; (b) the aluminum specimen with two PZT sensors; (c) The forced convection oven to control temperature; (d) the optical microscope for the crack inspection; (e) the observed crack. 83

5.3 The signal acquisition system. a) the schematic diagram of the Linear guided wave-based method, b) the schematic diagram of the nonlinear guided wave-based method, c) the schematic diagram of the Vibration-based method, d) EMI measurement system. 84

5.4 Dispersion curves of (a) phase velocity and (b) group velocity for Aluminum-5152 with 2mm thickness. 87

5.5 Temperature and damage effect on FRF. (a) the comparison between the baseline and the current FRF at 30℃ and 40℃, and (b) the comparison between the baseline and the current FRF after 420k and 440k cycles. 88

5.6 Temperature and damage effect on the guided-wave propagation. (a) The comparison between the baseline and the current signal at 30℃, (b) The comparison between the baseline and the current signal at 40℃, (c) The comparison between the baseline and the current signal after 400k cycles, (d) The comparison between the baseline and the current signal after 420k cycles. 90

5.7 (a) Position and function of PZT sensors for nonlinear lamb wave method, (b) specimen state before the fatigue test, (c) specimen state after 320k cycles, and the amplitude of the (d) fundamental frequency and (e) second harmonic before the fatigue test and after 320k cycles. 91

5.8 Crack effect on (a) fundamental and (b)second harmonic frequency. 92

5.9 Optical microscope images of fatigue crack of T1 at: (a) 300k cycles. (b) 320k cycles. (c) 340k cycles. 94

5.10 (a) DI values obtained using the linear guided wave method at 20°C with a baseline signal recorded at 20°C. (b) DI values obtained using the linear guided wave method at 30°C with a baseline signal recorded at 20°C. 95

5.11 The second harmonic parameters versus fatigue cycles under 20℃ environments. (b) The second harmonic parameters versus fatigue cycles under 30℃ and 40℃ environments. 95
5.12 The second harmonic parameters versus fatigue cycles were obtained by specimen (a) T1, (b)T2. 96
5.13 Results obtained using VSHM method under (a) a consistent temperature condition and (b) a 10℃ temperature difference. 98

6.1 The experimental platform for online fatigue crack monitoring, a) fatigue experiment setup, b) specimen geometry and c) the state of specimen at different number of cycles. 102
6.2 The data acquisition setup, a) the configuration of signal acquisition, b) sensor position and c) the data acquisition hardware. 103
6.3 The online crack monitoring process based on $\hat{\beta}'$. 105
6.4 The response obtained by sensor 1 during the fatigue test (1,000 loading cycles), a) time domain and b) frequency domain. 107
6.5 The relationship between the fatigue life, and a) the maximum amplitude of the time domain signal, and b) the amplitude of the fundamental and the second harmonic frequencies. 109
6.6 a) Photos taken by the camera for specimen C4 of crack initiation and propagation, b) the relationship between FCG rate and ΔK. 109
6.7 The relationship between fatigue life and $\hat{\beta}'$ obtained by sensor 1 and specimen, a) C1, b) C2, c) C3 and d) C4. 110
6.8 Correlation between the fatigue life and $\hat{\beta}'$ in first stage obtained by sensor 1, a) C1, b) C2, c) C3 and d) C4. 111
6.9 Correlation between the fatigue life and $\hat{\beta}'$ in the second stage obtained by sensor 1 on, a) C1, b) C2, c) C3 and d) C4. 113
6.10 The FCG model was obtained by specimen C4 for validation and C1-C3 for training, a) on the left side of the hole and b) on the right side of the hole. 115

6.11 The relationship between fatigue life and $\hat{\beta}'$ obtained by sensor 2 on specimen, a) C1, b) C2, c) C3 and d) C4. 117
6.12 Correlation between the fatigue life and $\hat{\beta}'$ in the first stage obtained by sensor 2 on, a) C1, b) C2, c) C3 and d) C4. 117
6.13 Correlation between the fatigue life and $\hat{\beta}'$ in the second stage obtained by sensor 2 on, a) C1, b) C2, c) C3 and d) C4. 118
6.14 The positions of four sensors on C5, and the relationship between fatigue life and $\hat{\beta}'$ obtained by (b) sensor 1, (c) sensor 2, (d) sensor 3, and (e) sensor 4. 120
6.15 The validation of the developed FCG model using data from sensor 2, on the a) left and b) right side of the hole. 121

7.1 The experimental platform for online fatigue crack monitoring: (a) experimental setup for fatigue test; (b) specimen geometry and sensor layout; (c) specimen with and without crack; (d) hardware components for the data acquisition; (e) schematic diagram of data acquisition. 127
7.2 Response of time and frequency domain obtained from the pristine specimen (1000 cycles, blue solid line) and specimen with a 1.8 mm fatigue crack (92×10^3 cycles, red dash line): (a) time-domain signals and (b) frequency-domain spectra. 129
7.3 The change of features during the fatigue experiment: (a) The maximum value of the time domain signals (b) The relative third harmonic parameter $\hat{\gamma}'$ 130
7.4 The framework of the proposed method in this work. 133
7.5 The structure of the deep LSTM, a) The LSTM model with multiple hidden layers and one fully connected layer, b) The structure of the LSTM single cell with the j_{th} layer at the time i, including an input gate, forget gate, output gate and tanh layer. 134
7.6 (a) Paris' law specimen data, C= 4.94×10^{-7}, and m=1.86; (b) The micromorphology of the hole and edges. 141

7.7 Results of crack detection: (a) The change of the $\hat{\gamma}'$ with respect to the fatigue loading cycles on S1, (b) The slope values obtained by the DPL method, and the Threshold= 2.5×10^{-9}, (c) The different fatigue stages divided by the DPL method, and the crack length detected by the method, (d) The running details of dynamic fitted lines between first and second stage, (e) The running details of dynamic fitted lines between second and third stage, (f) K-means clustering method result on S1. . 143

7.8 Results of crack detection obtained by: (a) The position of 4 sensors on S5, (b) The change in the third harmonic parameter and crack growth with respect to fatigue loading cycles, as recorded by sensor 1 on S5, (c) The slope values obtained by the DPL method, and the Threshold = 2.5×10^{-9}, (d) The different fatigue stages divided by the DPL method, and the crack length detected by the method, (e) The K-means clustering method result on S5. 144

7.9 Results of crack detection: (a) The slope values obtained by the DPL method, and the Threshold=2.5×10^{-9}, (b) The different fatigue stages divided by the DPL method, and the crack length detected by the method, the detectable crack length is 6.0 mm, and the corresponding number of cycles is 130k. (c) K-means clustering method result on S1, the detectable crack length is 8.0 mm, and the corresponding number of cycles is 135k. 145

7.10 Results of crack detection obtained by S6: (a) Time-domain of the sensor response when the loading frequency is 6 Hz and 10 Hz, (b) The slope values obtained by the DPL method, and the Threshold = 2.5×10^{-10}, (c) The different fatigue stages divided by the DPL method, and the crack length detected by the method. The detectable crack length is 1.6 mm, and the corresponding number of cycles is 130k. . 146

7.11 The framework of the proposed method in this work. 147

7.12 RMSE obtained by different hyperparameter combinations. 149

7.13 (a) Leave-one-out cross-validation results on different testing samples obtained by different methods. (b) Predictive FCG result of S3 using the PI-LSTM. 150

List of Tables

3.1 Confusion matrix. 45

3.2 Results obtained by different features and methods. 49

4.1 Properties and working conditions of experimental plates. 57

4.2 Experimental factors and levels. 60

4.3 $L_{25}\,(5^3)$ Orthogonal array and experimental datasets. 61

5.1 Mechanical properties of aluminium 5251 obtained from tensile testing. 81

5.2 Fatigue test details on different specimens under different temperatures 82

5.3 Crack length of different fatigue stage on specimens T1, T2, and T3 94

5.4 Detectable crack lengths and working temperature ranges of different methods. . . . 97

6.1 List of specimens, sensor positions and fatigue test parameters. 103

7.1 List of specimens, sensor positions and fatigue test parameters. 128

7.2 The range of input parameters and model hyperparameters for the PI-LSTM model. 139

7.3 Detection results obtained by DPL and K-means clustering method. 142

7.4 Detection results obtained by different sensors on S5. 146

Chapter 1

Introduction

1.1 Background

The structural integrity of aerospace components is critical to ensuring flight safety, operational efficiency, and cost-effectiveness. Aircraft structures are subjected to a wide range of operational stressors, including fatigue, corrosion, and accidental impacts, which can progressively degrade material properties, initiate cracks, and propagate structural damage. If not promptly detected, such damage can lead to catastrophic structural failures, posing severe risks to flight operations and passenger safety [1,5,6]. Aviation safety reports consistently highlight the pivotal role of structural failures in aircraft accidents, underscoring the necessity of early damage detection and prevention. Historically, incidents of undetected structural damage have led to devastating outcomes, further emphasizing the importance of robust inspection protocols and advanced monitoring systems. These observations underscore the urgent need for reliable and efficient damage detection methods to mitigate risks and improve structural health management of aerospace components [7].

The global aviation industry is undergoing rapid expansion, with more than 24,000 commercial aircraft currently in operation, and it is expected to exceed to 40,000 by 2040 [8]. This growth imposes significant demands on maintenance and inspection processes. As air traffic increases, the frequency and complexity of inspections required to ensure airworthiness also increase. Traditional inspection methods, including manual visual checks, dye penetrant testing, and radiography, while moderately effective, are inherently labor-intensive, time-consuming, and reliant on operator ex-

pertise, thereby increasing the potential of human error [9,10]. Additionally, these techniques are predominantly reactive, often identifying damage only after it has progressed to a critical stage. Many traditional methods also require extensive structural disassembly, resulting in prolonged operational downtime. The increasing adoption of advanced materials, such as composites, in modern aircraft exacerbates these challenges. While composites offer superior performance and weight reduction, their anisotropic properties and complex damage mechanisms pose significant difficulties for conventional detection techniques [7, 11]. These limitations highlight the urgent need for real-time damage detection and assessment that facilitate a paradigm shift from reactive to proactive maintenance. Real-time monitoring technologies enable early detection of incipient or subsurface damage, allowing timely intervention to mitigate safety risks and prevent catastrophic failures. Such a proactive approach not only enhances safety but also improves operational efficiency and cost-effectiveness, aligning with the evolving demands of the aerospace industry. As the global fleet continues to expand, the integration of advanced monitoring technologies will be essential for maintaining aviation safety and reliability.

To address the limitations of traditional visual and contact-based inspection techniques, non-destructive testing (NDT) has become an essential and well-established approach for structural damage detection. NDT methods enable the evaluation of structural health without compromising the functionality of inspected components, making them particularly advantageous in the aerospace industry. These techniques offer superior sensitivity, adaptability, and precision in identifying damage at various stages [12–14]. Among the most widely employed NDT methods are:

- **Ultrasonic Testing (UT):** This technique employs high-frequency sound waves to detect internal defects such as cracks, delaminations, and voids. Ultrasonic testing is highly sensitive, capable of identifying minute defects, and provides precise information on damage size and location [15].

- **Eddy Current Testing (ECT):** Utilizing electromagnetic induction, ECT is effective for detecting surface cracks and subsurface flaws in conductive materials. This method is particularly advantageous for inspecting metallic components with coatings or layers [16].

- **Thermography:** Infrared imaging is used to detect surface and subsurface defects based on

temperature variations. Thermography is a non-contact method, offering high efficiency in inspecting large areas, especially in composite materials [16].

Despite their numerous advantages, NDT methods have some limitations. These techniques often require highly skilled operators, making them susceptible to variability arising from operation factors and environmental conditions. Additionally, they face challenges in accurately detecting distributed microcracks or subtle defects, particularly in components with complex geometries. Furthermore, most NDT methods are primarily designed for periodic inspections, limiting their applicability for continuous monitoring during operational phases. This restricts their effectiveness in real-time damage detection and proactive maintenance strategies [17].

Building on the foundation of NDT, SHM represents a transformative advancement in damage detection. While NDT methods typically rely on periodic inspections conducted at scheduled intervals, SHM employs advanced sensor technologies and data analytics to enable continuous, automated monitoring of structural health throughout the operational life of the structure [18]. Unlike the passive and reactive nature of NDT-based maintenance, which often involves manual inspections and significant operational downtime, SHM adopts a proactive, condition-based approach. This approach facilitates real-time detection, localization, and quantification of damage, thereby enhancing maintenance efficiency and reducing both downtime and costs. By embedding or strategically bonding sensor networks to the structure, SHM systems eliminate the need for frequent manual inspections, substantially reducing downtime and maintenance costs. Additionally, SHM utilizes a range of advanced sensing technologies, carefully tailored to specific structural and operational requirements, ensuring precision and reliability even under challenging conditions. This integration of intelligent sensing and predictive analytics underscores SHM's potential in structural health management, offering a more efficient, cost-effective, and reliable alternative to traditional maintenance practices. Among the diverse sensing technologies utilized in SHM, these sensing technologies include:

- **Piezoelectric Transducers** Widely employed in both active and passive SHM methods, piezoelectric transducers, as shown in Figure 1.1(a), can be used as both actuators and sensors for ultrasonic-guided waves. Operating based on the piezoelectric effect, they convert mechanical stress into electrical signals and vice versa. Their high sensitivity and broad

frequency response make them particularly effective for guided wave-based SHM in damage detection, localization, and characterization [19].

- **Strain Gauges** Strain gauges (Figure 1.1(b)) are widely used for localized strain measurement, operating on the principle of electrical resistance changes induced by mechanical deformation. Their high sensitivity allows for the identification of stress concentration zones, which are critical indicators of crack initiation. By continuously monitoring strain evolution, these sensors facilitate early damage detection and support proactive maintenance in aerospace, civil, and mechanical engineering applications [20].

- **Fiber Optic Sensors** These sensors (Figure 1.1(c)) are widely used in SHM due to their high sensitivity, immunity to electromagnetic interference, and ability to measure strain and temperature over large areas [21]. They operate by detecting strain- or temperature-induced variations in the optical signal propagating through the fiber. Techniques such as fiber Bragg gratings (FBG) utilize wavelength shifts caused by periodic refractive index changes, while interferometric methods measure phase differences in light waves to capture structural deformations. Their lightweight and flexibility make them particularly suitable for composite structures, where traditional sensors may induce stress concentrations or material incompatibility.

- **Accelerometers** Essential for vibration-based SHM methods, accelerometers measure structural acceleration responses over time, enabling the assessment of dynamic behavior and structural integrity [22]. These sensors detect variations in modal properties, such as shifts in natural frequencies, damping ratios, and mode shapes, which can serve as indicators of potential structural damage. By analyzing these modal properties, accelerometers help identify stiffness degradation, crack initiation, or changes in boundary conditions, as illustrated in Figure 1.1(d).

- **Acoustic Emission (AE) Sensors** AE sensors play a crucial role in SHM by detecting transient elastic waves generated by damage mechanisms such as crack propagation and fiber breakage. Their high sensitivity to dynamic structural changes makes them particularly effective for early-stage damage detection in critical applications, the AE sensor is illustrated

in Figure 1.1(e).

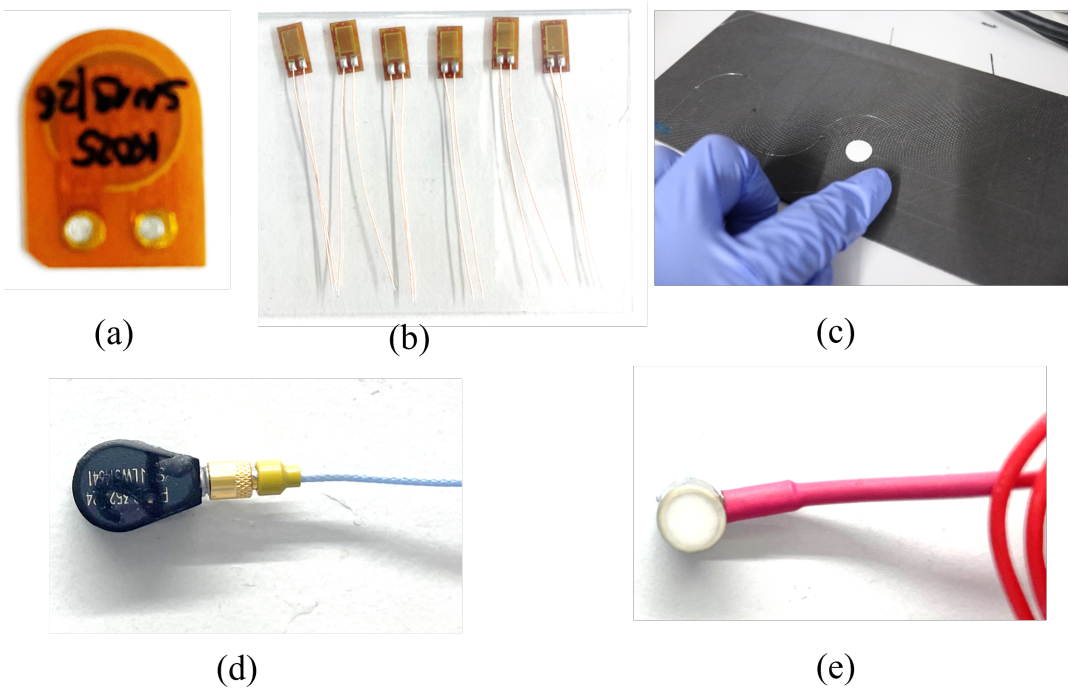


Figure 1.1: Different types of sensors used in SHM.

Among SHM techniques, the use of piezoelectric transducers to monitor ultrasonic wave propagation in solid media has gained increasing attention in recent years. This is due to their ability to monitor large areas of interest through an appropriately designed sensor network, eliminating the need for external loading, which is often required by traditional NDT methods. SHM techniques employing piezoelectric transducers are broadly classified into active and passive approaches [23, 24], as described in Figure 1.2.

In passive sensing, PZT transducers serve solely as receivers, capturing dynamic signals generated by external events such as impacts, dynamic loads and AE. Unlike active sensing, which requires transducers to both emit and receive signals, passive sensing relies entirely on these externally induced responses to gather diagnostic data. This approach offers several advantages, including reduced energy consumption, a simpler system architecture, and minimal interference with the structure under monitoring [25]. Active sensing utilizes PZT transducers as both actuators and sensors. As actuators, PZTs generate diagnostic signals, such as ultrasonic waves, which propagate through the structure. Simultaneously, as sensors, they capture the resulting wave responses, analyzing changes in wave characteristics to detect, locate, and quantify damage. Guided

wave-based methods(GWSHM), widely adopted in aerospace applications, exemplify active sensing and are particularly effective for assessing structural health across large areas [25–30].

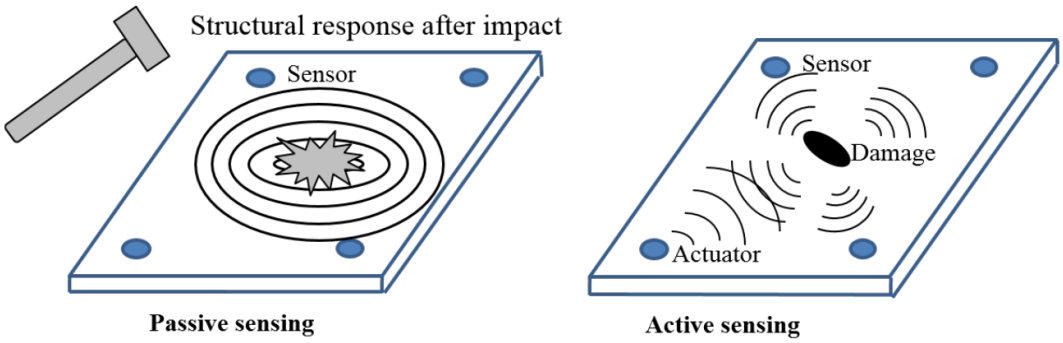


Figure 1.2: The principles of the passive sensing and active sensing [1].

In addition to GWSHM, vibration-based SHM (VSHM) is another widely used approach for aerospace structures, valued for its robustness against environmental and operational conditions (EOCs) [31,32]. VSHM detects damage by analyzing changes in the modal response of structures and can be categorized into natural frequency-based [33], mode shape-based [34], and FRF-based [35,36] approaches. A key advantage of VSHM is its ability to monitor structural integrity under real operating conditions, as modal parameters can be readily extracted from in-service structures. Moreover, unlike GWSHM, which relies on high-frequency excitations and mounted piezoelectric sensors, VSHM provides a more global assessment of structural health and does not require baseline data from an undamaged state, making it particularly suitable for long-term monitoring applications. Due to these advantages, VSHM has been extensively explored for aerospace structures, with applications ranging from laboratory experiments to full-scale structural monitoring.

1.2 Aims and objectives

Despite significant advancements in SHM methods for aerospace structures, several challenges remain that restrict their practical application, particularly when applied to dynamic and complex real-world conditions.

Environmental and Operational Effects A major limitation of GWSHM is its susceptibility to thermal variations, which significantly complicates the damage detection in aerospace structures

exposed to fluctuating environmental conditions. For instance, aircraft are often subjected to a wide operational temperature range, from $-40°C$ to $60°C$. Such temperature fluctuations induce changes in the material properties and guided wave propagation characteristics, which can obscure or mimic damage-induced signal variations. These effects limit the reliability and practicality of GWSHM methods in real-world applications. Consequently, developing robust SHM techniques capable of distinguishing damage from temperature-induced effects is essential to improving the performance and reliability of these systems under diverse environmental conditions.

The Trade-off Between Temperature Insensitivity and Small Damage VSHM methods demonstrate sensitivity to structural damage while maintaining robustness against EOCs. However, a key limitation is their reduced sensitivity to minor damage, as modal parameters exhibit limited responsiveness to small-scale damage. Additionally, mode shapes, commonly employed in VSHM, are predominantly sensitive to localized damage, making them less effective for detecting damage in large structures. Thus, addressing this inherent trade-off between environmental insensitivity and the ability to detect small-scale damage is crucial for advancing VSHM techniques and ensuring their effectiveness in real-world aerospace applications.

Reliance on Baseline Signals Many SHM methods rely on baseline signals obtained from a healthy structure to calculate damage indices for damage detection. Ensuring consistency between baseline signals and those obtained during real-time operations poses a substantial challenge, particularly in dynamic and long-term in-service environments. Variations in environmental and operational conditions can lead to discrepancies that compromise the accuracy of damage detection. As a result, SHM systems heavily reliant on baseline data are often confined to controlled experimental settings, limiting their applicability in real-world aerospace applications.

In-Service SHM Method Development Existing SHM techniques are predominantly offline or ground-based NDT, which increases maintenance costs and pose a risk of undetected damage, especially for progressive or rapidly propagating defects. This limitation is particularly critical for detecting structural deterioration that may develop between scheduled inspections. The development of in-service SHM systems capable of continuous, real-time monitoring during operation is

essential to address this gap. Such advancements would enable early detection of damage, reduce maintenance costs, and enhance the safety and reliability of aerospace structures in operational environments.

1.3 Thesis Outline

This thesis presents a series of novel, experimentally validated SHM methodologies that advance the state of the art in fatigue crack detection, quantification, and life prediction under realistic and variable service conditions. The research addresses long-standing challenges such as baseline dependency, temperature sensitivity, limited detection accuracy for small cracks, and poor adaptability to complex structural configurations. The original contributions of this work are outlined as follows:

Chapter 2 presents a comprehensive overview of the fundamental concepts and theoretical background of this research. The chapter begins with an introduction to both linear and nonlinear GWSHM methods, with particular emphasis on their applications to plate-like structures. This is followed by an examination of VSHM, focusing on the utilization of FRF and modal parameters for vibration analysis. Additionally, the chapter outlines auxiliary techniques that are integral to this study, including electromechanical impedance methods, fatigue-induced damage analysis and machine learning applications, highlighting their roles in enhancing the overall effectiveness of SHM methodologies.

Chapter 3 proposes a hybrid SHM method to address the challenges of conventional GWSHM and VSHM methods. This chapter highlights the integration of GWSHM and VSHM, focusing on their respective strengths and limitations in detecting and localizing structural damage. The proposed approach involves the extraction of damage-sensitive features from both guided wave and vibration responses, which are then analyzed using a neural pattern recognition and a Backpropagation Neural Network (BPNN). By leveraging the complementary characteristics of GWSHM and VSHM, the hybrid method achieves improved accuracy and reliability in damage detection and localization. Furthermore, this chapter establishes the theoretical framework for the hybrid approach, providing a foundation for further validation in subsequent sections.

Chapter 4 introduces an advanced hybrid SHM methodology that leverages the multifunctional-

ity of PZT transducers and the temperature resilience of modal analysis. This innovative approach leverages the multifunctionality of PZTs, which serve as both actuators and sensors for guided wave actuation and sesning, as well as for extracting transmissibility functions (TFs) for modal analysis. By combining these techniques, the proposed method eliminates the reliance on extensive baseline data or temperature compensation, enabling robust damage detection in structures with varying material properties across diverse temperature conditions.

Chapter 5 presents a novel methodology that integrates and extends multiple SHM approaches to detect and monitor fatigue-induced progressive damage under varying environmental conditions. Rather than performing a simple comparative analysis, this chapter develops a unified framework that systematically incorporates linear and nonlinear ultrasonic guided wave techniques alongside vibration-based methods. The proposed approach leverages the multifunctionality of PZT transducers to extract both guided wave features and modal parameters from a single hardware platform. This integrated methodology not only reveals the complementary strengths of each technique in capturing progressive damage at different scales, but also provides enhanced robustness against temperature variations. By combining high sensitivity, reduced baseline dependency, and environmental resilience, the developed framework offers a practical and scalable solution for reliable damage detection in complex structural systems. The innovation lies in the methodological integration and multifunctional sensing strategy, which together support the advancement of hybrid SHM systems tailored for real-world engineering applications.

Chapter 6 presents a novel baseline-free method for online fatigue crack detection and life prediction using second harmonic parameters. This method eliminates the need for baseline signals and enables early-stage damage detection in real time. By establishing a quantitative relationship between the second harmonic parameter and crack length, the method accurately detects cracks smaller than 2 mm and provides reliable fatigue life estimations. The approach is validated through comprehensive error analysis and robustness tests involving varied sensor positions, confirming its adaptability and consistency across different configurations. This chapter lays the foundation for practical, real-time SHM solutions that combine sensitivity and baseline independence, contributing to improved safety and maintenance planning in engineering structures.

Chapter 7 presents an advanced in-service, baseline-free SHM methodology for real-time crack

detection and growth modeling using passive PZT sensors. By utilizing the relative third harmonic parameter $\hat{\gamma}'$ under actual vibration loading, a dynamic piecewise linear (DPL) method is proposed to enable early crack detection in real-time. The method demonstrates superior predictive capability compared to traditional clustering methods, identifying cracks as small as 1.3 mm. A robustness analysis confirms the influence of sensor placement on detection sensitivity and verifies that the observed nonlinear features originate from the crack rather than noise. In addition, a physics-informed Long Short-Term Memory (PI-LSTM) model is developed for crack size quantification, achieving significantly higher accuracy than conventional LSTM or Paris' Law-based approaches. This chapter demonstrates the potential of combining passive sensing and machine learning for accurate and autonomous fatigue crack monitoring under in-service conditions, and establishes a promising direction for future SHM applications in complex environments.

The thesis finishes with conclusions and suggestions for future research.

1.4 Thesis Contribution

The main contributions of this research and the corresponding publications are listed below:

(1) Proposed a SHM method to address the challenges of GWSHM and VSHM methods.

- Yuhang Pan, Zahra Sharif Khodaei, and M.H. Aliabadi. A hybrid method based on vibration and guided waves for damage detection and localization. *Procedia Structural Integrity*, volume 52, pages 699-708, 2024 [37].

(2) Proposed a higher-level hybrid SHM methodology, integrating the damage sensitivity of guided waves with the temperature resilience of modal analysis.

- Yuhang Pan, Zahra Sharif Khodaei, and M.H. Aliabadi. A robust hybrid method for damage detection under varying environmental conditions. *Structural Health Monitoring*, pages 1-16, 2024 [38].

(3) Presented a comparative analysis of linear and nonlinear ultrasonic-guided wave methods and vibration-based methods highlighting their trade-offs in sensitivity, baseline dependency, and temperature robustness.

- Yuhang Pan, Zahra Sharif Khodaei, and M.H. Aliabadi. Progressive damage detection under varying temperatures: linear versus nonlinear ultrasonic-guided waves and vibration-based methods. *Waiting to submit*.

(4) Proposed a baseline-free method for online fatigue crack detection and growth modelling, addressing real-time monitoring challenges.

- Yuhang Pan, Zahra Sharif Khodaei, and M.H. Aliabadi. Online fatigue crack detection and growth modelling through higher harmonic analysis: A baseline-free approach [39]. *Mechanical System Signal Processing*, volume 224, 112167, 2025.

(5) Proposed an in-service fatigue crack monitoring method through baseline-free automated detection and physics-informed neural network quantification.

- Yuhang Pan, Zahra Sharif Khodaei, and M.H. Aliabadi. In-service fatigue crack monitoring through baseline-free automated detection and physics-informed neural network quantification [40]. *NDT & E International*, volume 153, 103360, 2025.

Chapter 2

Fundamental Concepts and Theoretical Background

2.1 Introduction

Ultrasonic-GWSHM and VSHM methods have been extensively studied for their applications in damage detection and integrity assessment. This chapter provides a comprehensive overview of the theoretical and practical foundations of these techniques. It begins with the principles of ultrasonic-guided wave propagation, covering both linear and nonlinear approaches. The discussion then transitions to vibration-based SHM, highlighting the importance of FRFs and modal parameters, such as natural frequencies, mode shapes, and damping ratios, in detecting and characterizing structural damage. Furthermore, auxiliary techniques, including fatigue-induced damage modeling, electromechanical impedance methods and machine learning algorithms, are introduced to enhance the performance of SHM methods. The chapter concludes with a summary of key findings and references for further exploration of the methodologies discussed.

2.2 Ultrasonic-guided wave based SHM

Ultrasonic GWSHM methods are broadly classified into linear and nonlinear approaches based on wave propagation characteristics and their interaction with structural damage [41, 42]. Linear methods leverage the predictable behavior of guided waves as they propagate through the material,

detecting damage such as cracks or delamination by analyzing changes in wave amplitude, phase, or time-of-flight. These techniques are widely used due to their simplicity and effectiveness in identifying visible or moderately sized damage [27, 32, 43]. In contrast, nonlinear methods utilize the generation of higher harmonics or wave modulation effects that arise when guided waves interact with micro-scale damage, such as early-stage fatigue or micro-cracks, which often remain undetectable by linear approaches [44–46]. The nonlinear features in the wave response significantly enhance sensitivity to subtle damage, making these methods particularly effective for detecting and monitoring the early stages of structural degradation.

2.2.1 Ultrasonic guided wave based SHM

Horace Lamb first described the propagation of elastic waves in thin plate and shell structures in 1917, a phenomenon now widely known as Lamb waves or ultrasonic guided waves [47]. In a thin isotropic and homogeneous plate, the lamb wave can be described in Cartesian tensor form as follows [48]:

$$\mu \cdot u_{i,jj} + (\lambda + \mu) \cdot u_{j,ji} + \rho \cdot f_i = \rho \cdot \ddot{u}_i, \quad (i, j = 1, 2, 3) \tag{2.1}$$

where u_i and f_i denote the displacement and body force in the x_i direction, respectively. The parameters ρ and μ are the density and shear modulus of the plate, and $\lambda = \frac{2\mu\nu}{1-2\nu}$ is the Lamé constant, with ν being the Poisson's ratio.

The displacement potential method, based on Helmholtz decomposition [49], is an effective approach to simplify this equation into two decoupled components under plane strain conditions:

$$\frac{\partial^2 \phi}{\partial x_1^2} + \frac{\partial^2 \phi}{\partial x_3^2} = \frac{1}{c_L^2} \frac{\partial^2 \phi}{\partial t^2}, \quad \text{governing longitudinal wave modes} \tag{2.2a}$$

$$\frac{\partial^2 \psi}{\partial x_1^2} + \frac{\partial^2 \psi}{\partial x_3^2} = \frac{1}{c_T^2} \frac{\partial^2 \psi}{\partial t^2}, \quad \text{governing transverse wave modes} \tag{2.2b}$$

Here, the potentials ϕ and ψ are expressed as:

$$\phi = [A_1 \sin(px_3) + A_2 \cos(px_3)] \cdot \exp[i(\xi x_1 - \omega t)] \tag{2.3a}$$

$$\psi = [B_1 \sin(qx_3) + B_2 \cos(qx_3)] \cdot \exp[i(\xi x_1 - \omega t)] \tag{2.3b}$$

where A_1, A_2, B_1, and B_2 are determined by the boundary conditions. The parameters ξ, ω, and λ_{wave} represent the wave-number, circular frequency, and wavelength of the wave, respectively. The wave numbers p and q are given by:

$$p^2 = \frac{\omega^2}{c_L^2} - \xi^2, \quad q^2 = \frac{\omega^2}{c_T^2} - \xi^2 \tag{2.4}$$

where $\xi = \frac{2\pi}{\lambda_{\text{wave}}}$ represents the wavenumber, and λ_{wave} is the wavelength of the propagating wave.

The velocities of the longitudinal (c_L) and transverse/shear (c_T) modes are defined as:

$$c_L = \sqrt{\frac{E(1-\nu)}{\rho(1+\nu)(1-2\nu)}} = \sqrt{\frac{2\mu(1-\nu)}{\rho(1-2\nu)}}, \quad c_T = \sqrt{\frac{E}{2\rho(1+\nu)}} = \sqrt{\frac{\mu}{\rho}} \tag{2.5}$$

where E denotes Young's modulus, $E = 2\mu(1+\nu)$. Lamb waves are thus the superposition of longitudinal and transverse/shear modes. An infinite number of modes coexist and superimpose on each other between the upper and lower surfaces of the plate.

Under plane strain conditions, the displacements in the wave propagation direction (x_1) and normal direction (x_3) are given by:

$$u_1 = \frac{\partial \phi}{\partial x_1} + \frac{\partial \psi}{\partial x_3}, \quad u_2 = 0, \quad u_3 = \frac{\partial \phi}{\partial x_3} - \frac{\partial \psi}{\partial x_1} \tag{2.6}$$

The corresponding stresses are:

$$\sigma_{31} = \mu \left(\frac{\partial u_3}{\partial x_1} + \frac{\partial u_1}{\partial x_3} \right) = \mu \left(\frac{\partial^2 \phi}{\partial x_1 \partial x_3} - \frac{\partial^2 \psi}{\partial x_1^2} + \frac{\partial^2 \psi}{\partial x_3^2} \right) \tag{2.7}$$

$$\sigma_{32} = \lambda \left(\frac{\partial u_1}{\partial x_1} + \frac{\partial u_3}{\partial x_3} \right) + 2\mu \frac{\partial u_3}{\partial x_3} \tag{2.8}$$

$$\sigma_{33} = \lambda \left(\frac{\partial^2 \phi}{\partial x_1^2} + \frac{\partial^2 \phi}{\partial x_3^2} \right) + 2\mu \left(\frac{\partial^2 \phi}{\partial x_3^2} + \frac{\partial^2 \phi}{\partial x_3 \partial x_1} \right) \tag{2.9}$$

For a plate with free upper and lower surfaces, the boundary conditions at both surfaces are applied as follows:

$$\begin{gathered} u(x,t) = u_0(x,t), \quad \text{displacement}, \\ t_i = \sigma_{ij} n_j, \quad \text{traction}, \\ \sigma_{31} = \sigma_{33} = 0 \quad \text{at } x_3 = \pm d/2 = \pm h. \end{gathered} \tag{2.10}$$

Given that d is the plate thickness and h is the half thickness, the general description of Lamb waves in an isotropic and homogeneous plate is expressed as:

$$\frac{\tan(qh)}{\tan(ph)} = \frac{4\xi^2 qp\mu}{(\lambda\xi^2 + \lambda p^2 + 2\mu p^2)(\xi^2 - q^2)} \tag{2.11}$$

Rearranging the equation and considering that the tangent trigonometric function is defined of sine and cosine, which exhibit symmetric and anti-symmetric properties, the equation can be divided into two parts: one representing symmetric modes and the other representing anti-symmetric modes. This demonstrates that Lamb waves in a plate consist of both symmetric and anti-symmetric modes.

$$\frac{\tan(qh)}{\tan(ph)} = -\frac{4\xi^2 qp}{(\xi^2 - q^2)^2}, \quad \text{for symmetric modes} \tag{2.12a}$$

$$\frac{\tan(qh)}{\tan(ph)} = -\frac{(\xi^2 - q^2)^2}{4\xi^2 qp}, \quad \text{for anti-symmetric modes} \tag{2.12b}$$

For clarity, the symbols S_i and A_i $(i = 0, 1, \dots)$ are used to denote symmetric and anti-symmetric Lamb modes, respectively. The illustration of the symmetric and anti-symmetric Lamb modes is shown in Figure 2.1.

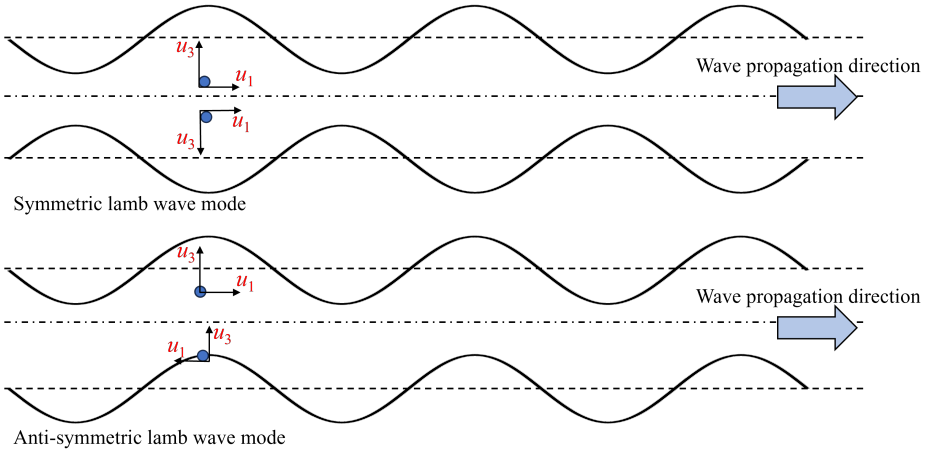


Figure 2.1: The symmetric and anti-symmetric Lamb modes.

The propagation of guided waves is influenced by various factors, including the elastic constants, density, geometry of the solid structure, and excitation frequency [50]. Guided waves exhibits dispersion, meaning their velocities depend on the wave frequency and plate thickness. For a homogeneous isotropic plate, the propagation of guided waves follows the Rayleigh-Lamb equation

[51]. Finite plates support two infinite sets of dispersive guided waves modes: the symmetric modes and the anti-symmetric modes. Determining the group velocity is crucial for interpreting signals, as it provides insights into the types of modes traveling through the structure. The traditional method for computing the group velocity c_g involves calculating a wave group (of the envelope) derived from the phase velocity c_p. The phase velocity is calculated as:

$$c_p = \frac{\omega}{\xi} \tag{2.13}$$

where the group velocity is defined as the derivative of ω with respect to ξ:

$$c_g = \frac{d\omega}{d\xi} = c_p^2 \left[c_p - f \frac{dc_p}{df} \right]^{-1} \tag{2.14}$$

Dispersion curves are developed by plotting phase or group velocities versus the frequency-thickness. For the aluminum plate considered, with material properties including a density of $\rho = 2700\,\mathrm{kg/m^3}$, Poisson's ratio of $\nu = 0.33$, and Young's modulus of $E = 64\,\mathrm{GPa}$, the dispersion curve is presented in Figure 2.2 [48]. The multi-mode behavior observed in the dispersion curve, combined with the dispersive nature of guided waves, leads to complex waveforms that are challenging to interpret. Understanding the presence of multiple guided wave modes and their dispersion behavior is crucial for the application of GWSHM. By selecting frequencies below the cut-off frequency, where only the A_0 and S_0 modes are present, signal interpretation becomes more effective. It is also evident that the S_0 mode travels at a significantly higher velocity than the A_0 mode, simplifying the distinction between the two modes in analysis.

Transducers of ultrasonic guided waves PZT is the most commonly employed low-profile transducers in guided wave applications. PZT, typically made from piezoelectric lead zirconate titanate, are widely utilized in SHM due to their effectiveness in generating and receiving guided waves. These transducers are generally surface-mounted or embedded within the structure and are activated by AC signals to generate guided waves. Figure 2.3 illustrates aluminum plates embedded with two commonly used PZT sensors: Piezoelectric Ceramic Discs and DuraAct patch transducers). The intensity and directionality of waves generated by a single PZT transducer depend on its polarization direction and geometry. For instance, a circular transducer (Figure 2.3(a)) with

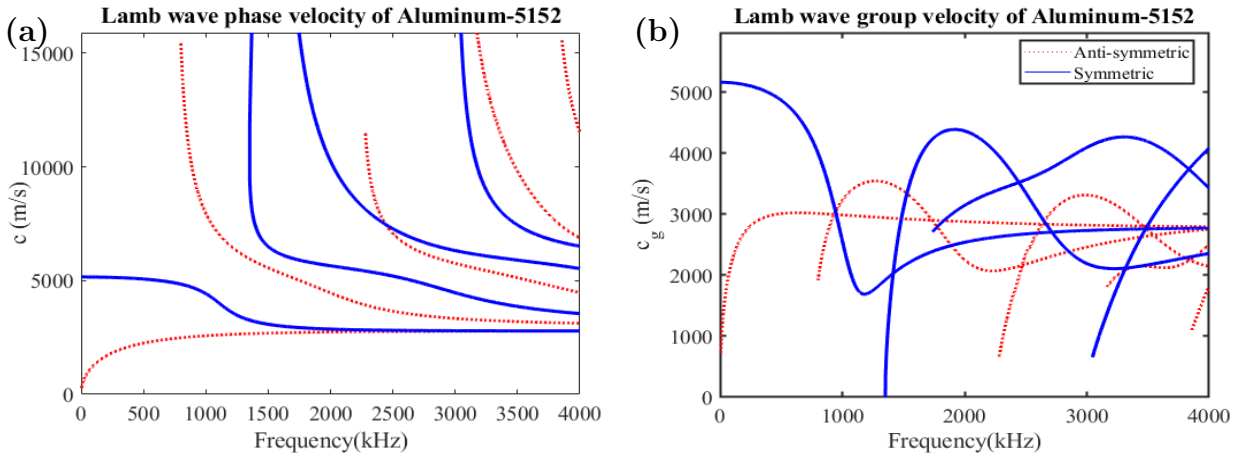


Figure 2.2: Dispersion curves of (a) phase velocity and (b) group velocity for Aluminum-5152 with 2 mm thickness.

polarization perpendicular to the host structure generates a uniform strain field in all in-plane directions, resulting in an omnidirectional wave field in an isotropic plate. Despite their advantages, these transducers are inherently brittle and prone to fracture, which limits their long-term durability in SHM applications. To address this limitation, laminated solutions such as the DuraAct transducer (PI Ceramics) have been developed (Figure 2.3(b)). The DuraAct transducer consists of a piezoceramic wafer encapsulated in a polyamide coating, which serves as both a mechanical protector and an electrical insulator. This encapsulation significantly enhances the transducer's durability and robustness [52], making it suitable for extended use in SHM applications.

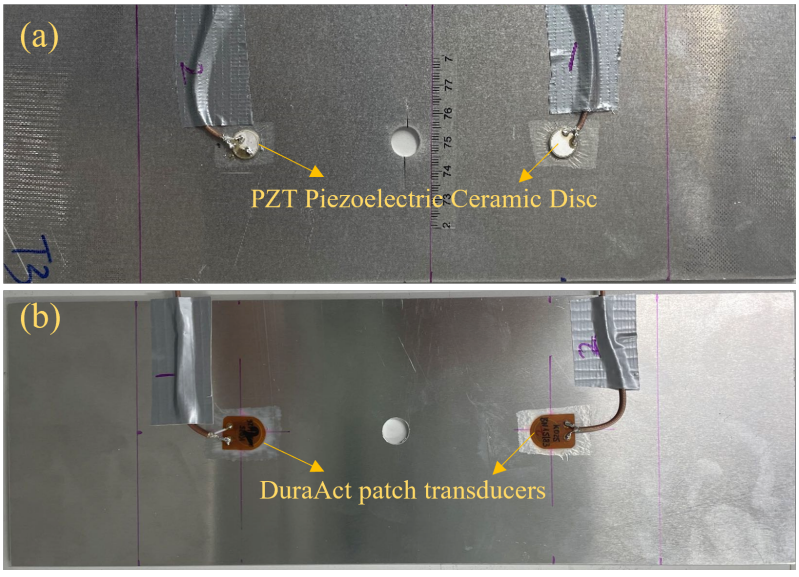


Figure 2.3: The specimens with (a) PZT piezoelectric Ceramic Disc and (b) DuraAct patch transducers.

Actuation and sensing of guided waves Ultrasonic guided waves are generated using a PZT by applying a time-varying voltage signal to its electrodes. Both narrow-band and broad-band frequency signals can be utilized for excitation. Typical narrow-band signals consist of three- to five-cycle tone bursts, windowed using functions such as Hanning or Gaussian. The selection of the number of cycles and the window function is crucial for generating a narrow pulse with a frequency spectrum centered around the desired excitation frequency. Instead of generating a narrow-band response at multiple frequencies, a broad-band frequency response can be generated using a linear chirp signal. This approach allows the generation of a broad-band response that can later be processed to reconstruct an equivalent narrow-band response at multiple frequencies. The mathematical expression for a linear chirp excitation signal is:

$$s^c(t) = w(t) \sin\left(2\pi f_0 t + \frac{f_1 - f_0}{T} t^2\right) \tag{2.15}$$

where f_0 and f_1 are the starting and ending frequencies, respectively, T is the duration of the chirp, and $w(t)$ is a rectangular window with a user-defined amplitude, starting at $t = 0$ and ending at $t = T$. For narrow-band excitation, a Hanning windowed tone-burst signal is often used. The Hanning window ensures a smooth tapering of the signal at both ends, minimizing spectral leakage. The equation for a Hanning windowed tone-burst excitation signal is:

$$s^b(t) = w(t) \sin(2\pi f_c t), \quad w(t) = \frac{1}{2}\left[1 - \cos\left(\frac{2\pi f_c t}{n_c}\right)\right] \tag{2.16}$$

where f_c is the center frequency, and n_c is the number of cycles in the tone-burst signal. The Hanning window serves to localize the excitation energy within a narrow frequency band, ensuring effective generation of guided waves. The response to a tone-burst excitation signal, denoted as $s^b(t)$, can be reconstructed from the chirp response in the frequency domain. This reconstruction process utilizes the frequency components of the chirp response to isolate the desired narrow-band response, as described in [53]:

$$R^b(\omega) = R^c(\omega) \frac{S^b(\omega)}{S^c(\omega)} \tag{2.17}$$

where $R^c(\omega)$ is the Fourier transform of the measured response to the chirp excitation $s^c(t)$, and $S^b(\omega)$ and $S^c(\omega)$ are the Fourier transforms of the tone-burst excitation $s^b(t)$ and chirp excitation

$s^c(t)$, respectively. The tone-burst response in the frequency domain is then transformed back to the time domain using an inverse Fourier transform. This method enables the reconstruction of narrow-band responses for any number of cycles and types of window functions from the broad-band chirp response.

2.2.2 Nonlinear ultrasonic guided wave-based SHM

Higher harmonic generation is a phenomenon where the waveform of an incident wave becomes distorted due to the nonlinear elastic response of the medium, leading to the appearance of higher harmonic components in the transmitted wave. This concept is illustrated in Figure 2.4, which demonstrates how material nonlinearity leads to higher harmonic generation. The schematic on the left describes an experimental setup where an actuator generates an incident wave propagating through a plate, while a sensor measures the resulting transmitted signal. As illustrated in the figure, when a low-frequency signal (f_a) and a high-frequency signal (f_b) are simultaneously applied to a structure, the resulting frequency spectrum differs depending on the structural condition. In an undamaged (linear) structure, the response contains only the original input frequencies f_a and f_b, as shown in the upper part of the figure. However, in a damaged (nonlinear) structure, the inherent material nonlinearity introduces distortion in the waveform, resulting in additional spectral components. These include higher harmonics (e.g., nf_a, nf_b) and modulation frequencies ($f_b \pm f_a$), as described in the bottom spectrum. The presence of these nonlinear frequency components provides clear evidence of structural damage and forms the basis for nonlinear ultrasonic-based damage detection techniques.

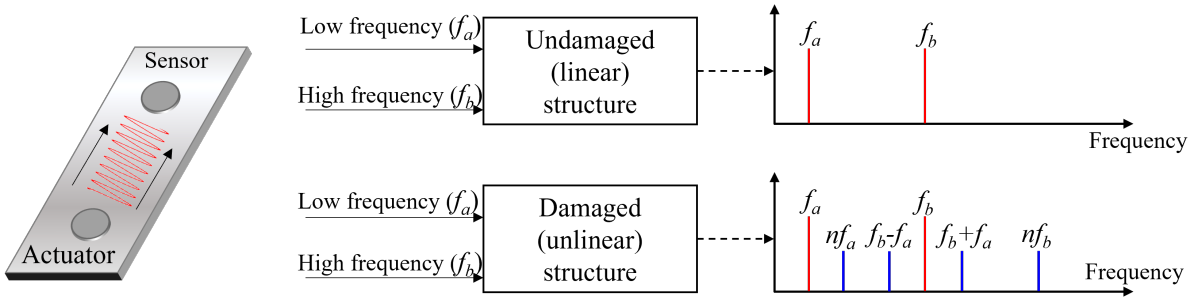


Figure 2.4: Distortion in the waveform during propagation by nonlinear elasticity and higher harmonic generation.

For a one-dimensional case, this relationship can be expressed as the nonlinear Hooke's law [54]:

$$\sigma = C_{11}\epsilon + \frac{1}{2}\beta C_{11}\epsilon^2 + \dots \tag{2.18}$$

where σ, ϵ, C_{11}, and β represent stress, strain, elastic constant, and second-order nonlinear parameter, respectively.

The generation of higher harmonics can be analogous to the behaviour of a nonlinear spring. In a spring with perfectly linear stiffness, the displacement response is directly proportional to the input force, maintaining a consistent linear relationship. However, when the spring exhibits nonlinear stiffness, the displacement becomes distorted due to asymmetry in the positive and negative phases, leading to the generation of harmonics in the frequency domain. Similarly, when an ultrasonic sinusoidal wave propagates through a nonlinear elastic medium, its waveform becomes distorted due to the medium's nonlinear stress-strain relationship. At low amplitudes, this relationship is nearly linear, resulting in a waveform that remains close to its original sinusoidal shape, with minimal generation of higher harmonics. However, as the amplitude of the ultrasonic wave increases, the effects of nonlinearity become significant, causing progressive distortion of the waveform. This distortion manifests in the frequency spectrum through the generation and amplification of higher harmonic components, as reported in previous studies [55–57]. The longitudinal wave propagation in an isotropic solid can be described by the following equation of motion:

$$\rho\frac{\partial^2 u(x,t)}{\partial t^2} = \frac{\partial \sigma_{xx}}{\partial x} \tag{2.19}$$

where ρ is the material density, $u(x,t)$ is the displacement of the particle along the propagation direction x at time t, and σ_{xx} is the normal stress along x. The constitutive equation for quadratic nonlinearity is [58]:

$$\sigma_{xx} = \sigma_0 + M_{11}\left(\frac{\partial u}{\partial x}\right) + M_{111}\left(\frac{\partial u}{\partial x}\right)^2 + M_{1111}\left(\frac{\partial u}{\partial x}\right)^3 + \dots \tag{2.20}$$

where σ_0 is the initial stress in the material, which is equal to 0 before the fatigue test. M_{11} and M_{111} are the second- and third-order elastic Huang coefficients, respectively [59]. These coefficients can be further calculated as:

$$M_{11} = C_{11} \tag{2.21}$$

$$M_{111} = 3C_{11} + C_{111} \tag{2.22}$$

$$M_{1111} = \frac{3}{2}C_{11} + 3C_{111} + \frac{1}{2}C_{1111} \tag{2.23}$$

Based on the above equations, the longitudinal wave propagation equation is expressed as:

$$\frac{\partial^2 u(x,t)}{\partial t^2} = c^2 \left[1 - \beta\frac{\partial u}{\partial x} - \gamma\left(\frac{\partial u}{\partial x}\right)^2\right]\frac{\partial^2 u}{\partial x^2} \tag{2.24}$$

where β and γ are the second- and third-harmonic nonlinear parameters, and c is the propagation velocity for the longitudinal wave within the material [60–62]. For a pristine material, β and γ can be calculated as:

$$\beta = -\frac{3(C_{111} + C_{1111})}{C_0 + C_{11}} \tag{2.25}$$

$$\gamma = -\frac{3(C_{1111} + C_{111})}{C_0 + C_{11}} \tag{2.26}$$

Perturbation theory is employed to solve equation (2.24), assuming the displacement u has a perturbation solution:

$$u = u_1 + u_2 + u_3 \tag{2.27}$$

where u_1, u_2, and u_3 are the first, second, and third-order perturbation solutions, respectively, corresponding to the displacement of the fundamental, second, and third harmonic displacements [63]:

$$u_1 = A_1\cos(kx - \omega t) \tag{2.28}$$

$$u_2 = A_2\cos(2kx - 2\omega t) = \frac{1}{8}\beta k^2 A_1^2 x\cos(2(kx - \omega t)) \tag{2.29}$$

$$u_3 = A_3\cos(3kx - 3\omega t) = \frac{1}{32}\gamma k^4 A_1^3 x^2\cos(3(kx - \omega t)) \tag{2.30}$$

In equation (2.28)-(2.30), A_1, A_2, and A_3 are the amplitudes of the fundamental, second, and third harmonic frequencies [63]. β is the second harmonic parameter in this research, which can be obtained by experiment or simulation, and it can be expressed as:

$$\beta = \frac{8A_2}{A_1^2 k^2 x} \tag{2.31}$$

The parameter γ denotes the third harmonic parameter, which can also be obtained by experiment or simulation, and is expressed as [64]:

$$\gamma = \frac{32A_3}{A_1^3 k^4 x^2} \tag{2.32}$$

The parameters β and γ are generally considered as the absolute second and third harmonic parameters, respectively. However, their direct measurements are challenging due to the extremely small amplitude of the second harmonic displacement, which is typically less than 1 nm [65]. To address this issue, the relative second harmonic parameter β' and the relative third harmonic parameter γ' are often employed as practical alternatives for crack detection. These relative parameters are more accessible to measure and provide valuable insights into the detection and progression of damage.

$$\beta' = \frac{A_2'}{(A_1')^2} \tag{2.33}$$

$$\gamma' = \frac{A_3'}{(A_1')^3} \tag{2.34}$$

where A_1' represents the amplitude of the fundamental frequency component obtained from the received signal, while A_2' and A_3' are the amplitudes of the second and third harmonic frequency components, respectively. Compared to the absolute parameters β and γ, the relative parameters β' and γ' are more practical and easier to measure, as they rely solely on the amplitudes of the fundamental and second harmonic signals in the frequency domain [66, 67]. This simplifies the experimental process while still providing reliable indicators for damage detection.

However, generating the cumulative harmonic waves requires synchronism and non-zero power flux. Specifically, synchronism involves matching the phase and group velocity between the fundamental and corresponding harmonic modes, facilitating energy transfer from the fundamental mode to its harmonic components. Non-zero power flux ensures a net energy flow between these modes. Many researchers have investigated phase-matching and non-zero power flux phenomena. Srivastava et al. [68] theoretically examined the symmetry characteristics of primary and secondary

waves, including higher harmonics beyond the second order, and validated their findings through comprehensive experiments. Similarly, Müller et al. [69] employed parity analysis based on the symmetric or antisymmetric nature of the displacement profile to identify secondary modes with zero power flux and to evaluate group velocity matching. Matsuda et al. [70] identified all phase-matching points for Lamb waves in plates and also assessed group velocity matching. Chillara et al. [71] further advanced the field by formulating the problem in terms of self- and mutual-wave interactions, providing a framework for solving various boundary value problems. The details of calculation process can be found in [54]. While these studies have significantly advanced the theoretical understanding of cumulative harmonic wave generation, they also reveal several limitations when applied to practical scenarios. Achieving synchronism and non-zero power flux is highly sensitive to structural geometry, material properties, and excitation parameters, which are difficult to control in real-world scenarios. Due to the complexity of precise mode tuning and boundary effects, this study instead focuses on more accessible nonlinear features—such as higher harmonics and modulation components—that do not rely on strict phase-matching conditions but still provide effective indicators of damage.

2.3 Vibration-based SHM

VSHM methods detect structural damage by monitoring changes in modal parameters, which serve as key indicators of a structure's dynamic properties. Modal parameters, including natural frequencies, mode shapes, and FRFs, are highly sensitive to variations in stiffness, mass, or damping caused by damage. This sensitivity makes them reliable for identifying and characterizing structural damage. Based on the type of modal parameter utilized, VSHM methods can be broadly categorized into three main categories: FRF-based methods and modal parameter-based methods.

2.3.1 FRF for vibration analysis

The FRF is a fundamental concept in structural dynamics, defined as a transfer function in the frequency domain. It characterizes the relationship between an input force and the resulting structural response, which is typically measured in terms of displacement, velocity, or acceleration

[72, 73]. The FRF is particularly valuable for identifying dynamic characteristics such as natural frequencies, damping, and mode shapes, parameters critical to VSHM. FRFs are complex functions comprising real and imaginary components, allowing for the extraction of magnitude and phase information. They are derived using Fourier transform techniques, enabling detailed analysis of structural behavior in the frequency domain. This makes FRFs a versatile tool for assessing both global and localized damage in structures [74]. The input-output relationship of a system in the frequency domain can be mathematically expressed as:

$$X(\omega) = H(\omega)F(\omega) \tag{2.35}$$

where $X(\omega)$ is the structural response (e.g., displacement or acceleration) in the frequency domain, $F(\omega)$ is the applied force in the frequency domain, and $H(\omega)$ is the FRF, representing the transfer function of the system. For a system with n degrees of freedom, the equation of motion is expressed as:

$$M\ddot{x}(t) + C\dot{x}(t) + Kx(t) = f(t) \tag{2.36}$$

where M, C, and K are the mass, damping, and stiffness matrices, respectively, $x(t)$ is the absolute displacement, $\dot{x}(t)$ denotes the first time derivative of displacement (i.e., velocity), and $\ddot{x}(t)$ denotes the second time derivative of displacement (i.e., acceleration). and $f(t)$ is the applied force. Considering a harmonic input, the force and displacement can be expressed as [75]:

$$f(t) = F(\omega)e^{i\omega t}, \quad x(t) = X(\omega)e^{i\omega t} \tag{2.37}$$

Substituting these expressions into equation (2.36), the FRF matrix $H(\omega)$ can be derived as:

$$H(\omega) = \left(-\omega^2 M + i\omega C + K\right)^{-1} \tag{2.38}$$

In addition to the FRF, the transmissibility function (TF) is another important metric widely used in vibration analysis and SHM. The TF is defined as the ratio between two measured outputs in the frequency domain [76]:

$$T_{ij}^{k}(\omega) = \frac{X_{ik}(\omega)}{X_{jk}(\omega)} \tag{2.39}$$

where $X_{ik}(\omega)$ is the frequency-domain response at the degree of freedom (DOF) i under the excitation force at DOF k, and $X_{jk}(\omega)$ is the frequency-domain response at DOF j under the same excitation. Unlike the FRF, the TF is determined solely by the locations of the excitation and response points and is independent of the amplitude of the excitation force [77].

The FRF, on the other hand, is defined as the ratio between the frequency-domain response at a specific point and the frequency-domain excitation force [77]:

$$H_{ik}(\omega) = \frac{X_{ik}(\omega)}{F_k(\omega)} \tag{2.40}$$

where $H_{ik}(\omega)$ represents the FRF, and $F_k(\omega)$ is the excitation force. By combining equation (2.39) and equation (2.40), the relationship between the TF and FRF can be derived as:

$$T_{ij}^{k}(\omega) = \frac{H_{ik}(\omega)}{H_{jk}(\omega)} \tag{2.41}$$

In FRFs, peaks correspond to the resonant frequencies of structures, while dips represent anti-resonant frequencies. Based on equation (2.41), these peaks and dips in FRFs correspond to similar features in TFs. Therefore, the TF can effectively reflect the modal properties of structures, similar to the FRF.

FRF and TF provide critical insights into structural properties by analyzing how structural responses are influenced by input forces (for FRF) or relative changes between measured responses (for TF). Changes in FRF characteristics, such as shifts in resonance peaks or alterations in damping, and variations in TF values, which depend exclusively on relative modal properties, can serve as reliable indicators of structural damage [78]. Additionally, FRF-based methods offer the flexibility to accommodate varying environmental and operational conditions by employing compensation techniques to mitigate noise and variability. In contrast, TF-based methods inherently eliminate the influence of excitation force amplitude, making them particularly robust in dynamic environments. By integrating the strengths of both FRF and TF analyses, VSHM methods can effectively detect and quantify damage in complex structures, ensuring a more reliable and comprehensive SHM.

2.3.2 Modal Parameters-Based SHM

Modal parameters, such as natural frequencies, mode shapes, and damping ratios, are widely used in SHM due to their sensitivity to damage-induced changes in structural properties. These parameters effectively characterize the dynamic behavior of structures, offering insights into stiffness reductions, mass variation, and changes in energy dissipation caused by damage. As a result, parametric methods have been developed to compare the dynamic properties of pristine and damaged structures even under uncertain conditions, enabling the monitoring of structural deterioration [79]. These approaches utilize accelerometers to capture vibration signals, which are then processed to extract modal parameters—such as damping, stiffness, mode shapes, and natural frequencies—serving as critical features for damage detection.

Natural frequency-Based Damage Index Natural frequency-based methods use changes in natural frequencies as fundamental features for damage detection [80]. The primary advantage of these methods lies in their ease of measurement at a few accessible points on the structure and their relative insensitivity to experimental noise. By analyzing variations in natural frequencies, these methods provide a robust theoretical framework for determining the location and severity of structural damage. Gudmundson et al. [81] employed an energy-based perturbation approach to derive explicit expressions for the resonance frequencies of various damaged structures, accounting for both stiffness loss and mass reduction. Liang et al. [82] investigated frequency sensitivity in simply supported and cantilevered beams with a single crack, developing analytical relationships between first-order changes in eigenfrequencies and the location and severity of the damage. This approach involves symbolic computation of the characteristic equation. Similarly, Morassi [83] demonstrated that the frequency sensitivity of a cracked beam is proportional to the potential energy stored at the cracked cross-section of the undamaged beam. The ratio of frequency changes across different modes depends solely on the damage location. Both Liang's and Morassi's methods are based on Euler-Bernoulli beam theory, modeling the crack as a massless, infinitesimal rotational spring, and are valid only for small defects. Kasper et al. [84] extended these approaches by deriving explicit expressions for wavenumber and frequency shifts in cracked symmetric uniform beams. These expressions apply to both shallow and deeper cracks but rely on high-frequency

approximations, limiting their accuracy for the fundamental mode and for cracks near boundary regions.

Modal Strain Energy-Based Damage Index The modal strain energy (MSE) approach has gained significant recognition as one of the most reliable vibration-based damage detection methods due to its adaptability and effectiveness [85]. Initially introduced by Stubbs and Kim in 1996, the MSE-based damage index technique detects anomalies by identifying reductions in modal strain energy. Such reductions correspond to stiffness degradation in the structure, which hinders its ability to restore energy—behavior consistent with Bernoulli-Euler beam theory [86]. Over time, four main categories of MSE-based methods have been developed: the damage index, modal strain energy changes, cross-modal strain energy, and iterative modal strain energy approaches [87]. Based on the work of Tan et al. [88], the modal strain energy, denoted by U, can be mathematically expressed as:

$$U = \int \frac{EI}{2} \left(\frac{d^2 y}{dx^2} \right)^2 dx \tag{2.42}$$

where EI represents the flexural rigidity of the section, and $\frac{d^2y}{dx^2}$ denotes the curvature (with y as the vertical deflection and x as the distance along the structural length). From equation (2.42), the MSE-based damage indicator β_{ji} can be defined to compare the damaged and pristine states for the i-th mode at the j-th location:

$$\beta_{ji} = \frac{(U_{\text{intact}})_{ji} - (U_{\text{damaged}})_{ji}}{(U_{\text{intact}})_{ji}} \tag{2.43}$$

where $(U_{\text{intact}})_{ji}$ and $(U_{\text{damaged}})_{ji}$ denote the modal strain energies of the i-th mode at the j-th location in the pristine and damaged states, respectively [89]. A higher value of β_{ji} indicates greater deviation from the reference (intact) state, thus signaling more severe structural damage.

The modal flexibility-based damage index Beyond MSE-based indices, modal flexibility provides an alternative approach for structural damage identification by leveraging natural frequency and mass-normalized mode shapes. Initially proposed by Pandey and Biswas [90], this approach was later adopted by Wickramasinghe et al. [91] to detect deterioration in main cables and hangers of suspension bridges. Additionally, it has been integrated with modal curvature

methods to identify multiple cracks in beam structures [92]. Due to its demonstrated efficiency and accuracy, modal flexibility has become a critical parameter in SHM applications. Modal flexibility, denoted as F, is mathematically expressed as:

$$F = \sum_{i=1}^{n} \frac{1}{\omega_i^2} \phi_i \phi_i^T \tag{2.44}$$

where ϕ_i is the i^{th} mode shape, ω_i is the i^{th} modal frequency, and n represents the number of degrees of freedom. Damage-induced reductions in structural stiffness increase structural flexibility, which can be quantified as the variability in modal flexibility:

$$\Delta[F] = [F^{(*)}] - [F] \tag{2.45}$$

where $F^{(*)}$ represents the damaged state of the structure. The absolute maximum value in each column of $\Delta[F]$ corresponds to the modal flexibility change, ΔF, at the associated node. Based on the work of Tan et al. [89], the percentage change in modal flexibility ($\Delta F\%$) is further defined as shown in equation (2.45).

Modal Assurance Criterion (MAC) The MAC is widely acknowledged as a key modal indicator in SHM, which provides a quantitative measure of changes in mode shapes, making it valuable tool for identifying the transition from an undamaged (healthy) to a damaged state [93]. Commonly applied in bridge health monitoring, MAC has been used to evaluate the stability of measured mode shapes in long-span cable-stayed bridges [94] and to assess uncertainties arising from operational modal analysis in health monitoring [95]. Since changes in a structure's dynamic characteristics often indicate the onset of damage, MAC serves as a dimensionless metric to correlate mode shapes between two states. The i^{th}-order MAC value is defined as:

$$MAC_i = \frac{\left(\{\phi_i\}^T \{\phi_i^*\}\right)^2}{\left(\{\phi_i\}^T \{\phi_i\}\right)\left(\{\phi_i^*\}^T \{\phi_i^*\}\right)} \tag{2.46}$$

Here, $\{\phi_i\}$ represent the i^{th}-order modal vibration mode of the undamaged structure, while $\{\phi_i^*\}$ represents the corresponding mode of the damaged structure.

Modal Curvature-Based Damage Index Modal curvature has demonstrated significant advantages in structural damage detection, particularly in its ability to accurately localize damage

and its higher insensitivity to environmental variations compared to natural frequencies [96]. To estimate the modal curvature at a specific measurement point j, the central difference approximation is commonly utilized, relying on the displacement data of the mode shape. The modal displacement function, which forms the basis for this estimation, is expressed as:

$$\phi''_{ij} = \frac{\phi_{i,j+1} - 2\phi_{i,j} + \phi_{i,j-1}}{L^2} \tag{2.47}$$

ϕ_{ij} denotes the modal displacement for the j^{th} mode shape at the i^{th} measurement point, and L is the spacing between successive measurement points. This approach enables deriving the damage index directly from the modelled data, eliminating the need for baseline measurements of the undamaged structure. To mitigate the influence of measurement noise and reduce spurious peaks, the damage index is adjusted by its standard deviation. Consequently, the extent of damage can be quantified by assessing the change in mode shape curvature, as summarized by Altunışık et al. [92].

$$\phi''_{ij} = \sum_{j=1}^{n} \left| (\phi^*_{ij})'' + (\phi_{ij})'' \right| \tag{2.48}$$

In the above equation, the superscript $(\cdot)^*$ denotes the damaged state, and n represents the number of modes considered. Additionally, hybrid techniques that integrate modal curvature with modal flexibility have been employed to detect multiple cracks in beam structures [92], enhancing the accuracy and robustness of damage detection [92].

2.4 Auxiliary techniques

This section so far have presented the theoretical background required for GWSHM and VSHM utilized in this research. This section further provides introduction on other methods that have been key enablers in this PhD research: Electro-mechanical Impedance analysis, fatigue life analysis and machine learning application. Detailed descriptions of these techniques and their respective methodologies are provided in this section.

2.4.1 Electro-mechanical Impedance for Integrity assessment of piezoelectric transducers

Piezoelectric transducers operate by converting electrical energy into mechanical energy, or vice versa, through electromechanical coupling. The mechanical interaction between the transducer and the structure influences the electrical characteristics of the piezoelectric transducers. This relationship enables the use of electromechanical impedance or admittance measurements to evaluate the integrity of both the transducer and its bonding, as well as to detect changes in the mechanical properties of the structure.

Electrical admittance is defined as the ease with which a circuit or device allows current to flow, represented as the ratio of input voltage V to the current I. Sirohi and Chopra [97] formulated the electrical admittance of a piezoelectric transducer under free boundary condition as:

$$Y_{\text{free}}(\omega) = \frac{I}{V} = i\omega \frac{wl}{t_c} \left[\varepsilon_{33}^{T}(1 - i\delta)\right] \tag{2.49}$$

where w, l, and t_c are the width, length, and thickness of the PZT transducer, δ is the dielectric loss tangent, and ε_{33}^{T} is the dielectric permittivity of the PZT transducer.

Liang et al. [98] demonstrated that when a PZT transducer is bonded to the surface of a host structure, the electrical admittance $Y(\omega)$ is directly influenced by the mechanical impedance of the structure, $Z_s(\omega)$, and the mechanical impedance of the PZT transducer itself, $Z_a(\omega)$. This relationship is expressed as:

$$Y(\omega) = i\omega \frac{wl}{t_c} \left[\varepsilon_{33}^{T}(1 - i\delta) - d_{31}^2 Y_p^E + \frac{Z_a(\omega)}{Z_a(\omega) + Z_s(\omega)} d_{31}^2 Y_p^E \left(\tan kl/kl\right)\right] \tag{2.50}$$

where Y_p^E is the Young's modulus of the PZT transducer at zero electric field, d_{31} is the piezoelectric coupling constant, and k is defined as:

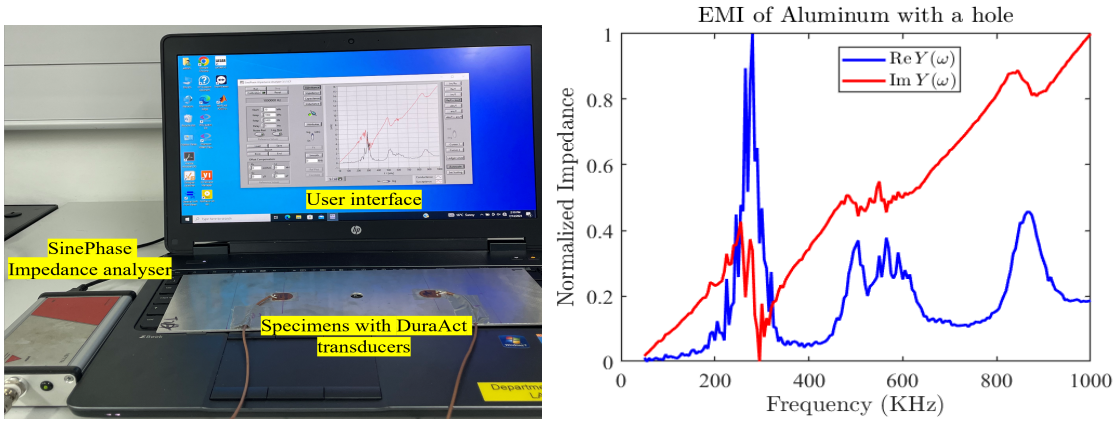
$$k = \omega \sqrt{\frac{\rho}{Y_p^E}} \tag{2.51}$$

Electrical impedance, denoted as Z, is the measure of the opposition that a circuit presents to a current when a voltage is applied. Electrical impedance is the inverse of electrical admittance

and can be derived as:

$$Z(\omega) = \frac{\mathrm{Re}Y(\omega)}{\mathrm{Re}Y(\omega)^2 + \mathrm{Im}Y(\omega)^2} - i\frac{\mathrm{Im}Y(\omega)}{\mathrm{Re}Y(\omega)^2 + \mathrm{Im}Y(\omega)^2} \tag{2.52}$$

The impedance spectrum of a piezoelectric transducer bonded to a structure serves as a reliable indicator of the transducer's integrity and the presence of damage in the structure. In this study, the electrical impedance and admittance of piezoelectric transducers were measured using a SinePhase Impedance Analyzer (see Figure 2.5(a)). As shown in Figure 2.5(b), when the sensor is attached to an aluminum structure, its resonance frequency falls within the range of 200–400 kHz. Consequently, this resonance frequency range is employed to evaluate the bonding state of the transducer.



(a) **(b)**

Figure 2.5: (a) SinePhase Impedance analyser with measurement setup and User interface, (b) Real and imaginary parts of the impedance of a DuraAct transducer being attached to the Aluminum.

2.4.2 Fatigue Life Analysis

Fatigue Life analysis is a key design consideration for metallic structures, particularly in aerospace and other high-performance industries. Even when applied stresses remain below the material's ultimate tensile strength, repeated stress cycles can progressively accumulate microscopic damage, ultimately leading to crack initiation and propagation. If left undetected, such damage can cause catastrophic failure. Figure 2.6 shows the structural areas prone to fatigue damage in early Airbus A300 design [2]. Fatigue damage arises from cyclic stress, which induces localized plastic

deformation. These repeated deformations cause microstructural changes, such as dislocation accumulation and grain boundary weakening, ultimately leading to crack formation. The fatigue failure process is conventionally divided into three stages [3], as illustrated in Figure 2.7.

The fatigue crack propagation model characterizes the behavior of cracks under cyclic loading, dividing the process into three distinct stages: In Stages I and II, crack propagation is governed by the fatigue mechanism. The stress state of the crack during these stages is described by the stress intensity factor (SIF) range, ($\Delta K = K_{\max} - K_{\min}$), which represents the difference between the maximum and minimum SIFs during a loading cycle. In Stage III, however, the crack propagation transitions to being governed by the fracture mechanism, where the stress state of the crack is described by the maximum SIF ($K_{\max}$) [59].

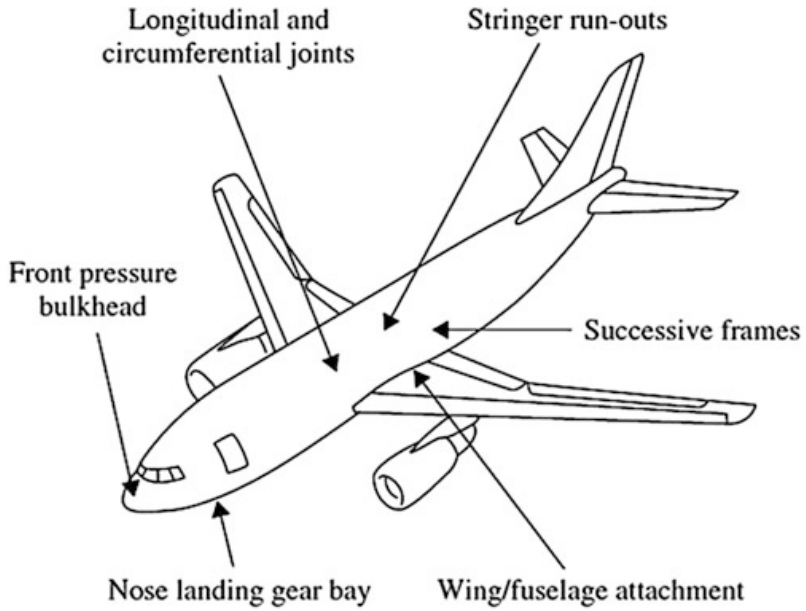


Figure 2.6: Common fatigue failure zones for Airbus A300 [2].

Crack Initiation Fatigue initiates with the nucleation of microscopic cracks, often originating at material defects such as surface roughness, grain boundaries, or inclusions. This initial stage is heavily affected by the material's microstructure, the surface condition, and the presence of residual stresses. During this stage, cracks are normally too small to be detected using conventional techniques. The fatigue life during this phase is often characterized using the S–N (stress–life) curve, which describes the relationship between the applied cyclic stress amplitude and the number of cycles to failure for specimens without visible cracks.

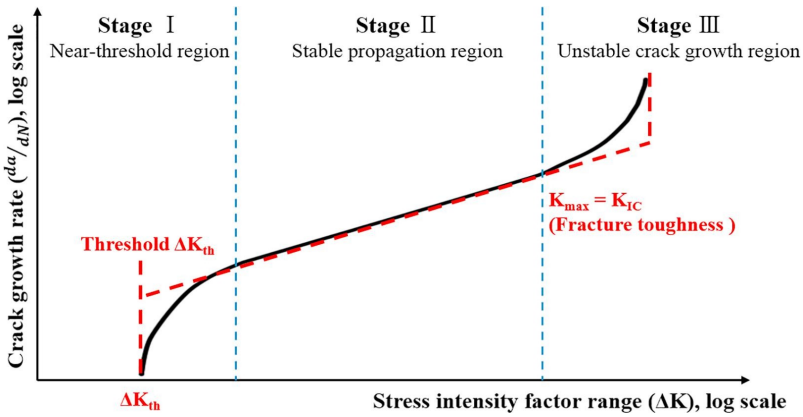


Figure 2.7: Stages of fatigue crack growth (FCG) based on the fatigue crack propagation model [3].

Crack Propagation Once initiated, cracks grow increasingly with each loading cycle. The rate of crack propagation ($\frac{da}{dN}$), is governed by the Paris law, which is expressed as:

$$\frac{da}{dN} = C(\Delta K)^m \tag{2.53}$$

where $\frac{da}{dN}$ represents the crack growth rate, ΔK is the SIF range, C is a material-specific coefficient, and m is the material's fatigue exponent. In Stage II of Figure 2.7, the crack propagates in a stable and predictable manner. This stage is of particular interest for engineering applications, as it not only enables the development of maintenance strategies and life predictions based on the measured or estimated crack growth rate, but also ensures structural safety by allowing the crack to grow in a stable and slow manner—making it more likely to be detected and repaired before catastrophic failure occurs.

Final Fracture As the crack grows, the effective load-bearing cross-section of the material decreases, leading to an increase in the SIF (K) near the crack tip. When K exceeds the material's fracture toughness (K_c), unstable crack growth occurs, resulting in sudden and catastrophic failure. In Stage III, as described in Figure 2.7, the crack propagation is governed by the fracture mechanism, and the stress state is determined by the maximum SIF ($K_{\max}$). Fatigue damage progression is affected by multiple factors, including stress amplitude, loading cycles, material properties, environmental conditions, and temperature effects.

Higher stress amplitudes and increasing loading cycles accelerate fatigue, while materials with

higher fracture toughness, lower residual stresses, and fine-grain microstructures demonstrate greater resistance to fatigue. Environmental factors, such as corrosive conditions, can exacerbate damage through mechanisms like stress-corrosion cracking. Increasing temperatures further affect fatigue by changing material properties, such as elastic modulus and yield strength, and thermal cycling induces additional damage through differential expansion or phase transformations. The challenge of fatigue-induced damage is particularly critical in safety-sensitive industries like aerospace and civil engineering, where structural integrity is important. Early detection and continuous monitoring are essential to prevent catastrophic failures. NDT methods, including ultrasonic and eddy current testing [99], are widely used to detect cracks and material flaws without compromising structural performance. Currently, SHM systems utilize embedded sensors for real-time condition monitoring, leveraging techniques like guided waves and vibration analysis to monitor crack propagation. Despite these advances, significant challenges remain. Conventional detection techniques frequently fail to detect microscopic crack initiation, particularly under complex loading scenarios such as multi-axial or variable-amplitude conditions, which present significant challenges to the precise prediction of fatigue life. Moreover, environmental factors, including corrosion and increasing temperatures, further exacerbate the difficulty of accurate assessments. Addressing these multifaceted challenges necessitates the development of advanced detection methods and the innovation of high-performance materials to ensure the safety and reliability of critical structural systems.

2.4.3 Machine learning development for SHM

Machine learning (ML) has become a critical component of SHM due to its ability to process large volumes of structural data and provide actionable insights for real-time damage detection and maintenance decision-making. Recent advancements in ML techniques have profoundly affected SHM methodologies, enabling a shift from traditional statistical approaches to advanced deep learning methods. Figure 2.8 describe the evolution of machine learning, divided into three stages: the infancy period, characterized by foundational developments; the upsurge period, marked by the introduction of more advanced algorithms; and the booming period, defined by the widespread adoption of deep learning and its integration into SHM applications.

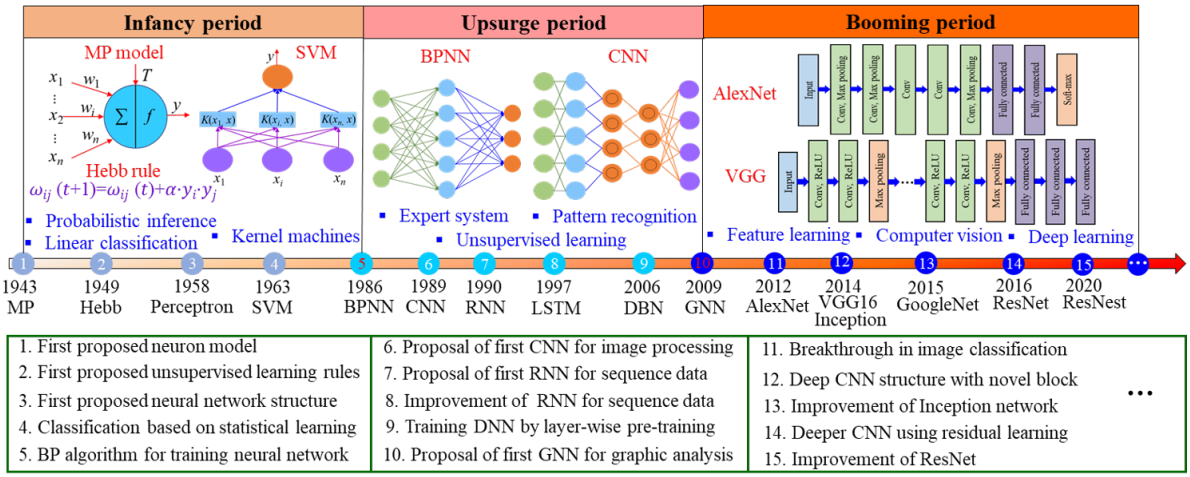


Figure 2.8: Development history of machine learning categorized into infancy, upsurge, and booming periods, highlighting major models and breakthroughs.

Development history and current status of machine learning During its early stages, foundational concepts of machine learning emerged with models like the McCulloch-Pitts (MP) model [100] and the Hebbian learning rule [101]. These developments were followed by advancements in probabilistic inference and linear classification methods, forming the basis for supervised learning algorithms such as Support Vector Machines (SVM) and kernel-based approaches [102]. Although simple, these models were instrumental in addressing linear problems and establishing a foundation for more sophisticated systems. In the growth phase, machine learning experienced rapid advancements. The introduction of BPNN enabled the training of multi-layer networks [103], facilitating pattern recognition and feature extraction in non-linear systems. Unsupervised learning techniques, including clustering and dimensionality reduction, also gained prominence during this period. Additionally, Convolutional Neural Networks (CNNs) [104] were developed, revolutionizing image-based applications and pattern recognition tasks in SHM, such as crack detection in structural images. The current era, marked by deep learning and high-performance computing, represents the booming phase. Advanced architectures like AlexNet [105] and VGG [106] have significantly enhanced model accuracy in complex tasks, including damage classification and localization in SHM. With the advancement of deep CNN, recurrent networks, and transformer-based models, machine learning has achieved unprecedented success in extracting high-level features, even from noisy or incomplete data. Furthermore, the integration of big data, cloud computing, and Internet of Things(IoT) has enhanced the scalability and real-time applicability of these models in

SHM.

Machine learning methods classification ML in SHM can be broadly categorized into two main approaches: supervised and unsupervised learning [4]. These approaches, as illustrated in Figure 2.9, form the foundation of most ML-based SHM applications.Supervised learning involves training predictive models using labeled datasets, in which each input instance (e.g., sensor signal features) is associated with a known output label, such as "pristine," "minor crack," or "delamination." The top section of Figure 2.9 outlines a typical supervised learning workflow: the process begins with data acquisition and preprocessing, followed by feature extraction—either manually or through automated techniques. Classical supervised algorithms such as Support Vector Machines (SVM), BPNN, and linear regression models are then trained to learn a functional mapping from input features to known output labels. These models are widely applied in damage classification tasks, where the objective is to categorize structural states or assess damage severity based on the input data. Due to the presence of ground truth labels, supervised learning often achieves high accuracy and robust performance, making it particularly effective for targeted applications such as crack classification, damage severity estimation, and health state prediction. However, despite these strengths, supervised learning presents certain limitations. Most notably, its performance is heavily dependent on the availability of high-quality labeled datasets. In many real-world SHM scenarios—especially those involving large-scale civil or aerospace structures—acquiring labeled damage data is both costly and time-consuming, often requiring controlled experiments, destructive testing, or expert manual labeling. Moreover, supervised models may suffer from poor generalization when exposed to structural conditions that were not adequately represented during training, particularly under variable environmental or operational conditions.

In contrast, unsupervised learning methods operate without the need for labeled data, making them inherently more flexible and scalable, particularly for online monitoring and early-stage damage detection. As shown in the bottom section of Figure 2.9, unsupervised learning typically starts with the extraction of relevant features from raw structural signals, followed by the application of pattern recognition or clustering techniques. Algorithms such as K-means clustering, Density-Based Spatial Clustering of Applications with Noise (DBSCAN), and Principal Component Analysis (PCA) are frequently used to uncover latent structures in the data, group similar

structural states, or reduce the dimensionality of complex feature spaces. This paradigm is particularly advantageous in scenarios where prior knowledge about the structure's health state is limited or unavailable, enabling the detection of anomalies or novel damage signatures without requiring predefined damage labels.Despite its flexibility, unsupervised learning also faces challenges. One key issue is interpretability: the clusters or components identified by the algorithm may not directly correspond to physically meaningful damage states, making it difficult to validate results or draw actionable conclusions. Furthermore, the performance of unsupervised methods can be highly sensitive to data characteristics, such as noise levels, signal variability, or feature selection. The results may also depend on algorithm-specific assumptions, such as the number of clusters in K-means or the density thresholds in DBSCAN, which may not generalize well across different structures or monitoring scenarios.

In summary, the choice between supervised and unsupervised learning approaches in SHM should be guided by several factors, including the availability of labeled data, the specific goals of the monitoring system (e.g., classification vs. anomaly detection), the complexity and variability of the monitored structure, and the practical constraints of deployment (e.g., cost, data volume, real-time processing requirements). In practice, hybrid strategies that combine the strengths of both paradigms—such as semi-supervised learning, transfer learning, or active learning—are also gaining traction, aiming to balance accuracy, interpretability, and data efficiency in complex SHM applications.

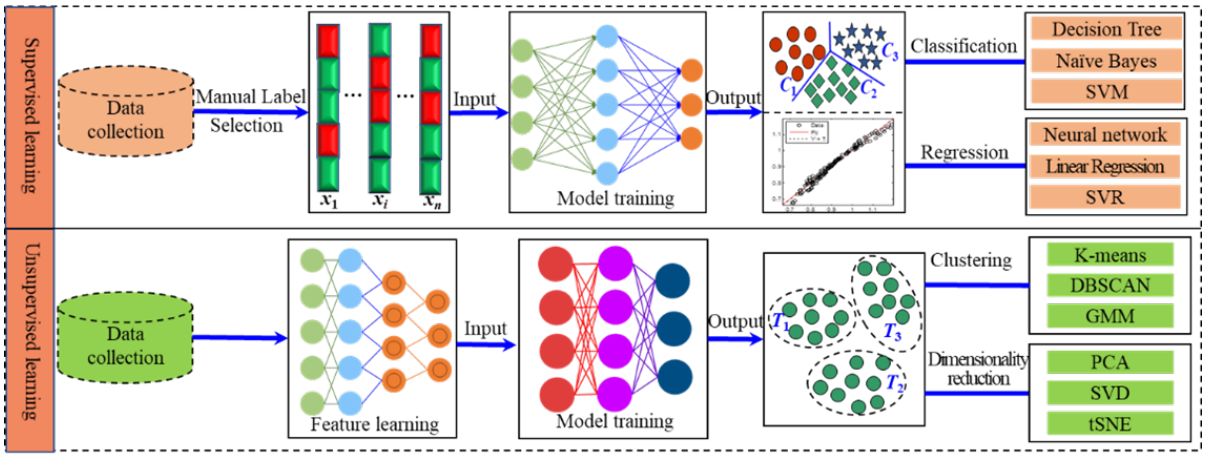


Figure 2.9: The difference between supervised and unsupervised learning [4].

2.5 Summary

This chapter provides a comprehensive overview of the fundamental concepts and theoretical background relevant to SHM. The discussions covered both ultrasonic-guided wave-based SHM and vibration-based SHM, highlighting their principles, methodologies, and applications. Ultrasonic-guided wave-based SHM was explored in detail, including both linear and nonlinear techniques, with an emphasis on their use in damage detection under various conditions. The key characteristics of vibration-based SHM were also presented, including the application of FRFs and modal parameters for structural integrity evaluation. Auxiliary techniques that support SHM methods were subsequently discussed, including the electro-mechanical coupling of piezoelectric transducers, mechanisms of fatigue-induced damage, and the integration of machine learning approaches to enhance SHM capabilities.

Chapter 3

A hybrid method based on vibration and guided waves for damage detection and localization

3.1 Introduction

A distinctive advantage of SHM is its capability to detect cracks in metallic structures and barely visible impact damage (BVID) in composites with minimal manual intervention. Such defects are often challenging to identify using conventional NDT techniques during routine maintenance. Moreover, SHM enables continuous prognosis of structural integrity throughout the service life of the component [107]. A great deal of research has been carried out on SHM methods for aerospace structures. The most commonly used methods can be categorized into GWSHM and VSHM depending on the type of integrated sensor [31, 108]. GWSHM methods use mounted PZT sensors to actuate and receive guided waves, detecting damage by comparing signals obtained from the current state of structures with a baseline pristine state. The main advantage of GWSHM is its ability to detect barely visible damage enabled by high-frequency ultrasonic waves. Another advantage is that PZT sensors are lightweight and easy to mount or embed into structures. As such, many GWSHM methods have been developed for aerospace structures, made of metal and composites in laboratory environments [109]. Yue et al. [18] presented a GWSHM approach for damage detection

and localization of flat plates and composite stiffened panels at different temperatures. Giannakeas et al. [110] presented a similar framework, validated by a large composite panel, and demonstrated that it could achieve both damage detection and localization under variable temperatures. VSHM methods use accelerometers to detect damage by comparing changes in modal parameters before and after damage initiation in the structures. The VSHM methods can be subdivided, by the type of modal parameters, into: natural frequency-based [33], mode shape-based [34], and FRF-based methods [35, 36]. As modal parameters are inherent to structures and insensitive to temperatures, VSHM methods are capable of detecting damage under different temperatures, which is a significant limitation of GWSHM methods.

This chapter explores the potential of a hybrid method that combines GWSHM and VSHM to achieve higher accuracy in damage detection and localization on an aluminum plate. The hybrid approach is developed using a combination of PZT transducers for guided waves and accelerometers for vibration analysis.

3.2 Experimental Set-up

Based on the aim of this research, a hybrid system combining vibration and guided waves is developed, as shown in Figure 3.1(a). Four PZT transducers are utilized to actuate and receive guided waves, which are evenly bonded to the aluminum plate, with a spacing of 120 mm between each transducer. Two accelerometers and a force transducer are attached on the front and back sides to obtain the modal properties of the plate, as shown in Figure 3.1(b) and (c). The shaker is used to vibrate the plate, the signal is captured by the Spider and Crystal Instruments EDM Software. The excitation signal is a sweeping sine with a frequency range from 5 to 2000Hz, as shown in Figure 3.1(c). The guided wave acquisition system comprises the arbitrary generator, data acquisition, switching modules, and the Lamb Waves Acquisition System for Aeronautic Research (LASAR) software [111]. The actuation signal used in this research is a chirp signal with a frequency between 25 KHz and 600 KHz, as shown in Figure 3.1(d). Since damage to the plate is irreversible, a magnet with a diameter of 0.8 cm is used to simulate damage in a non-destructive manner.

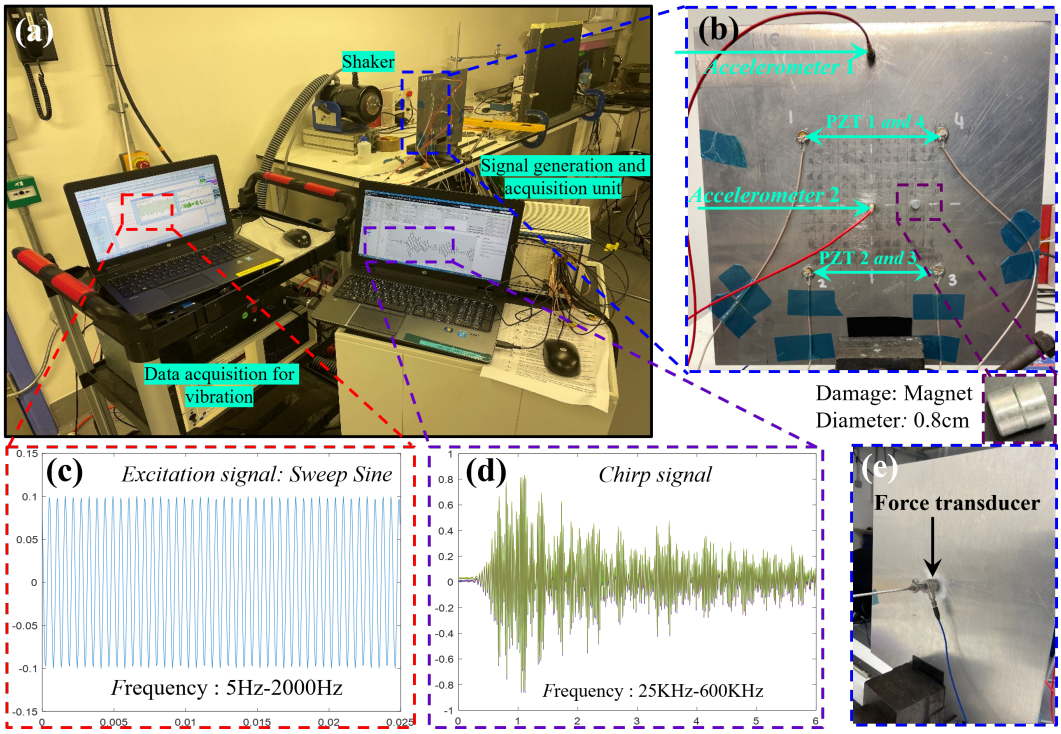


Figure 3.1: The hybrid system based on vibration and guided wave for damage detection and localization.

3.3 Hybrid Methodology

The hybrid method based on vibration and guided wave is proposed to detect and localize damage, which consists of four parts: data acquisition, feature extraction and fusion, model development, and validation. The roadmap is shown in Figure 3.2.

3.3.1 Feature Extraction

Based on the roadmap summarized in Figure 3.2, the signal acquisition was presented in Section 3.2. The Butterworth bandpass filter was used to remove noise from the signal. Subsequently, in order to detect and localize damage, some damage-sensitive features (DSFs) are needed to develop the damage index (DI) to compare the current and baseline signals. For the GWSHM method, three damage indices are used in this research, as shown in equations (3.1)–(3.3).

$$D_n^{(1)} = 1 - \rho_n = 1 - \frac{\sum_{t=0}^{T}[c_n(t) - \mu_n][b_n(t) - \mu_n]}{\sigma_{c_n}\sigma_{b_n}} \tag{3.1}$$

$$D_n^{(2)} = \frac{\max\{r_n(t)\}}{\max\{b_n(t)\}} = \frac{\max\{c_n(t) - b_n(t)\}}{\max\{b_n(t)\}} \tag{3.2}$$

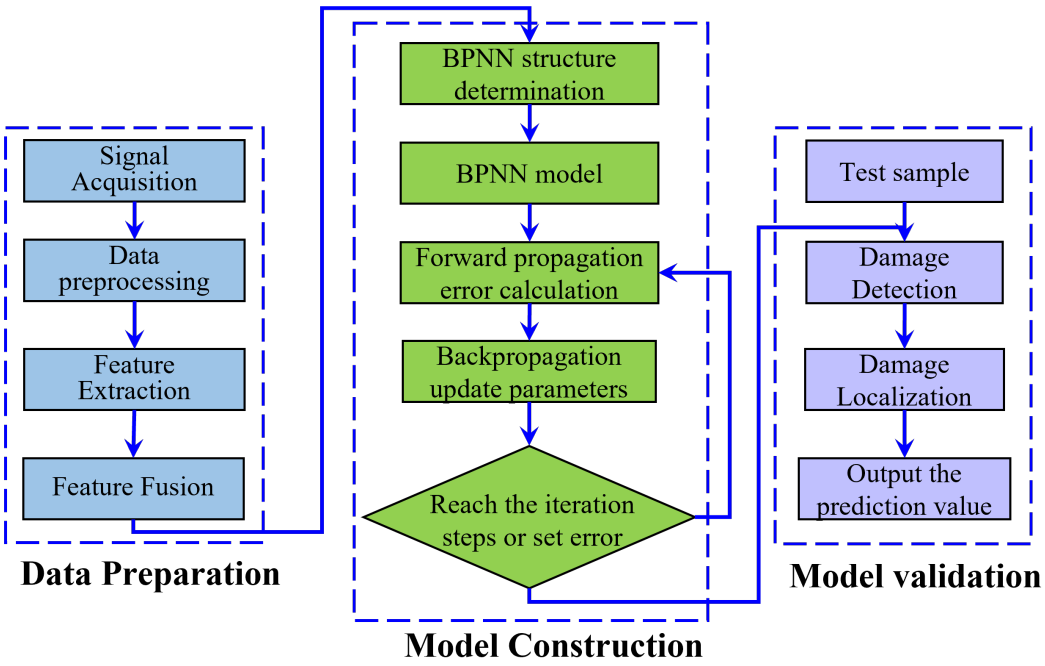


Figure 3.2: Roadmap of damage detection and localization based on the hybrid method.

$$D_n^{(3)} = \frac{\sum_{t=0}^{T}[c_n(t) - b_n(t)]^2}{\sum_{t=0}^{T} b_n(t)^2} \tag{3.3}$$

The first damage index expressed in equation (3.1) describes the correlation between the current signal and its baseline, where ρ_n is the correlation coefficient between the baseline signal $b_n(t)$ and the current signal $c_n(t)$, μ_n and σ_n represent the mean value and the standard deviation of the signal, and T is the time window of the signal used for comparison. The second damage index is defined as the ratio of the maximum value of the residue signal and the maximum value of the baseline signal, as shown in equation (3.2). Equation (3.3) shows the third damage index, which is defined as the normalized squared difference between the signal and its baseline. These damage indices are capable of describing the change of the signal's phase and amplitude under the same environmental condition. For the vibration-based method, the FRF is used to describe the change of the modal properties before and after damage, which is defined in equation (2.38), and some modal properties such as damping ratio and resonance frequency can be analyzed from it. The FRFs between 5Hz to 2000Hz obtained by pristine and damaged conditions are plotted in Figure 3.3(a). The figure reveals that the primary frequency components of the plate are concentrated within the 500-2000 Hz range. Consequently, this frequency band was chosen as the fundamental

information for the VSHM method. The comparison between pristine and damage in this frequency band is shown in Figure 3.3(b).

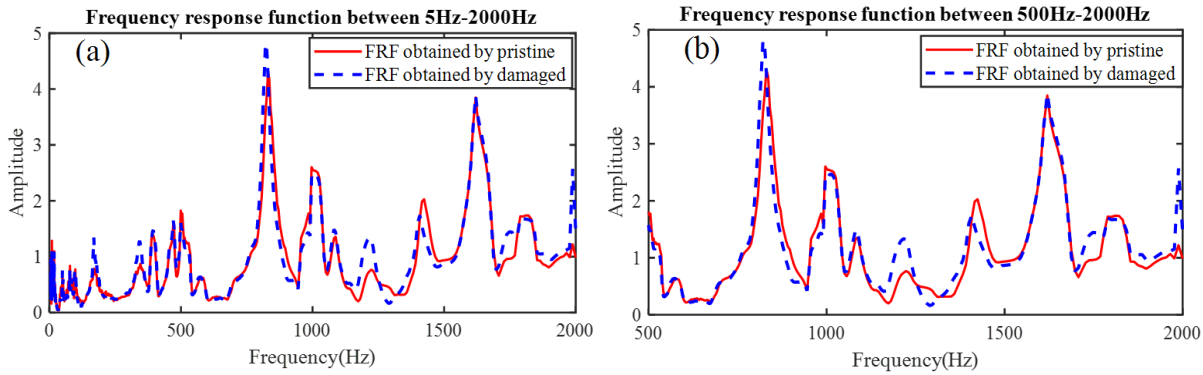


Figure 3.3: FRF obtained from pristine and damaged condition with frequency range: (a) 5-2000Hz, (b) 500-2000Hz

The FRF in the range of 500-2000Hz comprises a total of 237 data points. Inputting all these points into the neural network would increase both the efficiency and complexity of model learning. Therefore, the PCA method is used to reduce the number of input points. The eigenvalue and the cumulative percentage of FRF are summarized in Figure 3.4.

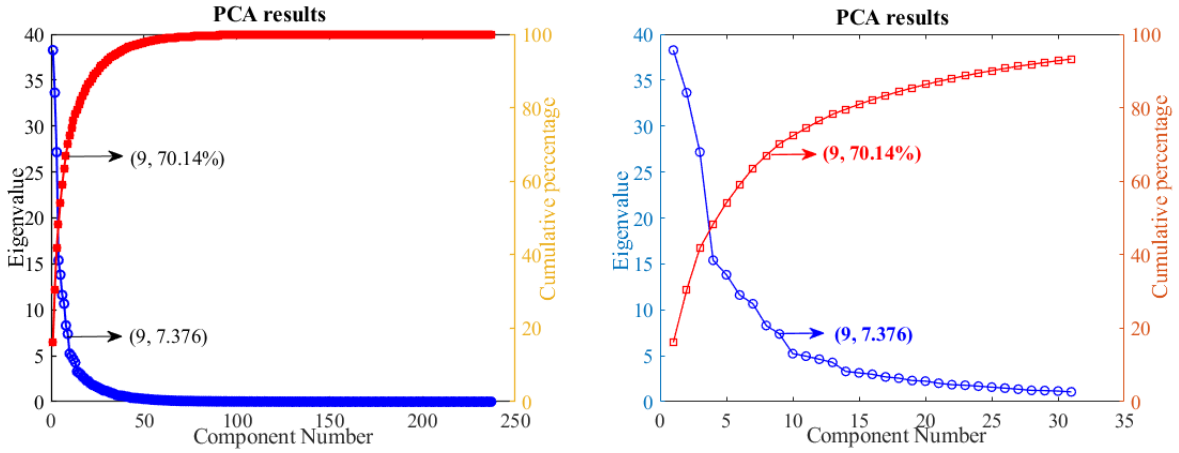


Figure 3.4: The eigenvalue and the cumulative percentage obtained from PCA: (a) All points, (b) First thirty-five points.

As shown in Figure 3.4, the cumulative contribution percentage of the first nine principal components is more than 70.14%, which indicates that these nine principal components represent most of the information of FRFs in the range 500-2000 Hz. Therefore, these nine principal components are selected as input features for the vibration-based method in the proposed hybrid method.

3.3.2 Model Development

After obtaining the features, the next step is to find a model to develop the relationship between these features and the structure's health. Assessing the state of a structure as damaged or undamaged represents a standard binary classification problem. Consequently, neural pattern recognition techniques are employed for detecting structural damage.

Moreover, to facilitate damage localization, a set of extracted features is provided as input, and the output is the location of the damage, including both x and y coordinates. Therefore, the BPNN is employed for the damage localization process [103]. The developed model is described in Figure 3.5.

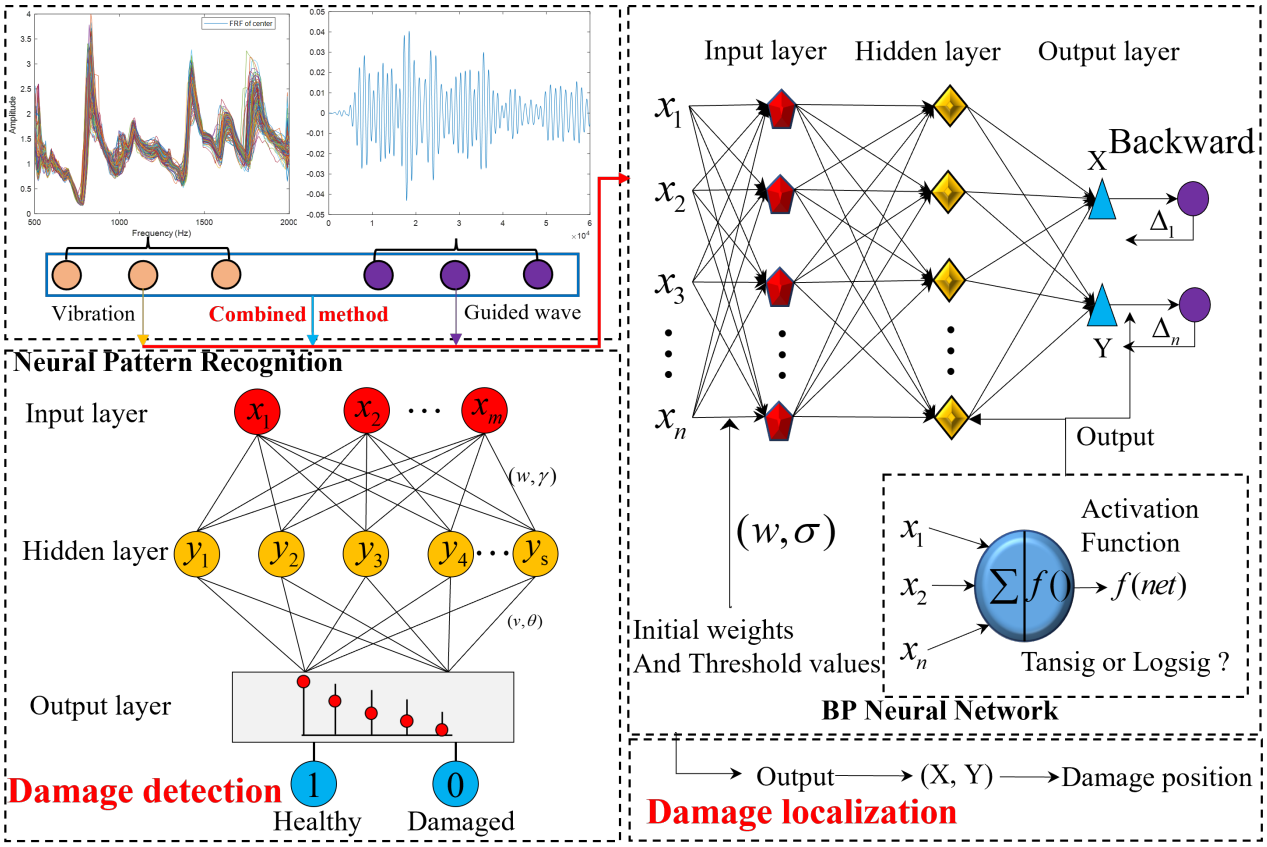


Figure 3.5: The developed model for damage detection and localization.

The developed model, shown in Figure 3.5, comprises two parts. The first part focuses on damage detection and localization by utilizing vibration and guided wave inputs individually. In the second part, all the features extracted from vibration and guided waves are combined for comparative analysis. Specifically, neural pattern recognition techniques are employed for damage

detection [112]. As the output is limited to damage and health conditions, the SoftMax is utilized for the activation function of the output layer. In terms of the model for damage localization, the output layer employs the Pureline activation function. Additionally, this study investigates the performance of two commonly used activation functions (*Logsig* and *Tansig*) for the hidden layer, and the expression is shown in equations (3.4) and (3.5), aiming to develop a high-performance model.

$$F_1 = \frac{1}{1 + e^{-x}} \tag{3.4}$$

$$F_2 = \frac{e^{x} - e^{-x}}{e^{x} + e^{-x}} \tag{3.5}$$

3.3.3 Model Evaluation and Validation

The confusion matrix, which comprises the true positive rate and false positive rate, is used to evaluate the performance of damage detection. Table 3.1 shows the confusion matrix for binary classification [113].

Table 3.1: Confusion matrix.

	$d = 0$	$d = 1$
$d' = 0$	True Negative (TN)	False Negative (FN)
$d' = 1$	False Positive (FP)	True Positive (TP)

Based on the confusion matrix, the probability of detection (POD) and probability of false alarm (PFA) is defined as:

$$POD = \frac{TP}{TP + FP} \tag{3.6}$$

$$PFA = \frac{TP}{TP + FN} \tag{3.7}$$

Then, Accuracy is proposed to measure the classification reliability of the proposed method, which is defined as:

$$Accuracy = \frac{TP + TN}{TP + TN + FP + FN} \tag{3.8}$$

In terms of damage localization, the normalized Mean Normalized Distance (MND), as shown in the equation (3.9), is used to evaluate the difference between the true value and the predicted value.

$$\mathrm{MND} = \frac{1}{N}\sum_{n=1}^{N}\sqrt{(x_n - x_{0,n})^2 + (y_n - y_{0,n})^2} \tag{3.9}$$

where $x^{(n)}$ and $y^{(n)}$ are the predicted values by BPNN, $x_0^{(n)}$ and $y_0^{(n)}$ are the true values obtained by the experiment, and N is the number of the points. The MND represents the average Euclidean distance between predicted and true coordinates, normalized over all prediction points. The accuracy of the model's prediction is considered higher when the MND value is smaller, indicating a closer match between predicted and actual damage locations.

3.4 Results and Discussion

In this section, the proposed method is first used to detect the damage on the aluminum, and the change of the damage index is also shown in this section. Then, the BPNN is used to localize the damage based on different features.

3.4.1 Damage Detection

To evaluate the effectiveness of the damage index for damage detection, the change of damage index of the guided-wave method before and after damage is summarized in Figure 3.6. Taking the damage index obtained by equation (3.1) as an example, Figure 3.6(a) shows the damage index at a pristine state, with values less than 0.01 on all paths. Figure 3.6(b) shows the damage index obtained from the vicinity of sensing paths 1-2 and 1-4, and it can be seen that the value of the damage index on the sensing paths close to the damage location increases a lot when the damage is introduced. This indicates the effectiveness of the damage index used in this study.

A total of 160 sets of data were obtained from the experiment, including 144 sets of data from different damage locations and 16 sets of data from the pristine state. 30 sets of data (15 damage samples and 15 pristine samples) were selected for the validation of the damage detection model, where 20 sets of data (10 damage samples, 10 pristine samples) were used for the training of the

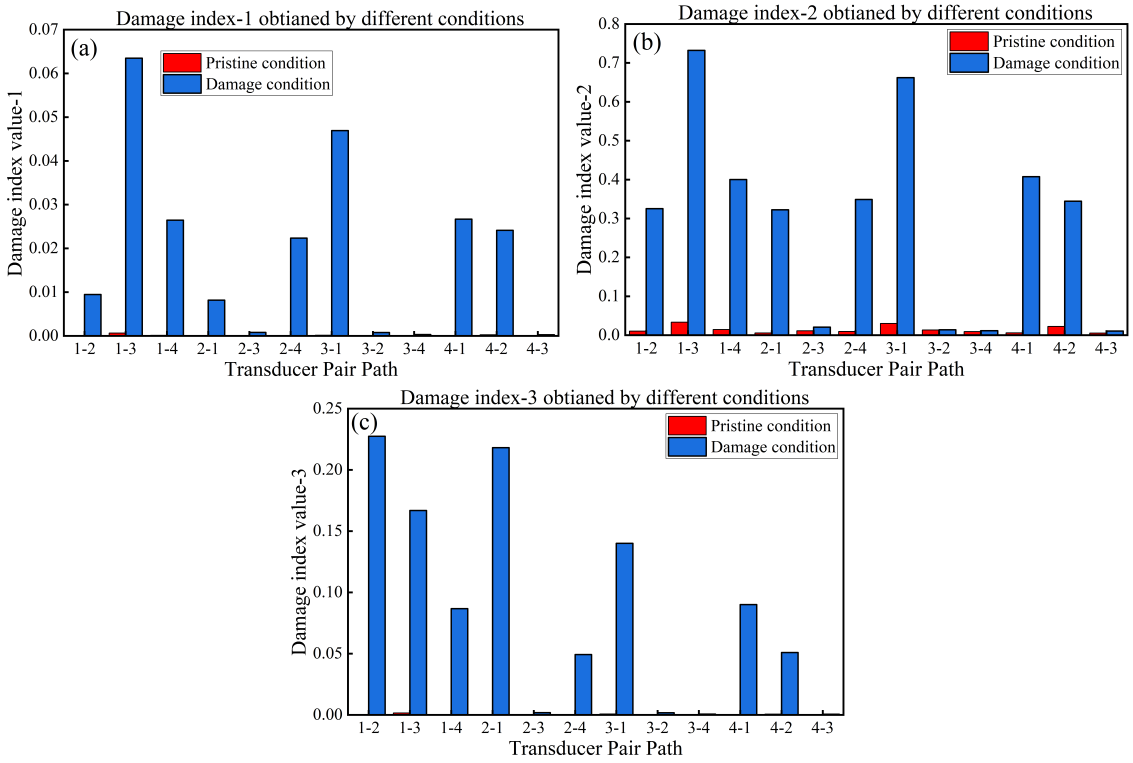


Figure 3.6: Damage index 1 obtained under different conditions: (a) Pristine state, (b) Damage state.

neural pattern recognition model, and 10 sets of data (5 damage samples and 5 pristine samples) were used as the testing of the neural network. The results of the testing based on different damage indices are summarized in Figure 3.7, which shows all three damage indices extracted from the guided wave method are capable of achieving 100% accuracy for damage detection. This indicates the effectiveness of the method used in this research.

As mentioned in the last section, for the vibrational method, the features used are the nine principal components of the FRF in the range of 500-2000 Hz after PCA dimensionality reduction. The values of these principal components obtained from pristine and damaged states are shown in Figure 3.8(a), which demonstrates that features used in this research can capture the state change of the plate. Then the extracted features are input into the neural pattern recognition, and the number of training and testing datasets are the same as the guided wave method. Results of the testing are summarized in Figure 3.8(b), which shows that the method is capable of identifying all of the damaged and pristine samples.

For damage detection, the above results indicate that the damage plates are clearly separated from the pristine samples by the proposed vibration-based and guided wave-based methods. After

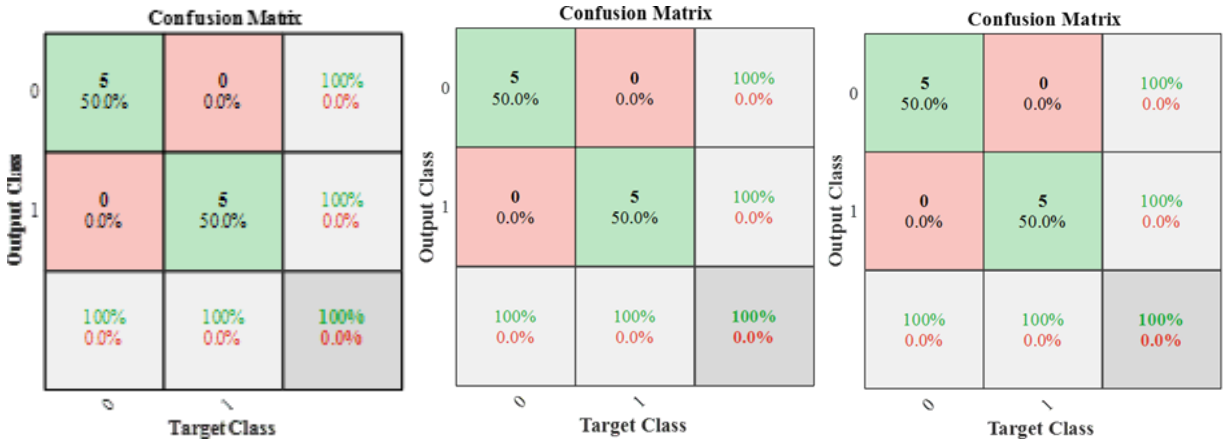


Figure 3.7: Damage detection results obtained from: (a) equation (3.1), (b) equation (3.2), (c) equation (3.3).

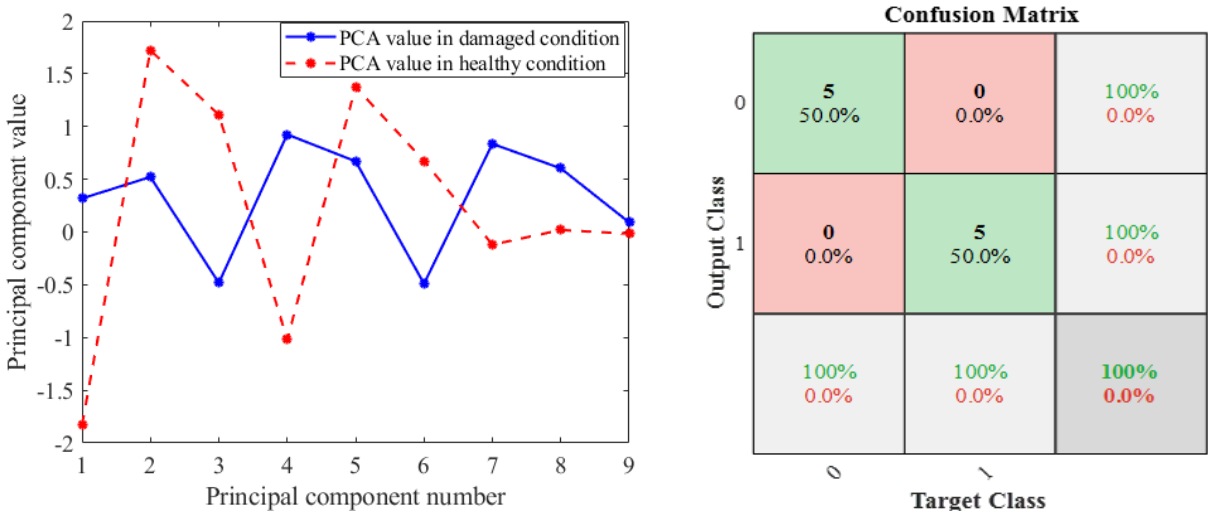


Figure 3.8: Damage detection results obtained by the vibration-based method: (a) Features used in the vibration method. (b) Detection results obtained by the neural pattern.

detecting the damage, the next step based on SHM is to localize the damage, which is addressed in the next section.

3.4.2 Damage Localization

To verify the effectiveness of the proposed hybrid method in this research, features extracted from guided wave, the nine principal components extracted from vibration signals, and their combination are selected as the input of BPNN model, respectively, and the damage location is selected as the output. As mentioned in Section 3.4.1, a total of 144 sets of damage samples are acquired from different locations, and based on these data, 128 sets of data are used as training samples, while 16

sets of data are used for model validation. The predicted locations and true positions by vibration signal and guided wave are shown in Figure 3.9.

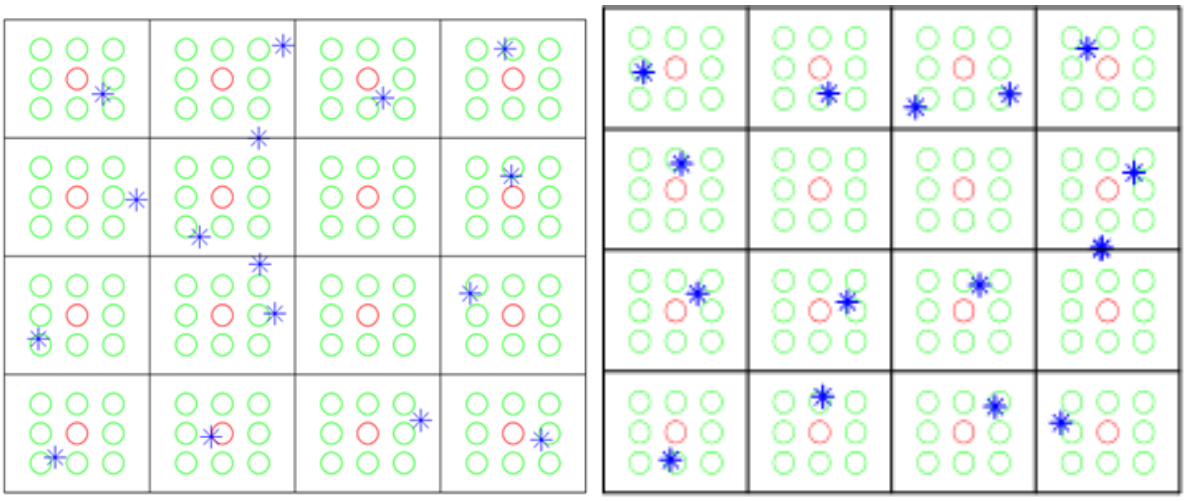


Figure 3.9: Damage localization results obtained by: (a) vibration-based method, (b) guided wave-based method-DI2.

As shown in Figure 3.9, the green circles indicate the damage locations used for training, while the red circles represent those used for testing. The blue asterisk markers denote the predicted damage locations. Some of the predicted locations based on single-signal features show significant deviations from the actual damage locations. Specifically, the mean Minimum Normalized Distance (MND) predicted using the PCA-FRF method is 2.05 cm, with a minimum of 1.18 cm. In contrast, the mean MND obtained using the guided-wave method based on equation (3.2) is 1.07 cm, with a minimum of 0.87 cm. A summary of these results is provided in Table 3.2.

Table 3.2: Results obtained by different features and methods.

Different method	**Active Sensing result**				**Hybrid method**
Features	DI(1)	DI(2)	DI(3)	DI(2) + DI(3)	PCA-FRF + DI(2) + DI(3)
MND (cm)	1.86	1.07	1.04	0.91	0.79
Min (MND)	1.55	0.87	0.80	0.66	0.38

Table 3.2 shows the average MND value and the minimum MND value obtained by different features and different methods. For the guided-wave based method, localization results obtained by the damage index 2 and 3 (equations (3.2) and (3.3)) are better than that of damage index 1 (equation (3.1)), and the average MND value and minimum MND value results obtained by

combining them is 0.91 and 0.66, respectively, which is better than each of them individually. In addition, the PCA-FRF method has the largest error compared with the guided-wave method.

Based on the above analysis, the guided-wave method demonstrates optimal performance when combining damage index 2 and 3 ((equations (3.2) and (3.3))), therefore, these two features in the guided wave are input into the neural network along with nine principal components obtained from FRF, and the predicted and true values of the damage location are summarized in Figure 3.10(a). More importantly, the predicted average MND value is shown in Figure 3.10(b) as 0.79 cm and the minimum MND value is 0.38 cm. These results indicate that the hybrid method is capable of achieving better performance compared with the individual methods, which verifies the effectiveness of the hybrid method proposed in this research.

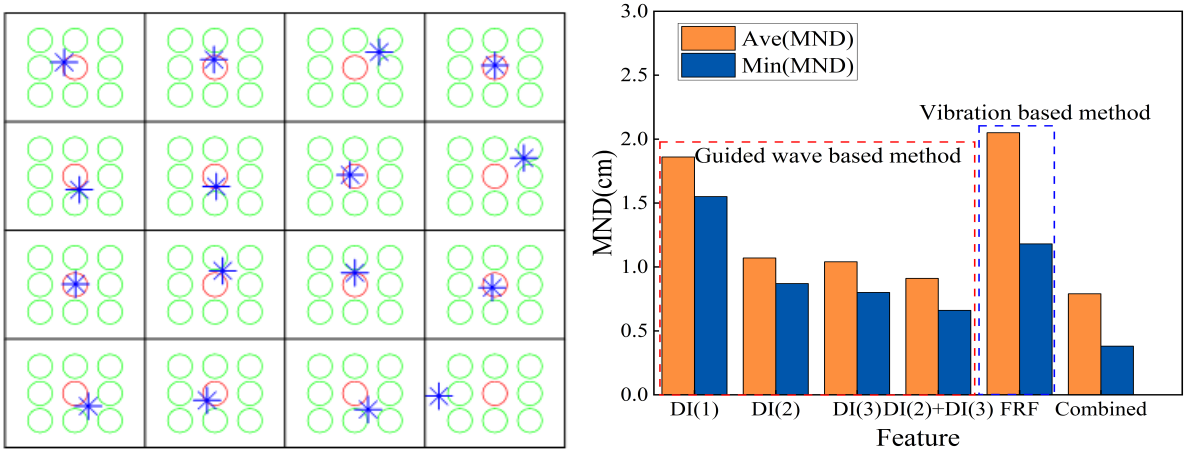


Figure 3.10: (a) Damage localization results obtained by the combined method. (b) The average MND and minimum MND obtained by the different methods.

3.5 Summary

This chapter presents a hybrid method combining vibration and guided-wave responses of the structure to detect and localize damage for an aluminium plate. Firstly, three damage-sensitive features are extracted from the guided wave, and FRF is used as the basic feature for the vibration-based method. Then, the damage detection and localization models are developed based on neural pattern recognition and BPNN, respectively. To verify the proposed method, different damage locations (represented by added mass) are considered. Experimental results show that both the individual vibration and guided-wave methods are capable of achieving 100% accuracy for damage

detection. However, for damage localization, the best performance with the average MND value and minimum MND value obtained by the guided wave is 0.91 cm and 0.66 cm, and the mean value of MND predicted based on PCA-FRF is 2.05 cm and the minimum value is 1.18 cm. For the hybrid method, the predicted average MND value is 0.79 cm and the minimum MND value is 0.38cm, which verifies the effectiveness of the hybrid method proposed in this chapter.

Chapter 4

A robust hybrid method for damage detection under varying environmental conditions

While the hybrid method presented in Chapter 3 effectively combines vibration and guided-wave responses for damage detection and localization, it has several notable limitations that must be addressed for real-world applications. First, although the experimental setup performs well in a controlled laboratory environment, it involves complex instrumentation and procedures. This complexity present significant challenges for practical implementation in engineering scenarios such as aerospace or civil infrastructure monitoring, where simplicity and reliability are important. Second, the validation of the method was limited to an aluminum plate, leaving its applicability to other structural materials, such as composites, unexplored. This limitation restricts the generalizability of the method to a broader range of materials commonly used in engineering structures. Furthermore, for the hybrid method to be viable in real-world applications, it must account for external environmental factors, particularly temperature variations, which have a significant impact on guided wave. Temperature changes affect material properties, such as stiffness and density, thereby influencing wave propagation and vibrational responses. If not properly addressed, these variations could introduce uncertainties in damage detection and localization, ultimately limiting the method's reliability under operational conditions. To address these limitations, this chapter

explores the feasibility of the hybrid SHM approach in more realistic scenarios and proposes potential solutions to improve its robustness and applicability. Specifically, this chapter explores a hardware-level hybrid SHM strategy, wherein conventional PZT transducers used for guided wave excitation and reception are also employed for modal parameter extraction, enabling the derivation of TFs as robust, temperature-insensitive features. Experiments were carried out on aluminum, quasi-isotropic, and curved anisotropic composite plates. Correlation changes in TFs between baseline and current states were used as damage-sensitive features (DSFs), with Mahalanobis distance (MD) serving as a damage indicator. MD is a multivariate distance metric that accounts for the correlations between features and the scale of the data distribution. It measures the statistical deviation of a sample from a reference distribution, making it particularly effective for detecting outliers or anomalous conditions such as damage. This approach enhances temperature robustness while retaining high sensitivity to damage, reduces system complexity by eliminating the need for accelerometers, and enables effective damage detection across a broad temperature range using a single baseline signal—thus addressing key challenges for practical SHM applications.

4.1 Introduction

The major limitation of GWSHM methods is their susceptibility to variations in environmental and operational conditions (EOC), particularly to temperature due to the thermal sensitivity of guided waves. For example, aircraft operates in temperature ranges from -40℃ to 60℃, and temperature-induced changes in guided waves may obscure damage-induced changes, thereby restricting the practical application of GWSHM methods. Consequently, extensive efforts have been made to mitigate the impact of temperature on GWSHM methods in recent years [110, 113]. Two widely used methods are optimal baseline selection (OBS) [114] and baseline signal stretch (BSS) methods [115]. The OBS method selects the waveform that best matches the current signal from large baseline signal datasets obtained from different temperatures. OBS has demonstrated high accuracy in damage detection across a broad temperature range. However, OBS requires a large baseline signal database, which may not always be feasible in real-world applications. In aerospace, for example, collecting sufficient baseline signals to cover the full operational temperature range can be resource-intensive and time-consuming. This dependence on a comprehensive database

also limits OBS's scalability, as environments with unpredictable temperature shifts require frequent data updates. In contrast, the BSS method only needs one baseline signal to compensate the temperature, which corrects the baseline signal to match the current signal by using the stretch factor [115, 116]. However, BSS faces limitations when temperature-induced changes are non-linear [117], as its stretch factor primarily accounts for linear adjustments, which can reduce accuracy under complex thermal conditions. This is because the stretch factor is designed to correct linear changes in the signal, whereas real temperature variations often introduce more complex, non-linear modifications to wave propagation.

VSHM methods detect damage by identifying changes in the modal parameters of structures, which can be classified based on natural frequency [33], modes shape [34], FRF [35, 36]. These approaches are resilient to EOCs, as variations in modal properties due to factors like temperature and humidity are typically minimal or predictable [118–122]. Therefore, VSHM methods have also attracted attention in the SHM field [80,123–125]. Salawu [120] and Zhang et al. [122] emphasized the robustness of mode shapes, noting that mode shapes often remain relatively unchanged even under varying environmental conditions, thus providing an environment-insensitive parameter basis for VSHM. Zhao et al. [121] further supported this perspective, demonstrating that even with significant temperature and humidity fluctuations, mode shape-based damage detection methods can effectively distinguish between healthy and damaged structural states. Despite these advancements, the main challenge of these methods is their limited sensitivity to minute damage [43,126]. In addition, modal parameters, especially mode shapes, are typically only sensitive to the local damage [80], and fail to provide a reliable result for SHM of large structures.

Given these constraints, a hybrid approach that leverages the strengths of both GWSHM and VSHM offers a promising solution to address each method's limitations. This combined approach can integrate GWSHM's sensitivity to subtle structural changes with VSHM's resilience to environmental variations, thereby enhancing damage detection reliability across diverse EOCs. In the method proposed in Chapter 3 [37], the feasibility of integrating guided wave and vibration-based methods for damage detection and localization was demonstrated, showing that combining the two methods produces more stable and precise monitoring and localization results. However, previous experiments utilized separate acquisition systems for both PZT and accelerometer sen-

sors, which added the complexity of the setup. Thus, a simplified sensing scheme is necessary. For example, if PZT transducers could perform modal shape measurements traditionally achieved by accelerometers, this would streamline the experimental process. Recent studies have shown the feasibility of using PZT transducers in low-frequency modal analysis, traditionally dominated by accelerometers. For instance, Wang et.al [127] conducted a detailed analysis on the application of PZT transducers in modal testing of cantilever beams. Their study examined four types of sensor-actuator pairs: accelerometer–point force, accelerometer–PZT, PVDF (polyvinylidene fluoride)–point force, and PVDF–PZT. The results demonstrated that each combination effectively captured natural frequencies and damping ratios, theoretically validating the use of PZT in experimental modal testing of cantilever beams. Similarly, Zonzini et al. [128] presented a heterogeneous sensor network incorporating MEMS accelerometers and PZT for effective and low-cost modal analysis of structures. Their experiments verified the physical relationship between data collected from PZT transducers and accelerometers, confirming the feasibility of using PZT for low-frequency modal analysis. Building upon this technical feasibility, exploring features that can enhance SHM robustness under varying EOCs becomes essential. A particularly promising direction in hybrid SHM is the extraction of temperature-insensitive features (TIFs) that remain sensitive to damage while minimizing sensitivity to EOCs, which have not yet been tested. TFs have been demonstrated to be less sensitive to temperature fluctuations in some research [129,130], and it is a mathematical relationship between two outputs and is insensitive to the influences of the input variation, making them well-suited for PZT system [131–133]. Another advantage of TF is its capability to detect damage without the need to develop any analytic or discretized model of the structure [134, 135]. As such, TF-based damage detection may have the potential to address the existing challenges of temperature variation. However, limited research has explored the application of TF-based methods for damage detection in this area.

This chapter investigates the feasibility of the hybrid SHM approach and the application of TFs as temperature insensitive features, based of modal analysis carried out by PZT transducers. Experiments were conducted on an aluminum plate, a quasi-isotropic composite plate, and an anisotropic curved composite plate using PZT transducers to generate and receive guided waves and derive TF values. Changes in the correlation coefficient of TF between baseline and current

states were identified as DSFs, with the MD calculated as an indicator of structural damage. The proposed hybrid SHM methodology combines the high sensitivity of PZT transducers with the temperature resilience of VSHM, enabling accurate damage detection under varying temperatures. It also leverages the multifunctionality of PZT transducers for both guided waves and low-frequency modal analysis, reducing system complexity and cost by eliminating the need for separate accelerometers. Furthermore, the method requires only a single baseline signal for effective damage detection across a broad temperature range and demonstrates the potential of TFs to address temperature compensation challenges, providing a promising solution for damage detection in structures subjected to varying environmental conditions. Section 2 presents the methodology, detailing the processes of data acquisition, feature extraction, decision-making, and performance analysis. Section 3 provides the experimental setup and procedures. Section 4 focuses on damage detection and uncertainty quantification, while Section 5 concludes with a comprehensive summary of the proposed methodology.

4.2 Experimental Setup

4.2.1 Test specimens

Three plates with different materials and properties are used in the experiment to validate the proposed method. Specifically, M1 is an aluminium plate, which is a typical isotropic structure. IM7/8552 is used to manufacture a composite plate M2, which is quasi-isotropic due to the symmetrical and balanced lay-up. M3 is an anisotropic curved composite plate, and it is manufactured by 16 layers of M21 prepreg plies. M1 and M2 have the same dimensions (300×300 mm), while M3 measures 297×294 mm. The geometry of these specimens are summarized in Figure 4.1. The working temperature of all plates is between 20°C and 60°C. This temperature range was selected because 20°C corresponds to typical laboratory room temperature, while 60°C approximates the upper limit of operational temperatures for aircraft structures. In aerospace applications, components are generally expected to operate in environments ranging from –50°C to 60°C; therefore, the 20–60°C range reflects realistic yet practical conditions for validating the proposed method. The properties and working conditions of these plates are summarized in Table 4.1.

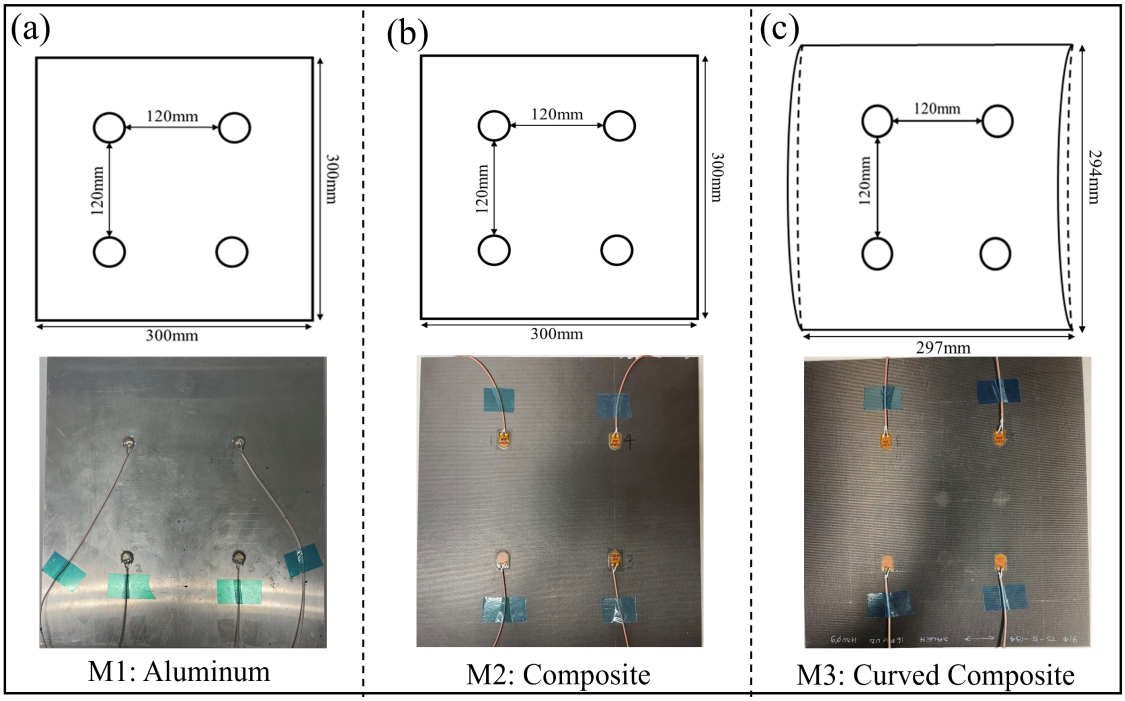


Figure 4.1: Schematic diagram of the experimental setup.

Table 4.1: Properties and working conditions of experimental plates.

Label	Structure Items	Material	Property	Stacking Sequence	Thickness (mm)	Dimension (mm × mm)	Temperature (°C)
M1	Metal	Aluminium	Isotropic		2	300 × 300	20-60
M2	Composite	IM7/8552	Quasi-isotropic	$[0 / 90 / \pm 45]_{2s}$	2	300 × 300	20-60
M3	Curved Composite	M21	Anisotropic	Unidirectional	2	297 × 294	20-60

4.2.2 Sensor integration

PZT transducers are used for guided wave propagation. For the installation of PZT, they are firstly attached to the plates by two layers of thermoplastic films and adhesive tapes, the plates with the PZT transducers are then put in the vacuum heated table for bonding. The bonding process is carried out in a vacuum environment at 140℃ for an hour, the temperature is then turned off and the vacuum environment is kept making the thermoplastic film fully melt.

4.2.3 Experimental setup

(1) The actuation signal A 12V peak-to-peak linear chirp signal, with a frequency sweeping from 500 Hz to 2000 Hz, was generated by a National Instruments PXI 5412 waveform generator and applied to a PZT over a window of 1000 ms. The sensor response was recorded using a PXI

5105 oscilloscope at a 1 MHz sampling frequency for 1000 ms to ensure complete signal capture. Each test was repeated five times to minimize environmental interference.

(2) The experimental platform The experimental platform is shown in Figure 4.2, and M2 is taken as an example of the setup. The plate is lifted by the fixture and strings to gain more freedom, and four PZT transducers are symmetrically bonded to all three plates in a square configuration with sides of 120 mm. A heating blanket is placed under the plate to control the temperature. Additionally, two temperature sensors, each with a resolution of 0.1°C, are attached on opposite sides of the plate to monitor the real-time temperature. Experiments were carried out with a temperature difference of less than ±0.2°C between the two temperature sensors.

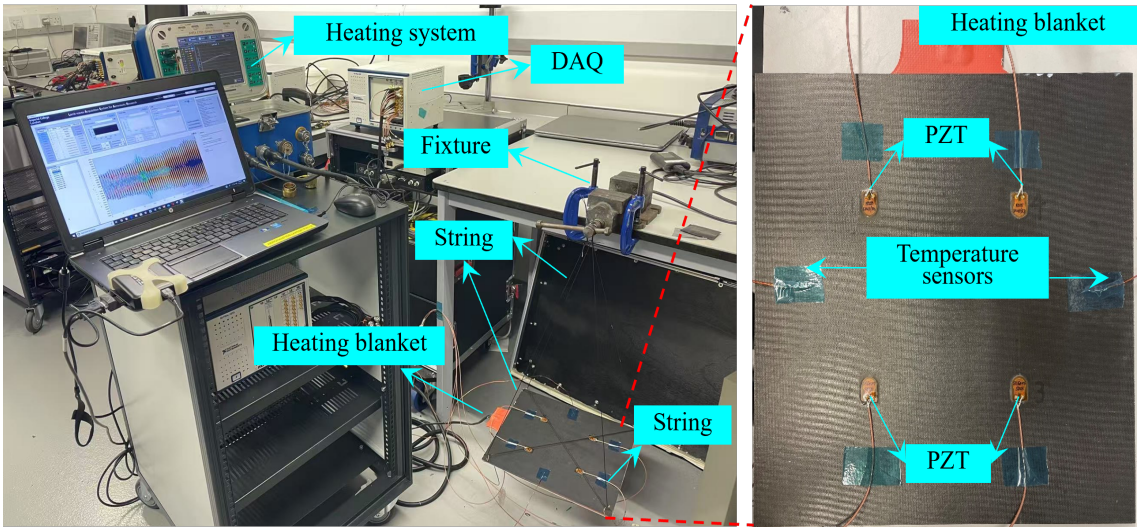


Figure 4.2: Schematic diagram of the experimental setup.

In addition to different types of materials, different damage sizes are also tested to investigate the minimum damage that can be detected by the proposed method, and five damage locations are used to demonstrate the applicability of the method. Three of these locations are located inside the area covered by PZT transducers, while another two are located outside this area. Considering that plates are irreversible after damage, added masses were used to simulate damage. Different sizes and locations of damage are shown in Figure 4.3.

D_s is calculated to quantify the minimum damage that can be detected by the proposed method, as expressed by the following equation:

$$D_s = \frac{S_d}{S_c} \tag{4.1}$$

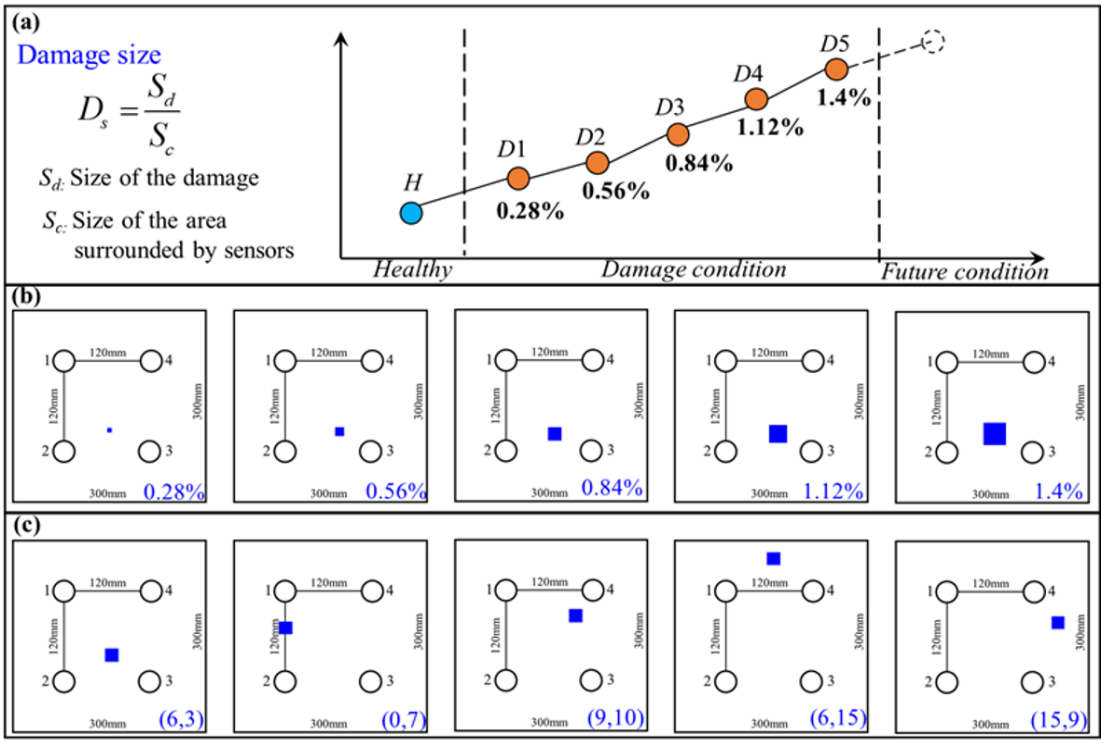


Figure 4.3: Different experimental conditions. (a) The definition of the damage size, (b) Damage with different sizes on the plates, and (c) Damage positions inside and outside the sensor area.

where S_d represents the size of the damage, and S_c is the area covered by PZT sensors, as shown in Figure 4.3. Therefore, the five damage sizes are 1.4%, 1.12%, 0.84%, 0.56% and 0.28%, respectively. Using PZT 2 as the origin (0,0), the three damage locations within the area surrounded by PZT transducers are (60,30), (0,70), and (90,100) respectively. Two locations outside the sensor area are (60,150) and (150,90) respectively. As such, three factors—temperature, damage size, and damage location—are considered in the experiments, each with five distinct levels. Table 4.2 summaries these factors and their values. However, if all these factors and values are taken into consideration, the number of experiments required in this research is 125, which is time-consuming. To address this issue, an orthogonal array is designed to systematically reduce the number of required experiments while preserving statistical integrity. Each damage scenario was repeated twice, and ten sets of data were collected per placement to reduce the influence of positional tolerances. Results of $L_{25}\,(5^3)$ orthogonal array are presented in Table 4.3.

Table 4.2: Experimental factors and levels.

	Temperature	Damage size	Damage location
1	20°C	1.4%	(60, 30)	
2	30°C	1.12%	(0, 70)	Inside sensor area
3	40°C	0.84%	(90, 100)	
4	50°C	0.56%	(60, 150)	Outside sensor area
5	60°C	0.28%	(150, 90)	

4.3 Damage detection methods

This section aims to differentiate between damaged and intact structures under varying temperature. The key challenge lies in identifying whether changes in signal features stem from damage or temperature variation. To achieve this objective, all stages of the proposed methodology are outlined in Figure 4.4, including data acquisition, feature extraction (comprising TF computation, damage index vector derivation, and MD computation), outlier analysis, and performance evaluation.

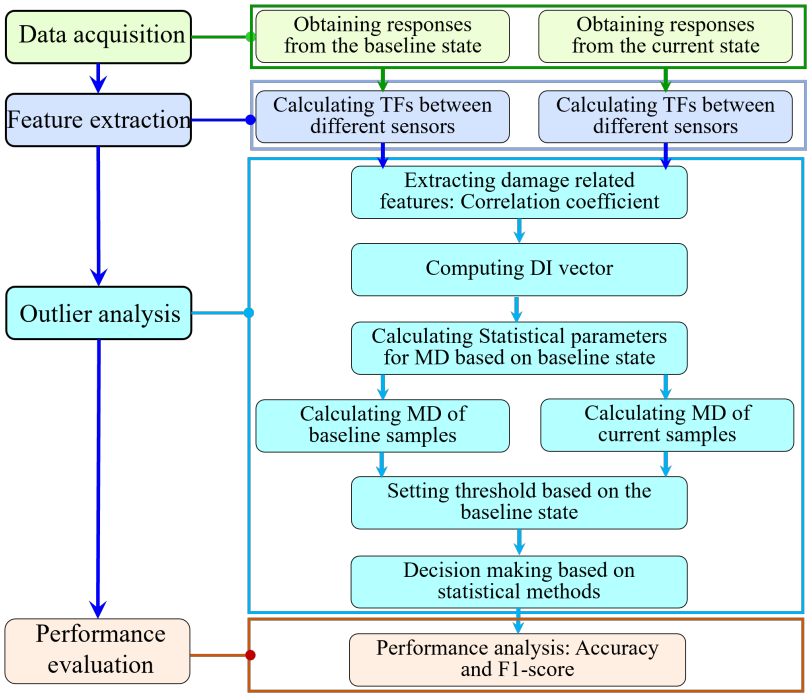


Figure 4.4: The framework of the proposed damage detection methodology.

Table 4.3: $L_{25}\,(5^3)$ Orthogonal array and experimental datasets.

Run	Temperature	Damage size (%)	Damage location	Dataset No.	
				Placement 1	Placement 2
1	20°C	1.40	(150, 90)	1 − 10	11 − 20
2	20°C	1.12	(60, 150)	21 − 30	31 − 40
3	20°C	0.84	(90, 100)	41 − 50	51 − 60
4	20°C	0.56	(0, 70)	61 − 70	71 − 80
5	20°C	0.28	(60, 30)	81 − 90	91 − 100
6	30°C	1.40	(90, 100)	101 − 110	111 − 120
7	30°C	1.12	(0, 70)	121 − 130	131 − 140
8	30°C	0.84	(60, 30)	141 − 150	151 − 160
9	30°C	0.56	(150, 90)	161 − 170	171 − 180
10	30°C	0.28	(60, 150)	181 − 190	191 − 200
11	40°C	1.40	(60, 30)	201 − 210	211 − 220
12	40°C	1.12	(150, 90)	221 − 230	231 − 240
13	40°C	0.84	(60, 150)	241 − 250	251 − 260
14	40°C	0.56	(90, 100)	261 − 270	271 − 280
15	40°C	0.28	(0, 70)	281 − 290	291 − 300
16	50°C	1.40	(60, 150)	301 − 310	311 − 320
17	50°C	1.12	(90, 100)	321 − 330	331 − 340
18	50°C	0.84	(0, 70)	341 − 350	351 − 360
19	50°C	0.56	(60, 30)	361 − 370	371 − 380
20	50°C	0.28	(150, 90)	381 − 390	391 − 400
21	60°C	1.40	(0, 70)	401 − 410	411 − 420
22	60°C	1.12	(60, 30)	421 − 430	431 − 440
23	60°C	0.84	(150, 90)	441 − 450	451 − 460
24	60°C	0.56	(60, 150)	461 − 470	471 − 480
25	60°C	0.28	(90, 100)	481 − 490	491 − 500

4.3.1 Data acquisition

Following the procedure described in Figure 4.4, the initial stage involves collecting data at varying temperatures, as will be described in the next section. The data obtained at a specific temperature is defined as a signal vector x_{mn}, where m is the id of the structure, and n represents the number of temperatures studied in this investigation. The data obtained are expressed as:

$$x_{mn} = (x_{11}, x_{12}, \ldots, x_{1n}, \ldots, x_{mn}) \tag{4.2}$$

$$X = \left(x_{mn}^1, x_{mn}^2, \ldots, x_{mn}^N\right) \tag{4.3}$$

Where N is the number of data samples obtained from intact and damaged structures across various temperatures. These samples constitute the datasets X, which are subsequently used for feature extraction in the following section. The research investigates three different materials at four temperatures, with ten samples collected under each experimental condition.

4.3.2 Feature extraction

TFs Following data acquisition, the next step is feature extraction, which is the most important step in damage detection. Previous studies [18, 113] typically involved extracting some DSFs such as time of arrival (TOA) to detect damage. However, due to the temperature sensitivity of guided waves, such methods may prove unreliable in environments with fluctuating temperatures. Therefore, it is imperative to select features that are sensitive to damage while remaining resistant to temperature fluctuations for effective damage detection across varying temperatures [136, 137]. Thus, TFs are proposed to detect damage in this research, following the methodology demonstrated in Figure 4.5.

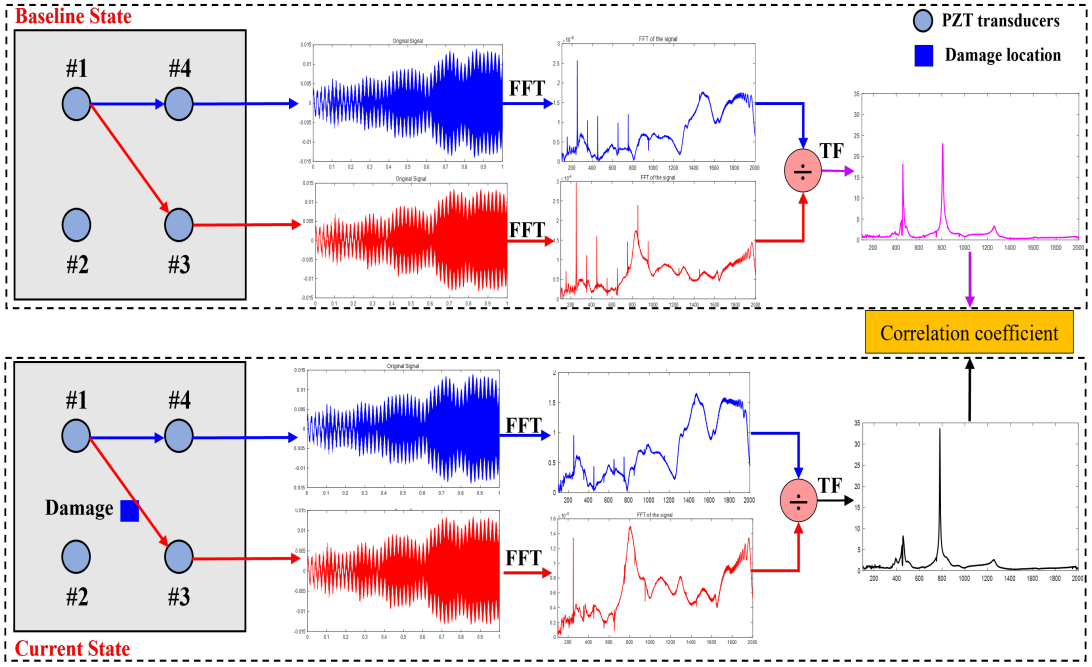


Figure 4.5: The process of feature extraction.

As illustrated in Figure 4.5, TFs are defined as the ratio between two measured outputs in the frequency domain [76], as given in equation (2.39). Therefore, the TF value is determined

solely by the location of the excitation and is not related to the amplitude [18]. Additionally, the FRF is defined as the ratio between the frequency domain of the output signal measured at a specific point on the plate and the frequency domain of the excitation force [77], as shown in equation (2.40). The relationship between TF and FRF is provided in equation (2.41). In the FRF, peaks correspond to the resonant frequencies of the structure, and dips represent the antiresonant frequencies. Based on equation (2.41), the dips in the FRF correspond to the peaks in the TF, and vice versa. Therefore, the TF effectively reflects the modal properties of a structure.

Since the TF is the ratio of two measured outputs, a minimum of three PZT transducers are required to obtain one TF of the host structure. Specifically, one transducer is used as an actuator to send signals, while the other two serve as sensors to receive these signals. From the signals of the two measured outputs, two reciprocal TFs are obtained, both reflecting identical modal parameter information. Therefore, only one of these TFs is used as a feature for damage detection. The relationship between the number of sensors and the number of TFs, denoted as TF_n, is expressed as:

$$TF_n = \frac{n_s * (n_s - 1)}{2} \tag{4.4}$$

where TF_n is the number of TFs obtained from different sensor pairs, and n_s is the number of PZT transducers used in the experiment.

Damage related feature After obtaining TFs from different sensor pairs, the damage-related features should be extracted from these TFs. In this study, the correlation coefficient between baseline TF_b^p and current TF_c^p is used to calculate the damage index (DI) from sensor pair p, and it is expressed as:

$$DI_p = 1 - \frac{\sum_{t=0}^{T} \left[TF_c^p(w) - \mu_n^c\right] \left[TF_b^p(w) - \mu_n^b\right]}{\sigma_n^c \sigma_n^b} \tag{4.5}$$

where $TF_c^p(w)$ is the TF obtained from sensor pair p at the current condition, $TF_b^p(w)$ is the TF obtained from sensor pair p at the baseline condition, μ_n^c and μ_n^b are the average values of $TF_c^p(w)$ and $TF_b^p(w)$, and σ_n^c and σ_n^b are the standard deviations of $TF_c^p(w)$ and $TF_b^p(w)$. Equation (4.5) describes the difference in terms of amplitude and phase between two TFs obtained from different conditions. Therefore, the DI vector is defined as:

$$DI = (DI_1, DI_2, \ldots, DI_{p-1}, DI_p) \tag{4.6}$$

4.3.3 Decision making: outlier analysis

After obtaining the DI vector, the next step is to find a reliable method to divide the damaged and undamaged (intact) samples. One of the potential methods is outlier analysis, which is used to detect the presence of anomalous data (i.e., damage) from normal data (i.e., intact). Outlier analysis has been widely used in SHM problems [138]. To distinguish whether a DI vector is an outlier or inlier, the Mahalanobis distance (MD) is used to calculate the distance between samples and the baseline for the outlier analysis. The MD is expressed as:

$$MD = \sqrt{\left(D - \overline{D_r^0}\right)^T [\sigma]^{-1} \left(D - \overline{D_r^0}\right)} \tag{4.7}$$

where $\overline{D_r^0}$ and σ represent the mean value and the covariance of features obtained from the baseline state data D_b. D is the data from the current state. Equation (4.7) calculates the MD between two samples D and D_b. To divide the intact and damaged samples, a threshold based on the baseline state is set, as expressed in:

$$MD_T = \mu_{MD_b} + \alpha\sigma_{MD_b} \tag{4.8}$$

where MD_T is the threshold used to divide the intact and damaged samples, μ_{MD_b} and σ_{MD_b} are the mean value and standard deviation of the MD between the baseline samples, and α is a constant to be defined. Two hypotheses are then set for damage detection, defined as:

$$\begin{aligned} &\mathrm{H}_1: \quad MD_i > MD_T \quad \text{Outliers (Damaged)} \\ &\mathrm{H}_2: \quad MD_i \leq MD_T \quad \text{Inliers (Intact)} \end{aligned} \tag{4.9}$$

As shown in equation (4.9), the samples are labeled as outliers (damaged) when the MD_i calculated from the current samples is greater than the set threshold MD_T. For MD_i less than or equal to MD_T, they are regarded as inlier (intact) samples.

4.3.4 Performance analysis

Accuracy and F_1-score calculated from the confusion matrix are used to measure the classification reliability of the proposed method. The *Accuracy* is defined as:

$$Accuracy = \frac{TP + TN}{TP + TN + FP + FN} \tag{4.10}$$

where TP and TN are the true positive and the true negative divided by thresholds, and FP and FN are the false positive and the false negative. The range of *Accuracy* is from 0 to 1, and the closer its value is to 1, the better the performance of the proposed method. *Accuracy* is a more appropriate indicator to evaluate the performance of the model when the datasets are balanced (same number of positives as negatives).

As such, another indicator, F_1-score, is used to evaluate the performance of the model when the datasets are unbalanced, which is expressed as:

$$F_1 = \frac{2 \times P_{\text{pre}} \times P_{\text{rec}}}{P_{\text{pre}} + P_{\text{rec}}} \tag{4.11}$$

The recall P_{rec} is defined as:

$$P_{\text{rec}} = \frac{TP}{TP + FN} \tag{4.12}$$

4.4 Damage detection results

Temperature changes are known to affect wave propagation by altering material properties such as elastic modulus and density, which in turn modify wave speed, amplitude, and attenuation characteristics. These effects can complicate damage detection by masking or mimicking signal changes caused by actual structural damage. To address this challenge, our method is based on the assumption that, within a limited temperature range (20°C to 60°C), the influence of temperature on the guided wave signal is smaller than that of structural damage. Therefore, features extracted from the signals are expected to remain sufficiently sensitive to damage even under moderate temperature variations. While no explicit temperature compensation model was applied, the robustness of the proposed method was demonstrated by its ability to distinguish damaged from pristine states across the entire examined temperature range.

4.4.1 Temperature and damage effects on TFs

Many previous studies on TF-based methods have shown that temperature changes has minimal affect on the modal properties of structures, especially at low frequencies. However, damage significantly affects the modal properties of the structure. As mentioned in the previous section, features extracted in this research should be damage-sensitive and temperature-insensitive. Therefore, the effects of temperature and damage on the TF are first studied. TFs (obtained by sensors 2 and 3) of M1, M2 and M3 in intact condition and damage with different sizes and locations are reported in Figure 4.6-4.8. Solid and dashed lines represent the baseline and current TFs.

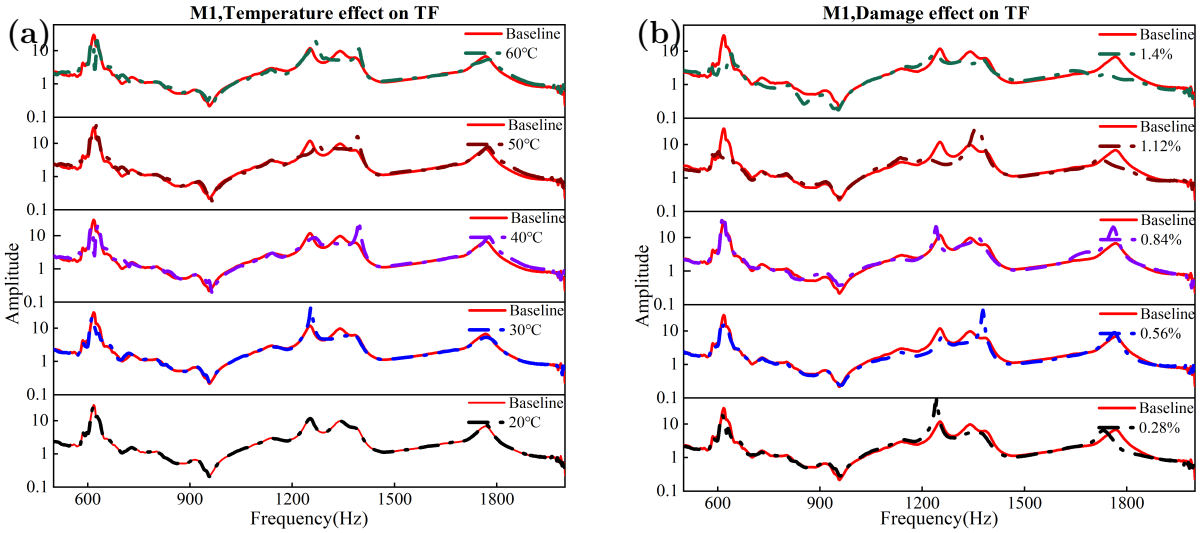


Figure 4.6: TF of M1 obtained by sensors 2 and 3 under different conditions.(a) The effect of different temperatures(20°C, 30°C, 40°C, 50°C and 60°C, from bottom to top respectively) on TF and (b) the effect of damage sizes (D_s= 0.28%, 0.56%, 0.84%, 1.12%, 1.40%, from bottom to top respectively) on TF.

Figure 4.6(a) shows that the TF values fluctuate when the temperature increases, particularly within the range of 1200 Hz to 1500 Hz, and this fluctuation gradually increases with increasing temperature. This is because temperature changes affect the material properties, such as thermal expansion, elasticity modulus, damping and nonlinear properties, all of which affect the modal properties. However, upon the introduction of damage, there are obvious variations in both amplitude and phase within some frequency bands. For example, the amplitude of TF in the vicinity of 600 Hz remains almost the same in response to temperature fluctuations (Figure 4.6(a), but a noticeable variation is observed when the damage size is 1.12% and 1.4% (Figure 4.6(b), respectively. In addition, the peak at approximately 1800 Hz shows notable variations with the smallest

damage size of 0.28%.

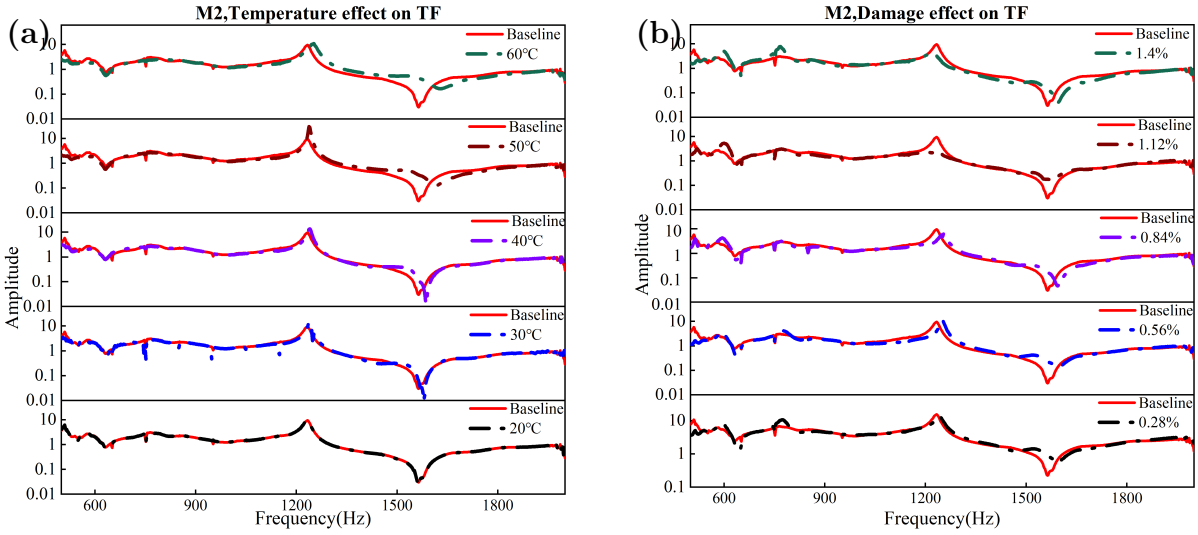


Figure 4.7: TF of M2 obtained by sensors 2 and 3 under different conditions. (a) The effect of different temperatures(20°C, 30°C, 40°C, 50°C and 60°C, from bottom to top respectively) on TF and (b) the effect of damage sizes (D_s= 0.28%, 0.56%, 0.84%, 1.12%, 1.40%, from bottom to top respectively) on TF.

For the TFs of M2 obtained by sensors 2 and 3, as illustrated in Figure 4.7, an increase in temperature results in a gradual change in TF compared to the baseline. This is primarily attributed to temperature-induced changes in material properties, such as the modulus of elasticity and stiffness, which in turn affect the vibration response and the resulting TFs. As illustrated in Figure 4.7, the peak around 1500 Hz remains nearly constant at $\Delta T = 10°$. However, with increasing temperature, the frequency corresponding to this peak progressively increases, with a gradual reduction in the peak amplitude. When damage is introduced, even minor damage (0.28%) induces considerable variability in this frequency band. Additionally, the band centered around 1200 Hz undergoes more substantial changes in response to the introduction of damage than to temperature variations. This observation suggests that this specific frequency band is sensitive to damage but insensitive to temperature fluctuations. This indicates that the TF-based method has the potential to detect damage in composite plates reliably, within a certain temperature range.

The guided wave propagation in the M3 plate is more complex due to its curved shape and anisotropic properties. Figure 4.8 shows the difficulty in identifying the temperature effects and damage effects through the change of a specific frequency. Regarding temperature effects illustrated in Figure 4.8(a), TFs gradually increase with increasing temperature, In particular the amplitude

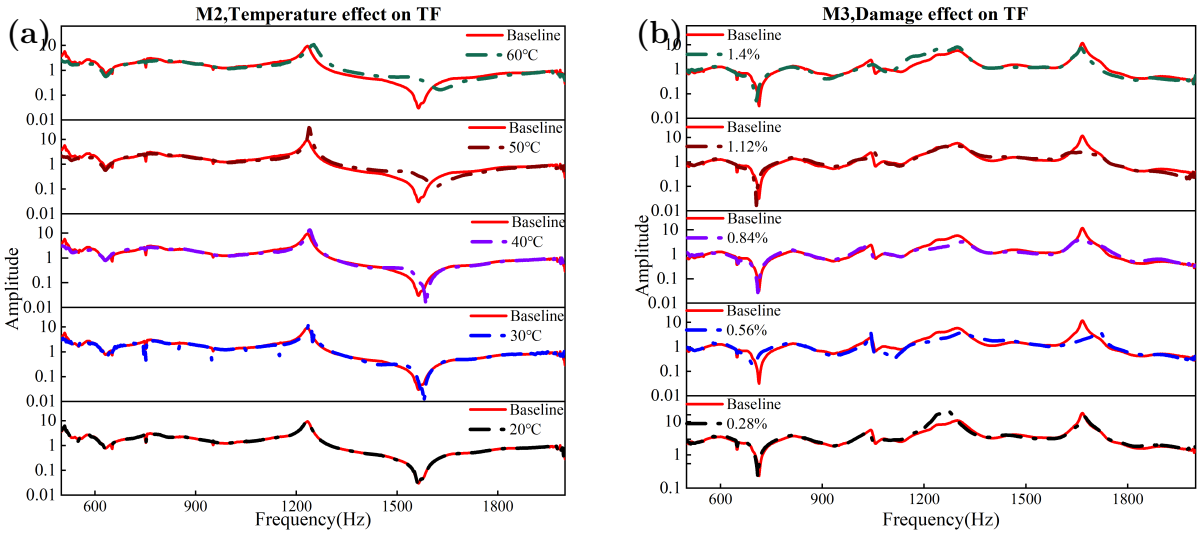


Figure 4.8: TF of M3 obtained by sensors 2 and 3 under different conditions. (a) The effect of different temperatures(20°C, 30°C, 40°C, 50°C and 60°C, from bottom to top respectively) on TF and (b) the effect of damage sizes (D_s= 0.28%, 0.56%, 0.84%, 1.12%, 1.40%, from bottom to top respectively) on TF.

of TF within 600-900 Hz and 1500-1800 Hz. In terms of the damage effect in Figure 4.8(b), there is a slight change in TFs after damage is introduced between 500 and 1,000 Hz. However, for a higher frequency range (1500-1800 Hz), the frequencies and amplitudes corresponding to the peaks have a significant change.

4.4.2 Detection results

The results presented in the previous section enable the distinction between temperature-induced and damage-induced effects using correlation coefficients. The primary goal of this study is to detect damage under varying temperature conditions, with the aim of achieving 100% detection accuracy at different locations. However, as temperature increases, its effects on TFs may overshadow those caused by damage. To address this, a threshold derived from equation (4.8) is applied to differentiate between intact and damaged samples across various temperature ranges. Furthermore, *Accuracy* and F_1-score, calculated using equations (4.10) and (4.11), respectively, are employed to assess the uncertainty of the proposed method under different conditions, including variations in location, damage size, and temperature differences. The results for different plates are summarized in Figures 4.9 to 4.11, providing a comprehensive evaluation of the proposed method's performance.

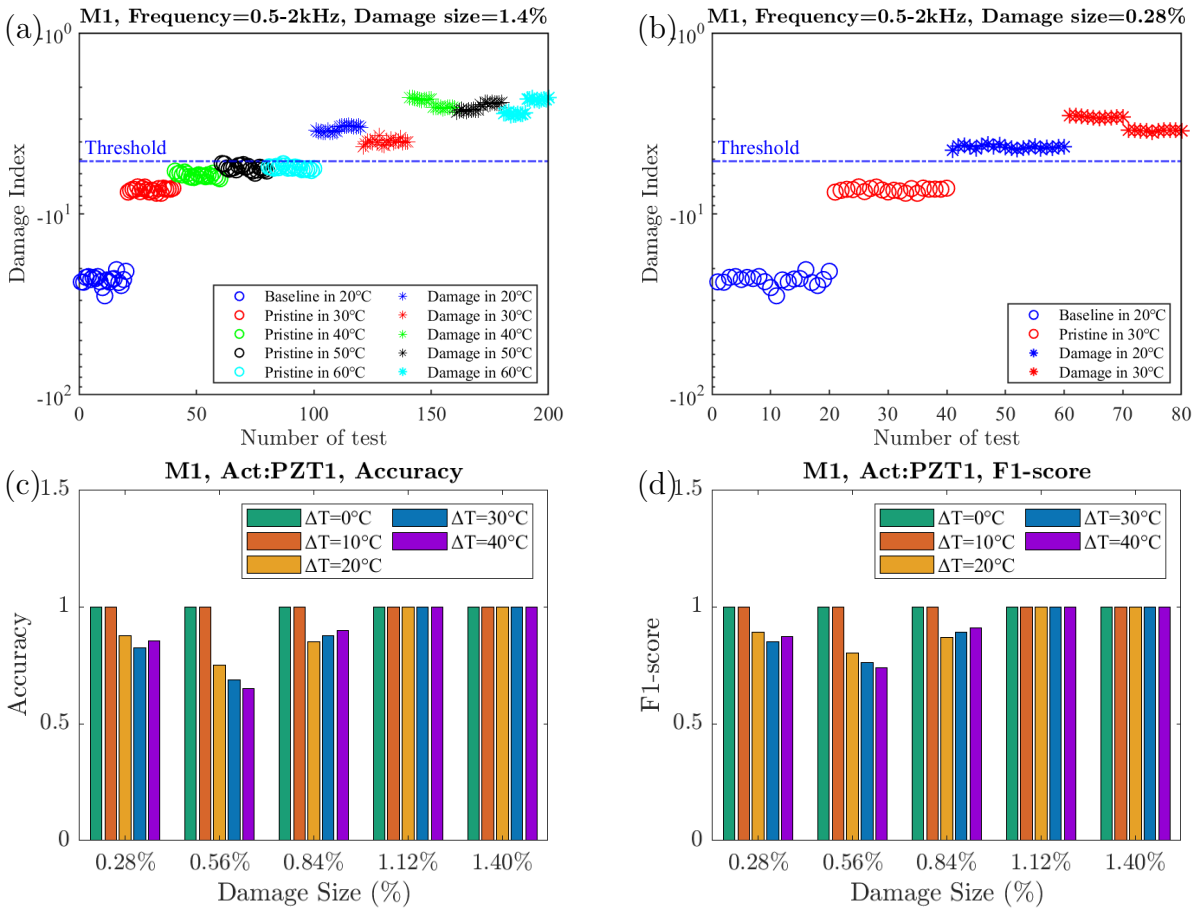


Figure 4.9: Results of M1 obtained by different conditions: (a) Damage index obtained by M1 at different temperatures when damage size =1.4%, (b) Damage index obtained by M1 at different temperatures when damage size =0.28%, (c) *Accuracy* obtained by actuator PZT1 and Specimen M1, (d) $F1-score$ obtained by actuator PZT1 and Specimen M1.

Figure 4.9(a) shows the performance of the proposed method in detecting damage on M1, under varying temperature when the damage size is 1.4%. It is found that the method is capable of detecting the damage within the temperature difference of 40°C, and the threshold calculated based on μ_{MD_b} and σ_{MD_b} is -5.12 for M1 test case. Regarding the smallest detectable damage size of 0.28% investigated in this study, Figure 4.9(b) indicates that using the same threshold set at -5.12, all damage scenarios on both inside and outside the sensor area can be detected when $\Delta T = 10°$. Figures 4.9(c) and 4.9(d) further summarise the results obtained for different temperatures and locations on the aluminium plate, and for the highest temperature difference $\Delta T = 40°$, the minimum damage size that can be detected is 1.12%, as both the *Accuracy* and $F1-score$ are 100%. However, when the damage size was further reduced to 0.84% or even smaller, there were some false alarms when the temperature difference exceeded 10°C.

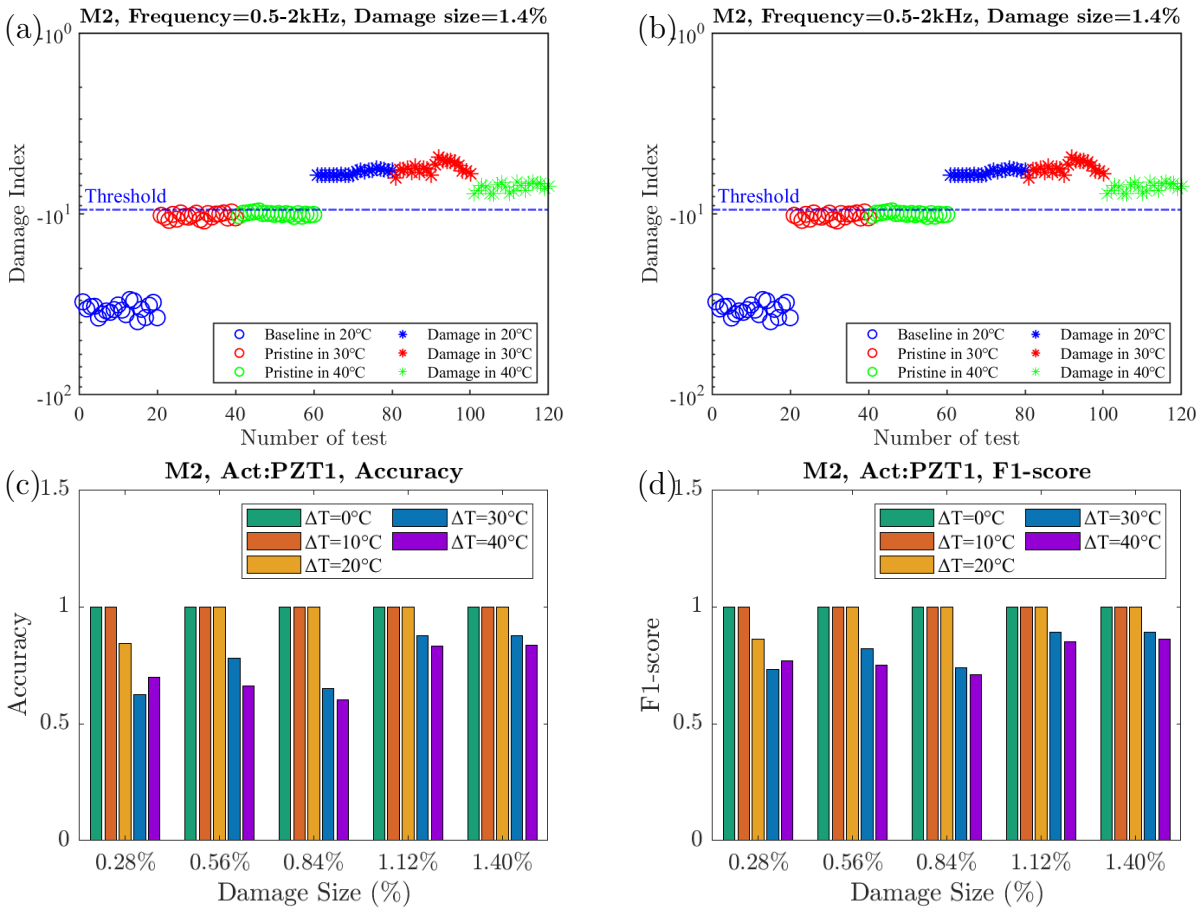


Figure 4.10: Results of M2 obtained by different conditions: (a) Damage index obtained by M2 at different temperatures when damage size =1.4%, (b) Damage index obtained by M2 at different temperatures when damage size =0.28%, (c) *Accuracy* obtained by actuator PZT1 and Specimen M2, (d) $F1-score$ obtained by actuator PZT1 and Specimen M2.

Figure 4.10 summarizes the results obtained from the analysis of composite plate M2. Figure 4.10 (a) indicates the maximum effective working temperature difference for detecting the damage size 1.4% is 20°C, with the detection threshold calculated as -9.48 based on μ_{MD_b} and σ_{MD_b}. In terms of the smallest damage size 0.28%, the method is only effective when $\Delta T = 10°$. In addition, Figure 4.10 (c) demonstrates that when the temperature difference is 20°C, the minimum damage size detected by the method is 0.56%, achieving the *Accuracy* and the $F1score$ of 1 (highlighted in yellow on the bar chart). However, at higher temperature differences of 30°C and 40°C, there are some false alarms even for considerable damage sizes of 1.4% and 1.12%, as illustrated in Figure 4.10 (c) and 4.10 (d), respectively.

The M3 plate is a curved composite plate that exhibits anisotropic behaviour due to its layup, which results in a more complex guided wave propagation in the plate. The performance of the

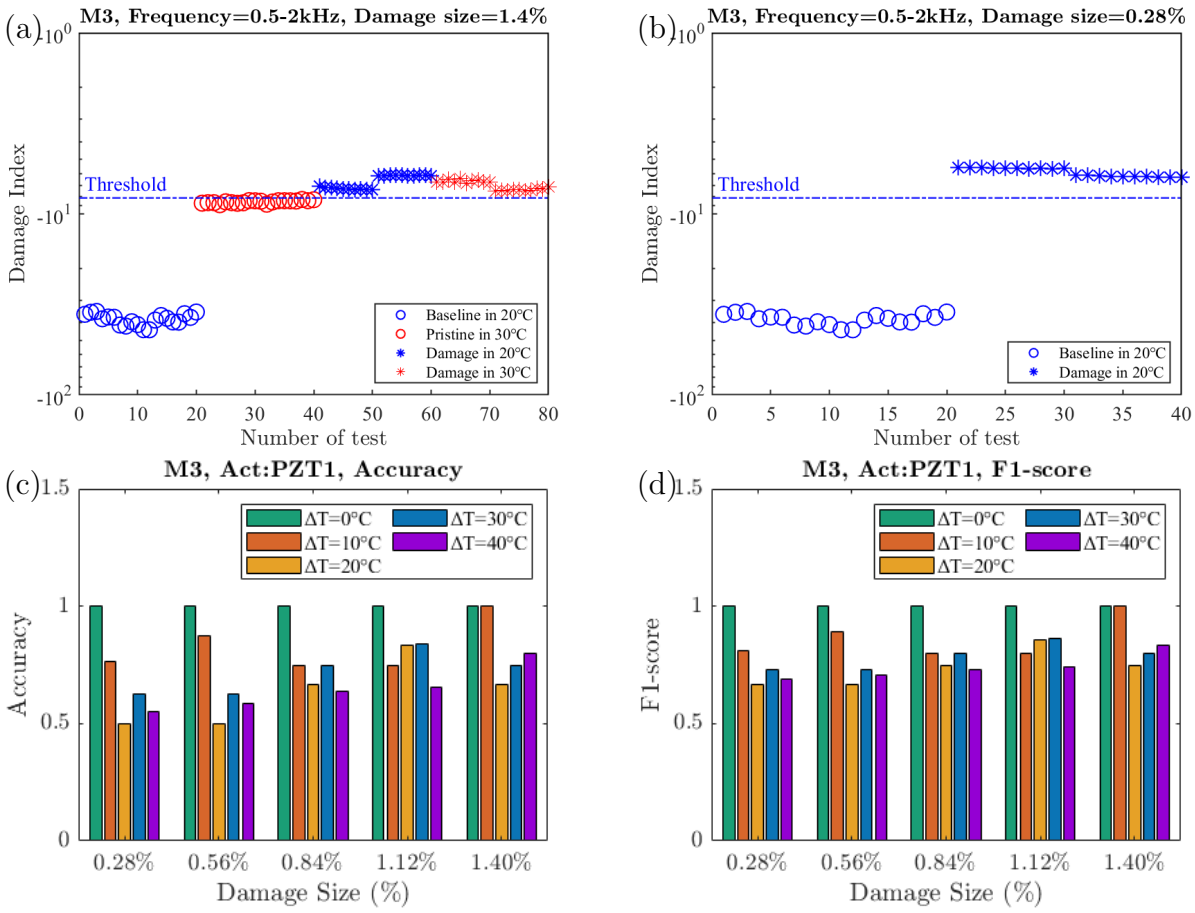


Figure 4.11: Results of M3 obtained by different conditions: (a) Damage index obtained by M3 at different temperatures when damage size =1.4%, (b) Damage index obtained by M3 at the same temperature when damage size =0.28%, (c) *Accuracy* obtained by actuator PZT1 and Specimen M3, (d) $F1-score$ obtained by actuator PZT1 and Specimen M3.

proposed method in detecting damage on M3 is presented in Figure 4.11 under different conditions. It is demonstrated that the proposed method can accurately detect damage size equivalent to 1.40% within and outside the sensor area under a temperature difference of $\Delta T = 10°$ with a 100% *Accuracy*. The damage detection threshold calculated using μ_{MD_b} and σ_{MD_b} is -8.17. However, this threshold becomes invalid with regard to a smaller damage size. For the damage size of 0.28%, it proves to be effective only when the temperature remains consistent with the baseline condition, as shown in Figure 4.11(b)

4.4.3 Uncertainty quantification

As discussed in the previous section, TFs are sensitive to damage and temperature within a specified threshold, which provides the possibility to detect damage within a temperature range.

However, TFs over the frequency band may also be affected by various experimental conditions, particularly the variation in the sensor location. As such, another PZT is used as an actuator to evaluate the effect of sensor location. Figure 4.12 shows the configuration of the setup, where PZT 2 is used as an actuator, and the remaining three PZTs are used as sensors. TFs obtained by different actuator locations are reported in Figure 4.13 to evaluate the sensitivity of the TF to sensor positioning.

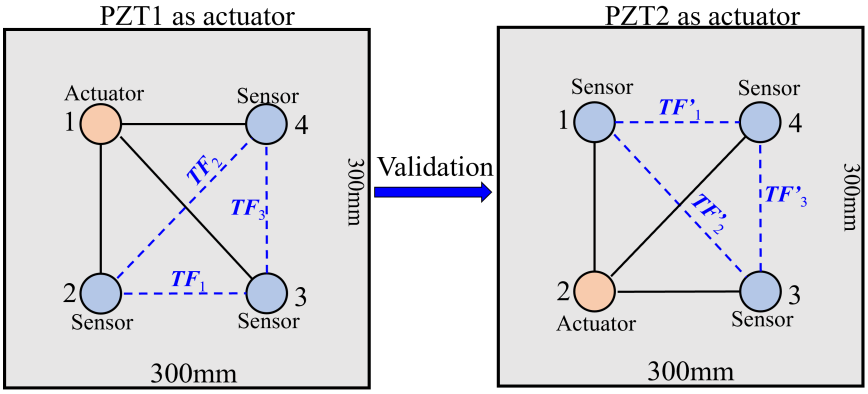


Figure 4.12: The configuration of different actuator locations.

Figure 4.13 presents the detection results obtained from M1, M2 and M3 plates under different conditions, including different temperatures, damage location and sizes, using PZT 2 as the actuator. Figure 4.13(a) and Figure 4.13(d) indicate that when PZT2 is acting as the actuator, the proposed method correctly identifies the intact and damaged scenarios for all locations within and outside the sensing area, over a temperature difference of 40 ℃, with in detectable damage size of 1.12%. In addition, when $\Delta T = 10°$, the minimum detectable damage size is increased to 0.28%. In terms of detection results on composite plates M2, Figure 4.13(b) and Figure 4.13(e) show that the proposed method is capable of fully detecting damage inside and outside the sensing area within a temperature difference of 20 ℃, and a minimum detectable damage size of 0.56%. Figure 4.13(c) and Figure 4.13(f) show that for the anisotropic plate M3, the proposed method can fully detect 1.4% damage over a temperature difference range of 10℃. These results are entirely consistent with the previous results that employed sensor 1 as the actuator, demonstrating that the location of the sensor does not affect the detection results of the proposed method.

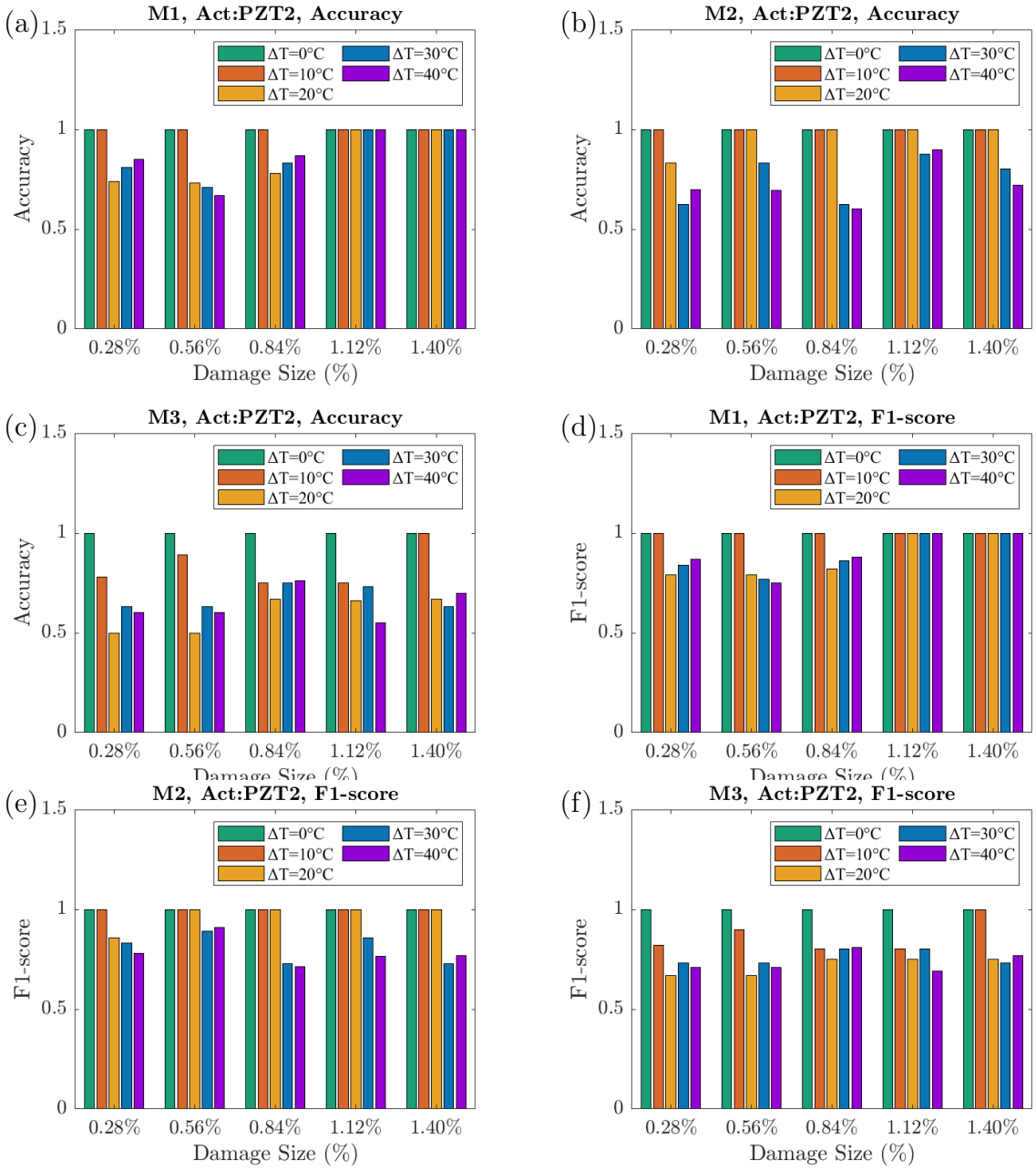


Figure 4.13: *Accuracy* and $F1-Score$ results for M1 (a, d), M2 (b, e), and M3 (c, f) Using PZT2 as Actuator.

4.5 Summary

This chapter presents a novel and practical damage detection methodology that leverages the multifunctional capabilities of piezoelectric (PZT) transducers. Traditionally employed for guided wave-based structural health monitoring (SHM), these transducers are here repurposed to perform both ultrasonic excitation and modal analysis, thereby enabling the extraction of transmissibility functions (TFs)—a type of temperature-insensitive feature critical for robust performance under varying environmental conditions. By exploiting TFs that encapsulate the modal characteristics of structures, the proposed approach effectively distinguishes between damage-induced changes and those arising from temperature variations, eliminating the need for complex temperature compensation strategies. Subsequently, outlier analysis is employed as a statistical tool to identify anomalies indicative of damage. The key outcomes of this study are summarized below:

For the isotropic aluminum plate (M1), the methodology demonstrated exceptional performance, achieving 100% accuracy in detecting damage both within and beyond the sensor coverage area. The minimum detectable damage size was 1.12% across a 40℃ temperature variation. Additionally, the approach achieved a 100% accuracy rate in identifying damage as small as 0.28% under a 10℃ temperature difference.

In the quasi-isotropic composite plate (M2), the methodology fully detected damages as small as 1.4%, both inside and outside the sensing area, under a temperature variation of 20℃. The smallest detectable damage size within this range was determined to be 0.56%.

For the anisotropic curved composite plate (M3), the methodology demonstrated robust performance, successfully identifying damages equivalent to 1.4% both within and beyond the sensor area under a temperature difference of 10℃.

Furthermore, consistent results from various sensor locations verified that sensor placement did not influence the detection efficacy, confirming the robustness of the proposed methodology. This approach requires only a single baseline signal, significantly reducing reliance on extensive baseline data, while ensuring effective damage detection across wide temperature ranges. It also extends detection capabilities beyond immediate sensing areas, demonstrating adaptability to diverse structural configurations, including those with increased complexity and anisotropy.

Overall, the proposed methodology offers a comprehensive, reliable, and efficient solution for

damage detection under complex environmental conditions. It highlights the potential of TF analysis to address temperature compensation challenges in SHM, paving the way for broader applications in real-world engineering scenarios.

Chapter 5

Progressive damage detection under varying temperatures: linear versus nonlinear ultrasonic guided waves and vibration-based methods

5.1 Introduction

As discussed in previous sections, unlike traditional NDT methods, which are typically performed at scheduled intervals and requiring operational downtime [139], SHM provides continuous monitoring without disrupting normal operations. This capability reduces both maintenance costs and downtime, making it particularly valuable in diverse domains, such as aerospace [140, 141], civil engineering [142, 143], wind turbines [144, 145], and power generation [146, 147]. Among SHM techniques, linear and nonlinear guided wave techniques, alongside vibration-based modal analysis, have gained prominence, each providing unique benefits and addressing different aspects of structural assessment [42, 50].

Linear guided wave methods employ embedded PZT transducers to generate and receive ultrasonic guided waves, detecting damage by comparing current signals with those from a baseline (undamaged) state [148]. The increasing interest in linear methods is due to their ability to trans-

mit ultrasonic guided waves over long distances with minimal energy loss, as well as their high sensitivity to subtle structural changes. When ultrasonic guided waves interact with structural damage, such as cracks, delamination, and corrosion, their scattering and attenuation properties enable effective damage detection and assessment. To enhance the accuracy and automation of linear guided wave-based SHM, various signal processing and machine learning algorithms have been developed. Time-of-arrival [149,150], time-reversal techniques [151,152], and artificial intelligence (AI) [153] have all demonstrated promising results. He et al. [154] conducted experiments on crack detection and quantification in riveted lap joints, showing a correlation between fatigue crack length and damage indices, such as signal correlation coefficients and amplitude-phase changes. Similarly, Mardanshahi et al. [155] integrated linear wave propagation with AI to classify matrix cracking in glass/epoxy composites. By extracting features like wave velocity and amplitude ratios, their SVM model achieved a high classification accuracy of 91.7%, demonstrating its robustness in automated crack density classification. Building on these advancements, Nan et al. [156] proposed a hierarchical approach for designing linear guided wave-based SHM systems to detect barely visible impact damage in composite airframe structures. This framework not only enhances detection accuracy but also provides a systematic method for evaluating SHM system performance under uncertain conditions, paving the way for broader application across diverse structural types.

Unlike linear guided wave methods, which rely on baseline data for damage detection, nonlinear guided wave techniques identify damage by analyzing wave-induced nonlinear phenomena. Nonlinear techniques are categorized based on the interaction characteristics of the input guided wave into two primary types: signal modulation methods (cross-interaction) [157, 158] and harmonic methods (self-interaction), which include subharmonic [159, 160], second harmonic [161, 162], and third harmonic approaches [163, 164]. Nonlinear ultrasonic guided waves are particularly sensitive to early-stage defects at the microscale, such as micro-cracks and dislocations, which induce nonlinear responses in the waveforms that are often undetectable by linear methods. For instance, Espinoza et al. [42] conducted a comparative analysis of linear and nonlinear resonant ultrasound spectroscopy for quantifying dislocation density in aluminum and copper samples. The results demonstrated that the nonlinear method exhibits 2–6 times greater sensitivity than the linear method, as confirmed by second harmonic generation (SHG) measurements showing 14-62%

higher sensitivity. Su et al. [50] introduced a hybrid approach for fatigue damage characterization in engineering structures, leveraging both linear and nonlinear features of acousto-ultrasonic waves. This method employs PZT transducers for active monitoring, enabling early detection and continuous assessment of fatigue cracks in metallic structures. Results indicate that nonlinear features are more sensitive to small-scale damage, while linear features offer better noise tolerance and practicality. The combined use of linear and nonlinear indices enhances the prediction of multi-scale damage, from microscopic fatigue cracks to larger structural damage, supporting more robust health monitoring solutions. Yun et al. [165] provided a comprehensive review comparing nonlinear ultrasonic guided waves to linear ultrasonic guided waves, highlighting several advantages of nonlinear methods, particularly their sensitivity to early-stage damage.

Compared to linear and nonlinear guided wave methods, as discussed in the previous chapters, VSHM methods offer notable advantages, particularly their robustness to EOCs and the ease of obtaining modal parameters from operating structures. VSHM methods detect damage by analyzing changes in structural modal parameters, including natural frequencies, mode shapes, damping ratios, and FRF. Therefore, VSHM methods have also attracted attention in the SHM. Salawu et al. [120] noted that the effects of environmental factors, such as temperature and humidity, on dynamic characteristics are often small or predictable. Zhang et al. [166] proposed a method based on natural frequency to predict the location and size of delamination, which was validated by the modal analysis of reinforced polymer (FRP) composites with delamination. Khan et al. [123] reported a method for detecting delamination in composite laminates using low-frequency vibration response, an approach also proven effective in Minak's research [124]. Zhang et al. [167] presented a comprehensive review of the recent progress that used signal processing techniques for VSHM approaches.

Fatigue testing is widely used in SHM field, simulating progressive damage under cyclic loading to closely replicate real-world conditions. Structural damage often begins at imperceptible levels as fatigue mechanisms activate, leading to dislocation structures and the formation of persistent slip bands in practical applications [168]. These processes eventually result in macro-cracks, potentially reaching critical sizes and compromising structural integrity under continued loading. Fatigue testing provides a realistic framework for evaluating SHM methods, enabling the assessment of their

sensitivity across various stages of damage progression [50]. Despite advancements in both linear and nonlinear guided wave methods, as well as vibration-based methods, their comparative performance under identical experimental conditions—particularly for detecting progressive damage and their sensitivity to environmental changes, such as temperature—remains unclear. Therefore, this paper aims to address these gaps by systematically comparing the sensitivity and effectiveness of each method under different temperature conditions. The main novel contributions of this chapter are:

(i) This chapter introduces a pioneering multifunctional approach to PZT transducers by leveraging their unique ability to generate ultrasonic guided waves for both linear and nonlinear analyses, as well as to capture vibration-based measurements. This multifunctionality creates a versatile SHM platform that integrates multiple detection modes, thereby enhancing sensitivity and adaptability across diverse monitoring scenarios.

(ii) A novel investigation is conducted into the sensitivity thresholds of various SHM methods, specifically focusing on their ability to detect progressive damage. By identifying the minimum detectable damage for each method, this chapter establishes a benchmark for evaluating the accuracy and performance of SHM techniques in real-world scenarios involving gradual damage progression.

(iii) Recognizing the challenges posed by real-world operational conditions, this chapter systematically evaluates the influence of temperature variability on the performance of different SHM methods. The findings provide critical insights into how environmental changes affect detection capabilities, contributing to the development of SHM techniques that ensure reliable fatigue damage monitoring under fluctuating temperature conditions.

The remainder of this chapter is organized as follows: The experimental setup is presented in Section 2, which includes the fatigue experiment setup and the signal acquisition configuration. Section 3 presents details about the methods. Obtained results are discussed in Section 4, and the paper is concluded in Section 5.

5.2 Experimental Setup

5.2.1 Tensile test

The proposed online crack monitoring methodology is validated using aluminium 5251 plates with a central hole. Prior to the fatigue experiment, five tensile coupons (T1–T5) were designed and fabricated according to the ASTM E8M standard [169], as shown in Figure 5.1(c). These coupons were tested to determine the material's mechanical properties, with the experimental setup illustrated in Figure 5.1(a). During the test, a digital image correlation (DIC) camera was used to record the strain evolution, and the stress–strain curve obtained from T1 is presented in Figure 5.1(b), illustrating the three stages of tensile deformation: elastic (I), strain hardening (II), and necking (III). The test lasted for 334.6 seconds. In the elastic stage (I), the material reached an axial strain (ε_a) of 0.06% and a radial strain (ε_r) of –0.03%, indicating reversible elastic deformation. During the strain hardening stage (II), the material exhibited an axial strain of 6.00% and a radial strain of –2.06%, representing plastic deformation accompanied by permanent changes in shape. In the necking stage (III), localized reduction in cross-sectional area occurred, with the axial strain reaching 9.88% and radial strain reaching –3.52%, ultimately leading to fracture. The Young's modulus of the specimen was determined to be 64 GPa based on the slope of the elastic region. The yield strength, calculated using the 0.2% offset method [170], was 143.45 MPa, and the ultimate tensile strength was 195.14 MPa. The complete mechanical property data for all five specimens (T1–T5) are summarised in Table 5.1. The average values of Young's modulus, yield strength, and tensile strength were 63.85 GPa, 145.21 MPa, and 197.76 MPa, respectively. These values were used as the reference properties for the aluminium 5251 material employed in this study. To evaluate the material scatter, the standard deviations of the measured properties across the five specimens were also calculated. The results show a standard deviation of 0.89 GPa for Young's modulus, 1.36 MPa for yield strength, and 2.06 MPa for tensile strength. These relatively small deviations reflect good material consistency and support the validity of using the average values as representative material parameters.

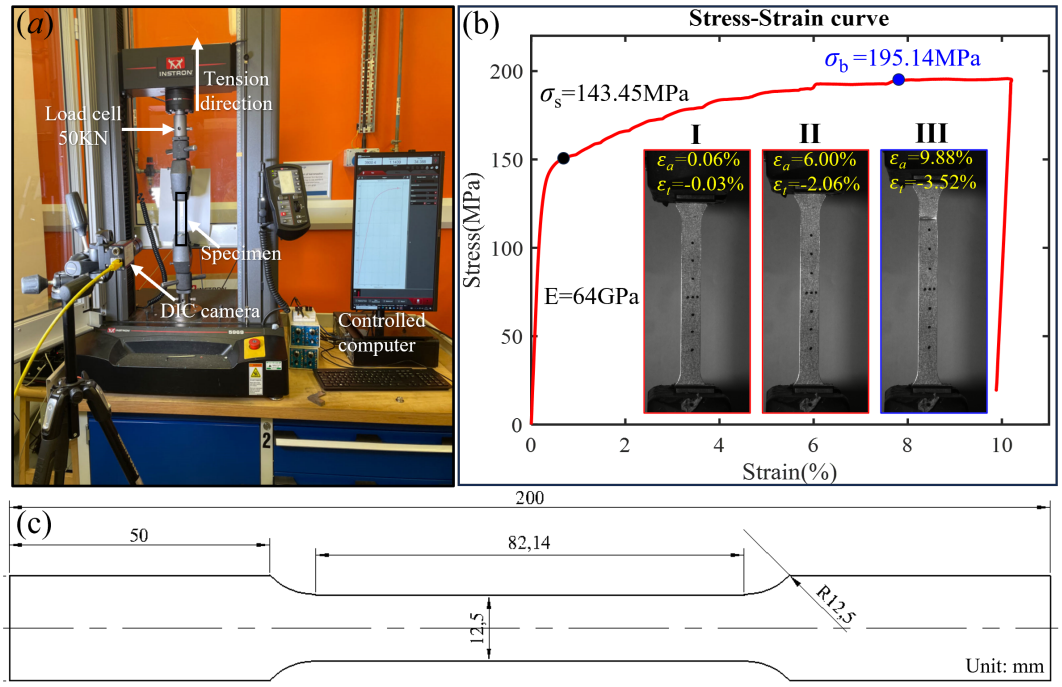


Figure 5.1: The experimental platform for the tensile test, a) tensile test setup, b) stress and strain curve and c) the geometry of the coupon.

Table 5.1: Mechanical properties of aluminium 5251 obtained from tensile testing.

	Young's modulus (GPa)	Yield strength (MPa)	Tensile strength (MPa)
T1	63.90	147.33	200.24
T2	64.96	145.47	198.89
T3	64.02	143.45	195.14
T4	63.88	143.64	195.91
T5	62.48	146.17	198.60
Ave	**63.85**	**145.21**	**197.76**

5.2.2 Fatigue experiment setup

In the experiment, three Al-5152 plates (300 mm × 100 mm × 2 mm) cut from the same aluminium sheet were used. Material property, including Young's modulus and tensile strength, were determined by tensile test, as detailed in our previous work [39]. A 10 mm diameter circular hole was initially machined at the center of each plate. Two piezoelectric sensors (DuraAct, PI) were bonded to the plates using Hexcel Redux 312 epoxy-based film adhesive, as shown in Fig. 5.2(b). These PZT sensors are multifunctional, enabling passive vibration measurement as well as linear and nonlinear Lamb wave measurement without the need for additional power sources, thereby simplifying sensor deployment and reducing power consumption. The cyclic loading tests were

conducted using an Instron hydraulic 250 kN fatigue machine, as shown in Fig. 5.2(a). Three specimens were labelled T1, T2, and T3. Cyclic uniaxial loading was applied with a maximum load of 15 kN (50% of the yield strength) and a minimum load of 1.5 kN, at a load ratio of 0.1 and a frequency of 10 Hz. In the early stages of the fatigue test, the loading was paused every 100k cycles. As the fatigue test progressed, the frequency of pausing was gradually reduced to capture more data on crack propagation. The plates were then removed and placed in a forced convection oven for linear and nonlinear Lamb wave acquisition, as well as vibration measurements during each interval, at varying temperatures between 20°C and 40°C, as shown in Fig. 5.2(c). After completing the measurements, crack initiation and propagation were observed using a Hirox 3D digital microscope, as illustrated in Fig. 5.2(d-e). Since the crack initiation time is different on three plates, the fatigue test progression is categorized into seven distinct phases, labeled 1 to 7. In the first four stages, all three plates were subjected to the same number of loading cycles, with stage 1 representing the state before the fatigue tests, and stages 2 to 4 representing 100,000, 200,000, and 300,000 loading cycles, respectively. The details of the fatigues test on different specimens are listed in Table 5.2.

Table 5.2: Fatigue test details on different specimens under different temperatures

Stage of fatigue test(cycles)	**T1**	**T2**	**T3**	**Working temperature**
1	0k	0k	0k	
2	100k	100k	100k	
3	200k	200k	200k	
4	300k	300k	300k	20–40°C
5	320k	350k	400k	
6	340k	370k	420k	
7	360k		440k	

5.2.3 The signal measurement

Four different tests were conducted intermittently during the fatigue experiment. For the linear guided-wave method, two PZT transducers were used alternately as actuators and sensors. As shown in Figure 5.3(a), a broadband chirp signal (25 kHz to 650 kHz) with a 12V peak-to-peak amplitude was generated by a National Instruments PXI 5412 waveform generator and applied over a 200 µs window. The plate's response was recorded by a PXI 5105 oscilloscope at a sampling

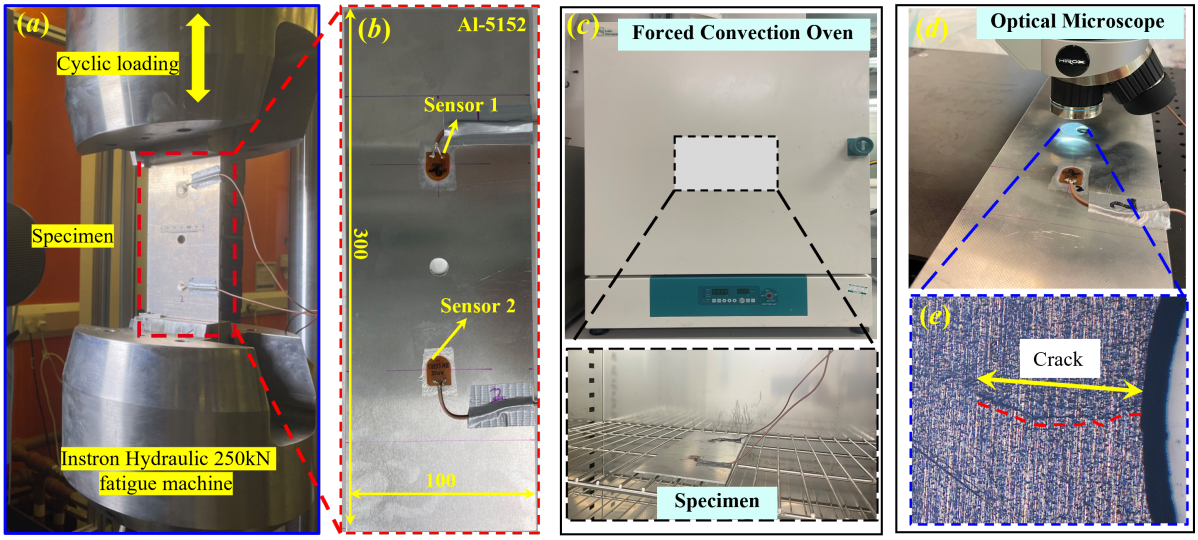


Figure 5.2: The experiment setup and facilities: (a) the fatigue experiment setup; (b) the aluminum specimen with two PZT sensors; (c) The forced convection oven to control temperature; (d) the optical microscope for the crack inspection; (e) the observed crack.

rate of 60 MHz, capturing data over a 500 µs. The nonlinear measurement system, depicted in Figure 5.3(b), comprised a PXI 5412 arbitrary waveform generator, a PXI 5105 oscilloscope, and a TEGAM x50 amplifier. A 1.73 MHz sine wave was applied to one PZT sensor, while the other sensor recorded the response at a 60 MHz sampling rate over 200 µs. For the vibration-based SHM, a chirp signal sweeping from 100 Hz to 2500 Hz was applied, with a sampling rate of 100 kHz and a duration of 1 second. One PZT acted as the actuator, while the other recorded the response, with both signals captured using the PXI 5105 oscilloscope at a 1 Ms/s sampling rate over 1 second. This test was repeated five times to mitigate environmental noise. The setup is shown in Figure 5.3(c). The SinePhase Impedance analyser was used to measure the EMI, ensuring the operational state of two PZTs and their bonding condition, and the equipment are summarized in Figure 5.3(d).

5.3 Methodology for the crack detection

5.3.1 ToF-based DI for linear methods

The crack detection in Aluminum structures using linear guided wave is achieved by comparing a baseline signal—recorded when the panel is in a pristine state—with signals collected in the

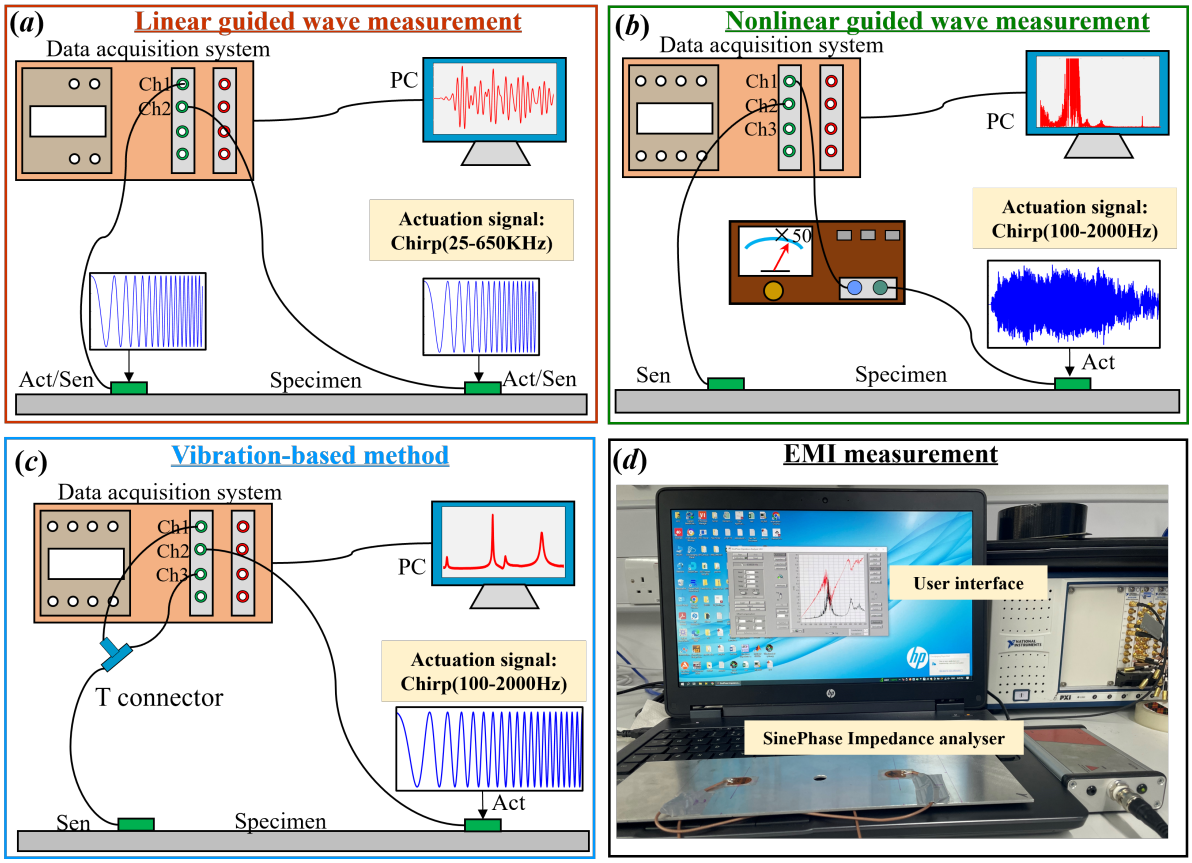


Figure 5.3: The signal acquisition system. a) the schematic diagram of the Linear guided wave-based method, b) the schematic diagram of the nonlinear guided wave-based method, c) the schematic diagram of the Vibration-based method, d) EMI measurement system.

current state (which could be either pristine or damaged). To ascertain the presence of damage, damage-sensitive features are extracted from the signals and quantified using the damage index. A threshold is set to differentiate between the pristine and damaged states, minimizing the probability of incorrectly predicting the state. Specifically, the damage detection is conducted by comparing the global DI γ_1 with a threshold γ_0: when $\gamma_1 < \gamma_0$, the state is identified as pristine; when $\gamma_1 > \gamma_0$, it is identified as damaged [141].

Let $c_n(t)$ represent the current signal and $b_n(t)$ the baseline signal for the n-th ($n = 1 \dots N$) recorded signal, where μ_{c_n} and μ_{b_n} denote their respective means, and σ_{c_n} and σ_{b_n} their standard deviations. The correlation-based damage index $DI_n^{(1)}$ is calculated using the formula [18]:

$$DI_n^{(1)} = 1 - \rho_n = 1 - \frac{\sum_{t=0}^{T}[c_n(t) - \mu_{c_n}][b_n(t) - \mu_{b_n}]}{\sigma_{c_n}\sigma_{b_n}}, \tag{5.1}$$

where ρ_n is the correlation coefficient between the baseline signal $b_n(t)$ and the current signal $c_n(t)$.

Here, μ_n and σ_n represent the mean value and standard deviation of the signal, respectively, and T is the time window of the signal used for comparison.

5.3.2 Second harmonic-based DI for nonlinear methods

Theoretical background In nonlinear guided wave theory, the guided wave dispersion relation describes the propagation behavior of the fundamental frequency (first harmonic) and the second harmonic generated due to material nonlinearity [171]. The dispersion relation for ultrasonic guided waves is expressed as:

$$\frac{\tan(\beta h)}{\tan(\alpha h)} = -\left[\frac{4\alpha\beta k^2}{(k^2-\beta^2)^2}\right]^{\pm 1} \tag{5.2}$$

where α and β are defined as:

$$\alpha = \sqrt{\left(\frac{\omega}{c_l}\right)^2 - k^2}, \quad \beta = \sqrt{\left(\frac{\omega}{c_t}\right)^2 - k^2} \tag{5.3}$$

The longitudinal and transverse wave speeds are given by:

$$c_l = \sqrt{\frac{\lambda + 2\mu}{\rho_0}}, \quad c_t = \sqrt{\frac{\mu}{\rho_0}} \tag{5.4}$$

where c_l and c_t are the longitudinal and transverse wave velocity, k is the wavenumber, and h is half the plate thickness. Due to material nonlinearity, the propagation of the fundamental wave generates a second harmonic with twice the frequency of the original wave ($2f$). The dispersion relation for the second harmonic is given by:

$$\frac{\tan(2\beta h)}{\tan(2\alpha h)} = -\left[\frac{4\alpha\beta k^2}{(k^2-\beta^2)^2}\right]^{\pm 1} \tag{5.5}$$

The propagation velocity of the second harmonic and its phase-matching conditions are closely linked to those of the fundamental wave. The phase-matching condition is satisfied when:

$$\frac{\tan(\beta h)}{\tan(\alpha h)} = \frac{\tan(2\beta h)}{\tan(2\alpha h)} \tag{5.6}$$

Further derivation leads to the nonlinear coupling condition:

$$\sin(\beta h)\sin(2\alpha h)\cos(2\beta h)\cos(\alpha h) = \sin(2\beta h)\sin(\alpha h)\cos(\beta h)\cos(2\alpha h) \tag{5.7}$$

Simplifying this expression yields:

$$\sin(\beta h)\sin(\alpha h)\cos(\beta h)\cos(\alpha h)\sin(\beta h + \alpha h)\sin(\beta h - \alpha h) = 0 \tag{5.8}$$

For second harmonic generation, it is typically assumed that $\beta h = n\pi$ and $\alpha h \neq n\pi$, with α potentially approaching zero. This ensures that the second harmonic propagates synchronously with the fundamental wave. For symmetric modes of the fundamental and second harmonic, the dispersion relation simplifies to $4k^2\alpha\beta = 0$. When $\alpha = 0$, the phase velocity equals c_l. Substituting $c_p = c_l$ into the condition $\beta h = n\pi$ gives:

$$\omega = \frac{n\pi c_l c_t}{h\sqrt{c_l^2 - c_t^2}} \tag{5.9}$$

This simplifies the relationship between the second harmonic frequency and waveguide conditions to:

$$f \cdot 2h = \frac{n c_l c_t}{\sqrt{c_l^2 - c_t^2}} \tag{5.10}$$

The phase velocity matching condition for the second harmonic is expressed as:

$$2f \cdot 2h = \frac{2n c_p c_t}{\sqrt{c_p^2 - c_t^2}} \tag{5.11}$$

where c_p represents the phase velocity of the second harmonic, which is influenced by the material's nonlinear properties and initial stress state. Thus, second harmonic generation is not only related to the propagation characteristics of the fundamental wave but is also significantly affected by the material's nonlinear properties.

Figure 5.4(a) illustrates the phase velocity matching of two modes: the fundamental S1 mode and the second harmonic S2 mode, occurring at frequencies of 1.73 MHz and 3.46 MHz, respectively. As shown in Figure 5.4(b), the group velocities of the fundamental S1 mode and the second

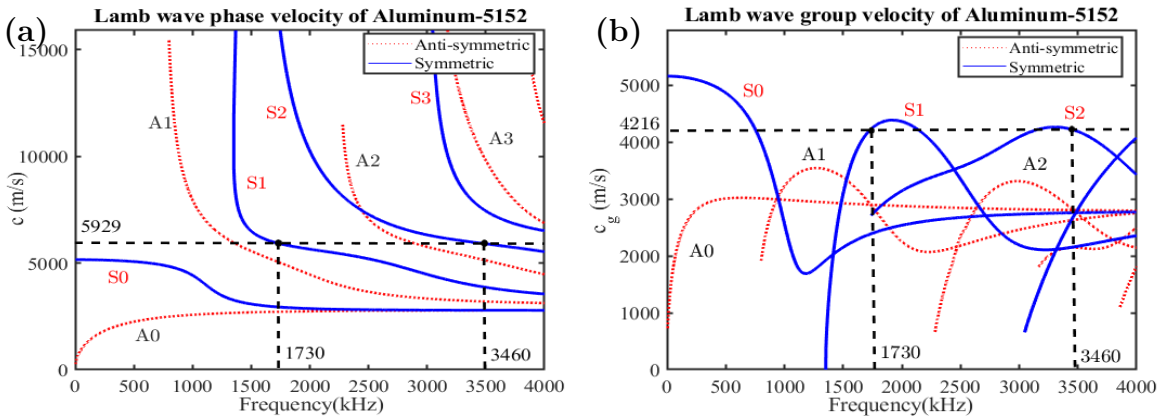


Figure 5.4: Dispersion curves of (a) phase velocity and (b) group velocity for Aluminum-5152 with 2mm thickness.

harmonic S2 mode are higher than those of other modes at the same frequency. Thus, the fundamental S1 mode appears as the first wave packet (direct wave) in the response signal. Additionally, both modes satisfy the group velocity matching condition, enabling the second harmonic S2 mode to propagate simultaneously with the fundamental S1 mode.

In this research, the parameter β', calculated from the fundamental and second harmonic amplitudes, is proposed to analyze the frequency domain of the response, which is defined as:

$$\beta' = \frac{A_2'}{A_1'^2} \tag{5.12}$$

where A_1' represents the amplitude of the fundamental frequency obtained from the response, and A_2' is the amplitude of the second harmonic frequency component of the response. The calculation process of β' can be found in our previous work [39]. β' is easier to measure, as it only requires the amplitudes of the fundamental and third harmonic signals in the frequency domain.

5.3.3 FRF-based DI for Vibration methods

For the vibration-based method, the FRF is employed to characterize changes in modal properties before and after damage, enabling the analysis of parameters such as the damping ratio and resonance frequency [172]. The FRF is defined as:

$$H_{ik}(\omega) = \frac{X_{ik}(\omega)}{F_k(\omega)} \tag{5.13}$$

where $H_{ik}(\omega)$ represents the FRF obtained from the excitation force and the corresponding response at a specific point. Here, $F_k(\omega)$ denotes the excitation force in the frequency domain, while $X_{ik}(\omega)$ refers to the vibration response captured by the PZT in the frequency domain. Then equation (5.1) is used to quantify the difference between the current FRF and its baseline, facilitating the detection of changes in the vibration response attributable to potential damage. By analyzing deviations in the $DI_n^{(1)}$ from zero, the extent of the crack can be detected. Larger values of $DI_n^{(1)}$ indicate a greater deviation from the pristine state, signalling potential structural damage.

5.4 Results and discussion

5.4.1 Temperature and crack effect on the features

Temperature and crack effect on the FRF Many previous studies on FRF-based methods have demonstrated that temperature changes have minimal impact on the modal properties of structures, particularly at low frequencies. In contrast, damage significantly alters the modal properties [120]. As discussed in the previous section, the features extracted in this research are designed to be damage-sensitive and temperature-insensitive. To validate this, the effects of both temperature variations and structural damage on the FRF are analyzed, and results are summarized in Figure 5.5.

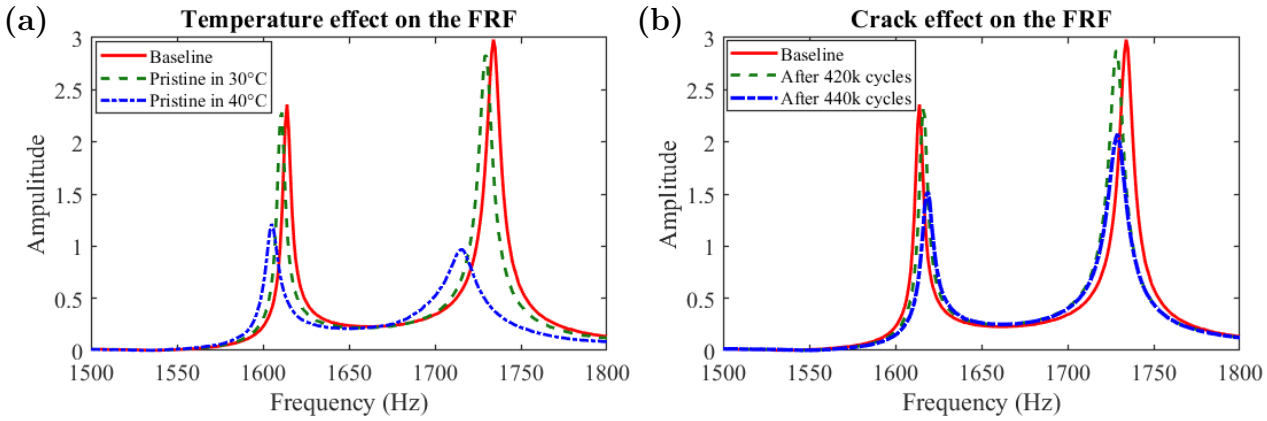


Figure 5.5: Temperature and damage effect on FRF. (a) the comparison between the baseline and the current FRF at 30℃ and 40℃, and (b) the comparison between the baseline and the current FRF after 420k and 440k cycles.

As illustrated in Figure 5.5(a), the FRF exhibits significant variation between 1500 and 1800 Hz

under different temperatures conditions. The red solid line represents the baseline FRF, while the green dashed line indicates the change in FRF at 30°C, and the blue dotted-dashed line corresponds to the FRF at 40°C. A temperature increase of 10°C causes noticeable shifts in the frequency and amplitude of the peaks within the ranges of 1600–1650 Hz and 1700–1750 Hz. At 40°C, both the amplitude and frequency of these peaks decrease more substantially. Specifically, the frequency of the first peak decreases by 0.56%, with a corresponding 48.64% reduction in amplitude, while the frequency of the second peak decreases by 1.03%, accompanied by a 67.6% reduction in amplitude. Previous studies have reported that the FRF reflects the intrinsic properties of the structure and is generally insensitive to environmental changes, such as temperature [173–175]. However, most of these studies derived the FRF using accelerometers, which do not account for wave propagation on or within the structure. In contrast, this study utilizes PZT sensors to acquire the FRF, which is influenced by factors such as the bonding condition of the PZT sensors and material property changes due to thermal expansion and contraction. These factors account for the observed frequency and amplitude variations with a 20°C temperature increase. Figure 5.5(b) illustrates the influence of a crack on the FRF. After 420k loading cycles, within the 1500-1800 Hz frequency range, the first peak's frequency increases while its amplitude decreases, and both the frequency and amplitude of the second peak decline. At this stage, the crack length measures 3.27 mm. As loading cycles increase, the first peak's frequency continues to rise, while its amplitude decreases further. Meanwhile, the second peak's frequency remains relatively stable, although its amplitude consistently diminishes. These results demonstrate that both temperature and cracks affect the FRF. However, the distinct nature and extent of these effects highlight the potential of using FRF for damage detection under varying temperature conditions.

Temperature and crack effect on the guided wave Previous studies suggested that the temperature effect of guided wave signals is dependent on the material and geometrical properties of the host plate, adhesive layer and transducers [176–178]. Figure 5.6 summarizes the effect of damage and temperature on the guided wave.

Figure 5.6 (a) and (b) illustrate the temperature effect on guided wave propagation, revealing that the propagation characteristics of ultrasonic guided waves change significantly under different temperature conditions (30°C and 40°C). As the temperature increases, the amplitude of the

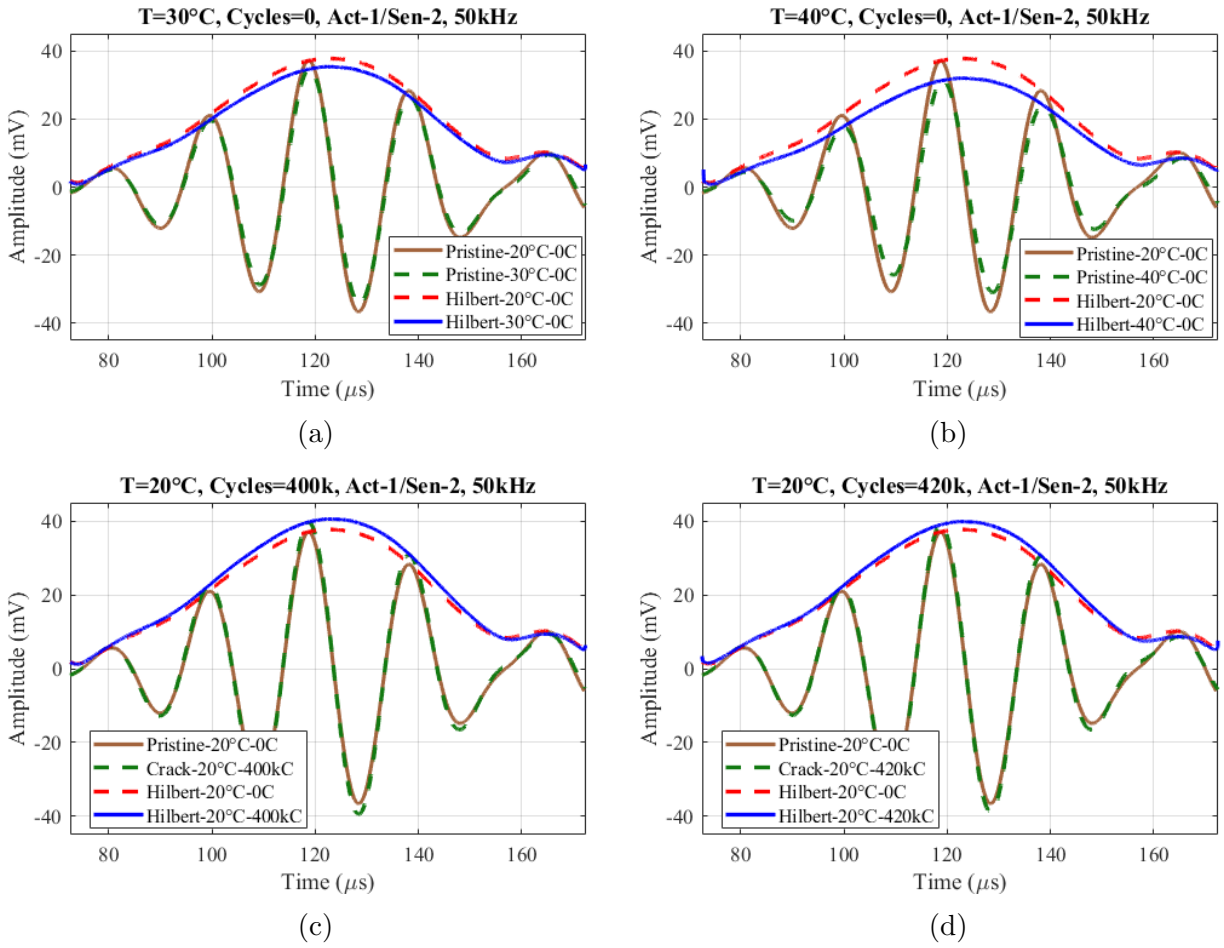


Figure 5.6: Temperature and damage effect on the guided-wave propagation. (a) The comparison between the baseline and the current signal at 30℃, (b) The comparison between the baseline and the current signal at 40℃, (c) The comparison between the baseline and the current signal after 400k cycles, (d) The comparison between the baseline and the current signal after 420k cycles.

guided wave decreases. For instance, at 30°C, the amplitude in the pristine state decreases by 6.46% compared to the baseline, while at 40°C, the reduction reaches 15.48%. This phenomenon can be attributed to the influence of temperature on the material's elastic modulus and wave speed. Increasing temperatures reduce the material's elastic modulus, which results in a decrease in wave speed and increased energy attenuation. The reduction in stiffness results in slower wave propagation and greater attenuation of wave energy, which in turn lowers the amplitude of the first wave packet, extracted through the Hilbert transform under different temperature conditions. Figure 5.6 (c) and (d) demonstrate the effect of cracks on guided wave propagation. At a constant temperature of 20°C, as the number of loading cycles increases, the amplitude of the guided wave in the damaged state also increases. For example, the amplitude increases by 7.22% at 400k cycles

and by 5.30% at 420k cycles. This increase can be attributed to the initiation and propagation of micro-cracks within the material. As loading cycles accumulate, the internal microstructure evolves, changing wave propagation paths. The development of micro-cracks changes wave energy concentration or scattering in the damaged regions, thereby influencing the detected wave amplitude.

In summary, the above results indicate that both temperature variations and the cracks influence the propagation of ultrasonic guided waves, as reflected in the amplitude changes of the extracted first wave packet. However, it remains challenging to quantify the extent to which temperature variations obscure the impact of cracks on guided wave propagation. To address this issue, the DI derived from equation (5.1) is used to evaluate this effect, as detailed in the subsequent section.

Temperature and crack effect on the SH In nonlinear guided wave theory, the initiation of cracks enhances the material's local nonlinearity, thereby affecting the frequency components of the guided wave. Specifically, the amplitude of the fundamental frequency decreases, while the amplitude of the second harmonic increases. The effects of the crack is summarised in Figure 5.7.

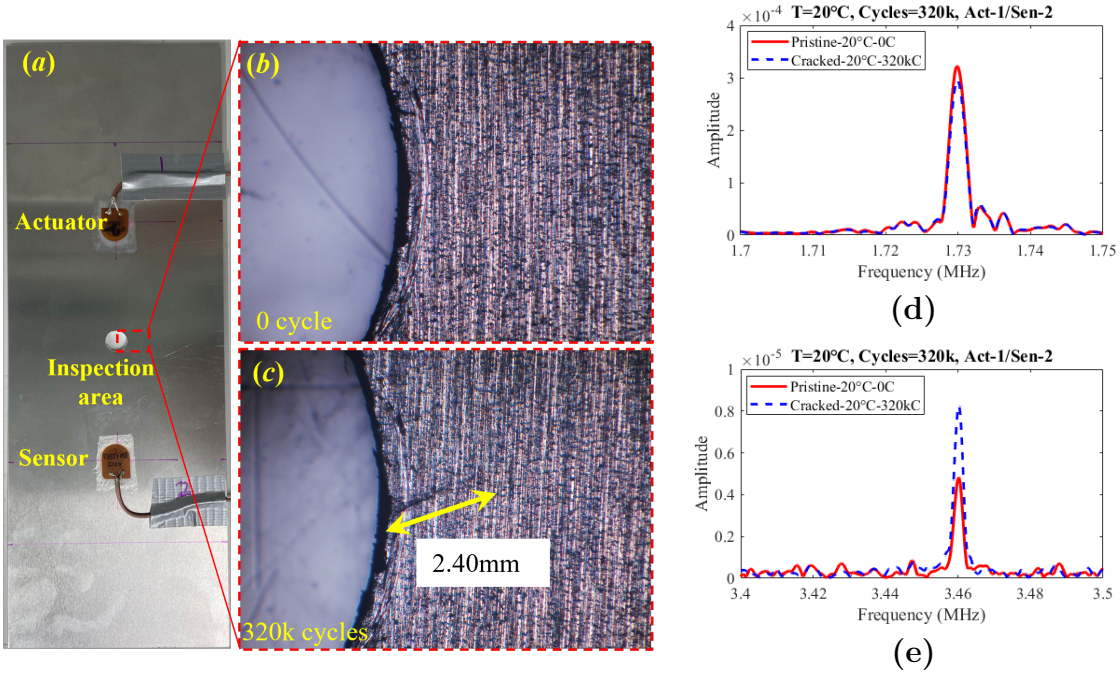


Figure 5.7: (a) Position and function of PZT sensors for nonlinear lamb wave method, (b) specimen state before the fatigue test, (c) specimen state after 320k cycles, and the amplitude of the (d) fundamental frequency and (e) second harmonic before the fatigue test and after 320k cycles.

Fig.5.7(a) illustrates the placement of two PZT sensors used in the nonlinear Lamb wave method, with one serving as the actuator and the other as the sensor. Fig. 5.7(b) and (c) illustrate the specimen's condition before the fatigue test and after 320k cycles, respectively, showing the crack propagation from 0 mm to 2.3 mm crack. The amplitudes of the fundamental and second harmonic frequency components under these two states are compared and summarized in Fig. 5.7(d) and (e). As shown in Fig. 5.7(d), the appearance of crack results in an approximately 8.49% reduction in the amplitude of the fundamental frequency, along with a slight leftward shift in the corresponding frequency. In contrast, the second harmonic amplitude increased by 70.58% following crack initiation, indicating a redistribution of energy across different frequency components in the cracked region. This phenomenon arises primarily from the increased local nonlinearity of the material near the crack. As the crack propagates, the stress-strain relationship in the affected material becomes increasingly nonlinear, facilitating the generation of higher-order harmonics. Consequently, the increase in the second harmonic amplitude serves as a sensitive indicator of crack formation, effectively reflecting the nonlinear characteristics of the material and their influence on Lamb wave propagation.

Research on the influence of temperature on the nonlinear guided wave coefficient is still limited. Nevertheless, existing studies suggest that the nonlinear guided wave coefficient increases with temperature [179, 180]. To enhance the understanding of nonlinear ultrasonic guided waves under varying temperature conditions, detailed investigations into the specific effects of temperature are essential.

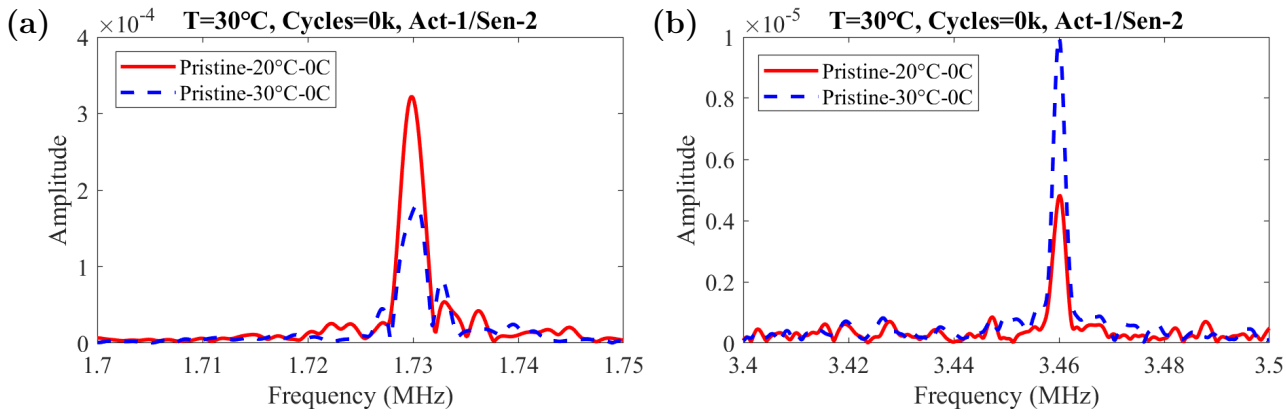


Figure 5.8: Crack effect on (a) fundamental and (b)second harmonic frequency.

Figure 5.8 illustrates the effect of temperature on the amplitudes of both the fundamental frequency and the second harmonic. When the temperature increases from 20°C to 30°C, the amplitude of the fundamental frequency decreases by 44.16%, while the amplitude of the second harmonic significantly drops by 107.1%. This phenomenon can be attributed to temperature-induced changes in the material's mechanical properties, such as elastic modulus and shear modulus. These changes, in turn, affect the material's nonlinear response, leading to alterations in the second harmonic coefficient. As the temperature rises, the material softens or exhibits more pronounced plastic deformation, which enhances its nonlinear behaviour and consequently increases the second harmonic parameter [181]. Since the effects of temperature and cracks on the nonlinear ultrasonic guided waves follow the same trend, the decrease in both the fundamental frequency and second harmonic amplitudes due to rising temperature is significantly greater than the impact of cracks. As a result, it becomes challenging to differentiate between the effects of damage and temperature on monitoring performance when using this method under varying temperature conditions.

5.4.2 Crack propagation result

Magnifications of 20x, 30x, 50x, 80x, and 120x were employed using the Hirox microscope to capture both the overall crack morphology and localized microcrack details. Lower magnifications provided an overview of crack propagation, while higher magnifications revealed more crack details. Specifically, Fig. 5.9 illustrates the crack propagation on the right side under different loading cycles, captured at 30x magnification. At 300k loading cycles, the right-side crack measured 1.78 mm in length. After an additional 20k cycles, the crack extended to 2.40 mm, eventually propagating to 6.97 mm after 340k cycles. The crack growth results obtained from three specimens are summarized in Table 5.3.

5.4.3 Crack detection results

Crack detection based on linear guided wave method The results of the linear Lamb wave method are summarized in Fig. 5.10. Due to the variations in the crack initiation times across the three plates, the X-axis is labelled numerically from 1 to 7, representing different phases of the

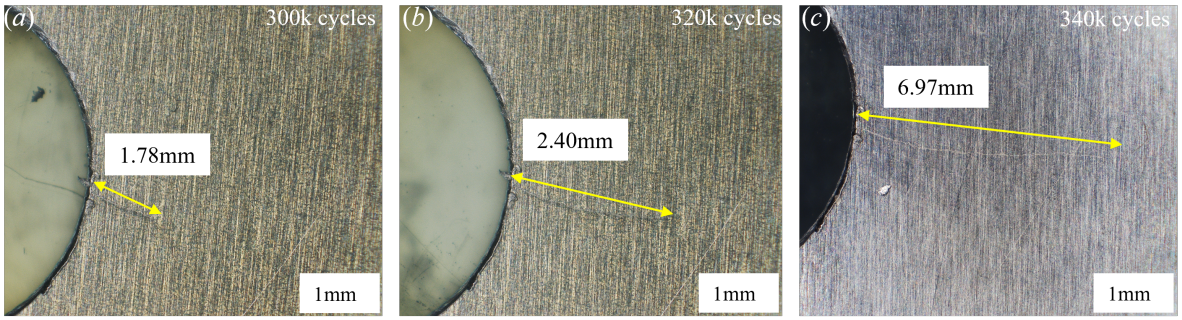


Figure 5.9: Optical microscope images of fatigue crack of T1 at: (a) 300k cycles. (b) 320k cycles. (c) 340k cycles.

Table 5.3: Crack length of different fatigue stage on specimens T1, T2, and T3

Stage	T1 (mm)			T2 (mm)			T3 (mm)		
	Cycles	a_l	a_r	Cycles	a_l	a_r	Cycles	a_l	a_r
1	0k	0	0	0k	0	0	0k	0	0
2	100k	0	0	100k	0	0	100k	0	0
3	200k	0	0	200k	0	0	200k	0	0
4	300k	0.42	1.78	300k	0	0	300k	0	0
5	320k	0.44	2.40	350k	0.80	1.30	400k	0.60	0
6	340k	2.11	6.97	370k	1.93	3.90	420k	3.27	0
7	360k	4.05	11.4				440k	6.71	1.4

fatigue tests. The results from the three plates demonstrate a progressive increase in the DI with the accumulation of fatigue loading. In the early stages (before 200k cycles), the increase in the DI is relatively small. However, as cracks begin to form in the later stages, the DI exhibits a more pronounced rate of increase. When the DI threshold is set to 5.0×10^{-4}, the linear Lamb wave method can detect crack lengths of $a_l = 0.42\,\text{mm}$ and $a_r = 1.78\,\text{mm}$ on specimen T1, $a_l = 0.8\,\text{mm}$ and $a_r = 1.3\,\text{mm}$ on T2, and $a_l = 0.6\,\text{mm}$ and $a_r = 0\,\text{mm}$ on T3, based on the corresponding fatigue stage shown in Table 5.3. However, the rate of increase in DI before and after crack initiation is not particularly significant under this threshold. When the threshold is increased to 1.0×10^{-3}, the detectable crack lengths remain unchanged for T2. In contrast, for T1, the detectable crack lengths increase to $a_l = 2.11\,\text{mm}$ and $a_r = 6.97\,\text{mm}$, and $a_l = 3.27\,\text{mm}$ and $a_r = 0\,\text{mm}$ for T3. These results highlight the linear Lamb wave method's capability to detect small cracks under consistent temperature conditions. As shown in Fig. 5.10(b), the DI values are calculated using the same

baseline signal at a temperature of 20°C. However, when the ambient temperature deviates from the baseline, distinguishing whether changes in the DI result from crack initiation or temperature variation becomes increasingly challenging. This limitation highlights the reduced reliability of the linear Lamb wave method in environments with temperature fluctuations.

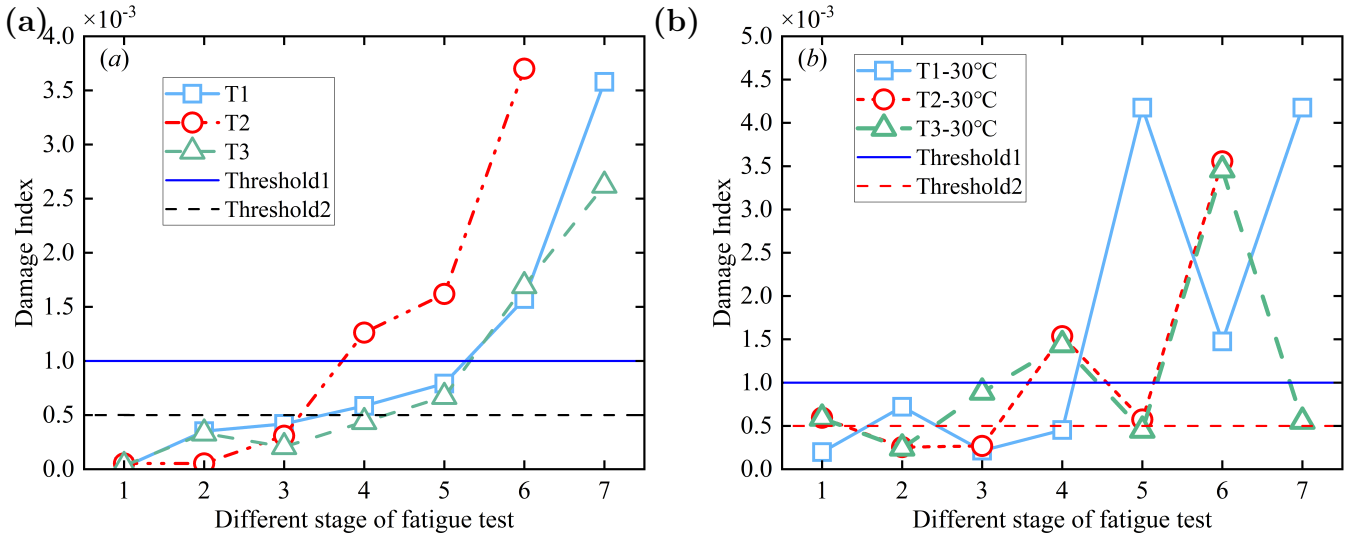


Figure 5.10: (a) DI values obtained using the linear guided wave method at 20°C with a baseline signal recorded at 20°C. (b) DI values obtained using the linear guided wave method at 30°C with a baseline signal recorded at 20°C.

Crack detection based on nonlinear guided wave method Using equation (5.12), the second harmonic values under different loading cycles and temperatures were calculated. Crack propagation at each stage was observed and recorded using the Hirox microscope. The variations of SH values with loading cycles and temperature are summarized and presented in Figure 5.11.

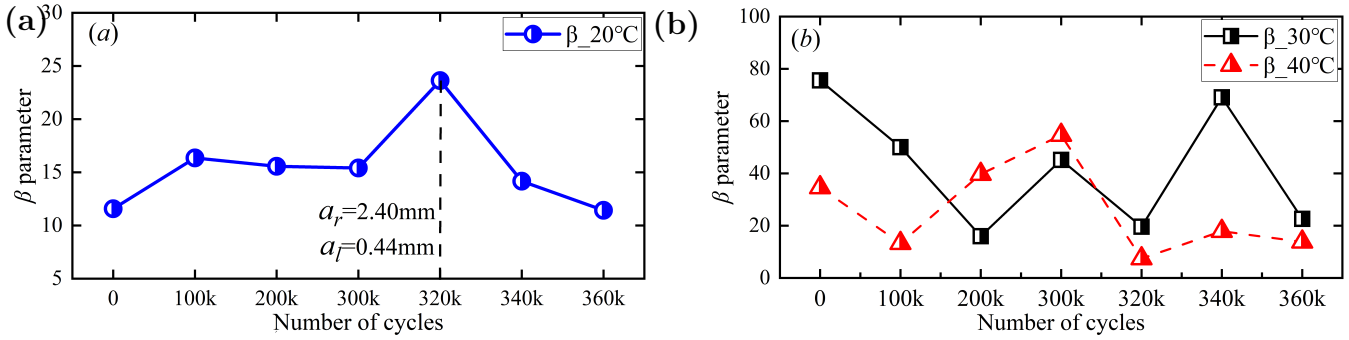


Figure 5.11: The second harmonic parameters versus fatigue cycles under 20℃ environments. (b) The second harmonic parameters versus fatigue cycles under 30℃ and 40℃ environments.

As shown in Fig. 5.11(a) and Table 5.3, the β' value obtained from T1 initially increases with the number of loading cycles and stabilises after 100k cycles. At 300k cycles, crack lengths measured using the Hirox microscope are 0.42 mm on the left side and 1.78 mm on the right side, yet the β' value remains relatively unchanged. However, after 320k cycles, the β' value experiences a sudden increase, corresponding to crack sizes of 0.44 mm on the left and 2.40 mm on the right. Subsequently, as the cracks continue to propagate, the β' value gradually decreases. This sudden change in β' is thus considered a potential indicator of crack detection during fatigue testing, aligning with findings reported in previous studies [39, 59]. In contrast, Fig. 5.11(b) shows that when the temperature increases to 30°C and 40°C, the β' value exhibits irregular behaviour with the loading cycles. For instance, at 30°C, the β' value initially decreases with increasing cycles, then increases, and continues to oscillate unpredictably. These findings highlight the necessity for the SH method to account for temperature effects to ensure consistent and reliable testing conditions. The results of β' value changes with loading cycles for the other two specimens are presented in Fig. 5.12.

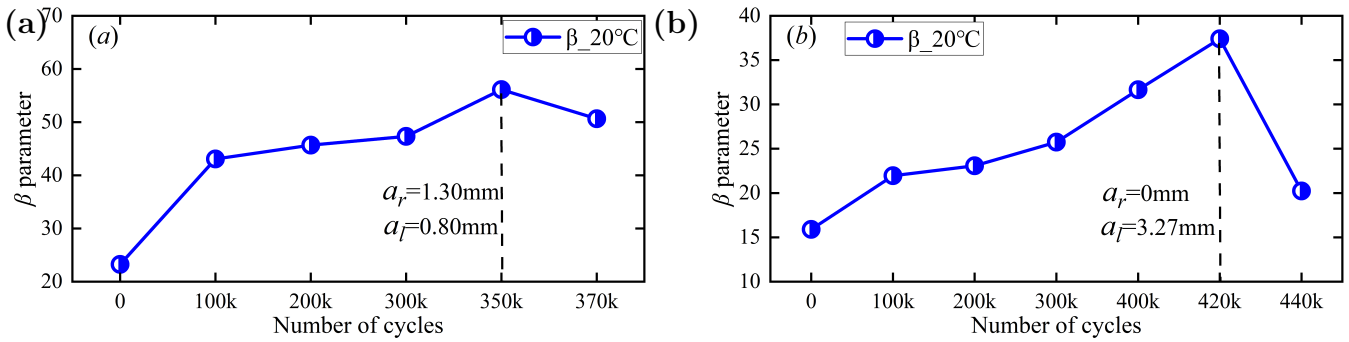


Figure 5.12: The second harmonic parameters versus fatigue cycles were obtained by specimen (a) T1, (b)T2.

As shown in Fig. 5.12, the β' value demonstrates a similar trend with the number of loading cycles in the other two specimens, with the maximum β' values corresponding to crack lengths of 2.1 mm and 3.27 mm, respectively. These findings further validate that, under stable temperature conditions, the SH method is effective in detecting cracks approximately 3 mm in size.

Crack detection based on vibration-based method The DI was calculated using the FRF method based on Eq. (5.1), and the results for the three specimens are summarized in Fig. 5.13.

As shown in Fig. 5.13(a) The DI consistently increases with the number of loading cycles. When applying a threshold of 0.15, the FRF-based method detects crack lengths of $a_l = 0.44$ mm and $a_r = 2.4$ mm on specimen T1, 1.93 mm and 3.90 mm on T2, and $a_l = 3.27$ mm on T3, based on the corresponding fatigue stage shown in Table 5.3. These results indicate that, compared to linear and nonlinear Lamb wave methods, the VSHM method exhibits notable limitations in detecting small cracks. Fig. 5.13(b) illustrates the variation of the DI under a 10°C temperature difference. The blue and purple bars represent the DI at each fatigue stage under 20°C and 30°C, respectively. The results demonstrate that, for the same number of loading cycles, the DI increases with rising temperature. However, the threshold of 0.15, as developed from Fig. 5.13(b), remains effective in distinguishing between before and after crack initiation stages within a 10°C temperature difference. Thus, while the VSHM method may be less sensitive to small-scale damage, it demonstrates greater robustness against temperature fluctuations than linear and nonlinear Lamb wave methods.

Overall, the crack detection results obtained using the three different methods, along with their corresponding working temperatures, are summarized in Table 5.4.

Table 5.4: Detectable crack lengths and working temperature ranges of different methods.

Detected length (mm)	Linear		Nonlinear		FRF	
Specimens	a_l	a_r	a_l	a_r	a_l	a_r
T1	0.42	1.78	0.44	2.40	0.44	2.40
T2	0.80	1.30	0.80	1.30	1.93	3.90
T3	0.60	0	3.27	0	3.27	0
Working temperature	$\Delta T = 0°C$		$\Delta T = 0°C$		$\Delta T = 10°C$	

5.5 Conclusion

The detection of fatigue damage under varying environmental conditions remains a significant challenge in SHM. This study provides a comparative analysis of linear Lamb wave, nonlinear Lamb wave, and VSHM methods to evaluate their respective strengths and limitations for crack detection under different temperature conditions. The detailed results are summarized in Table 5.4.

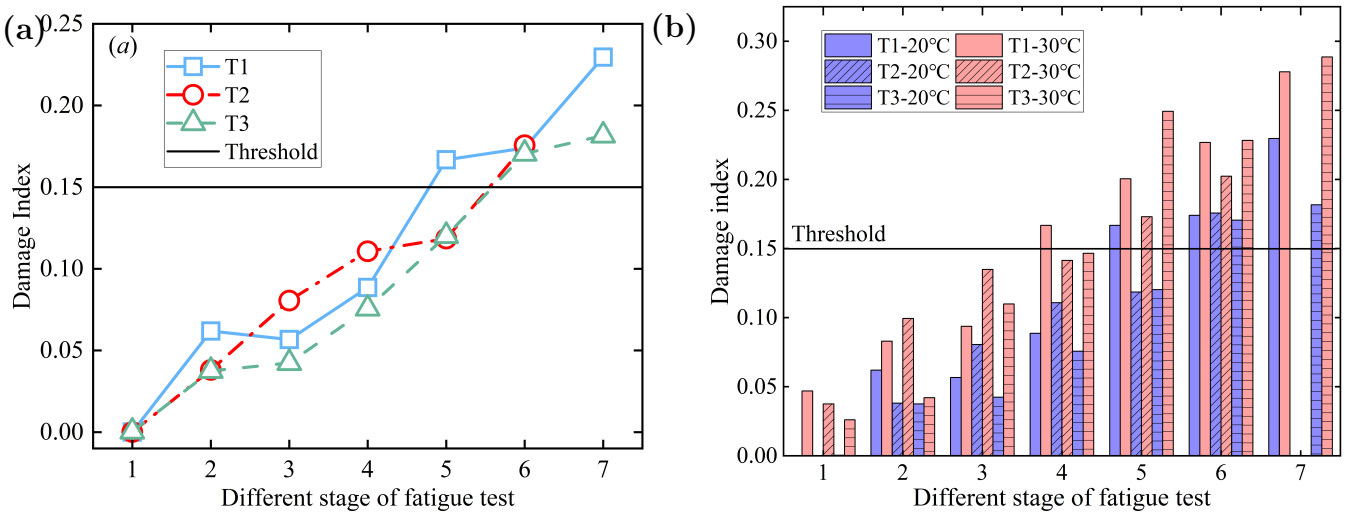


Figure 5.13: Results obtained using VSHM method under (a) a consistent temperature condition and (b) a 10℃ temperature difference.

The Linear Lamb wave approach demonstrated high sensitivity to small-scale damage under stable temperature conditions, with a minimum detectable crack size as small as 0.6 mm observed in specimen T3. However, its reliance on baseline signals and the pronounced influence of temperature variations hinder its applicability in environments with fluctuating temperatures. This underscores the method's trade-off between high sensitivity and environmental robustness. Although temperature compensation techniques were not applied in this study, they have the potential to mitigate temperature-related effects on this approach and will be considered in future work to improve its performance under varying environmental conditions.

As a baseline-free approach, the nonlinear Lamb wave method effectively detects cracks of approximately 3 mm. The sudden increase in nonlinear parameters β' serves as a reliable indicator of crack initiation and growth. However, this method is highly influenced by temperature fluctuations, with irregular behavior observed at elevated temperatures. While baseline independence enhances practical applicability, the pronounced temperature sensitivity underscores the need for compensation strategies to ensure consistent results under variable conditions.

Although less effective than Lamb wave methods in detecting small cracks, the VSHM method demonstrates superior robustness to temperature variations. Utilizing FRF, it can effectively detect crack under a 10°C temperature difference. For example, it detects a 3.27 mm crack on specimen T3, highlighting its capability to detect damage even under fluctuating environmental

conditions. While its sensitivity to microscopic damage is limited, this method is more suitable for applications where temperature stability is a critical factor.

This chapter provides a comprehensive evaluation of the progressive damage detection capabilities of different SHM methods under varying temperature conditions. By comparing linear Lamb wave, nonlinear Lamb wave, and VSHM approaches, the findings highlight their individual strengths in capturing damage evolution at different scales. The study emphasizes the practical significance of these methods in real-world scenarios, where temperature effects are a central concern. A key contribution of this work is the multifunctionality of PZT transducers, which can extract both linear and nonlinear Lamb wave features and facilitate vibration-based modal analysis, offering a versatile platform for exploring innovative solutions. This multifunctionality offers a potential pathway toward resolving the trade-offs among sensitivity, baseline dependency, and temperature robustness in SHM methods. Although the current study evaluates individual methods, the results suggest the future feasibility of developing a hybrid SHM approach that integrates their strengths, thereby ensuring reliable, practical damage detection while accounting for progressive damage and environmental variations.

Chapter 6

Baseline-free methods for online fatigue crack monitoring

Although Chapter 5 explored the performance of different methods for detecting damage under varying temperatures, all the methods discussed were implemented offline. In contrast, this chapter investigates two online crack detection methods, aiming to address the limitations of offline approaches and provide online real-time solutions for SHM under operational conditions.

6.1 Introduction

Despite numerous studies on linear [149–151, 182–188] and nonlinear Lamb wave methods [50, 166, 189–194], certain aspects of these methodologies have yet to be addressed. Firstly, attaining true real-time monitoring poses a challenge for both current linear and nonlinear methodologies due to the effect of the boundary conditions. Many studies have demonstrated the importance of the effect of boundary conditions on these lamb wave based methods [166, 195], and one commonly employed approach involves offline measurements with free boundary conditions, thereby mitigating its impact on the signal during the measurement process [196, 197]. The second limitation is the frequency dependency, many attempts have been made for online monitoring of cracks using second harmonic or signal modulation technologies. However, to generate cumulative harmonic waves, phase velocity matching and non-zero power flux need to be satisfied [198] which are highly dependent on several parameters like the frequency and amplitude of the excitation signal. Con-

sequently, the specific excitation condition makes it difficult to distinguish the harmonic sources induced by cracks from those caused by operational and environmental conditions.

To address the challenges of fatigue crack detection under varying environmental and operational conditions, this chapter proposes a novel baseline-free framework for real-time crack detection and FCG modeling. The method leverages the material's response under cyclic loading, extracting a newly defined feature, $\hat{\beta}'$, from second components to monitor and quantify crack growth. Unlike traditional nonlinear methods that require signal synchronism and are sensitive to power flux conditions, this approach derives $\hat{\beta}'$ at a fixed loading frequency, enhancing robustness and eliminating the dependency on zero power flux and strict signal timing. Most importantly, the method does not require any baseline signals from the undamaged (pristine) condition of the structure, thus avoiding false positives caused by variations in temperature, operational loads, and boundary conditions. This enables reliable online detection in realistic service scenarios. Furthermore, the proposed FCG model based on $\hat{\beta}'$ does not rely on prior knowledge of the initial crack size or crack initiation time, offering a practical solution for SHM of aluminum plates in service. The method's effectiveness is further demonstrated under continuously changing loading amplitudes and boundary conditions, reflecting complex operational environments. Section 2 introduces the experimental setup, including fatigue testing and signal acquisition systems. Section 3 presents the methodology, which includes the higher harmonic generation and the warning time point definition. Obtained results and uncertainty quantification are discussed in Section 4. Finally, Section 5 summarizes the key findings and highlights the contributions of this framework to online crack monitoring under variable and uncertain conditions.

6.2 Experimental Setup

6.2.1 Fatigue test

Fatigue tests were performed on aluminum-5251 plates with a geometry of 300 mm × 100 mm × 2 mm and a circular hole of 10 mm diameter in the center, as shown in Figures 6.1. Two sets of experiments were designed to evaluate the performance of online crack detection methods based on second harmonic responses.

Specimen Preparation and Test Setup For the second harmonic-based method, five specimens (labeled C1 to C5) were prepared from the same aluminum sheet. Fatigue testing was performed under a maximum load of 100 MPa (69% of the material's yield strength) and a minimum load of 10 MPa, with a loading frequency of 5 Hz [199]. The fatigue cracks initiated from the hole due to stress concentration and propagated under cyclic loading. For crack detection, the response signals were recorded using sensors and data acquisition systems detailed below.

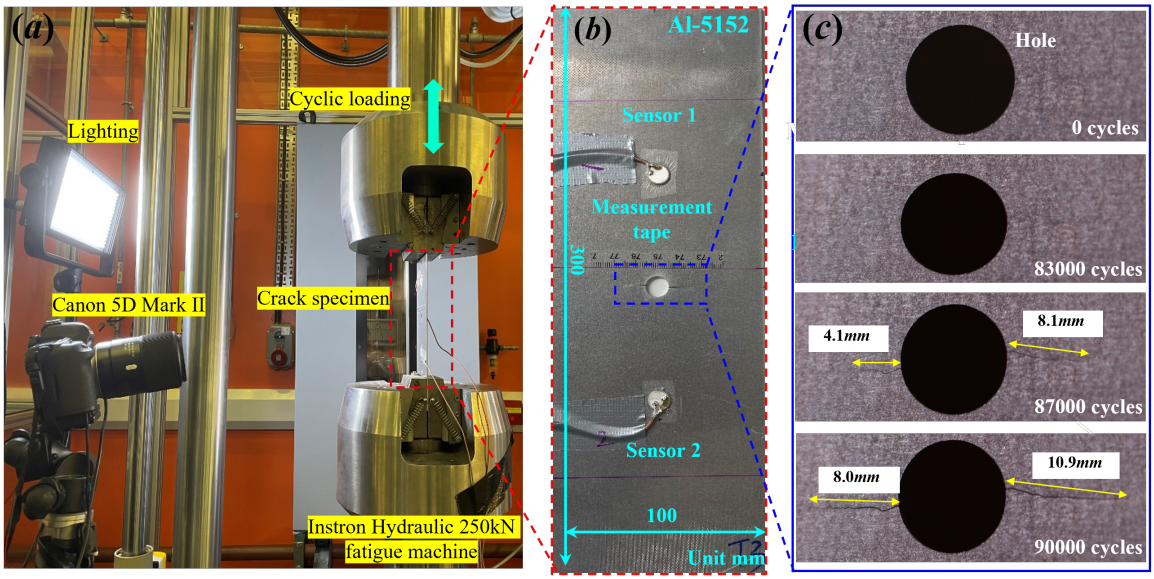


Figure 6.1: The experimental platform for online fatigue crack monitoring, a) fatigue experiment setup, b) specimen geometry and c) the state of specimen at different number of cycles.

Sensor Configuration For the C5, PZT sensors were mounted on the specimens with thermoplastic films [141]. As shown in Figure 6.1(b), the positions of the sensors were designed to investigate the effects of proximity of the sensor to the damage initiation site, as well as their configuration: P1–P2: Vertically aligned with and equidistant from the hole center. P3–P4: Positioned farther from the central line to assess the sensitivity to crack propagation. Taking the third harmonic based method as an example, all of the specimens and the fatigue test parameters are summarized in Table 6.1.

6.2.2 Data acquisition system

As mentioned in the previous section, the actuation signal is the cyclic fatigue loading with the frequency of 5Hz, as shown in Figure 6.2(a), and the two PZTs were used to measure the fatigue

Table 6.1: List of specimens, sensor positions and fatigue test parameters.

Specimen	Loading frequency	Loading amplitude	Sensor position
1	5Hz	2-20KN	P1-P2
2	5Hz	2-20KN	P1-P2
3	5Hz	2-20KN	P1-P2
4	5Hz	2-20KN	P1-P2
5	5Hz	2-20KN	P1-P4

response of the specimen in real time. The response measured by the PZTs was digitized by a data acquisition system (Tiepie Handyscope Hs5) and then fed into the computer-controlled Multi channel oscilloscope as shown in Figure 6.2(c). The measurement was carried out every 1,000 cycles of loading without stopping the test with a sampling rate of 10 kHz and time length of 10 s, resulting in a total of 100 k samples at each measurement increment. The sampling rate of 10 kHz was chosen to ensure better noise reduction, more effective anti-aliasing, improved signal processing accuracy, and greater flexibility in practical applications.

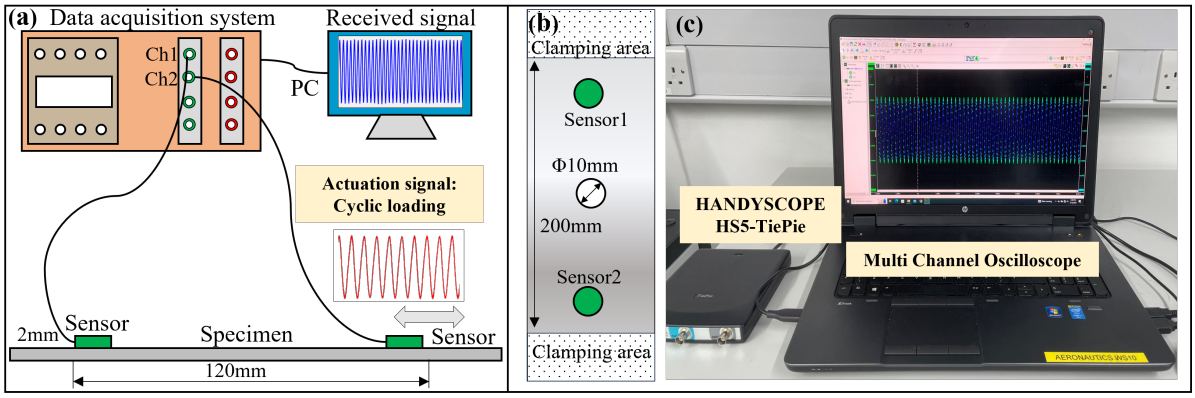


Figure 6.2: The data acquisition setup, a) the configuration of signal acquisition, b) sensor position and c) the data acquisition hardware.

6.3 Methodology

6.3.1 Higher harmonic generation

Higher harmonic wave generation is a typical phenomenon in which the waveform of the incident wave is distorted due to the nonlinear elastic response of the medium. Its generation is related to the material elastic nonlinearity, which arises from the inherent nonlinear relationship between

stress and strain, even in the elastic range. The test specimen used in this investigation is an aluminium plate, which is a typical isotropic material. When subjected to uniaxial cyclic loading, the aluminium plate generates longitudinal waves that propagate within the material due to its solid nature.

The calculation of the relative second harmonic parameter β' is summarized in equations (2.19)-(2.33). The calculation details are summarized in Section 2.2.2. However, to generate the cumulative harmonic waves, specific conditions of synchronism and non-zero power flux need to be satisfied. Specifically, synchronism entails matching the phase velocity and group velocity between the excited fundamental mode and the corresponding second harmonic mode. This matching facilitates energy transfer from the fundamental mode to its second harmonic mode. The requirement of non-zero power flux ensures that there is a net flow of energy between the fundamental and second harmonic modes [66]. These two conditions are highly dependent on several parameters such as the frequency and amplitude of the excitation signal, and it is crucial to maintain consistent measurement conditions, including the measurement instrument, signal frequency, acquisition settings, and plate dimensions when using β' to detect cracks. These limit the application of β' for online fatigue crack detection and growth modelling. However, the parameter β' used in this research has distinct characteristics: (1) Instead of external excitation through conventional structural sensors, low-frequency fatigue loading representative of in-flight loads is used to excite the structure, eliminating the need for precise excitation signal selection; (2) The low frequency of the fatigue loading simplifies the experimental setup, allowing for the detection and quantification of cracks during continuous fatigue testing. These characteristics make $\hat{\beta}'$ suitable for real-time crack detection and quantification. The process for measuring $\hat{\beta}'$ in this study is summarized in Figure 6.3, which is defined as:

$$\hat{\beta}' = \frac{A_2'}{(A_1')^2} \tag{6.1}$$

As shown in Figure 6.3, two PZT sensors were mounted at different locations on the specimens to investigate the impact of sensor location on the proposed method. The response of the structure under fatigue load is acquired in real time by these two sensors. Subsequently, the Fast Fourier Transform (FFT) is employed to obtain the frequency response of the signals. $\hat{\beta}'$ is computed

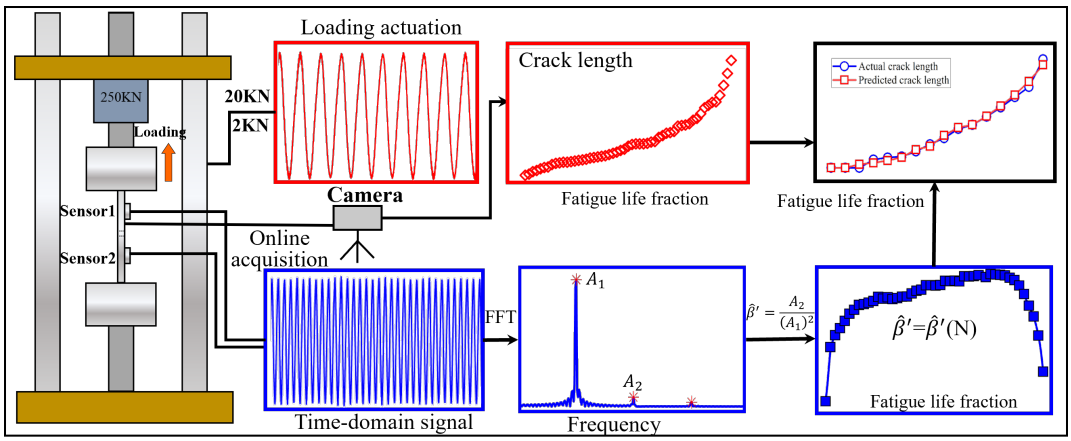


Figure 6.3: The online crack monitoring process based on $\hat{\beta}'$.

based on the amplitude of the fundamental frequency (A_1) and the second harmonic frequency (A_2). Furthermore, the crack length is continuously captured and measured by a Canon EOS 5D mark II camera with high resolution (21.1 effective megapixel full-frame CMOS digital single-lens reflex camera) during the fatigue test. The initiation and growth of the crack are then discussed and analysed by monitoring the change of $\hat{\beta}'$.

6.3.2 Early Warning for Fatigue Life Assessment

Under cyclic loading, structural components experience progressive crack growth due to fatigue. Within the framework of Linear Elastic Fracture Mechanics (LEFM), the rate of FCG [200] in the stable propagation regime is commonly described by Paris' law [193]:

$$\frac{da}{dN} = C(\Delta K)^m \tag{6.2}$$

Here, a is the crack length, N is the number of load cycles, and ΔK is the range of the SIF. The material-dependent constants C and m are determined empirically. The SIF range ΔK serves as the driving force for crack extension and depends on applied loading, geometry, and crack size. It is given by:

$$\Delta K = \Delta\sigma\, Y \sqrt{\pi a} \tag{6.3}$$

where $\Delta\sigma = \sigma_{\max} - \sigma_{\min}$ is the cyclic stress range, and Y is the dimensionless geometry factor that accounts for boundary conditions and crack configuration. As reported in [201], for cracks

initiating from a circular hole, Y stabilizes in the range 1.0 to 1.05 once the crack length exceeds one-fifth of the hole radius R.

According to the LEFM-based fatigue model by Totten [3], fatigue crack propagation occurs in three distinct stages:

- Stage I: involves microstructural crack initiation and short crack growth, typically below a threshold SIF ΔK_{th}.
- Stage II: governed by Paris' law, represents stable and predictable crack propagation.
- Stage III: occurs when the maximum SIF during a cycle, $K_{\max}$, approaches the material's fracture toughness K_{IC}, leading to rapid, unstable crack growth and failure.

In this study, it is assumed that the transition from stable crack growth (governed by fatigue) to unstable crack growth (governed by fracture) occurs when $K_{\max} = K_{IC}$. This condition is used to define the critical crack length denoted by a_c^{th}, beyond which failure is imminent [200]. From the definition of $K_{\max}$, the threshold crack length can be derived as:

$$a_c^{\text{th}} = \frac{1}{\pi}\left(\frac{K_{IC}}{Y\sigma_{\max}}\right)^2 \tag{6.4}$$

This expression is directly rooted in LEFM, linking crack length to the material's intrinsic fracture resistance and the applied loading conditions. As such, a_c^{th} represents an early warning indicator for imminent fracture.

In this research, a fatigue warning metric is developed using the proposed parameter $\hat{\beta}'$, and its effectiveness is validated by comparing the theoretical threshold crack length a_c^{th} with the measurable crack length a_c^{m}, obtained through vision-based inspection systems.

6.4 Results and discussion

6.4.1 Feature extraction

An example of a time-domain signal acquired by sensor 1 during the fatigue test is presented in Figure 6.4(a). The applied fatigue loading is a sinusoidal load, the corresponding signal obtained

by the PZT is also sinusoidal, and its amplitude oscillates between 4 and -4 V. Figure 6.4(b) shows the frequency components of the received signal. As mentioned in Section 6.2, the loading frequency is 5 Hz, so the fundamental frequency of the response is also 5 Hz. In addition, the second harmonic at 10 Hz and the third harmonic at 15 Hz are observed, with the amplitudes of these harmonic frequencies significantly lower than the fundamental frequency.

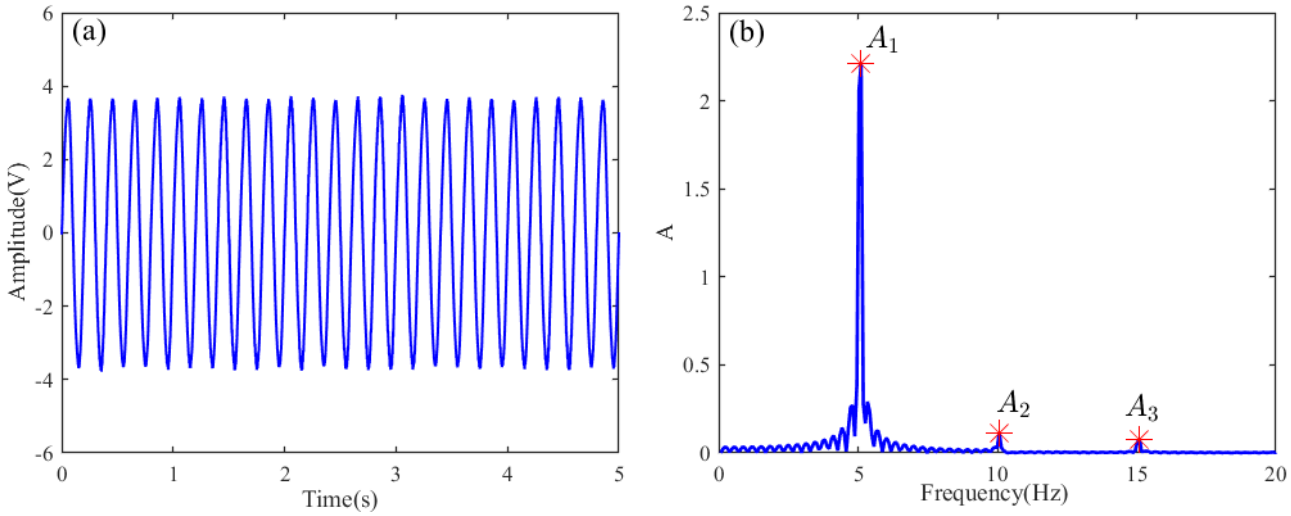


Figure 6.4: The response obtained by sensor 1 during the fatigue test (1,000 loading cycles), a) time domain and b) frequency domain.

Figure 6.5(a) demonstrates that with the increase in the number of cycles, the maximum value of the signal in time domain continuously decreases, with a slower decrease in the early stage and a faster decrease in the later stage. This phenomenon can be attributed to the initial stage of the test, during which the aluminium material may demonstrate superior elastic properties, enabling it to partially recover its original state. As such, the amplitude of the received signal decreases at a slower rate. However, as the fatigue experiment progresses, the internal microstructure of the material changes and its elastic behaviour gradually weakens. Consequently, the amplitude of the loading signal decreases at a faster rate in the later stages of the experiment. In addition, the stress concentration at the crack tip converts a portion of the strain energy into thermal energy, causing energy loss and dissipation. As such, the amplitude reduction of the signal increases. Although Figure 6.5 shows a similar trend obtained from sensors 1 and 2, determining the initial point of the crack based on the maximum amplitude of the time domain signal is challenging because the maximum value continuously decreases with the increase of loading.

Figure 6.5(b) illustrates the relationship between the features in the frequency domain of the acquired signal and the fatigue life. Specifically, for the fundamental frequency, its amplitude continues to decrease with the increase of loading cycles, exhibiting a slow decrease in the early stage and a gradual acceleration in the later stage. This trend is closely related to the amplitude reduction observed in the time-domain signal. The reason behind this similarity lies in the fundamental frequency's representation of the main frequency component in the frequency-domain signal. In the time-domain signal, the amplitude reflects the signal's energy or amplitude value, while in the frequency-domain, the amplitude represents the signal's energy at the corresponding frequency. As such, as the amplitude of the time-domain signal decreases with the increase of loading cycles, the amplitude of the fundamental frequency in the frequency-domain signal also decreases accordingly. In terms of the amplitude of the second harmonic, its value initially increases in the early stage and then stabilizes. The signal obtained by sensor 1 stabilizes between 2.4 and 2.5 dB, while the signal obtained by sensor 2 stabilizes between 2.3 and 2.4 dB. However, with the increase in loading cycles, both sensors experience a noticeable decrease in the amplitude of the second harmonic at the end of the fatigue test. This phenomenon occurs because during the loading process, the energy in the frequency domain signal gradually transfers to the higher harmonic frequencies due to the nonlinearity, resulting in a flattening of the spectrum [58]. As such, the amplitude of the second harmonic frequency increases initially. Moreover, with the increase in loading cycles, the elastic properties of the aluminium gradually weaken, leading to energy dissipation. The balance between the energy increase from spectrum flattening and the decrease from energy dissipation results in a stable state in the intermediate stage. However, after the crack initiation and propagation, the energy dissipation accelerates, causing a significant decrease in the amplitude of the second harmonic at the end of the experiment. The crack propagation leads to a faster reduction in the amplitude of the second harmonic as energy dissipation becomes more prominent.

6.4.2 The FCG results

Figure 6.6(a) presents photographs of specimen C4 taken by the camera, illustrating the occurrence of a detectable crack and its propagation on the right side. For specimen C4, the fatigue crack is first observed at 80,000 cycles, and the minimum detectable crack is 1.8 mm. Subsequently, the crack grows to 6.3 mm at 85,000 cycles and further expands to 11.1 mm at 90,000 cycles. Then,

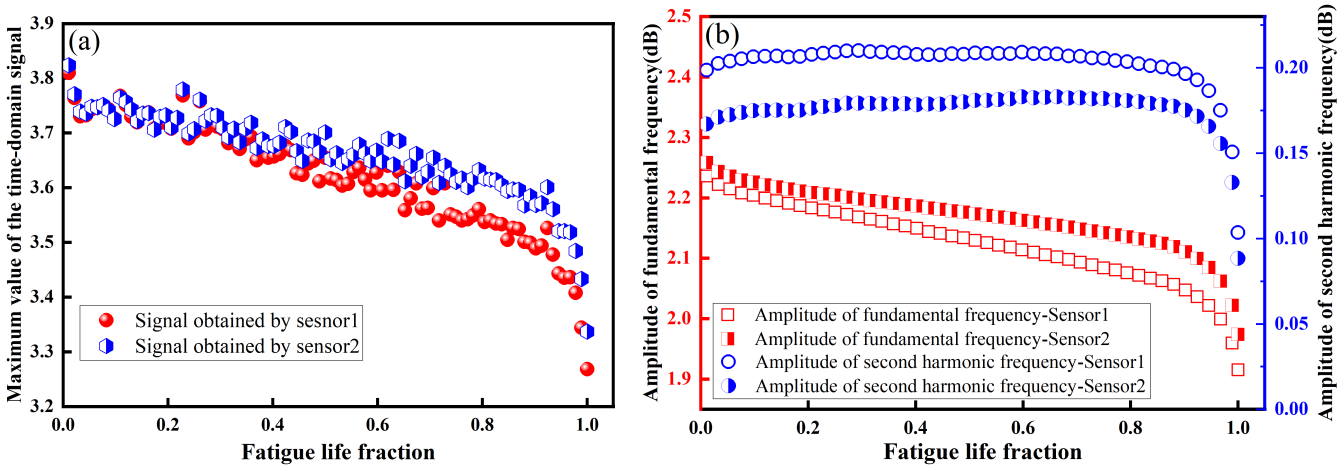


Figure 6.5: The relationship between the fatigue life, and a) the maximum amplitude of the time domain signal, and b) the amplitude of the fundamental and the second harmonic frequencies.

the relationships between FCG and SIF range ΔK obtained from equations (6.2)–(6.4) from four specimens are summarized in Figure 6.6(b). It can be found that the relationships obtained from all the specimens exhibit consistency, and the variation of da/dN against ΔK shows a linear trend in the logarithmic coordinate system, obeying the Paris law throughout the whole fatigue life. The FCG under various stress values is over the range of 2.49×10^{-5} to 2.37×10^{-4} mm/cycle. The initial ΔK is around 6.7 MPa $\cdot$ m$^{1/2}$, and the final ΔK is 22.8 MPa $\cdot$ m$^{1/2}$.

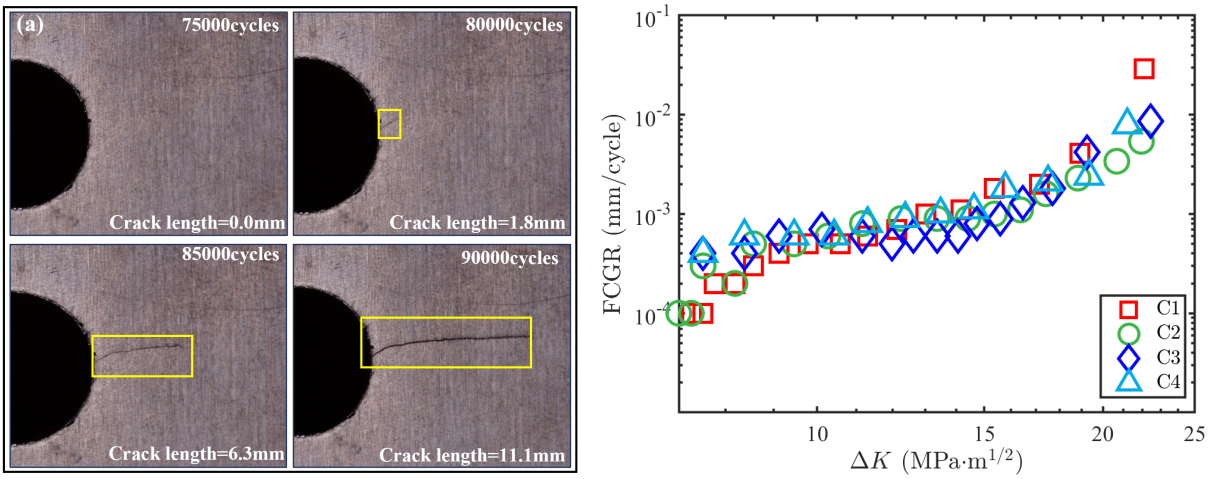


Figure 6.6: a) Photos taken by the camera for specimen C4 of crack initiation and propagation, b) the relationship between FCG rate and ΔK.

6.4.3 Crack detection results

The change of $\hat{\beta}'$ during the fatigue process Section 6.4.1 summarizes the relationship between the commonly used features in the time and frequency domains and the number of loading cycles. While these features offer certain insights into the state of the aluminium plates during fatigue testing, identifying a critical threshold to definitively detect crack initiation is still challenging. As such, the relative second harmonic parameter $\hat{\beta}'$ is extracted based on equation (6.1).

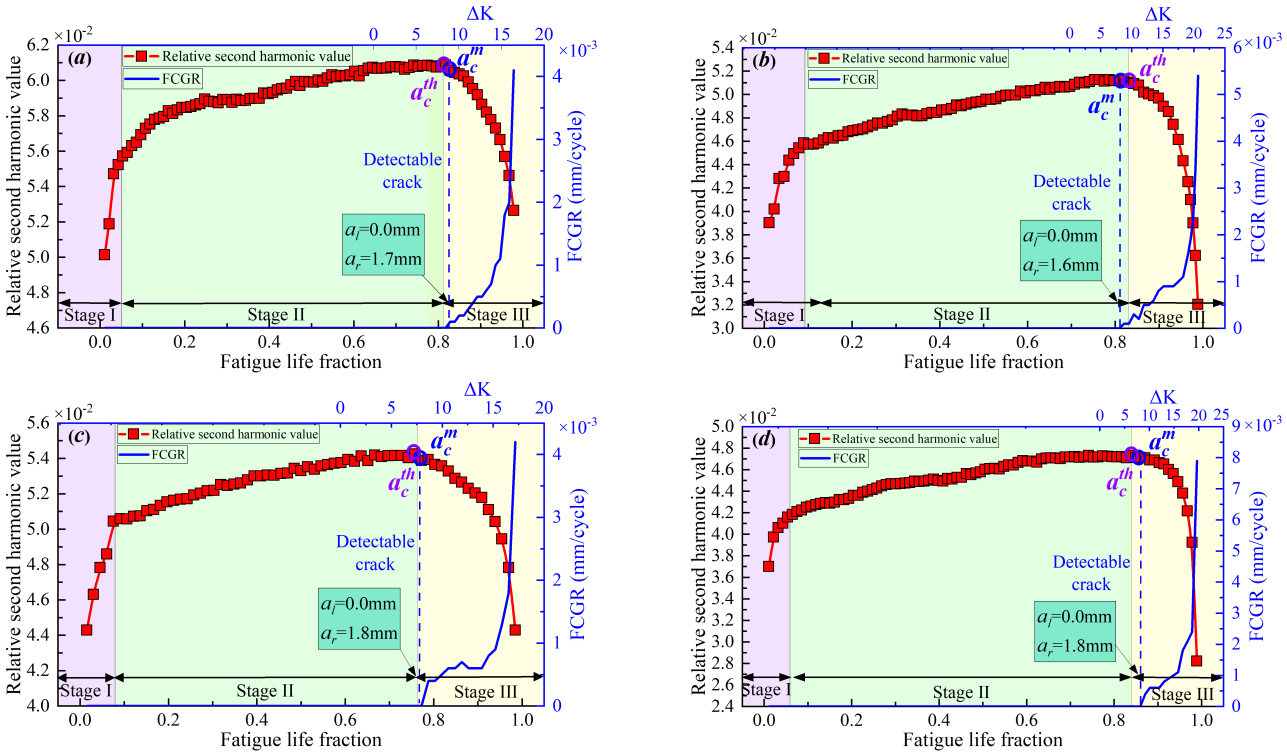


Figure 6.7: The relationship between fatigue life and $\hat{\beta}'$ obtained by sensor 1 and specimen, a) C1, b) C2, c) C3 and d) C4.

Figure 6.7 illustrates the relationship between $\hat{\beta}'$ measured from specimen C1-C4 with regard to the fatigue life obtained by sensor 1. The change of parameter $\hat{\beta}'$ undergoes three stages with the progression of the fatigue test. Specifically, the curve corresponding to Stage I (the purple shaded area) and Stage II (the green shaded area) can be considered as a strongly bilinear plot, with significantly different slopes for each part. Therefore, the change of the slope can be used as the inflection point between Stage I and II, and the proposed method for detecting this point is summarized in the next section.

Inflection point Between Different Stages of Fatigue Life The linear fitting method is employed to obtain the slopes in different stages of fatigue life. The proposed method and the results obtained from specimens C1-C4 are summarized in Figure 6.8.

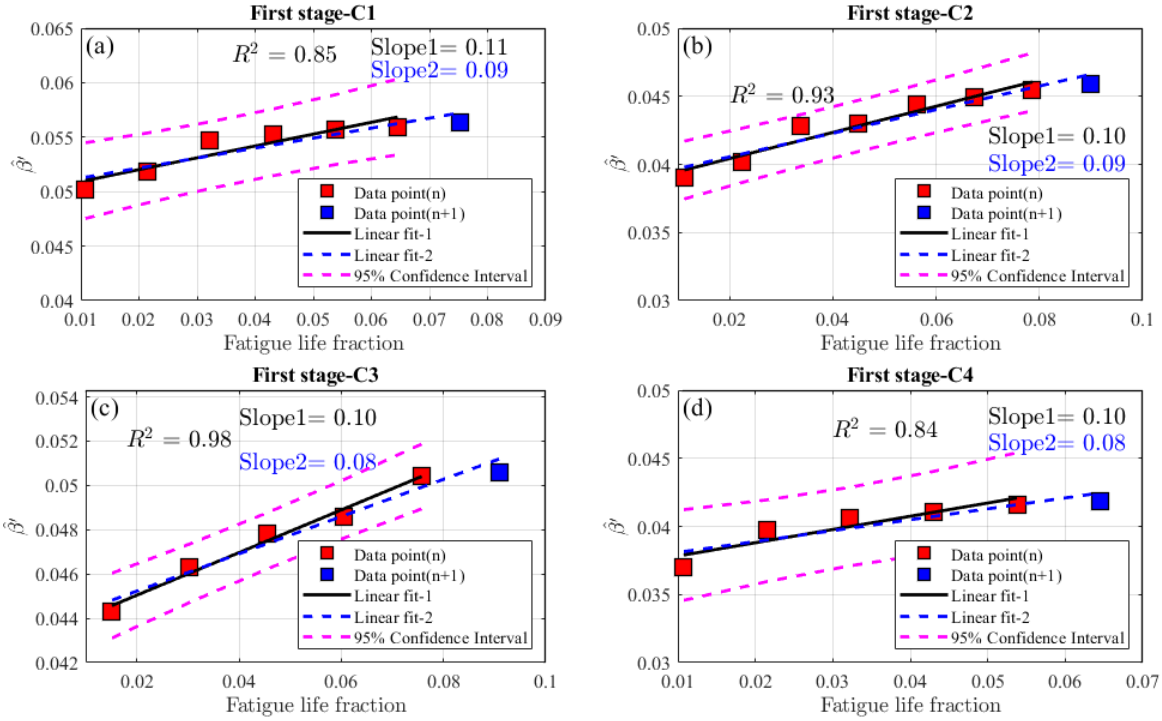


Figure 6.8: Correlation between the fatigue life and $\hat{\beta}'$ in first stage obtained by sensor 1, a) C1, b) C2, c) C3 and d) C4.

In Figure 6.8(a), slope values are obtained for fitting the first six sets of data (marked by red squares) and after the addition of a new set of data (marked by the blue square) for specimen C1. When fitting the first six sets of data, the slope of the fitted line (the black line) is 0.11 (slope1), with an R^2 value of 0.85. Following the inclusion of additional data, the slope of the fitted straight line (illustrated by the blue curve) changes to 0.09 (slope2). Consequently, a slope value of 0.10 serves as a threshold to detect the inflection point between Stage I and Stage II. Based on this threshold, inflection points between Stage I and Stage II are also detected on specimen C2-C4, as demonstrated in Figure 6.8(b-d). This indicates that $\hat{\beta}'$ experiences rapid growth in the early-stage fatigue process (Stage I, at about 7% of fatigue life (6,000 cycles). This aligns with Stage I reported in [199], characterized by microcrack nucleation (pre-formation of the microcrack), which can be caused by the deformation inharmony between the inclusion particles and the matrix. Yan et al. [202] used scanning electron microscopy (SEM) to investigate the microcrack nucleation in

the fatigue experiment of aluminium alloy, and the nucleation can be observed after 5,100 loading cycles, with the specimen ultimately fracturing after 127,022 loading cycles. Despite these insights, no studies have confirmed that PZT-based methods have the capability to detect such early-stage microcrack nucleation. Instead, variations in the parameter $\hat{\beta}'$ during this stage appear to be influenced by the bonding technique used with the thermoplastic film. Previous studies indicate that in the early phase of fatigue testing, the thermoplastic film may exhibit slight instability [203, 204], such as stress relaxation or minor slipping, due to initial molecular adjustments under load. These early instabilities, however, can be minimized through preloading, allowing the film to adapt to the testing conditions and improving data stability. While minor instabilities are observed initially, we selected the thermoplastic film for its reusability and adaptability, which offer distinct advantages over other adhesive methods without compromising crack detection accuracy [52].

In Stage II shown in Figure 6.9, as the number of cycles increases, $\hat{\beta}'$ maintains an increase, but at a reduced rate in comparison to stage I until its maximum value is reached, and data in this stage shows a strong linear relationship. Figure 6.9 summarises the fitted results obtained from specimens C1-C4. The slope of the fitted straight line in this sage is less than 0.01 for all specimens, and the strong linearity is reflected in the fact that the R^2 values are all greater than 0.9. At this stage, numerous microcracks nucleated in various inclusion particles, and a crack at one of these particles propagates along the preferred slip plane at a 45° angle with the loading direction, and crack length at this stage is generally considered to be between 0.01 mm and a_c^{th}, where a_c^{th} is the critical crack length at the warning time point in this research [185].

In Stage III, after reaching its peak value, $\hat{\beta}'$ exhibits a rapid and pronounced decline as the fatigue test progresses. The crack propagation is governed by the fracture mechanism rather than the fatigue mechanism, and the wave propagation is hindered within the fatigue region, resulting in a reduction in transmitted energy [205]. Most importantly, $\hat{\beta}'$ reaches its maximum value at around 80.6% (averaged values from four specimens) of the service life, which can serve as a predictive feature for the 20% remaining life of the specimen. As such, $\hat{\beta}'$ is effective in estimating microcrack initiation, propagation, and remaining life throughout the fatigue process.

In addition, the crack length corresponding to the maximum value of $\hat{\beta}'$ is used as the warning time, defined as (a_c^{th}). On C1, $\hat{\beta}'$ reaches a_c^{th} at 81.7% of the fatigue life, with the crack initially

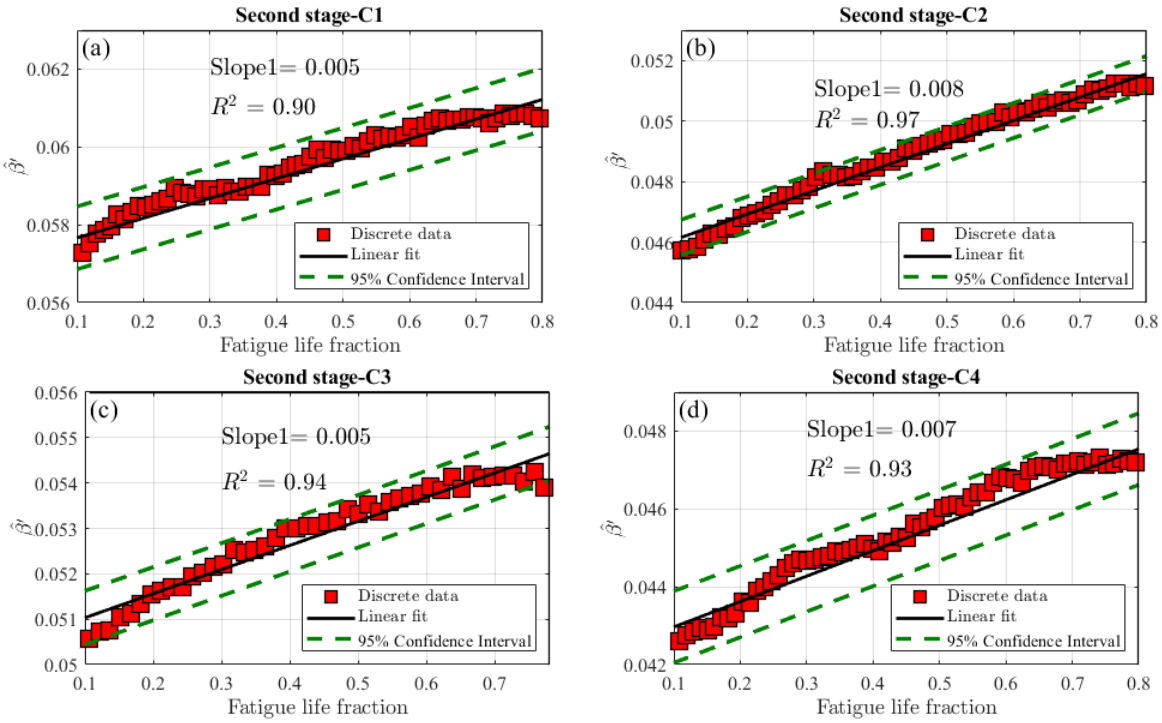


Figure 6.9: Correlation between the fatigue life and $\hat{\beta}'$ in the second stage obtained by sensor 1 on, a) C1, b) C2, c) C3 and d) C4.

observed (a_c^m) at 82.8% of the fatigue life, and the detectable crack length a_l and a_r are 0.0 and 1.7 mm, respectively. For specimen C2, when the fatigue life reaches 82%, $\hat{\beta}'$ reaches its maximum value. The detectable crack is observed at 80.9%, with corresponding crack lengths a_l and a_r of 0.0 and 1.6 mm. For C3, the corresponding fatigue life of a_c^{th} and a_c^m are 75.7% and 77.2%, respectively. The observed a_c^m on the left and right sides are 0.0 and 1.8 mm, respectively. In specimen C4, the minimum detectable crack lengths a_l and a_r are 0.0 and 1.8 mm, respectively, at 86% of fatigue life, while $\hat{\beta}'$ reaches its maximum value at 83.9%. The above results indicate that there is a small difference between the fatigue life corresponding to a_c^{th} and a_c^m. In specimens C1, C3, and C4, the corresponding fatigue life of a_c^m lags that of a_c^{th}, indicating that crack has started propagating before its detectability threshold, with a_c^{th} corresponding to smaller crack lengths compared to a_c^m. In contrast, In C2, the fatigue life corresponding to a_c^m is lower than that of a_c^{th}, occurring at 82.8% with corresponding crack length of 0.0 and 1.8 mm. This indicates that the $\hat{\beta}'$ presented in this research is not only effective in monitoring crack state and remaining life but also highly efficient in online detecting cracks less than 2 mm.

Moreover, the blue line in Figure 6.7 illustrates the relationship between FCGR and ΔK, with

ΔK values on the top x-axis and FCGR values on the right y-axis. It can be observed that as the fatigue test progresses to the third stage, $\hat{\beta}'$ decreases at an accelerating rate, while FCGR consistently increases with higher ΔK values. This comparison allows for a clearer visualization of the relationship between the second harmonic parameter and crack growth, highlighting the potential of this parameter to characterize crack growth.

6.4.4 Crack growth modelling results

Dataset construction After the online crack detection based on the proposed baseline-free method, the subsequent step is to develop the FCG model, which aims to monitor the state of the plate in real time. The data obtained from specimens after the fatigue experiment consists of two parts. The first part is the $\hat{\beta}'$ dataset, which is expressed as:

$$\hat{\beta}'_{mn} = \left[\hat{\beta}'_{1n}, \hat{\beta}'_{2n}, \hat{\beta}'_{3n}, \cdots, \hat{\beta}'_{mn}\right] \tag{6.5}$$

where m is the number of the specimen, and n is the number of cycles conducted on the $m-th$ specimen. The second part is the crack length a_l and a_r recorded by the camera, which are defined as:

$$a_{lmn} = [a_{l1n}, a_{l2n}, a_{l3n}, \cdots, a_{lmn}] \tag{6.6}$$

$$a_{rmn} = [a_{r1n}, a_{r2n}, a_{r3n}, \cdots, a_{rmn}] \tag{6.7}$$

where a_{lmn} and a_{rmn} represent the left and right crack length measured at $n-th$ cycles on the $m-th$ specimen, where m=4, which means four specimens are used for the development of the FCG model. The FCG model is defined as the relationship between $\hat{\beta}'_{mn}$ and a_{lmn}, a_{rmn}, respectively. As shown in Figure 6.7, the range of $\hat{\beta}'_{1n}$ obtained from C1 is between 0.051 and 0.061 and the range of $\hat{\beta}'_{2n}$, $\hat{\beta}'_{3n}$ and $\beta'_{4n}$are 0.032-0.051, 0.044-0.054, 0.037-0.047, respectively. The variability in $\hat{\beta}'$ values complicates the modelling of their relationship with the crack length. As such, $\Delta\hat{\beta}'_{mn}$ is introduced as an independent variable for developing the model, and defined as:

$$\Delta\hat{\beta}'_{mn} = \hat{\beta}'_{m(n+1)} - \hat{\beta}'_{mn} \tag{6.8}$$

where $\hat{\beta}'_{m(n+1)}$ is the $\hat{\beta}'$ value measured at the $(n+1000)-th$ cycle on the $m-th$ specimen. Therefore, $\hat{\beta}'$ dataset is further expressed as:

$$\Delta\hat{\beta}'_{mn} = \left[\Delta\hat{\beta}'_{1n}, \Delta\hat{\beta}'_{2n}, \Delta\hat{\beta}'_{3n}, \cdots, \Delta\hat{\beta}'_{mn}\right] \tag{6.9}$$

Results obtained by the model In this study, the relationship between $\Delta\hat{\beta}'_{mn}$ and a_{lmn}, a_{rmn} are developed based on the data obtained from four specimens, respectively. The performance of the fitting model is evaluated using the Root Mean Square Error (RMSE), which is expressed as:

$$RMSE = \sqrt{\frac{\sum_{n=1}^{N}(a_{mn} - a'_{mn})^2}{N}} \tag{6.10}$$

where N is the total number of experimental measurements, a_{mn} and a'_{mn} are the measured and predicted crack length of the $m-th$ specimen at the $n-th$ measurement on the validation dataset. RMSE is employed to evaluate the prediction accuracy on the validation dataset, with a smaller RMSE value, indicating higher prediction accuracy and better generalisation ability of the fitted model. In this study, the experimental data from specimens C1-C3 were used to develop the model between $\Delta\hat{\beta}'_{mn}$ and a_{lmn}, a_{rmn}, and data obtained from C4 was used for validation. The obtained results are summarized in Figure 6.10.

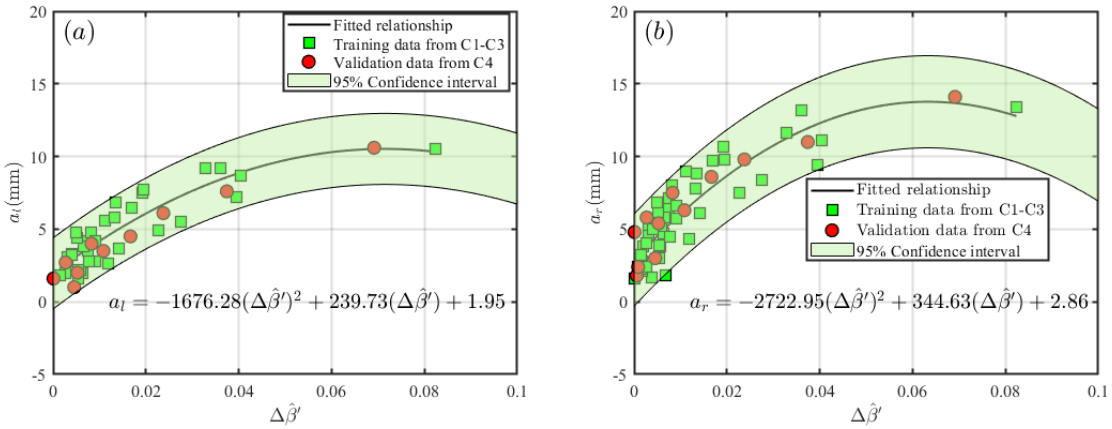


Figure 6.10: The FCG model was obtained by specimen C4 for validation and C1-C3 for training, a) on the left side of the hole and b) on the right side of the hole.

Figure 6.10(a) illustrates the FCG modelling results obtained through the validation process using data from specimen $[\Delta\hat{\beta}'_{4n}, a_{l4n}]$, marked by the red circles in Figure 6.10(a). The quadratic polynomial, employed to develop the relationship between a_{lmn} and $\Delta\hat{\beta}'_{mn}$ is deter-

mined based on the training data, $[\Delta\hat{\beta}'_{1n}, a_{l1n}]$, $[\Delta\hat{\beta}'_{2n}, a_{l2n}]$, $[\Delta\hat{\beta}'_{3n}, a_{l3n}]$, which are labelled by green squares in Figure 6.10(a). In addition, Fig. 11a indicates the quadratic polynomial equation $a_l = -1676.28(\Delta\hat{\beta}')^2 + 239.73(\Delta\hat{\beta}') + 1.95$ well describes the relationship between a_{lmn} and $\Delta\hat{\beta}'_{mn}$, with all of the validation points falling within the 95% confidence interval (the green shaded area). In addition, based on this equation, the RMSE of the predicted a_l on C4 is 0.9 mm. In terms of the FCG model on the right side, as plotted in Figure 6.10(b), the quadratic polynomial equation $a_r = -2722.95(\Delta\hat{\beta}')^2 + 344.63(\Delta\hat{\beta}') + 2.86$ effectively describes FCG on the right side, as both predicted and actual crack sizes are involved within the 95% prediction interval of probabilistic prediction derived from it. Moreover, the prediction RMSE on the validation dataset is 1.2 mm. This result demonstrates an improved ability to model crack growth compared to other sensor-based techniques, such as those constructed using acoustic emission [206], as all validation data points lie within the 95% confidence interval. Furthermore, in similar studies using PZT sensors, such as Chen et al.'s work employing artificial neural networks (ANNs) for crack size prediction, an RMSE of 1.2 mm was achieved [197]. However, their approach required stopping the machine to gather data rather than providing real-time monitoring. These results confirm that the model based on $\hat{\beta}'$ can reliably predict crack status online.

6.4.5 Uncertainty quantification

Crack detection using the sensor at a different location As discussed in Sections 6.4.3, results obtained from sensor 1 have proved to be efficient in crack detection and FCG modelling. However, the proposed method may also be affected by experimental conditions, particularly the variation in the sensor location. As such, sensor 2 is used to evaluate the effect of the sensor location on the performance of the method, and the change of $\hat{\beta}'$ with the fatigue life is reported in Figure 6.11.

Figure 6.11 illustrates the relationship between $\hat{\beta}'$ measured from specimen C1-C4 and the fatigue life obtained by sensor 2. Similar to the findings obtained from sensor 1, the evolution of $\hat{\beta}'$ undergoes three stages during the fatigue experiment. The linear fitting method is employed to determine the inflection point between Stage I and Stage II. Results are summarized in Figure 6.12.

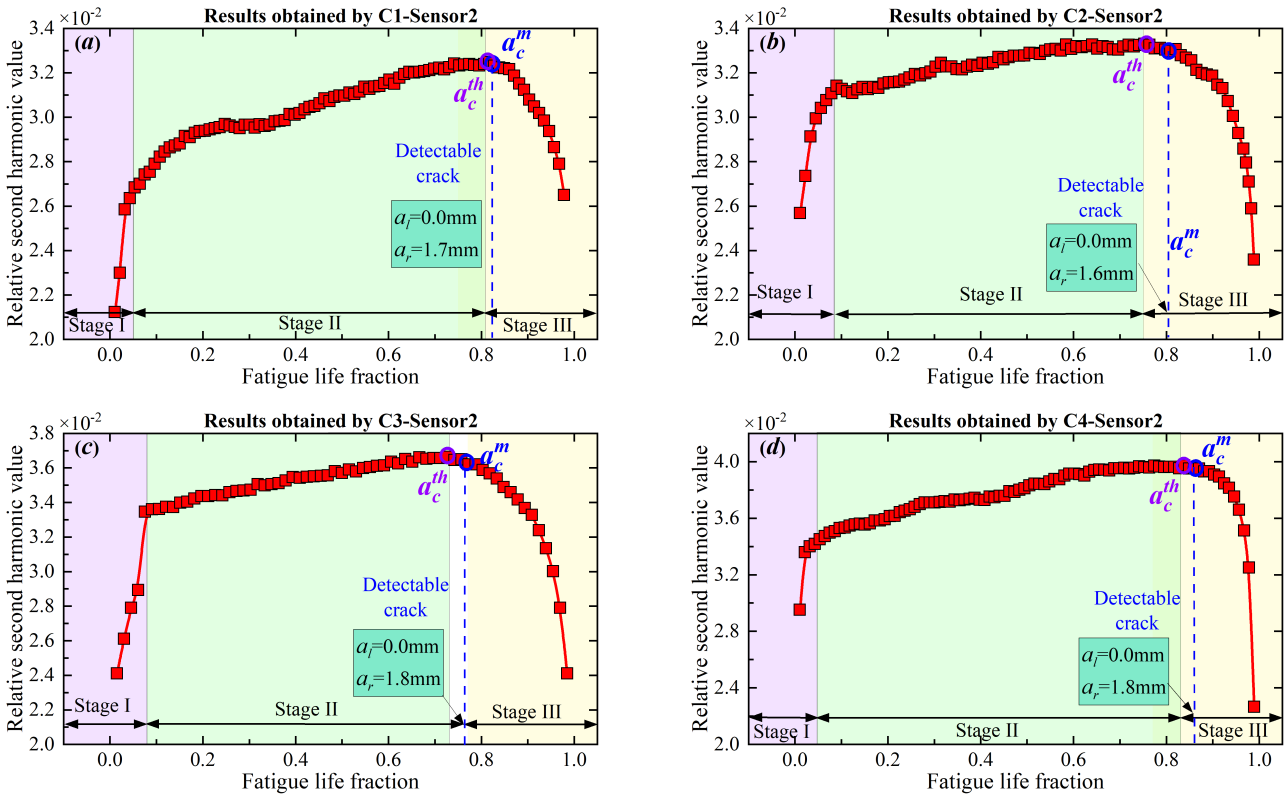


Figure 6.11: The relationship between fatigue life and $\hat{\beta}'$ obtained by sensor 2 on specimen, a) C1, b) C2, c) C3 and d) C4.

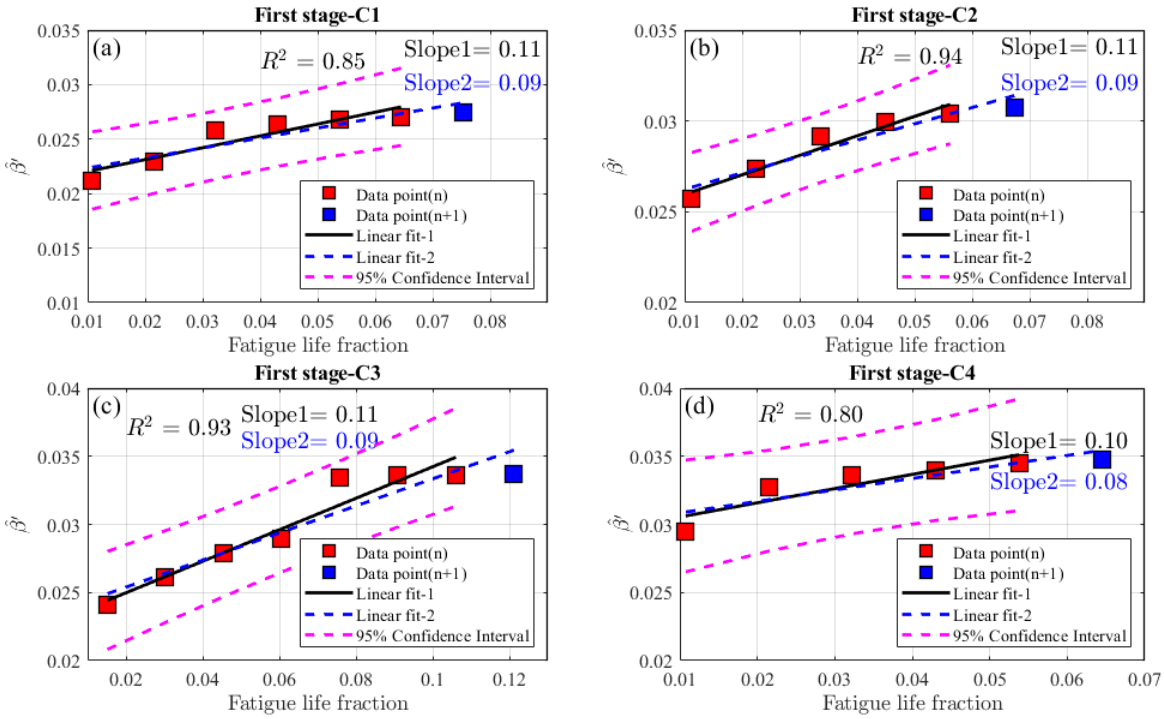


Figure 6.12: Correlation between the fatigue life and $\hat{\beta}'$ in the first stage obtained by sensor 2 on, a) C1, b) C2, c) C3 and d) C4.

Figure 6.12 illustrates the detection of the inflection point between Stage I and II using the same slope threshold value of 0.1, occurring approximately at around 7% of fatigue life (6,000 cycles). In Stage II, $\hat{\beta}'$ increases with the number of loadings but at a slower rate than in Stage I, eventually reaching its peak value. Figure 6.12 summarises the fitted results obtained by sensor 2 on specimens C1-C4. The slope of the fitted line in this stage is less than 0.01 for all specimens, indicating strong linearity, as reflected by R^2 values are all greater than 0.9. This result is the same as the results obtained from sensor 1.

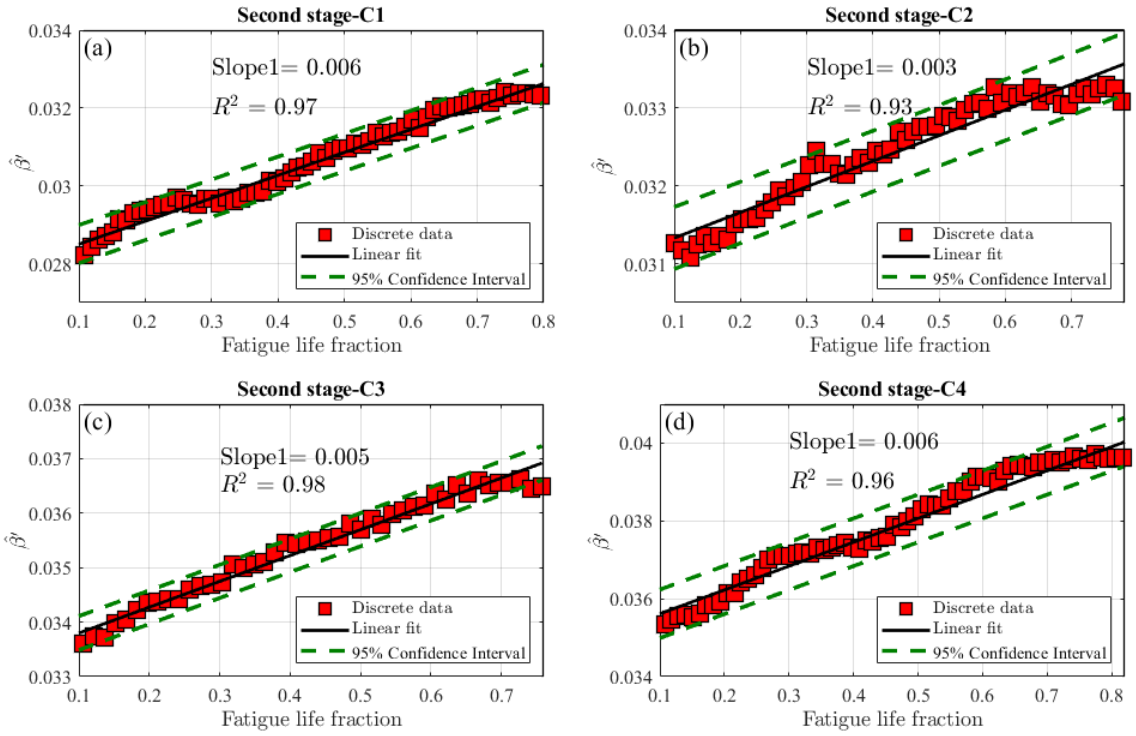


Figure 6.13: Correlation between the fatigue life and $\hat{\beta}'$ in the second stage obtained by sensor 2 on, a) C1, b) C2, c) C3 and d) C4.

In Stage III, $\hat{\beta}'$ experiences a sudden and accelerated decrease as the fatigue test progresses. Additionally, Figure 6.13 shows the second harmonic parameter reaches its maximum value at approximately 78.4% of the service life (an average calculated from four specimens), closely aligning with the result obtained from sensor 1 (80.8%). Specifically, On specimen C1, $\hat{\beta}'$ reaches a_c^{th} at 81.7% of the fatigue life, with the crack initially observed (a_c^m) at 82.8% of the fatigue life, and the minimum detectable crack length a_l and a_r are 0.0 and 1.7 mm, respectively. For specimen C2, when the fatigue life reaches 75.3%, $\hat{\beta}'$ reaches its maximum value. The minimum detectable crack is observed at 80.9%, with corresponding crack lengths a_l and a_r of 0.0 and 1.6 mm. For C3,

the corresponding fatigue life of a_c^{th} and a_c^m are 72.72% and 77.27%, respectively. On specimen C4, the minimum detectable crack lengths a_l and a_r are 0.0 and 1.8 mm, respectively, at 86% of the fatigue life, while $\hat{\beta}'$ reaches its maximum value at 83.9%. The minimum detectable crack length observed on the left and right are 0.0 and 1.8 mm, respectively. Most importantly, the occurrence time of the a_c^{th} is very closely aligned with the detectable time of the crack, with a_c^{th} appearing before a_c^m on all four plates. This indicates that the results obtained by sensor 2 at this position are also capable of online detecting crack less than 2 mm, and the maximum value of $\hat{\beta}'$ contributes significantly to estimating the remaining life of the specimen. These findings demonstrate that the sensor location does not affect the performance of the proposed method in detecting critical crack states.

Further evaluation of the sensor location effect. On specimens 1-4, two sensors are symmetrically placed along the plate's centerline. As previously discussed, these sensors can detect crack and its growth in real time. Cracks typically start at the edge of the central hole due to stress concentration, and fatigue loading generates waves that produce a second harmonic component when passing through a crack. This second harmonic component is critical to the effectiveness of the proposed method in this research. To confirm that the second harmonic is caused by the evolution of crack and not by the sensors or hydraulic machine, two additional sensors are attached to another specimen (C5). Figure 6.14(a) shows their locations, with sensor 3 positioned 20 mm from the centerline and sensor 4 positioned 30 mm from the centerline.

As shown in Figure 6.14, the results obtained from sensors 1 and 2, symmetrically installed along the specimen's centerline, are consistent with the findings in Section 6.4.3. When the fatigue loading reaches 77.22% of the specimen's fatigue life, the detectable crack length (a_c^m) is 1.5 mm, with the maximum values of $\hat{\beta}'$ occurring at 75.95% and 73.42% of the fatigue life, respectively, which are earlier than the detectable crack length. This demonstrates the effectiveness of the proposed method in detecting cracks smaller than 1.5 mm on specimen C5. However, the results from sensors 3 and 4, positioned farther from the centerline, Figure 6.14(d) shows that for sensor 3, the maximum value of $\hat{\beta}'$ occurs at 86.08% of the fatigue life, with corresponding crack lengths (a_c^{th}) of 1.4 mm (a_l) and 3 mm (a_r). For sensor 4, positioned farther from the centerline, Figure 6.14(e) shows that the maximum change in $\hat{\beta}'$ occurs at approximately 90% of the fatigue life,

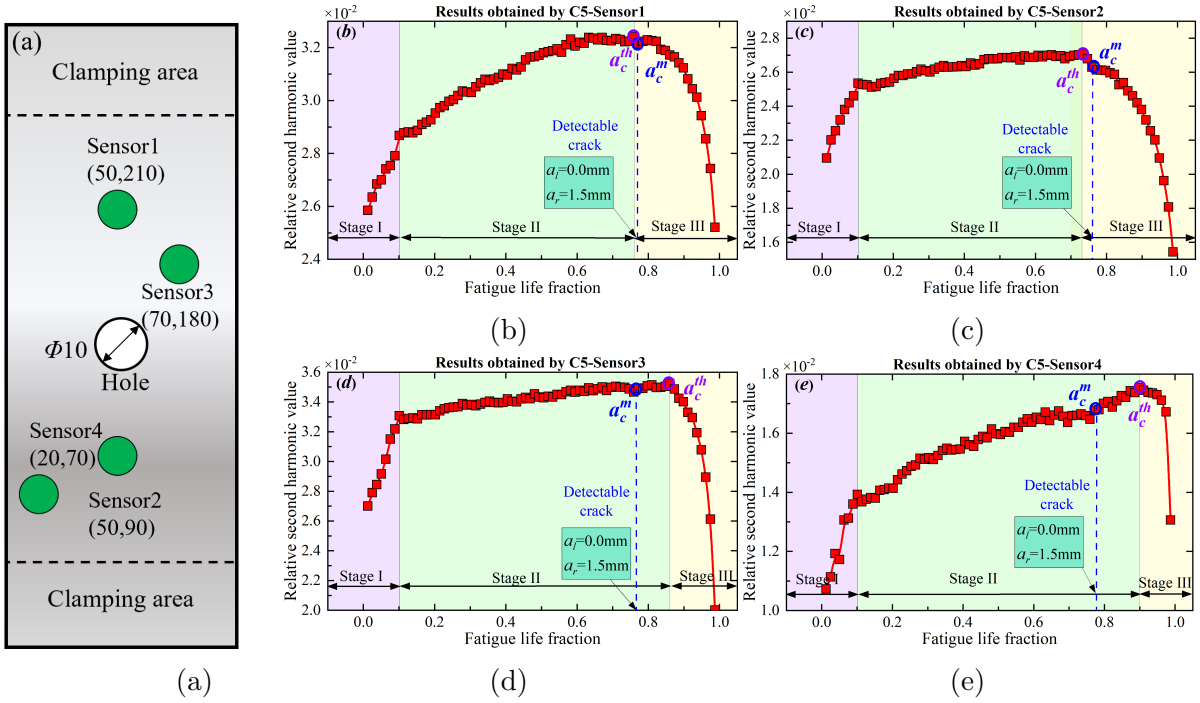


Figure 6.14: The positions of four sensors on C5, and the relationship between fatigue life and $\hat{\beta}'$ obtained by (b) sensor 1, (c) sensor 2, (d) sensor 3, and (e) sensor 4.

with crack sizes of 2.7 mm (a_l) and 3.8 mm (a_r), the largest among the four sensors. These results indicate that the source of $\hat{\beta}'$ generation is the crack, rather than other factors such as the inherent nonlinearity of electrical equipment and background noise, thereby validating the effectiveness of the method proposed in this thesis.

Most importantly, the region around the hole in the specimen, as shown in Figure 6.14(a), is where stress is most likely to concentrate under fatigue loading. This makes the line perpendicular to this area, such as the centerline used in this study, an optimal location for sensor placement, as stress concentration often serves as the initiation point for crack propagation. In addition, results from sensors 1 and 2 suggest that only one sensor is necessary along the centerline to achieve effective detection, eliminating redundancy without compromising sensitivity. This finding highlights that sensor placement should prioritize areas of expected stress concentration, such as the centerline in this study, to enhance early crack detection. In addition, the spacing between sensors is critical for optimizing detection efficiency. The distance between sensors should be adjusted according to the expected crack size and growth rate. If the spacing is too wide, smaller cracks may not be detected until they reach an advanced stage; if too narrow, the data may

become redundant, reducing efficiency. For instance, in Figure 6.14(e), the delayed detection by sensor 4, which is positioned farther from the centerline, illustrates that sensors located away from stress concentration areas tend to detect cracks later, often when the cracks are larger. Therefore, in practical applications of the proposed method, sensors should be placed in hot spots, i.e. potential stress concentration areas, where cracks are most likely to initiate. The spacing between sensors should be carefully optimized based on the crack lengths that need to be detected, ensuring that even small cracks are detected early in their propagation. Strategic sensor placement can significantly improve the sensitivity and accuracy of the crack detection system, allowing for timely intervention to prevent further damage.

FCG model developed based on sensor 2 To evaluate the robustness of the FCG model against uncertainties related to sensor locations, the performance of the FCG model described in Section 6.4.3 was assessed using only data obtained from sensor 2. Data from sensors 3 and 4 were excluded based on prior validation experiments and data analysis, which indicated that these sensors exhibit latency in damage monitoring and cannot promptly reflect the actual damage condition. Therefore, to ensure the accuracy and timeliness of the monitoring data, only data from sensors 2 which is verified and reliable, are used for the evaluation. The results of this evaluation are summarized in Figure 6.15.

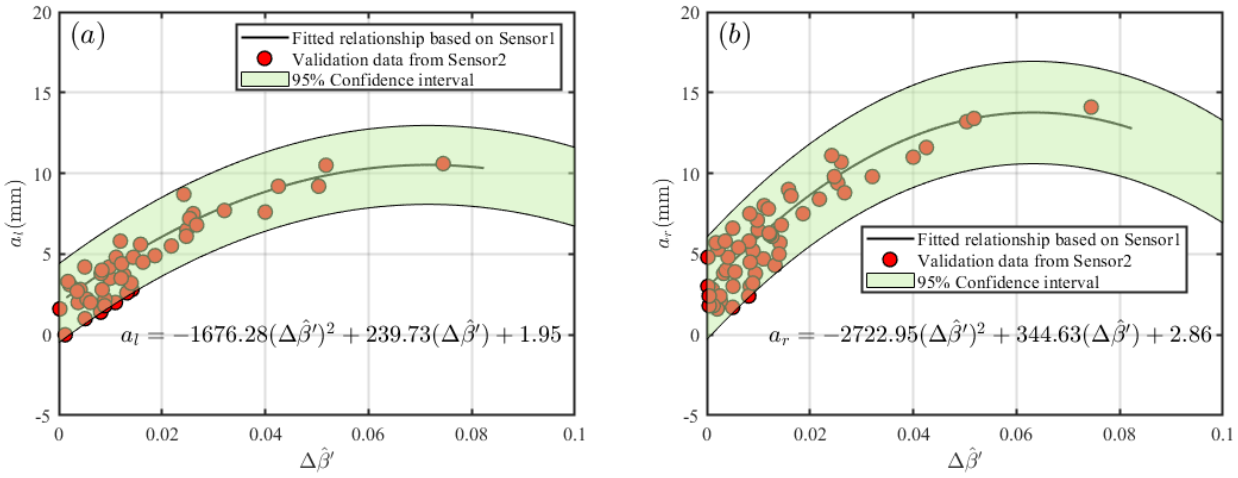


Figure 6.15: The validation of the developed FCG model using data from sensor 2, on the a) left and b) right side of the hole.

Figure 6.15(a) illustrates the validation of the left FCG model $a_l = -1676.28(\Delta\hat{\beta}')^2 + 239.73(\Delta\hat{\beta}') +$

1.95 developed using data from sensor 1, with data obtained from sensor 2. All data obtained on the four specimens fell within the 95% confidence interval, and the RMSE value for crack length prediction is 1.1 mm. Figure 6.15(b) shows the results of using the data obtained from sensor 2 to validate the right crack length model $a_r = -2722.95(\Delta\hat{\beta}')^2 + 344.63(\Delta\hat{\beta}') + 2.86$ developed in Section 6.4.3. Results reveal that both predicted and actual crack sizes fall within the 95% prediction interval, with an RMSE value of 1.4 mm. These results demonstrate the robustness of the FCG model developed in this research across different sensor locations.

6.5 Summary

In this chapter, a baseline-free approach for online crack detection and growth modelling is proposed based on $\hat{\beta}'$, which is calculated by the ratio of the amplitude of the fundamental frequency A_1 over the square of the second harmonic frequency A_2, obtained from the response under cyclic fatigue loading. The conclusions obtained from this method are summarized as follows:

(1) The parameter $\hat{\beta}'$ undergoes a sharp increase, followed by a gradual increase, reaching its maximum value when the fatigue life reaches approximately 80%, with the corresponding crack size less than 2 mm. This indicates that $\hat{\beta}'$ is an effective parameter for online detecting the critical crack state and estimating the remaining life, without requiring a baseline signal obtained from the pristine condition. This avoids false alarms due to the differences in the environmental and operational conditions between baseline and current signals.

(2) The quantitative relationship between FCG and parameter $\hat{\beta}'$ is developed based on the quadratic polynomial fitting, without requiring knowledge about the initial crack size or its initiation time. Statistical and regression validation demonstrates that all experimental and predicted data fall within the 95% confidence interval, with RMSE values of 0.9 mm and 1.2 mm on the left and right sides, respectively.

(3) The robustness of the newly introduced approach is evaluated by changing the location of the sensor. For crack detection, the inflection points between different states obtained by sensor 2 are consistent with sensor 1. In addition, another specimen with four sensors indicates that detectable crack size increases with distance from the centerline. Specifically, sensors 1 and 2, detect cracks of 1.5 mm, whereas sensors 3 and 4, positioned further away, detect cracks of 3 mm

and 3.8 mm, respectively. This indicates that the change in $\hat{\beta}'$ is attributable to the crack, rather than other factors such as the inherent nonlinearity of electrical equipment or background noise. The FCG models developed based on the data from sensor 1 are evaluated by using data from sensor 2, and the RMSE of the crack growth estimation is 1.1 mm and 1.4 mm, with all validation data falling within the 95% confidence interval, demonstrating the proposed method's robustness regarding the sensor location.

Overall, the proposed baseline-free method provides a new perspective for online fatigue crack detection and growth modelling. Once $\hat{\beta}'$ is extracted from the response of fatigue loading, the crack can be detected in real-time. Future studies will focus not only on the application of the method to more complex structures, such as stiffened plates, but also on investigating the influence of several key factors, including the type of loading, material properties, stress ratio, crack size, and the geometry of test specimens. Moreover, the effect of variations in loading frequency and ratio on the performance of the proposed method will be thoroughly examined.

Chapter 7

In-service baseline-free method for fatigue crack monitoring

7.1 Introduction

Although the method presented in Section 6 provides a novel perspective for online fatigue crack detection and growth modeling, it is not yet suitable for in-service applications. This limitation arises because classification relies on obtaining the complete lifecycle of $\hat{\beta}'$, which restricts its practical applicability. Additionally, the prediction error associated with the crack length quantification model remains significant and cannot be neglected.

To address these limitations, an automated online crack detection method and a more accurate crack quantification approach are urgently needed. Regarding automated crack detection, no reliable and generalized solution exists. For crack quantification methods, extensive research has been conducted, including the development of physical, simulation-based, and machine-learning approaches [207]. The Paris-Erdogan equation (Paris' law) represents a widely used physical approach for predicting FCG and has been widely employed for fatigue crack prognosis [208]. This equation, based on the fracture mechanics properties of materials, describes the relationship between crack growth rate and the range of SIF (ΔK), effectively predicting FCG behaviour. Despite its robust theoretical foundation and clear physical meaning, Paris' law requires extensive parameter adjustments and experimental calibration to handle complex environments and varying loading

conditions. Another challenge is the necessity for manual and continuous measurement of crack length under different loading cycles, which is labour-intensive and time-consuming [209]. Numerically, the crack propagation paths and rates can be predicted using Finite Element Analysis (FEA) [210, 211] and Boundary Element Method (BEM) [212, 213], which simulates stress and strain distributions. The key advantage of these methods is their capability to handle complex geometries and loading conditions. However, these methods are computationally intensive, requiring significant computational resources. In addition, the accuracy of the predictions heavily depends on the quality of the input data and the assumptions made during the modelling process, which limits their applicability in real-world scenarios. Therefore, machine learning approaches are increasingly gaining attention due to recent advances in computing and breakthroughs in artificial intelligence. These methods include Artificial Neural Network (ANN) [197,209], Gaussian processes (GP) [214], which combine linear and nonlinear features, and CNN methods integrated with image processing techniques [215]. For instance, Chen et al. [197] proposed an online fatigue crack prognosis method for hole-edge-cracked structures based on energy and phase change extracted from linear Lamb waves using ANN. Lim et al. [209] developed an online monitoring system for continuous fatigue crack quantification and remaining fatigue life estimation for plate-like structures using nonlinear ultrasonic modulation and ANN. Long et al. [215] introduced a deep learning-based FCG rate measurement method using a faster region-based convolutional neural network (Faster R-CNN), This method overcomes the limitations of traditional flexibility and potential methods, adapting effectively to non-standard specimens and accurately quantifying the size and growth rate of small cracks in these specimens. These methods can rapidly and accurately predict crack length and remaining life by learning from extensive historical data. However, they depend significantly on large volumes of high-quality training data. Additionally, the black-box nature of these models results in poor interpretability.

Despite the extensive research on fatigue crack quantification, traditional physical methods like Paris' law face significant limitations for in-service prediction, as their accuracy declines under real-world conditions. These methods assume that crack growth is influenced solely by SIFs, neglecting material nonlinearity and complex loading conditions. On the other hand, machine learning methods, although effective, suffer from challenges such as the dependency on high-quality

data and limited generalization capabilities, making them less reliable for unseen scenarios or different environmental conditions.

To address these challenges, this study introduces an in-service, baseline-free method for fatigue crack detection and quantification based on operational loading response analysis. The key contributions of this methods are as follows:

(i) Automated and Baseline-Free Crack Detection: This method leverages natural loading vibrations to enable in-service, real-time crack detection by analyzing the third harmonic component in the material's response to fatigue loading, eliminating the need for baseline data. By reflecting in-flight conditions, it provides continuous monitoring, reduces uncertainties associated with environmental variations and periodic inspections, and moves beyond conventional ground-based inspection approaches.

(ii) Energy-Efficient PZT Sensor Deployment: Instead of conventional sensors for vibration analysis, this method employs PZT sensors, which offer multifunctionality for passive impact detection, active damage monitoring, and automatic damage tracking without requiring additional power sources. This configuration simplifies deployment, reduces power consumption, and maintains a consistent monitoring framework that enhances reliability and minimizes uncertainties in crack detection during flight.

(iii) Robust PI-LSTM Model for Crack Quantification: For quantifying cracks, an LSTM network model is developed, integrating Paris' law to maintain the interpretability of the physical model while enhancing predictive accuracy for crack growth under complex environmental conditions. The proposed method has been experimentally validated on six specimens with varying sensor locations and loading ratios, demonstrating robust generalization across different scenarios.

7.2 Experimental setup

Following the acquisition of the properties of aluminum-5251 plates, six identical 300×100×2 mm (Fig. 7.1(b)) plates with a circular hole in the centre were designed and fabricated for fatigue tests. These plates were labelled S1-S6. The Instron Hydraulic 250 kN (as shown in Fig. 7.1(a)) fatigue machine was utilised to subject the specimen to cyclic loading, with a maximum load of 90 MPa (62% of the yield strength) and a minimum load of 9 MPa at a ratio of 0.1. The fatigue

crack initiated and propagated from both sides of the hole due to the stress concentration. The crack was continuously captured by a Canon EOS 5D mark II camera, a high resolution with a 21 effective megapixel full-frame CMOS sensor, and measured by the measurement tape on the specimen during the fatigue test. P-876 DuraAct PZTs made by PI ceramics are mounted on the specimens by thermoplastic films [140], the position (The lower left corner of the sample is the origin) and geometry of these sensors are summarised in Fig. 7.1(b). Specifically, P1 and P2 are equidistant from and vertically aligned with the centre of the hole, where the crack is expected to initiate and propagate due to stress concentration. In contrast, P3 and P4 are positioned farther from the central line. The objective of placing the sensors in different configurations is to test the reliability of the proposed algorithm. The loading frequency used in this research is 6 Hz [199], and the response generated from the fatigue loading was recorded by TiePie Handyscope Hs5 oscilloscopes and then saved by the Multi-channel oscilloscope software as shown in Fig. 7.1(d). The connection between sensors and oscilloscope is shown in Fig. 7.1(e). Measurements were conducted every 1000 loading cycles without interrupting the machine, using a sampling rate of 10 kHz and duration of 10s, resulting in 100 k samples at each measurement. The cyclic fatigue test was stopped when the crack propagated to approximately 15 mm in length.

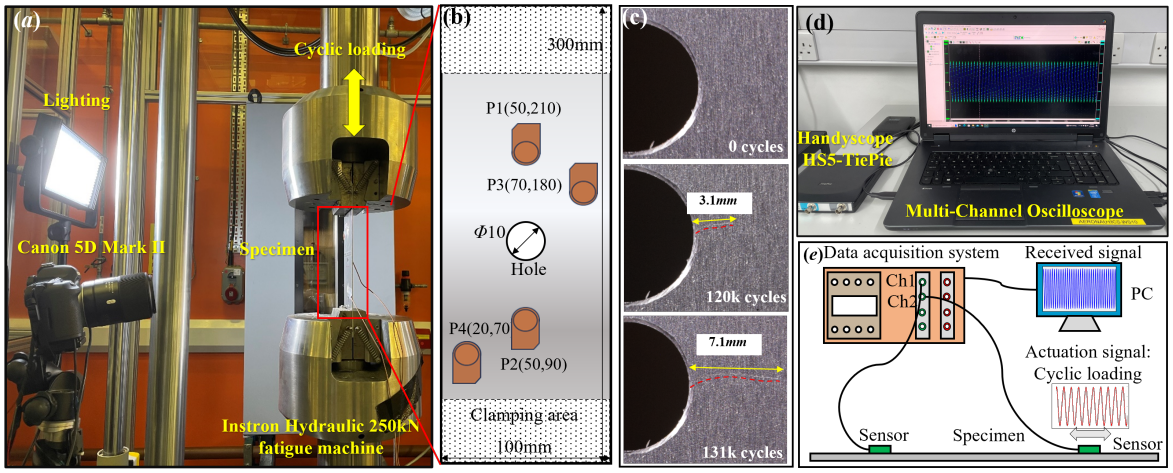


Figure 7.1: The experimental platform for online fatigue crack monitoring: (a) experimental setup for fatigue test; (b) specimen geometry and sensor layout; (c) specimen with and without crack; (d) hardware components for the data acquisition; (e) schematic diagram of data acquisition.

Specimens S1-S4 were used to develop the method, while S5-S6 were used to evaluate the performance of the proposed method under different experimental conditions to ensure the uncertainty

of the method to varying parameters such as loading magnitude, loading frequency and sensor placement. Specifically, S5 increased the number of sensors at different locations to investigate the effect of the sensor location on the performance, while a higher loading frequency of 10 Hz was applied to S6 to investigate its effect on the results. All of the specimens and the fatigue test parameters are summarized in Table 7.1. The data acaqusition are provided in Section .

Table 7.1: List of specimens, sensor positions and fatigue test parameters.

Specimen	Loading frequency	Loading amplitude	Sensor position
1	6Hz	1.8-18KN	P1-P2
2	6Hz	1.8-18KN	P1-P2
3	6Hz	1.8-18KN	P1-P2
4	6Hz	1.8-18KN	P1-P2
5	6Hz	1.8-18KN	P1-P4
6	10Hz	1.8-18KN	P1-P2

7.3 Methodology

7.3.1 In-service automated crack detection based on higher harmonic analysis

Feature selection The signal obtained from fatigue loading can be analysed in both the time domain and frequency domain. A comparative study was performed on pristine and fatigue-cracked specimens to investigate the changes in the time and frequency domains of the responses before and after cracking. The results are visualized in Figure 7.2.

Figure 7.2(a) shows the time domain response obtained from a pristine specimen and a specimen with a 1.8 mm fatigue crack. Both responses exhibit a similar pattern, as the actuation signal in this research is sinusoidal fatigue loading. However, the amplitude of the time-domain signal decreases after the crack initiation. In this research, the maximum amplitude is used to represent the information in the time domain. Figure 7.2(b) shows the difference in the frequency domain without and with a 1.8 mm crack. As mentioned in Section 7.2 , the actuation signal is the sinusoidal fatigue loading at 6 Hz, so the fundamental frequency of the response is also 6 Hz. In addition, the second harmonic at 12 Hz and the third harmonic at 18 Hz are observed, with

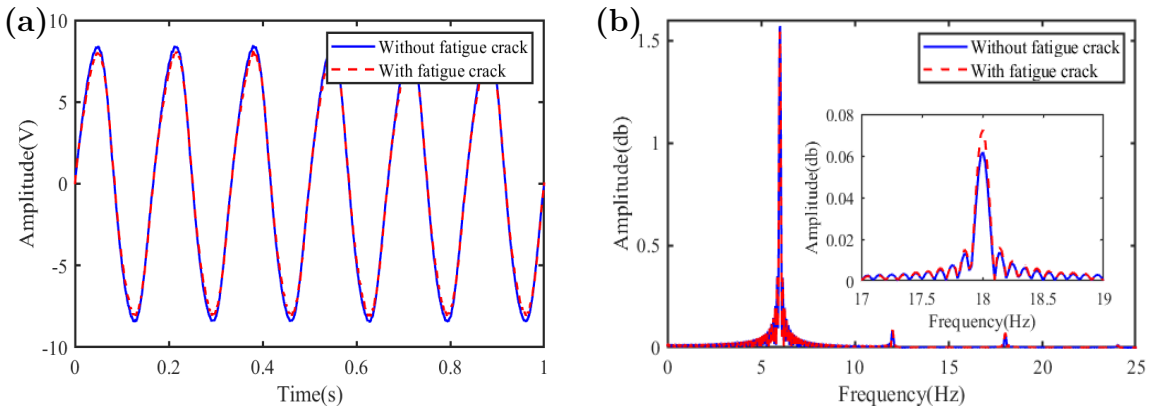


Figure 7.2: Response of time and frequency domain obtained from the pristine specimen (1000 cycles, blue solid line) and specimen with a 1.8 mm fatigue crack (92×10^3 cycles, red dash line): (a) time-domain signals and (b) frequency-domain spectra.

the amplitudes of these harmonic frequencies significantly lower than the fundamental frequency. Most importantly, the amplitude of the fundamental frequency decreases by approximately 4% before and after the crack initiation, whereas the amplitude of the third harmonic frequency at 18 Hz increases by approximately 17.5%. This is because the crack-induced nonlinear response of the material, transfers energy from fundamental frequency to the high-frequency harmonics, resulting in a reduction in the fundamental frequency amplitude and an increase in the third-harmonic amplitude [63, 163]. Therefore, in this research the parameter γ', calculated from the fundamental and third-harmonic amplitudes, is proposed to analyse the frequency domain of the response, which is defined as in equation (7.1).The calculation details are summarized in Section 2.2.2.

$$\gamma' = \frac{A'_3}{(A'_1)^3} \tag{7.1}$$

γ' is easier to measure, as it only requires the amplitudes of the fundamental and third harmonic signals in the frequency domain. However, traditional harmonic methods require synchronism and non-zero power flux to generate cumulative harmonic waves. Synchronism involves matching the phase and group velocity between the fundamental and corresponding harmonic modes to facilitate energy transfer from the fundamental mode to its harmonic counterpart. Non-zero power flux ensures a net energy flow between these modes. These conditions depend on parameters like the frequency and amplitude of the excitation signal. Consistent measurement conditions, including instrument settings, signal frequency, acquisition settings, and plate dimensions, are crucial when

using γ' to detect the crack. These requirements limit the application of γ' for online fatigue crack monitoring. Unlike the γ' in traditional methods, the γ' used in this research has the following novel characteristics: (1) No additional source of excitation is required: External signals, specifically fatigue loading (low frequency) representative of in-flight load are used to excite the structure instead of the conventional structural sensor excitation; (2) Low frequency excitation: The frequency of the excitation (i.e. fatigue loading) is relatively low, enabling the detection and quantification of cracks during continuous fatigue testing. In this research, $\hat{\gamma}'$ is used to differentiate from traditional methods.

To identify the effective feature for crack detection, this section analyses the maximum value of the time domain signal and $\hat{\gamma}'$. Taking the measurements obtained from the whole life cycle of S1 as an example, Figure 7.3 summarises the relationship between these features and the number of loading cycles.

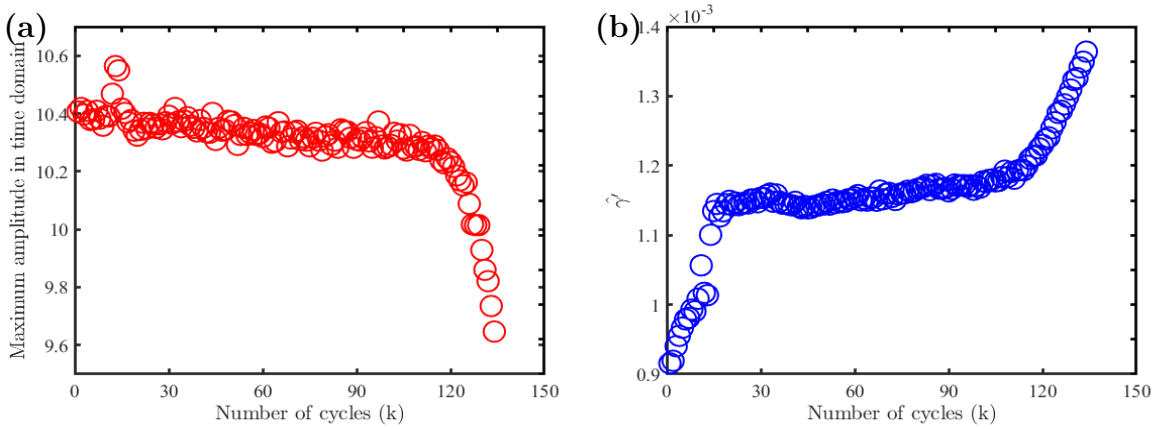


Figure 7.3: The change of features during the fatigue experiment: (a) The maximum value of the time domain signals (b) The relative third harmonic parameter $\hat{\gamma}'$

According to Figure 7.3 (a), the overall trend of the maximum amplitude of time domain signals initially shows a steady decline, followed by a rapid decrease. This rapid decline occurs because the presence of cracks reduces the material's stiffness hence reducing its response to the same excitation load. In addition, stress concentration at the crack tip converts part of the strain energy into thermal energy after crack initiation, causing energy loss and dissipation. This energy loss also contributes to the reduced amplitude in the time-domain response. Automatically detecting the crack initiation remains challenging. Firstly, the amplitude of the time-domain signal reflects the response of fatigue loading and is easily influenced by the machine's condition, such as the

stability of the hydraulic system, for example the variation observed around 15k cycle in Figure 7.3 (a). Furthermore, Figure 7.3 (a) shows that the changes in maximum amplitude fluctuate more than $\hat{\gamma}'$, making it less accurate for detecting crack initiation. Figure 7.3 (b) shows that the changes in $\hat{\gamma}'$ at different stages are clearer and more stable compared to the maximum value of the time-domain amplitude. The variation of $\hat{\gamma}'$ can be categorised in three stages:

1. $\hat{\gamma}'$ increases rapidly with the increase in loading cycles.
2. After approximately 20,000 cycles, it enters a stable state.
3. Subsequently, the $\hat{\gamma}'$ value increases rapidly again until specimen failure.

The trend observed in $\hat{\gamma}'$ resembles the three stages of fatigue life: Crack initiation, Stable growth and Rapid fracture. Therefore the objective of this work is to link the variation in $\hat{\gamma}'$ to the fatigue life of the material by correctly identifying the three intervals. The boundary between these three stages can be found based on empirical knowledge and experimentally detected cracks which can then be used for online crack detection based on variations in $\hat{\gamma}'$. However, this division is achieved only after obtaining the entire life cycle data of the specimen and lacks prior knowledge to detect damage. Furthermore, the patterns derived from empirical knowledge are not universally applicable. Therefore, a real-time automatic detection method is needed to identify the crack as it occurs, without relying on empirical patterns or complete life cycle data.

Dynamic piecewise linear (DPL) method To achieve real-time automatic crack detection and monitoring methodology, the most crucial step is to identify critical points in the recorded response of the material and to be able to classify the entire process based in these cirtical points. Therefore, this challenge can be considered an outlier detection problem. Common outlier detection methods include K-means [216] and Isolation Forest [217], but these methods are challenging to implement for dynamic outlier detection. Observing the changes in the $\hat{\gamma}'$ value in Figure 7.3 (b) shows that the slopes of the fitted lines vary significantly in the three different stages, which provides a possibility for monitoring outliers by analysing the changes in the slope. Therefore, this paper proposes a dynamic piecewise linear (DPL) method with a sliding window to automatically distinguish the fatigue process intervals.

The data obtained from fatigue experiments consist of the relative third harmonic dataset $\hat{\gamma}'_M = [\hat{\gamma}'_1, \hat{\gamma}'_2, \hat{\gamma}'_3, \ldots, \hat{\gamma}'_m]$, and the crack length dataset $a_M = [a_1, a_2, a_3, \ldots, a_m]$, where m is the number of data points. The DPL method involves fitting linear models to sequential segments of the data using a moving window approach. Firstly, the dataset obtained from the fatigue process within the i-th segment is expressed as:

$$[(\hat{\gamma}'_{i1}, a_{i1}), (\hat{\gamma}'_{i2}, a_{i2}), (\hat{\gamma}'_{i3}, a_{i3}), \ldots, (\hat{\gamma}'_{iw}, a_{iW})] \tag{7.2}$$

where W is the number of data points included in each segment, and the number of segments N generated from M data points is calculated as:

$$N = \left\lfloor \frac{M - W}{S} + 1 \right\rfloor \tag{7.3}$$

Therefore, the slope k_i and intercept b_i of the linear fit for the i-th segment are determined using the least squares method:

$$k_i = \frac{\sum_{j=1}^{W} (\hat{\gamma}'_{ij} - \bar{\hat{\gamma}}'_i)(a_{ij} - \bar{a}_i)}{\sum_{j=1}^{W} (\hat{\gamma}'_{ij} - \bar{\gamma}'_i)^2} \tag{7.4}$$

$$b_i = \bar{a}_i - k_i \bar{\gamma}'_i \tag{7.5}$$

where $\bar{\hat{\gamma}}'_i = \frac{1}{W} \sum_{j=1}^{W} \hat{\gamma}'_{ij}$ and $\bar{a}_i = \frac{1}{W} \sum_{j=1}^{W} a_{ij}$. The slope k_i is used to categorize the data into three distinct stages based on the thresholds.

Automatic SHM in-service crack detection procedure Based on the higher harmonic analysis and the DPL method, the automatic SHM in-service crack detection procedure is summarized in Figure 7.4, which includes four stages: 1) signal excitation, 2) data acquisition, 3) third harmonic calculation and 4) fatigue life characterisation. In the signal excitation stage, a fixed-frequency fatigue loading is employed as the excitation signal, with its time and frequency domains illustrated in Figure 7.4. In the data acquisition stage, PZT sensors on the aluminium plate collect responses from the fatigue loading. The time domain of the response, along with the fundamental and potential harmonic responses in the frequency domain, are summarized in Figure 7.4. In the third harmonic calculation stage, the third harmonic and fundamental frequency amplitudes are used to

calculate $\hat{\gamma}'$ using the equation in Figure 7.4. The DPL method then calculates the slope values (slope 1, slope 2, slope 3, ..., slope n) of the linear fit within the moving window, determining critical points for different stages of fatigue life by setting thresholds. Based on these points, the entire fatigue process on the aluminium plate is classified and modelled.

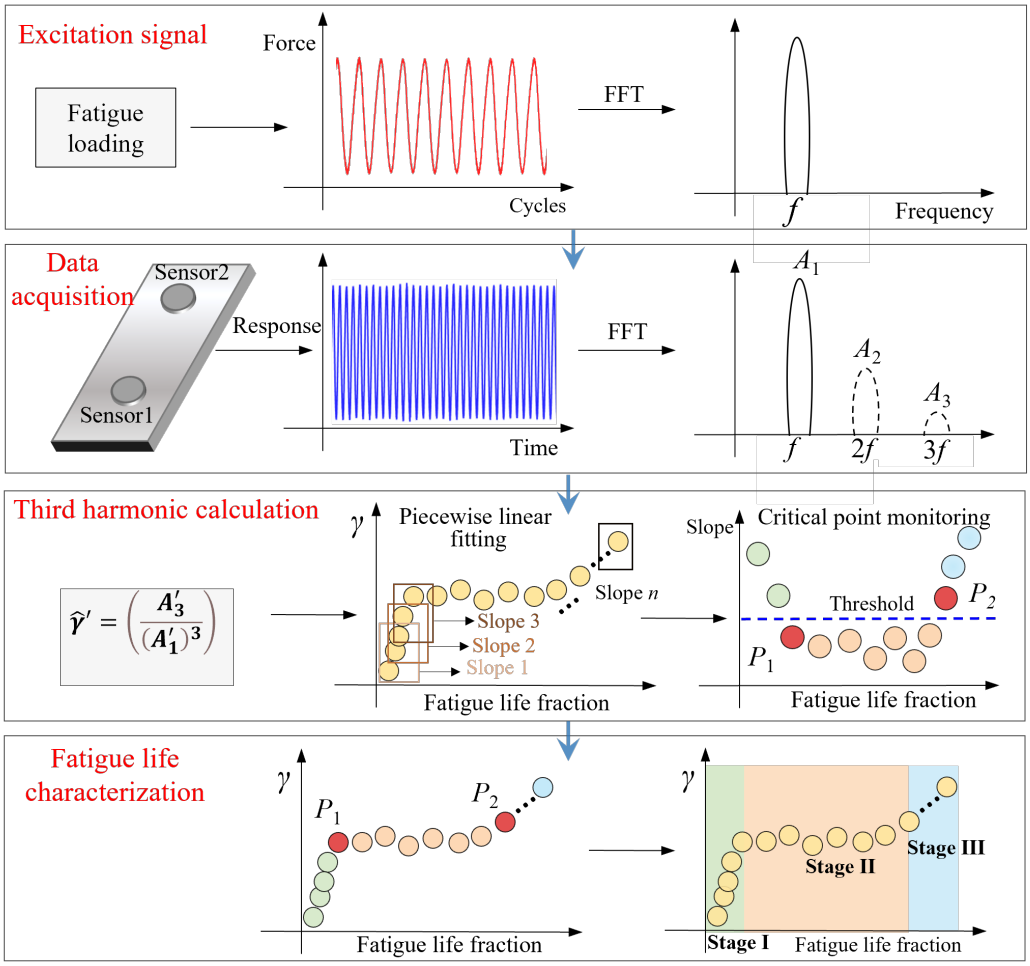
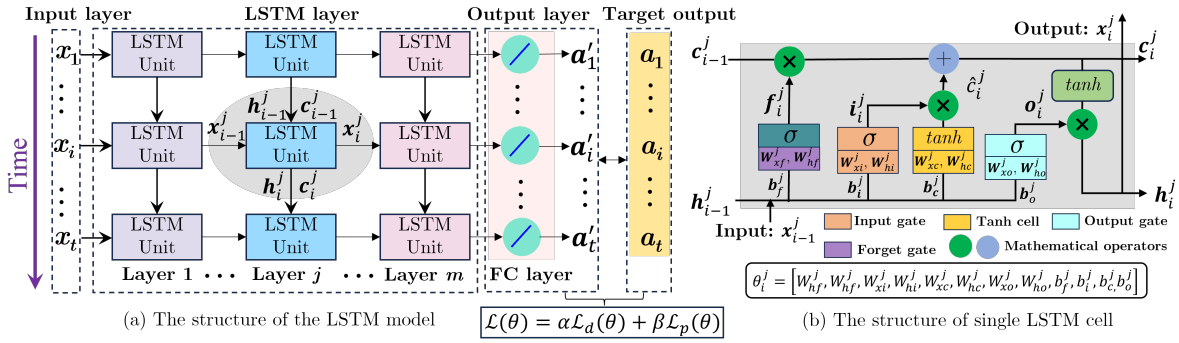


Figure 7.4: The framework of the proposed method in this work.

7.3.2 The crack growth model based on LSTM

LSTM network The LSTM network is a type of recurrent neural network (RNN) specifically designed for sequence-to-sequence modeling tasks. Unlike standard RNNs, which suffer from vanishing gradient problems when learning long-term dependencies, LSTM networks introduce memory cells and gated mechanisms (input, output, and forget gates) that enable them to retain and update information over longer time intervals. This makes LSTM particularly suitable for modeling processes that evolve over time. Given that FCG is inherently a time-dependent and cumulative

phenomenon—where the crack length at each time step is influenced by the entire history of loading and material response—LSTM is a natural choice for learning such sequential dependencies. In this study, the LSTM architecture is used to map a time series of input features (e.g., cycle number, SIF, and frequency response characteristics) to the corresponding crack length evolution. The network performs pairwise mapping of the input and output sequences in the time-space domain ($i = 1, 2, 3, \ldots, t$), as illustrated in Figure 7.5. This choice was made over other machine learning models such as feedforward neural networks (FNN), support vector machines (SVM), or decision trees, because those methods do not inherently capture temporal correlations or memory of past states. In contrast, LSTM allows the model to learn not only the instantaneous relationship between inputs and outputs but also the accumulated effects across time, which is essential for accurately predicting crack growth trajectories.



(a) The structure of the LSTM model (b) The structure of single LSTM cell

Figure 7.5: The structure of the deep LSTM, a) The LSTM model with multiple hidden layers and one fully connected layer, b) The structure of the LSTM single cell with the j_{th} layer at the time i, including an input gate, forget gate, output gate and tanh layer.

As illustrated in Figure 7.5(a), the LSTM model used in this study consists of an input layer that receives the sequence data $X = [x_1, x_2, x_3, \ldots, x_t]$ and an output layer that produces the predicted result $a = [a'_1, a'_2, a'_3, \ldots, a'_t]$. The hidden layer, comprising multiple LSTM layers, models the relationship between the input sequence X and the crack length a. Each LSTM layer consists of a sequence of LSTM units, each functioning similarly to a neuron in a conventional neural network. These units have independent sets of weights and biases, which are shared across the entire temporal space within the layer, as shown in Figure 7.5(b).

The notation θ_i^j represents the whole set of weights and biases in layer j at time i, which is expressed as:

$$\theta_i^j = [W_{hf}^j, W_{hi}^j, W_{xi}^j, W_{hc}^j, W_{xo}^j, W_{ho}^j, b_f^j, b_i^j, b_c^j, b_o^j] \tag{7.6}$$

Figure 7.5(b) shows a typical LSTM unit in layer j at time i, consisting of an input gate i_i^j, a forget gate f_i^j, an internal cell $\hat{c}_i^j$, and an output gate o_i^j. In addition, the sigmoid function $\sigma(x) = \frac{1}{1+e^{-x}}$ and $\tanh(x) = \frac{e^x - e^{-x}}{e^x + e^{-x}}$ introduce nonlinearity to the model, enabling the network to capture complex patterns in the data. Finally, a fully connected layer with a linear activation function is employed to map the relationship between the temporal features and the output.

The input gate regulates the flow of the new information by computing a weighted sum using the input weights W_{xi}^j, hidden state weights W_{hi}^j, and bias b_i^j. This sum is then passed through the activation function σ (typically a sigmoid function) to yield the gate value as defined by [218]:

$$i_i^j = \sigma(W_{xi}^j x_{(i-1)}^j + W_{hi}^j h_{(i-1)}^j + b_i^j) \tag{7.7}$$

The forget gate controls the extent to which old information is discarded. It performs a weighted sum using the input weights W_{xf}^j, hidden state weights W_{hf}^j, and bias b_f^j, followed by the activation function σ to get the gate value f_i^j:

$$f_i^j = \sigma(W_{xf}^j x_{(i-1)}^j + W_{hf}^j h_{(i-1)}^j + b_f^j) \tag{7.8}$$

The candidate memory generates new memory content by computing a weighted sum via the input weights W_{xc}^j, hidden state weights W_{hc}^j, and bias b_c^j. The activation function tanh is then applied to obtain the candidate's memory $\hat{c}_i^j$:

$$\hat{c}_i^j = \tanh(W_{xc}^j x_{(i-1)}^j + W_{hc}^j h_{(i-1)}^j + b_c^j) \tag{7.9}$$

The output gate governs the output of information from the memory cell. It computes a weighted sum with input weights W_{xo}^j, hidden state weights W_{ho}^j, and bias b_o^j, and applies the activation function σ to obtain the gate value o_i^j:

$$o_i^j = \sigma(W_{xo}^j x_{(i-1)}^j + W_{ho}^j h_{(i-1)}^j + b_o^j) \tag{7.10}$$

The cell state c_i^j is updated by the element-wise product of the input gate value i_i^j with the candidate's memory $\hat{c}_i^j$, and the element-wise product of the forget gate value f_i^j with the previous

cell state $c^j_{(i-1)}$:

$$c^j_i = i^j_i \odot \hat{c}^j_i + f^j_i \odot c^j_{(i-1)} \tag{7.11}$$

Finally, the hidden state h^j_i is derived by applying the activation function tanh to update the cell state c^j_i and performing an element-wise product with the output gate value o^j_i:

$$h^j_i = o^j_i \odot \tanh(c^j_i) \tag{7.12}$$

These equations enable LSTM networks to effectively capture and maintain crucial information over long sequences, mitigating the gradient vanishing and exploding issues typically associated with traditional RNNs.

The fatigue growth is an irreversible and cumulative process over the specimen's lifecycle, making it inherently time-dependent. LSTM networks were chosen for this study due to their superior capability in modeling sequential data with long-term dependencies. Unlike traditional machine learning models such as as BPNNs, which lack mechanisms for handling temporal information, or Recurrent Neural Networks (RNNs), which struggle with vanishing gradient issues, LSTMs utilize gated mechanisms to effectively capture both short- and long-term dependencies. This makes them particularly suited for quantifying the progressive nature of crack growth. Numerous studies have shown that LSTM models can achieve high prediction accuracy with sufficient data, even without understanding the physical mechanisms. However, these approaches may lack physical relation between the input and output parameters, which could result in weak generalization capabilities and a lack of interpretability. Physics-informed neural networks (PINNs) offer a solution by integrating physical mechanisms into the network, thus endowing the model with interpretability [219]. By incorporating prior physical knowledge, PINNs reduce the LSTM model's dependency on large datasets, enhancing the model's accuracy and reliability. PINNs have been widely applied in fields such as fluid dynamics [220], power systems [221], and structural engineering [222]. The most common method involves incorporating physical models as constraints into the model, for example, by integrating physical equations into the loss function of the model [223]. This guides the model to learn more generalized features, thereby improving the model's interpretability while maintaining accuracy and generalization capability.

The cumulative crack growth physical model Following the initiation of the crack, its growth becomes an irreversible and cumulative process throughout the whole life cycle of the specimens. As such, accurate cumulative crack growth models are essential for tracking the state of the specimen and predicting their service life. In this paper, a cumulative crack growth model is defined as in

$$a_t = a_{t-1} + \Delta a_t \tag{7.13}$$

where a_t and a_{t-1} are the crack lengths between two adjacent time steps, Δa_t is the crack increment, determined by a_{t-1} and the input x_i at time t. In the majority of current research focusing on the prediction of crack growth, the input variable x_i normally represents time-dependent factors such as applied stress or temperature [224]. Among many classic models, Paris' law is the most widely used to describe crack growth, which is expressed in equation 6.2. In this research, the number of cycles during the fatigue test is taken as time t. ΔK is the SIF range. C and m are the constants related to material property, which can be obtained by simulation or experimental data. The calculation of these two constants is summarized in the next section. Based on equation 6.2, the Paris' law model can be rewritten as a cumulative model in its discrete form [224].

$$a_t = a_{t-1} + C(\Delta K_t)^m \tag{7.14}$$

where the subscripts t and $t-1$ represent two adjacent time steps. In this study, the crack propagates under mode I loading conditions, where the loading stress is orthogonal to the crack plane. As such, ΔK_t is further expressed as:

$$\Delta K_t = \Delta\sigma_t F\sqrt{\pi a_{t-1}} \tag{7.15}$$

where $\Delta\sigma_t$ represents the time history of the stress range, and F is the shape factor. As reported in [201], during the stable crack propagation phase originating from the hole, the behaviour stabilizes when the crack length exceeds one-fifth of the hole radius R, with F varying between 1 and 1.05. In this paper, F was assumed to be constant during the crack growth [209].

PI-LSTM for crack growth model In this work, a physical-informed LSTM (PI-LSTM) neural network is proposed for modeling crack growth during the fatigue process. The cumulative

growth model, based on the discrete form of Paris' Law, is incorporated as prior physical knowledge into the loss function of the LSTM neural network. This incorporation serves as a physical constraint on the output of the LSTM model. The newly introduced loss function for PI-LSTM is expressed as:

$$L(\theta_i^j) = \alpha L_d(\theta_i^j) + \beta L_p(\theta_i^j) \tag{7.16}$$

where $L_d(\theta)$ and $L_p(\theta)$ are loss functions of the LSTM model and physical model, α and β are their weights, and $\alpha + \beta = 1$. $L_d(\theta)$ and $L_p(\theta)$ are further expressed as:

$$L_d(\theta_i^j) = \frac{1}{N}\sum_{t=1}^{N}(a_{mt} - a'_{mt})^2 \tag{7.17}$$

$$L_p(\theta_i^j) = \frac{1}{N}\sum_{t=1}^{N}\left(\left(\frac{da}{dN}\right)_{mt} - \left(\frac{da}{dN}\right)'_{mt}\right)^2 \tag{7.18}$$

where a_{mt} and $\left(\frac{da}{dN}\right)_{mt}$ are the actual crack length and FCG rate of specimen m at time t, and a'_{mt} and $\left(\frac{da}{dN}\right)'_{mt}$ are the corresponding predicted values, which can be obtained through the forward propagation based on the parameter θ_i^j. The loss function not only calculates the error to determine convergence but also affects the update of model parameters θ_i^j during the backpropagation process. In this section, the gradient descent method was used to update the trainable parameter θ_i^j. In terms of the LSTM model, the gradient of a'_{mt} with respect to θ_i^j is:

$$\frac{\partial L_d(\theta_i^j)}{\partial \theta_i^j} = 2\left(\frac{1}{N}\sum_{t=1}^{N}(a_{mt} - a'_{mt})\right)\cdot\frac{\partial}{\partial \theta_i^j}\left(\frac{1}{N}\sum_{t=1}^{N}(a_{mt} - a'_{mt})\right) \tag{7.19}$$

For the LSTM model, the gradient of $\left(\frac{da}{dN}\right)'_{mt}$ with respect to θ_i^j is calculated by:

$$\frac{\partial L_p(\theta_i^j)}{\partial \theta_i^j} = 2\left(\frac{1}{N}\sum_{t=1}^{N}\left(\left(\frac{da}{dN}\right)_{mt} - \left(\frac{da}{dN}\right)'_{mt}\right)\right)\cdot\frac{\partial}{\partial \theta_i^j}\left(\frac{1}{N}\sum_{t=1}^{N}\left(\left(\frac{da}{dN}\right)_{mt} - \left(\frac{da}{dN}\right)'_{mt}\right)\right) \tag{7.20}$$

In the backpropagation process, the trainable parameter θ_i^j is adjusted iteratively by $L(\theta_i^j)$ and the learning rate η updated by:

$$(\theta_i^j)' = \theta_i^j - \eta\frac{\alpha\cdot\partial L_d(\theta_i^j) + \beta\cdot\partial L_p(\theta_i^j)}{\partial \theta_i^j} \tag{7.21}$$

In this study, boundary and initial conditions were embedded into the LSTM-based PINN framework by incorporating corresponding residual terms into the loss function. Specifically, the initial condition was enforced by minimizing the mean squared error (MSE) between the predicted and known crack lengths at the initial time step. For the boundary condition, which involves the crack growth rate (da/dN) governed by Paris' law, and the corresponding ΔK, a physics-based penalty term was added to the loss function to constrain the predictions. This physics loss term penalizes any deviation from the expected relationship defined by Paris' law. By combining these constraints with data-driven training, the model ensures that the learned crack growth behavior aligns with both observed data and the underlying fracture mechanics.

Hyperparameter tuning in PI-LSTM In machine learning models, selecting an appropriate combination of hyperparameters is crucial for model performance, training efficiency, and generalization ability [225]. However, current methods typically rely on experience and trial-and-error, lacking systematic theoretical guidance. By thoroughly investigating these hyperparameters, we aim to reveal their specific impacts on model performance, optimize overall performance, and reduce trial-and-error costs during the training process. For the proposed PI-LSTM model in this paper, the focus was on optimizing batch size [226], learning rate [103], hidden layer size [112], number of hidden layers [4], and the alpha-beta pairs in the loss function to enhance model performance and improve generalization ability. The optimization ranges are summarized in Table 7.2, the proposed PI-LSTM framework was developed in Spyder 5.1.1 platform.

Table 7.2: The range of input parameters and model hyperparameters for the PI-LSTM model.

Parameters	Range	Definition
$\frac{da}{dt}$	$[4.04 \times 10^{-6}, 1.66 \times 10^{-4}]$	Input parameters
ΔK	$[3.66\ \text{MPa}\sqrt{\text{m}}, 25.11\ \text{MPa}\sqrt{\text{m}}]$	
$\hat{\gamma}'$	$[0.00204, 0.001926]$	
Batch size	$[8, 16, 32, 48, 64]$	Model hyperparameters
Learning rate	$[0.001, 0.002, 0.005, 0.01, 0.02]$	
Hidden layer size	$[2, 4, 6, 8, 10]$	
Number of hidden layers	$[1, 2, 3, 4, 5]$	
Alpha-beta pairs	$[(0.1, 0.9), (0.3, 0.7), (0.5, 0.5), (0.7, 0.3), (0.9, 0.1)]$	

Model performance evaluation In this study, the Root Mean Square Error (RMSE) is used to evaluate the model's performance. RMSE is sensitive to outliers, and lower values indicate better prediction performance. It can be expressed as:

$$\text{RMSE} = \sqrt{\frac{\sum_{n=1}^{N}(a_{mt} - a'_{mt})^2}{N}} \tag{7.22}$$

where a_{mt} is the crack length obtained by the experiment, and a'_{mt} is the crack length predicted by the model.

7.4 Results and discussion

7.4.1 Fatigue growth behaviour

Fig. 7.6 presents the crack growth initiated from the hole edges, as captured by the camera (Fig. 7.6(b)). For specimens S1 and S2, the first detectable crack on S1 appeared after approximately 110,000 loading cycles, with a corresponding crack length of 0.5 mm, while S2 exhibited a detectable crack at 105,000 cycles with a length of 0.7 mm (Fig. 7.6(a)). The observed variations in results across different specimens can be attributed to the machining quality of the centre hole, as shown in Fig. 7.6(b)). Despite these specimens being cut from the same aluminium sheet, minor differences in the dimensions and edge quality of the holes contribute to fluctuations in the results.

7.4.2 Automatic crack detection based on the DPL method

Automatic crack detection results The detection of the crack based on $\hat{\gamma}'$ is expected to demonstrate a sudden change when a crack is initiated. Taking S1 as an example, the variation of the $\hat{\gamma}'$ with the increase in loading cycles is shown in Figure 7.7(a) (blue circles). It can be seen that the inflection point in the $\hat{\gamma}'$ variation which indicates the 3rd stage of its variation, coincides with the initiation of the crack (black line). The pattern of their variation is also similar. Therefore, it can be concluded that the change in the $\hat{\gamma}'$ has a direct correlation with the initiation and growth of cracks and is a reliable parameter to be used. The challenge now is how to automatically detect these three stages of the fatigue life based on $\hat{\gamma}'$ variation.

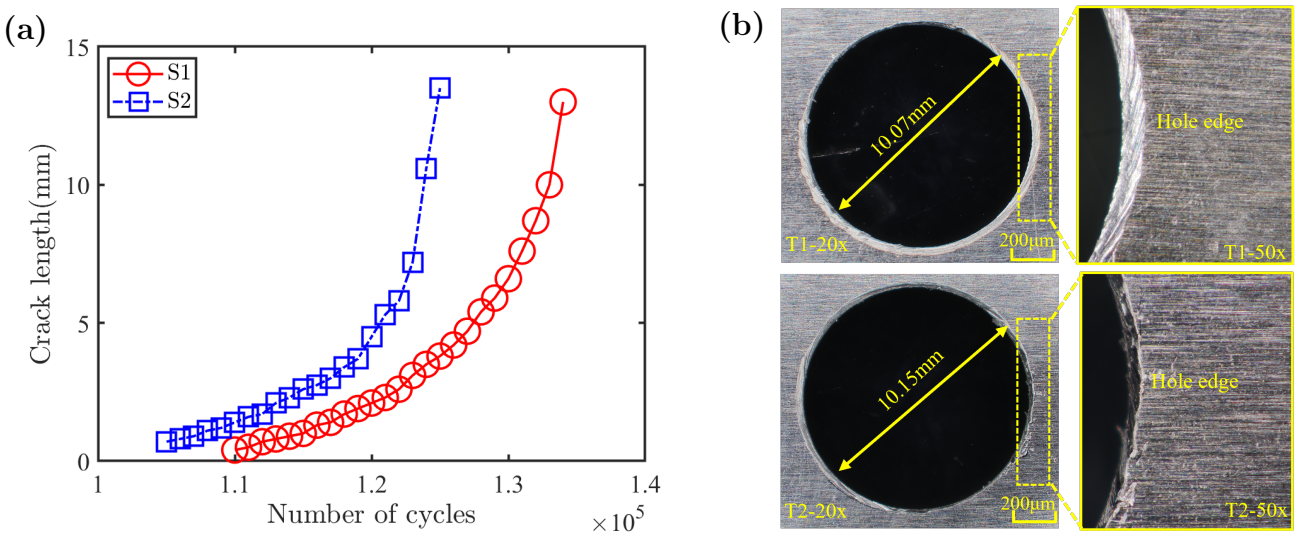


Figure 7.6: (a) Paris' law specimen data, C= 4.94×10^{-7}, and m=1.86; (b) The micromorphology of the hole and edges.

The DPL fitting method is then employed to automatically divide the fatigue process using a moving window. Based on extensive experiments, the window size is finally set to 10, meaning a fitting relationship can be obtained every 10,000 cycles, effectively avoiding the influence of outliers caused by noise and machine instability. Additionally, the step size of the moving window is set to 1, allowing for better capturing of the data variability. The dynamic fitting process can be seen in the supplementary video. Figure 7.7(c-d) show the methodology's capability in detecting the inflection points. Specifically, in Figure 7.7(c), during the first stage of the fatigue loading process, the slope of the fitted lines from different windows is relatively high. As the fatigue process proceeds, the slope gradually decreases, resulting in "spikes" at the critical points due to the low overlap degree of the fittings. Similar phenomena are observed during the transition from the second to the third stage (Figure 7.7(d), indicating that the proposed method can effectively capture the critical points of changes across different stages.

The "inflection point" between stage 1 and stage 2 is crucially referred to as microcrack nucleation, which represents the pre-formation of microcracks. This can occur due to the mismatch in deformation between inclusion particles and the surrounding matrix. This inflection point, occurring at around 23,000 cycles, constitutes approximately 17% of the total lifecycle. This observation aligns with findings reported in [199], where scanning electron microscopy (SEM) was employed to investigate microcrack nucleation in fatigue experiments involving aluminum alloys. The study

revealed that microcrack nucleation takes place in the early phase of the life cycle. However, it is important to highlight that microcrack nucleation below a certain length cannot be observed during the continuous operation of the experiment. As a result, in this research, the detectable crack length is defined as the onset of crack initiation.

Based on the DPL method, the slopes obtained from the fitting process during the S1 fatigue experiment are summarized in Figure 7.7(b).To achieve an automatic crack detection method, a slope threshold of 2.5×10^{-9} was set. Using this threshold, the first stage of the fatigue process is approximately 23,000 cycles, accounting for about 17% of the total lifecycle. The inflection point detected between the second and third stages is at 116,000 cycles, corresponding to a crack length of 1.3 mm. Additionally, Figure 7.7(e) shows the classification of the fatigue process based on the K-means clustering method. The results indicate that the inflection point between the second and third stages is detected at 120,000, these results demonstrate the effectiveness of the proposed method for in-service online crack detection.

Applying the proposed methodology on S2-S4 under the same experimental conditions, the detectable crack lengths and corresponding number of cycles are summarised in Table 7.3.

Table 7.3: Detection results obtained by DPL and K-means clustering method.

	DPL method		**K-means method**	
Specimen	**Number of cycles**	**Detected crack length**	**Number of cycles**	**Detected crack length**
1	116,000	1.3 mm	120,000	2.1 mm
2	111,000	1.8 mm	115,000	2.9 mm
3	92,000	1.8 mm	100,000	4.0 mm
4	105,000	1.9 mm	110,000	4.3 mm

As shown in Table 7.3, for S2-S4, the DPL method is capable of automatically detecting cracks ranging from 1.8 mm to 1.9 mm at cycle counts between 92,000 and 116,000. In contrast, the inflection points predicted by the K-means clustering method, corresponding to cycle counts between 100,000 and 120,000, show crack lengths ranging from 2.1 mm to 4.3 mm. Therefore, compared to the K-means clustering method, the DPL method proposed in this paper is more predictive in detecting fatigue cracks. This earlier detection capability is crucial for timely maintenance and prevention of significant damage, thereby enhancing the reliability and safety of the monitored structures.

In summary, the analysis demonstrates that the DPL method offers superior performance in

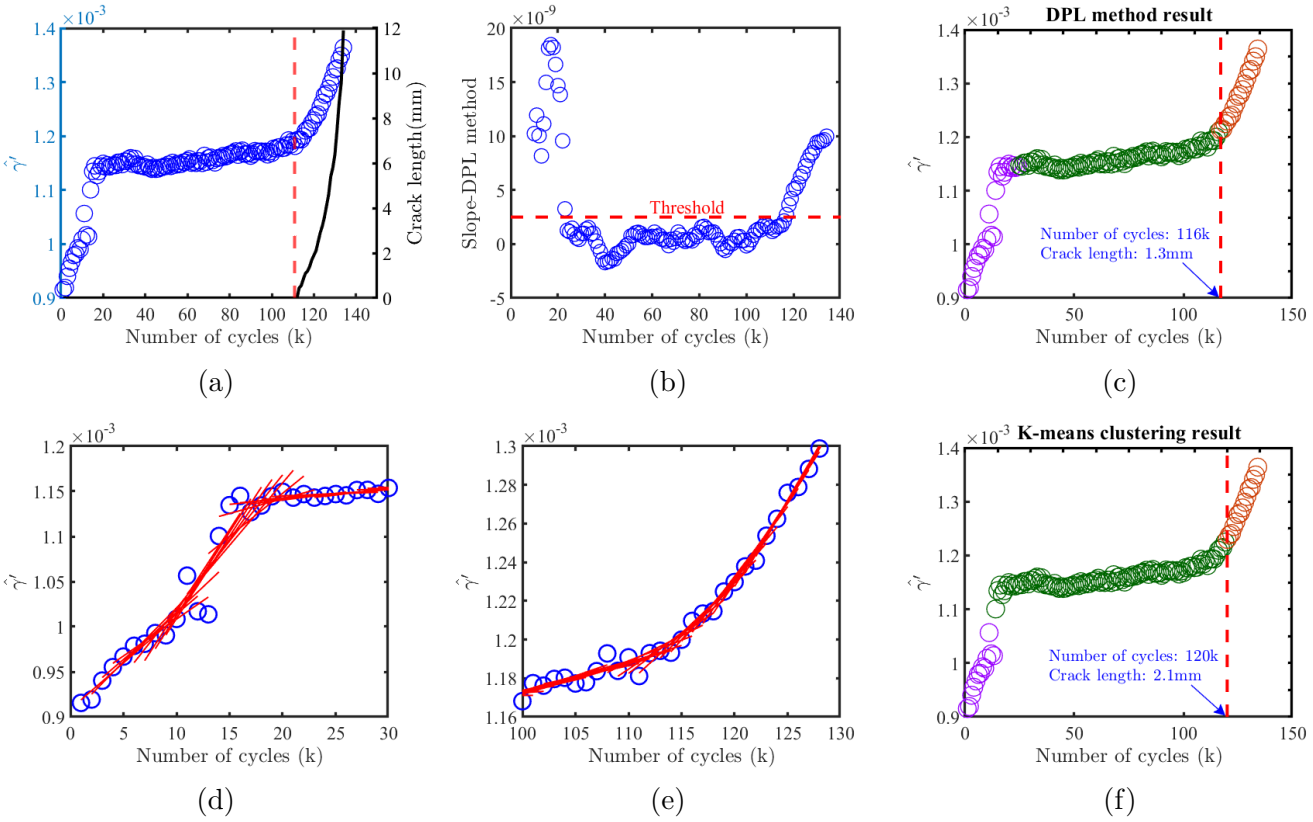


Figure 7.7: Results of crack detection: (a) The change of the $\hat{\gamma}'$ with respect to the fatigue loading cycles on S1, (b) The slope values obtained by the DPL method, and the Threshold= 2.5×10^{-9}, (c) The different fatigue stages divided by the DPL method, and the crack length detected by the method, (d) The running details of dynamic fitted lines between first and second stage, (e) The running details of dynamic fitted lines between second and third stage, (f) K-means clustering method result on S1.

early automatic crack detection, making it a more effective tool for real-time online monitoring of structural health. This advantage is particularly evident in the earlier detection of smaller crack lengths, underscoring the method's potential for early intervention and improved life cycle management of structures under fatigue.

7.4.3 Robustness analysis of the DPL method on the crack detection

The effect of the sensor location On S1-S4 specimens, two sensors are symmetrically positioned along the centerline of the plate. As previously discussed, sensors located on the centerline can detect the initiation and growth of cracks in real time. Cracks initiate from the edge of the central hole due to stress concentration, and the waves generated by the fatigue loading produce the third harmonic component as they pass through the crack. This third harmonic component

is crucial for the effectiveness of the method proposed in this research. To further verify that the third harmonic is caused by the crack rather than the sensors or the hydraulic machine, two additional sensors are attached on S5 specimen. Figure 7.8(a) shows the locations, with sensor 3 located 20 mm from the centerline and sensor 4 located 30 mm from the centerline.

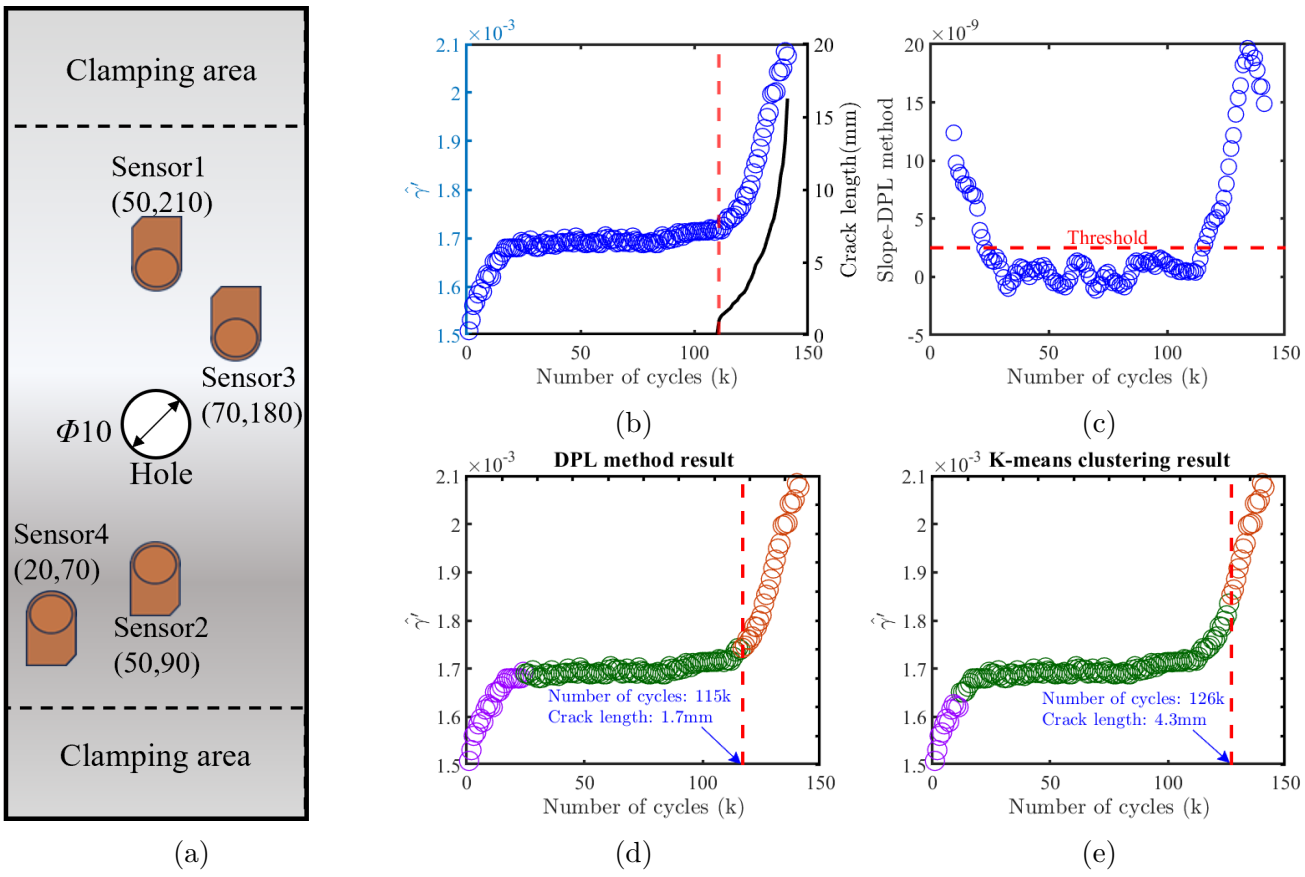


Figure 7.8: Results of crack detection obtained by: (a) The position of 4 sensors on S5, (b) The change in the third harmonic parameter and crack growth with respect to fatigue loading cycles, as recorded by sensor 1 on S5, (c) The slope values obtained by the DPL method, and the Threshold $= 2.5 \times 10^{-9}$, (d) The different fatigue stages divided by the DPL method, and the crack length detected by the method, (e) The K-means clustering method result on S5.

Figure 7.8(b) and(e) summarise the results obtained from sensor 1. Figure 7.8(b) illustrates the relationship between the variation in $\hat{\gamma}'$ and crack growth, demonstrating that the initiation of the crack coincides with the inflection point which marks the sudden increase in the $\hat{\gamma}'$. Figure 7.8(c) presents the slope values obtained using the proposed DPL method. Figure 7.8(d) shows the different stages of the fatigue process as detected by the DPL method. When the number of loading cycles reaches 115,000, the automatically detected crack length is 1.7 mm. In addition, Figure 7.8(e) indicates that the crack length detected by the K-means method is 4.3 mm, showing

a delay compared to the DPL method. These results are consistent with those obtained from S1-S4, verifying the effectiveness of the method on S5.

The same steps were repeated for the data obtained from sensors 2-4, and the results are summarized in Figure 7.9 and Table 7.4. Figure 7.9 shows results obtained from sensor 3 which is further from the crack initiation point. Figure 7.9(a) presents the classification of fatigue process stages using the same threshold value of 2.5×10^{-9}. At 130,000 loading cycles, the detectable crack length is 6.0 mm. This detection is delayed compared to the crack detected by sensor 1 which is closer to the crack initiation and hence can capture smaller variations earlier. Sensor 3, being farther from the centerline, requires the crack to grow to a certain length before significant $\hat{\gamma}'$ changes can be detected. In addition, results in Table 7.4 further verify this finding: as the distance from the centerline increases, the detectable crack length also increases. For instance, sensor 4, positioned 30 mm from the centerline, can detect cracks larger than 9.6 mm, the largest among the four sensors. These results indicate that the source of $\hat{\gamma}'$ generation is the crack, rather than other factors, such as the inherent nonlinearity of electrical equipment, and background noise [162], thereby validating the effectiveness of the method proposed in this chapter.

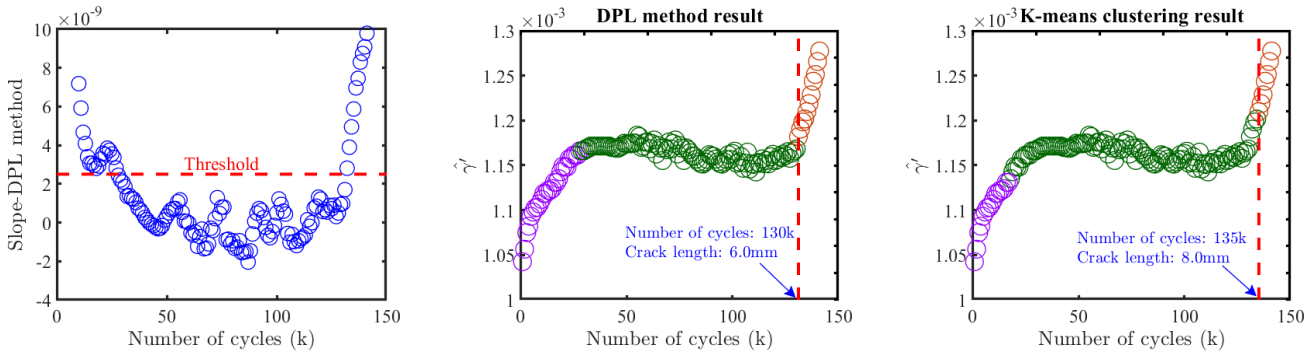


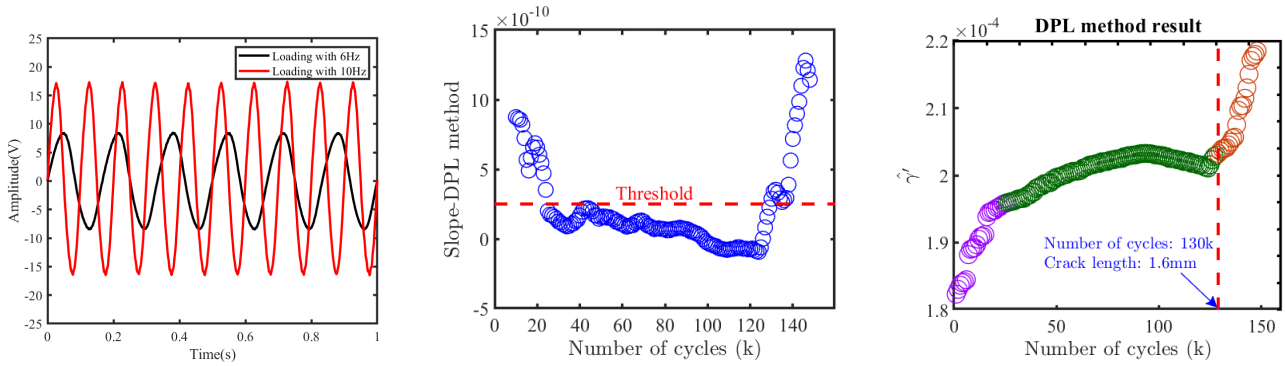
Figure 7.9: Results of crack detection: (a) The slope values obtained by the DPL method, and the Threshold=2.5×10^{-9}, (b) The different fatigue stages divided by the DPL method, and the crack length detected by the method, the detectable crack length is 6.0 mm, and the corresponding number of cycles is 130k. (c) K-means clustering method result on S1, the detectable crack length is 8.0 mm, and the corresponding number of cycles is 135k.

The effect of the loading frequency. In the previous section, the effect of sensor location on the robustness of the proposed methodology performance was analyzed, confirming that the increase of $\hat{\gamma}'$ originated from the crack rather than from other sources. However, since the pro-

Table 7.4: Detection results obtained by different sensors on S5.

	DPL method		K-means method	
	Number of cycles	Detected crack length	Number of cycles	Detected crack length
Sensor1	115,000	1.7 mm	126,000	4.3 mm
Sensor2	115,000	1.7 mm	126,000	4.3 mm
Sensor3	130,000	6.0 mm	135,000	8.0 mm
Sensor4	137,000	9.6 mm	139,000	11.7 mm

posed method relies on frequency domain response analysis, it is crucial to demonstrate that the methodology is not dependent on the loading frequency, and hence it is applicable in-service with variable external loading. Therefore, the loading frequency was increased to 10 Hz on the S6. The results obtained by the DPL method are summarized in Figure 7.10.



(a) (b) (c)

Figure 7.10: Results of crack detection obtained by S6: (a) Time-domain of the sensor response when the loading frequency is 6 Hz and 10 Hz, (b) The slope values obtained by the DPL method, and the Threshold $= 2.5 \times 10^{-10}$, (c) The different fatigue stages divided by the DPL method, and the crack length detected by the method. The detectable crack length is 1.6 mm, and the corresponding number of cycles is 130k.

Figure 7.10(a) shows a comparison of time-domain signals for S1 (6 Hz) and S6 (10 Hz). When the loading frequency is increased to 10 Hz, the time-domain amplitude of the response obtained by the PZT sensor significantly increases. This is because, at higher frequencies, the energy of the stress wave induced by the loading is more concentrated, resulting in increased local stress and strain, thereby significantly enhancing the response amplitude of the PZT sensor. Higher-frequency stress waves have shorter wavelengths and higher energy densities, making the mechanical vibration and the conversion to electrical signals more pronounced. Figure 7.10(b) presents all the slope values obtained during the fatigue test of S6 using the proposed DPL method. The change in

slope values for S6 follows the same trend as those for S1-S5, and it is easy to identify a threshold that divides the process into three stages, as shown in Figure 7.10(c). The detectable crack is 1.6 mm, and the corresponding loading cycle is 130,000. Notably, the threshold value determined for S6 is 2.5×10^{-10}, an order of magnitude smaller than the threshold value of 2.5×10^{-9} determined for S1-S5. This phenomenon occurs because the main frequency component is represented by the fundamental frequency in the frequency-domain signal. In the time-domain signal, the amplitude reflects the signal's energy, while in the frequency-domain signal, the amplitude represents the signal's energy magnitude at the corresponding frequency. Therefore, as the amplitude of the time-domain signal decreases with an increase in loading frequency, the amplitude of the fundamental frequency in the frequency-domain signal increases. According to equation 7.1, when the amplitude of the fundamental frequency increases, the value of $\hat{\gamma}'$ decreases.To further validate the frequency independence of the threshold in the proposed method, Z-score normalization [227] was applied to the slope values obtained from the DPL method, results are summarized in Figure 7.11.

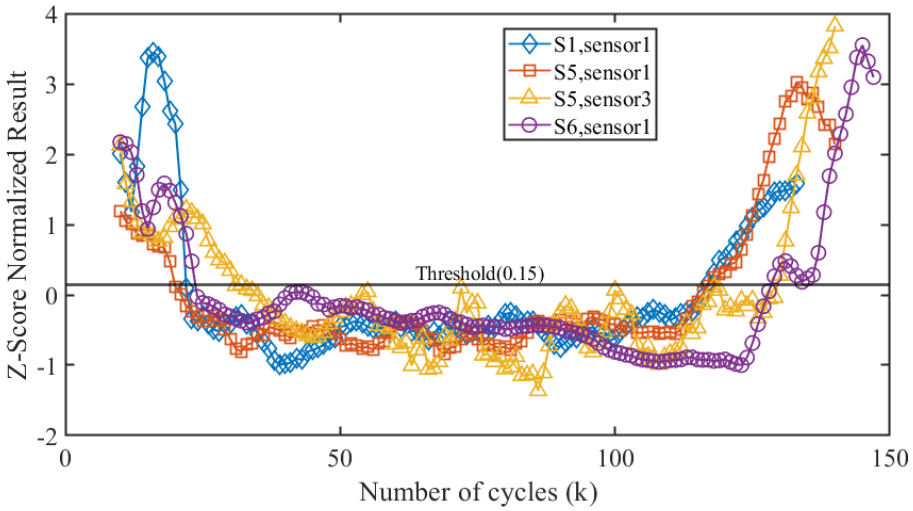


Figure 7.11: The framework of the proposed method in this work.

Following the Z-score normalization, a unified threshold value of 0.15 was determined across all samples, which effectively delineates the different stages of the fatigue process, as illustrated in Figure 7.11. Specifically, for Specimen 1 (S1), the critical point marking the transition between the second and third stages of fatigue occurs at 116,000 loading cycles. For S5, data obtained from Sensors 1 and 5 indicate that the critical points separating the second and third stages are 115,000 and 130,000 cycles, respectively. Most importantly, in terms of S6, which was subjected to

a different loading frequency, the critical point between the second and third stages is detected at 130,000 cycles. The critical points of all cases detected by the threshold 0.15 based on the Z-score are totally the same as those of the DPL method. The consistency of these critical points, all detected using the unified threshold of 0.15 based on Z-score normalization, aligns with the results obtained through the DPL method. This indicates that normalizing the slope values derived from the DPL method using Z-scores to a standardized range does not affect the general trend of $\hat{\gamma}'$ nor affect the method's performance. The use of a unified threshold under Z-score further underscores the independence of the method from loading frequency. This characteristic is critical for the accurate detection of fatigue damage stages under varied loading conditions, confirming both the robustness and versatility of the approach.

In summary, the experimental tests including variations in sensor location and loading frequency (S5-S6), demonstrated that the proposed baseline-free methodology is capable of reliably detecting crack initiation online, under varying operational conditions. This method offers a novel in-service SHM capability, without additional excitation sources.

7.4.4 Crack growth result

The hyperparameter optimization result As mentioned in Table 7.2, five parameters—batch size, learning rate, hidden layer size, number of hidden layers, and the alpha-beta pairs in the loss function are optimized to enhance model performance and improve generalization ability. Consequently, 3125 parameter combinations are studied in this research. The model with different parameter combinations is initially trained using the sub-training dataset and evaluated on the validation dataset for hyperparameter optimization. Results are summarized in Figure 7.12.

Figure 7.12 illustrates that different hyperparameter combinations significantly impact model performance. Specifically, a smaller batch size enhances accuracy, while a learning rate of 0.01 yields the lowest RMSE, indicating optimal performance. Additionally, selecting an appropriate number of hidden layer nodes (e.g., 8 nodes) substantially reduces RMSE and improves performance. The model achieves the best results with two hidden layers, as adding more layers neither improves performance nor adds value, while potentially increasing complexity. Adjusting the α and β parameters effectively reduces error, with a combination of $\alpha = 0.9$ and $\beta = 0.1$ leading

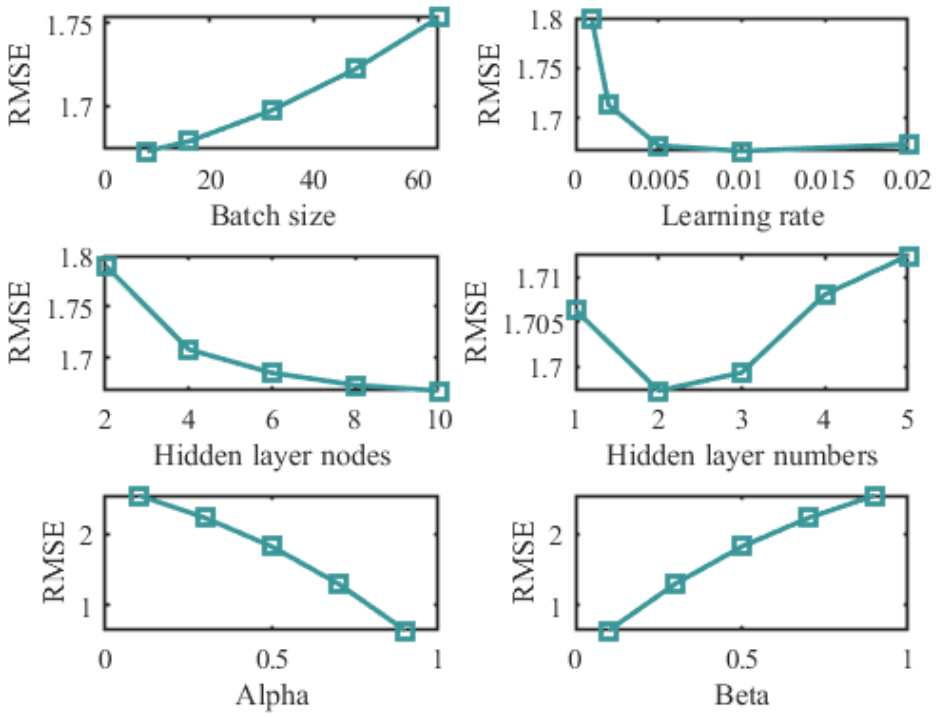
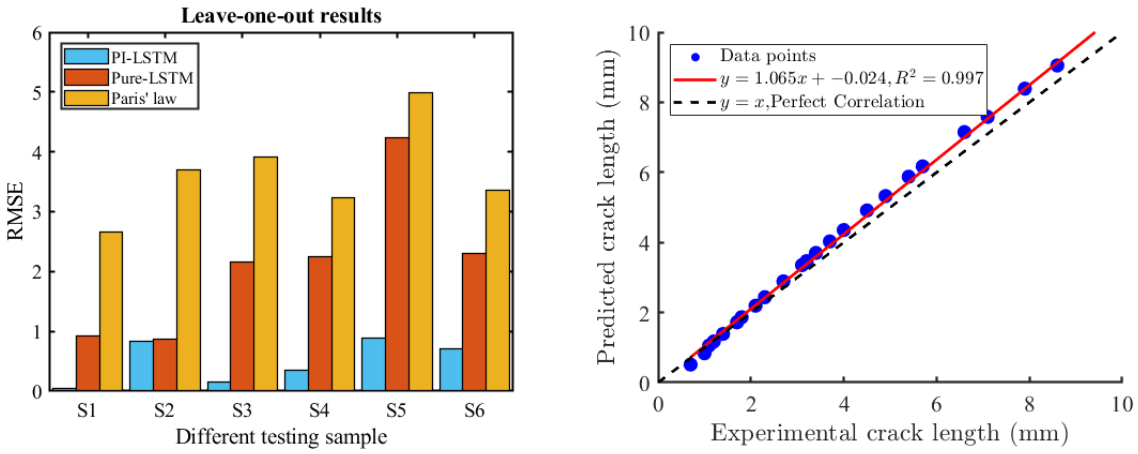


Figure 7.12: RMSE obtained by different hyperparameter combinations.

to notable improvements. The optimal hyperparameter combination is as follows: Batch size: 8, Learning rate: 0.01, Hidden layer nodes: 8, Number of hidden layers: 2, α-β pair: 0.9-0.1.

Crack growth modelling based on PI-LSTM The results in Section 7.4.2, indicate that $\hat{\gamma}'$ continuously increases with the number of loading cycles after crack initiation, which is related to the increase in crack length. Predicting crack size is crucial for assessing structural condition, schedule its maintenance and repair and predict its remaining life. Therefore, a PI-LSTM model is proposed to predict the crack size in real-time, and the leave-one-out cross-validation method is used to validate its performance. Specifically, the data obtained from five aluminium plates are used for model development, and the remaining dataset is used for model validation. For instance, when utilizing the data from S1 as the test set, the data from the remaining five specimens S2-S6 are used as the training sets. The results are summarized in Figure 7.13.

Among the six datasets, S1-S4 were conducted under identical experimental conditions, whereas S5 and S6 considered the variation in sensor location and loading frequency. Therefore, the model's performance on S5 and S6 reflects its generalization ability. Notably, the $\hat{\gamma}'$ values for S6 are significantly different from those of the other datasets, being an order of magnitude apart. Figure



(a) (b)

Figure 7.13: (a) Leave-one-out cross-validation results on different testing samples obtained by different methods. (b) Predictive FCG result of S3 using the PI-LSTM.

7.13(a) presents the RMSE values for various test samples obtained using different methods. The same hyperparameter optimization process was applied to the pre-LSTM, reflecting the optimal hyperparameter combinations. It is evident that Paris' Law consistently exhibits the poorest performance across all test samples. While the pure LSTM method outperforms Paris' Law, achieving higher prediction accuracy on some samples such as S1 and S2, it still shows high RMSE values on others, like S5. This suggests that the pure LSTM model has poor generalization ability. In contrast, the proposed PI-LSTM model, which integrates Paris' Law with LSTM, demonstrates superior performance across all test samples, with RMSE values ranging between 0.04 and 0.9. The average RMSE values for PI-LSTM, pure LSTM, and Paris' Law are 0.498, 3.205, and 3.641, respectively. These results indicate that the PI-LSTM model developed in this study has higher prediction accuracy and better generalization ability than the other two methods. Figure 7.13(b) illustrates the comparison between experimental crack length and predicted crack length using S3 as the testing sample. In the figure, the red solid line represents the fitted regression line between the experimental and predicted crack length, and the black dashed line represents their perfect correlation. The close alignment of the fitted regression line with the ideal line suggests that the model possesses high prediction accuracy. The regression equation is $y = 1.065x - 0.024$ with $R^2 = 0.997$, further confirming the high accuracy of the PI-LSTM model in predicting FCG.

7.5 Summary

In Chapter 7, an SHM in-service baseline-free method for online crack detection and growth modelling with passive PZT sensors is proposed. Specifically, the online model for crack monitoring is developed by assessing the relative third-harmonic parameter $\hat{\gamma}'$ obtained from the vibration load in real-time during the experimental process, enabling in-service crack monitoring. The conclusions obtained from the present work can be drawn as follows:

An SHM early in-service crack detection: A DPL method was employed to automatically detect the crack in-service based on $\hat{\gamma}'$. Results obtained from four specimens demonstrate that the proposed method is capable of accurately detecting cracks of 1.3 mm to 1.9 mm remotely, in real-time during service, whereas the K-means clustering method detects cracks of 2.1 mm to 4.3 mm. This indicates that the proposed DPL method is more predictive than the K-means clustering method, enabling earlier detection of smaller cracks.

Robustness analysis: Results from specimen 5 with four sensors at different locations indicate that as the distance from the centerline increases, the detectable crack size also increases. Specifically, sensors 1 and 2, located on the centerline, detect cracks of 1.7 mm, whereas sensors 3 and 4, positioned further away, detect cracks of 6 mm and 9 mm, respectively. This indicates that the change in $\hat{\gamma}'$ is attributable to the crack, rather than other factors such as the inherent nonlinearity of electrical equipment or background noise. Additionally, it also demonstrates the relation between the detectable crack size and proximity to the sensors, concluding that this method is ideal for hot spot monitoring, as the sensors have to be close to the initiation site. In addition, results from specimen 6, tested under a different loading frequency, show that the proposed method can still automatically detect 1.6 mm cracks in real-time during service. The loading frequency does not affect the method's effectiveness.

Crack growth modelling: A physics-informed LSTM (PI-LSTM) model is developed to online quantify the crack size. First, the optimal parameter combination is obtained through hyperparameter optimization, and the leave-one-out cross-validation is then employed to evaluate the model's performance. Results show that the proposed PI-LSTM achieves an average RMSE of 0.498 mm on six datasets. In contrast, the pure LSTM and traditional Paris' Law methods yield RMSE values of 3.205 mm, and 3.641 mm, respectively. This indicates that the proposed PI-LSTM has

better accuracy and generalization ability compared to traditional pure LSTM models and Paris' Law methods.

Overall, the proposed baseline-free method provides a new perspective on in-service solutions for the maintenance and safety of engineering structures. Future studies will focus on applying the method to more complex structures, such as stiffened plates, and examine the effect of environmental variations, such as temperature, on the method's performance.

Chapter 8

Conclusions and Future Work

8.1 Conclusions

The research reported in this thesis systematically developed and evaluated a series of innovative methodologies for SHM, focusing on damage detection, localization, and crack growth modelling under varying environmental and operational conditions. By integrating vibration- and guided-wave-based methods and leveraging the multifunctionality of PZT transducers, this research addressed key challenges in SHM, including sensitivity to minor damage, reliance on baseline data, and robustness to temperature variations. The main findings are summarized as follows:

1. **Hybrid Damage Detection and Localization** A hybrid SHM approach combining vibration and guided-wave responses was proposed and validated for damage detection and localization in aluminium plates. The results demonstrated that the hybrid method outperformed individual vibration-based and guided-wave-based approaches in localization accuracy. Specifically, the hybrid method achieved an average Minimum Normalized Distance (MND) of 0.79 cm, with the minimum MND reaching 0.38 cm. In comparison, the guided-wave-based method yielded an average MND of 0.91 cm, while the vibration-based method resulted in an average MND of 2.05 cm. These results highlight the advantage of integrating complementary techniques to improve the accuracy and robustness of SHM systems.

2. **Temperature-Insensitive Damage Detection** A vibration-based SHM method utilizing TFs was developed for damage detection in aluminum and composite plates under varying

temperature conditions. Unlike prior approaches that emphasize the integration of different sensing techniques, this methodology represents a conceptual integration by leveraging the response of PZT transducers for modal analysis. The method achieved 100% detection accuracy in both isotropic and anisotropic materials across wide temperature ranges without requiring temperature compensation. For the isotropic aluminum plate, the smallest detectable damage size was 0.28% under a 10°C variation and 1.12% under a 40°C variation. These results highlight the effectiveness of TF analysis in mitigating temperature effects, providing a robust and reliable solution for SHM under dynamic environmental conditions.

3. **Comparative Evaluation of SHM Methods** The thesis conducted a comprehensive evaluation of linear guided wave, nonlinear guided wave, and vibration-based methods for progressive damage monitoring under varying temperature conditions. Unlike previous studies that primarily relied on simulated damage, this research validated the proposed methods using real damage (fatigue crack), ensuring practical relevance and robustness. Additionally, it provided a more thorough comparison of existing SHM techniques, offering valuable insights into their respective strengths and limitations. The findings demonstrated that nonlinear guided wave methods excel in detecting early-stage damage, while vibration-based methods exhibit greater stability under fluctuating temperatures. This dual validation and comparison highlight the importance of hybrid approaches that integrate the strengths of these methods, overcoming their individual limitations and enhancing their practical applicability in complex and dynamic environments.

4. **Baseline-Free fatigue crack monitoring** A novel baseline-free methodology for online crack detection and FCG modeling is proposed, leveraging the second-harmonic parameter $\hat{\beta}'$, which is calculated from the ratio of the amplitude of the fundamental frequency (A_1) to the square of the second harmonic component (A_2) under cyclic fatigue loading. The method achieves real-time crack detection without requiring a baseline signal from the pristine condition of the structure, thereby avoiding false alarms due to environmental or operational condition changes. Experimental results demonstrate that $\hat{\beta}'$ exhibits a distinct increase when fatigue life reaches approximately 80%, corresponding to a crack size below 2 mm, indicating its sensitivity to early-stage crack growth. The proposed FCG model is established

via quadratic polynomial fitting, without prior knowledge of the initial crack size or initiation time. All experimental and predicted data fall within the 95% confidence interval, with RMSE values of 0.9 mm and 1.2 mm on the left and right sides, respectively. Robustness analyses using different sensor placements confirm the stability of $\hat{\beta}'$ as a crack-sensitive parameter. Crack detection and modeling results using data from different sensors yield RMSE values within 1.1–1.4 mm.

5. **In-service fatigue crack detection and growth modeling** An advanced baseline-free method for online SHM is presented using the third-harmonic parameter $\hat{\gamma}'$, extracted from the real-time response to operational vibration loading. A DPL method is developed for automated in-service crack detection. Experimental validation across six specimens shows that this method can detect cracks as small as 1.3 mm to 1.9 mm, significantly outperforming traditional K-means clustering, which detects cracks no smaller than 2.1 mm. The method's robustness is verified by sensor placement and loading frequency variation: sensors near the centerline consistently detect smaller cracks (1.6–1.7 mm), while those further away detect larger cracks (up to 9 mm), confirming that $\hat{\gamma}'$ is a valid crack-sensitive indicator and reinforcing the importance of sensor proximity for hot spot monitoring. Furthermore, a PI-LSTM model is proposed for real-time crack growth quantification. The PI-LSTM model achieves an average RMSE of 0.498 mm across six datasets, outperforming conventional LSTM (3.205 mm) and Paris' Law-based models (3.641 mm). These results demonstrate the accuracy and generalizability of the third-harmonic-based approach.

In conclusion, this thesis contributes to the advancement of structural health monitoring (SHM) technologies by addressing critical challenges such as environmental variation, baseline dependency, and real-time monitoring. The proposed methodologies demonstrate significant improvements in damage detection sensitivity, localization accuracy, and robustness under practical conditions, laying a solid foundation for real-world applications in engineering structures. While the methods have been validated primarily on aerospace-related specimens, their underlying principles—particularly the use of frequency response features, nonlinear guided waves, and physics-informed learning—are broadly applicable. These techniques hold strong potential for extension to other critical infrastructures such as wind turbine blades, offshore energy platforms, pipelines, and civil structures,

where similar challenges in damage detection under varying operational and environmental conditions exist. Future work will explore adapting the proposed framework to these domains, enabling scalable, data-efficient, and baseline-free SHM solutions across a wider range of engineering applications.

The key numerical findings reported in this thesis further substantiate the practical applicability of the proposed methodologies. For example, the hybrid damage localization approach achieved a minimum localization error (MND) of 0.38 cm, which demonstrates high spatial resolution suitable for small- to medium-scale structural components requiring precise fault identification. The temperature-insensitive TF-based method achieved 100% detection accuracy across a 40°C temperature variation, confirming its robustness for use in variable and outdoor environments. The baseline-free second- and third-harmonic methodologies were capable of detecting fatigue cracks as small as 1.3 mm and achieved crack length prediction root mean square errors (RMSE) below 1.4 mm, highlighting their effectiveness for early-stage damage detection and quantitative prognosis. Furthermore, the physics-informed LSTM model outperformed conventional LSTM and Paris' law-based models, achieving an average RMSE of 0.498 mm—representing a six-fold improvement in prediction accuracy. In summary, these results demonstrate the robustness, accuracy, and generalizability of the developed framework, indicating its strong potential for deployment in real-world SHM scenarios across various engineering domains.

8.2 Future Work

While this research has advanced the field of SHM, further efforts are necessary to enhance the applicability and robustness of the proposed methodologies. The following key directions are identified for future work:

1. **Validation on Complex Structures and Diverse Damage Scenarios**

   The methodologies developed in this study have primarily been validated on simple geometries, such as flat plates, and focused on cracks. Future research should extend these validations to more complex structural geometries, including stiffened panels, curved components, and aerospace-grade configurations. Additionally, the applicability of these methods

should be explored for other damage scenarios, such as delamination in composite materials and corrosion-induced degradation. These studies will provide a more comprehensive assessment of the robustness and versatility of the proposed approaches across diverse engineering applications.

2. **Investigation of Practical Environmental and Operational Factors**

   The proposed baseline-free methodology shows promise for in-service applications but requires further investigation to account for critical operational and environmental factors. Parameters such as loading ratio, loading magnitude, and varying dynamic loads may influence its performance and must be systematically studied. Additionally, environmental conditions, including temperature fluctuations and humidity, could introduce variability in the SHM response. Preliminary results suggest that variations in loading ratio and test frequency do not significantly affect the performance of the proposed method. Nevertheless, further validation is being conducted using multi-loading block tests to ensure robustness under different loading conditions. Furthermore, although the method is built on frequency response characteristics that are generally material- and geometry-independent, future studies will also focus on extending the framework to different structural materials and more complex geometries. This will allow for a more comprehensive assessment of its reliability and repeatability across diverse real-world scenarios. Future work should focus on developing advanced compensation models and adaptive strategies to mitigate these effects, ensuring reliable performance in real-world applications.

3. **Development of Autonomous SHM Systems**

   A critical direction for future research is the development of fully autonomous SHM systems capable of real-time damage detection and quantification without human intervention. These systems should integrate sensing, data processing, and decision-making capabilities into a cohesive framework. Leveraging advanced technologies such as edge computing, the IoTs, and artificial intelligence, these systems should aim to optimize operational efficiency, reduce power consumption, and enable seamless deployment in complex engineering environments.

Additionally, any simulation tools used to support the experimental findings should be further

refined by considering potential uncertainties in model assumptions, boundary conditions, and material properties. Future research may explore incorporating uncertainty quantification techniques into the simulation framework to better align model predictions with real-world variability. By pursuing these research directions, the methodologies proposed in this thesis can be refined and extended, advancing the development of innovative SHM solutions that effectively address the challenges posed by complex structures, environmental variability, and autonomous operation.

Bibliography

[1] Nan Yue. *Stochastic analysis of guided wave structural health monitoring for aeronautical composites*. PhD thesis, Imperial College London, 2020.

[2] C. Brand and C. Boller. Identification of life cycle cost reduction in structures with self-diagnostic devices. In *NATO RTO Symposium on Design for Low Cost Operation and Support*, Ottawa, Canada, October 1999.

[3] G. Totten. Fatigue crack propagation. *Adv Mater Processes*, 166:39, 2008.

[4] Y. Pan, P. Zhou, Y. Yan, A. Agrawal, Y. Wang, D. Guo, and S. Jain. New insights into the methods for predicting ground surface roughness in the age of digitalisation. *Precis Eng*, 67:393–418, 2021.

[5] I. Dayyani, A.D. Shaw, E.I. Saavedra Flores, and M.I. Friswell. The mechanics of composite corrugated structures: A review with applications in morphing aircraft. *Composite Structures*, 133:358–380, 2015.

[6] K. Sinha, T. Klimmek, M. Schulze, and V. Handojo. Loads analysis and structural optimization of a high aspect ratio, composite wing aircraft. *CEAS Aeronautical Journal*, 12:233–243, 2021.

[7] C. V. Oster, J.S. Strong, and C.K. Zorn. Analyzing aviation safety: Problems, challenges, opportunities. *Research in Transportation Economics*, 43:148–164, 2013.

[8] A. Arias, C.E. Nika, V. Vasilaki, G. Feijoo, M.T. Moreira, and E. Katsou. Assessing the future prospects of emerging technologies for shipping and aviation biofuels: A critical review. *Renewable and Sustainable Energy Reviews*, 197:114427, 2024.

[9] M. Gupta, M.A. Khan, R. Butola, and R.M. Singari. Advances in applications of non-destructive testing (ndt): A review. *Advances in Materials and Processing Technologies*, 8:2286–2307, 2022.

[10] S. Gholizadeh. A review of non-destructive testing methods of composite materials. *Procedia Structural Integrity*, 1:50–57, 2016.

[11] Q.Y. Lu and C.H. Wong. Applications of non-destructive testing techniques for post-process control of additively manufactured parts. *Virtual and Physical Prototyping*, 12:301–321, 2017.

[12] M. Jolly, A. Prabhakar, B. Sturzu, K. Hollstein, R. Singh, S. Thomas, P. Foote, and A. Shaw. Review of non-destructive testing (ndt) techniques and their applicability to thick walled composites. *Procedia CIRP*, 38:129–136, 2015.

[13] M. Inês Silva, E. Malitckii, T.G. Santos, and P. Vilaça. Review of conventional and advanced non-destructive testing techniques for detection and characterization of small-scale defects. *Progress in Materials Science*, 138:101155, 2023.

[14] B. Wang, S. Zhong, T.L. Lee, K.S. Fancey, and J. Mi. Non-destructive testing and evaluation of composite materials/structures: A state-of-the-art review. *Advances in Mechanical Engineering*, 12, 2020.

[15] Y. He, F. Luo, M. Pan, F. Weng, X. Hu, J. Gao, and B. Liu. Pulsed eddy current technique for defect detection in aircraft riveted structures. *NDT & E International*, 43:176–181, 2010.

[16] F. Ciampa, P. Mahmoodi, F. Pinto, and M. Meo. Recent advances in active infrared thermography for non-destructive testing of aerospace components. *Sensors*, 18:609, 2018.

[17] M.G.R. Sause and E. Jasiūnienė. *Structural Health Monitoring Damage Detection Systems for Aerospace*. Springer, 2021.

[18] N. Yue, Z.S. Khodaei, and M.H. Aliabadi. Damage detection in large composite stiffened panels based on a novel shm building block philosophy. *Smart Materials and Structures*, 30, 2021.

[19] B. Francisco. *Structural Health Monitoring of Complex Composite Structures under Environmental and Operational Conditions*. PhD thesis, Imperial College London, 2023.

[20] J.S. Hwang, J.M. Müller, R. Loendersloot, and T. Tinga. Modal strain energy-based structural health monitoring validation on rib stiffened composite panels. *Composite Structures*, 26:43–51, 2017.

[21] C. Xu. *Condition monitoring of composite structure with Fibre Optic Sensors Declaration of Originality*. PhD thesis, Imperial College London, 2022.

[22] D. García, I. Trendafilova, and D.J. Inman. A study on the vibration-based self-monitoring capabilities of nano-enriched composite laminated beams. *Smart Materials and Structures*, 25:045011, 2016.

[23] H. Fu, Z. Sharif-Khodaei, and M.H.F. Aliabadi. An energy-efficient cyber-physical system for wireless on-board aircraft structural health monitoring. *Mechanical Systems and Signal Processing*, 128:352–368, 2019.

[24] W.J. Staszewski, S. Mahzan, and R. Traynor. Health monitoring of aerospace composite structures – active and passive approach. *Composite Science and Technology*, 69:1678–1685, 2009.

[25] A.H. Seno. *Passive Sensing of Low Velocity Impact Damage on Composite Panels in Simulated Environmental and Operational Conditions Declaration of Originality*. PhD thesis, Imperial College London, 2021.

[26] E. Rabiei, E.L. Droguett, and M. Modarres. Damage monitoring and prognostics in composites via dynamic bayesian networks. In *Proceedings - Annual Reliability and Maintainability Symposium*, 2017.

[27] Z. Su and L. Ye. Lamb wave-based quantitative identification of delamination in cf/ep composite structures using artificial neural algorithm. *Composite Structures*, 66:627–637, 2004.

[28] W.J. Yan, D. Chronopoulos, S. Cantero-Chinchilla, K.V. Yuen, and C. Papadimitriou. A fast bayesian inference scheme for identification of local structural properties of layered composites based on wave and finite element-assisted metamodeling strategy and ultrasound measurements. *Mechanical Systems and Signal Processing*, 143:106802, 2020.

[29] G. Dib, O. Karpenko, E. Koricho, A. Khomenko, M. Haq, and L. Udpa. Ensembles of novelty detection classifiers for structural health monitoring using guided waves. *Smart Materials and Structures*, 27:015003, 2017.

[30] Y. Yu, C. Wang, X. Gu, and J. Li. A novel deep learning-based method for damage identification of smart building structures. *Structural Health Monitoring*, 18:143–163, 2019.

[31] C. Kralovec and M. Schagerl. Review of structural health monitoring methods regarding a multi-sensor approach for damage assessment of metal and composite structures. *Sensors*, 20:826, 2020.

[32] M. Mitra and S. Gopalakrishnan. Guided wave based structural health monitoring: A review. *Smart Materials and Structures*, 25:053001, 2016.

[33] I. Negru, G.R. Gillich, Z.I. Praisach, M. Tufoi, and N. Gillich. Natural frequency changes due to damage in composite beams. *Journal of Physics: Conference Series*, 628:012091, 2015.

[34] T Huang, M Chaves-Vargas, J Yang, and K-U Schröder. A baseline-free damage detection method based on node displacement in mode shape. In *Proceedings of SPIE - The International Society for Optical Engineering*, volume 11382, page 1138211, 2020.

[35] R.P. Bandara, T.H. Chan, and D.P. Thambiratnam. Structural damage detection method using frequency response functions. *Structural Health Monitoring*, 13:418–429, 2014.

[36] A. Nayyar, U. Baneen, M. Ahsan, S.A.Z. Naqvi, and A. Israr. Damage detection based on output-only measurements using cepstrum analysis and a baseline-free frequency response function curvature method. *Science Progress*, pages 1–25, 2022.

[37] Y Pan, Z S Khodaei, and M H Aliabadi. A hybrid method based on vibration and guided waves for damage detection and localization. In *Procedia Struct. Integr*, volume 52, pages 699–708, 2024.

[38] Yuhang Pan, Zahra Sharif Khodaei, and M.H. Aliabadi. A robust hybrid method for damage detection under varying environmental conditions. *Structural Health Monitoring*, 52:699–708, 2024.

[39] Y. Pan, Z. Sharif Khodaei, and M.H.F. Aliabadi. Online fatigue crack detection and growth modelling through higher harmonic analysis: A baseline-free approach. *Mech Syst Signal Process*, 224:112167, 2025.

[40] Yuhang Pan, Zahra Sharif Khodaei, and Ferri M.H. Aliabadi. In-service fatigue crack monitoring through baseline-free automated detection and physics-informed neural network quantification. *NDT & E International*, 153:103360, 2025.

[41] Z. Su, C. Zhou, M. Hong, L. Cheng, Q. Wang, and X. Qing. Acousto-ultrasonics-based fatigue damage characterization: Linear versus nonlinear signal features. *Mechanical Systems and Signal Processing*, 45:225–239, 2014.

[42] C. Espinoza, D. Feliu, C. Aguilar, R. Espinoza-Gonzalez, F. Lund, V. Salinas, and N. Mujica. Linear versus nonlinear acoustic probing of plasticity in metals: A quantitative assessment. *Materials*, 11:2217, 2018.

[43] M. Rautela and S. Gopalakrishnan. Ultrasonic guided wave based structural damage detection and localization using model assisted convolutional and recurrent neural networks. *Expert Systems with Applications*, 167:114189, 2021.

[44] P. Duffour, M. Morbidini, and P. Cawley. A study of the vibro-acoustic modulation technique for the detection of cracks in metals. *Journal of the Acoustical Society of America*, 119:1463, 2006.

[45] Z. Parsons and W.J. Staszewski. Nonlinear acoustics with low-profile piezoceramic excitation for crack detection in metallic structures. *Smart Materials and Structures*, 15:1110, 2006.

[46] F. Aymerich and W.J. Staszewski. Impact damage detection in composite laminates using nonlinear acoustics. *Composites Part A: Applied Science and Manufacturing*, 41:1084–1092, 2010.

[47] Horace Lamb. On waves in an elastic plate. *Proceedings of the Royal Society of London. Series A, Containing Papers of a Mathematical and Physical Character*, 93:114–128, 1917.

[48] J.L. Rose. *Ultrasonic Guided Waves in Solid Media*. Cambridge University Press, 2014.

[49] A. Linke. On the role of the helmholtz decomposition in mixed methods for incompressible flows and a new variational crime. *Computer Methods in Applied Mechanics and Engineering*, 268:782–800, 2014.

[50] Zhongqing Su and Lin Ye. *Identification of Damage Using Lamb Waves: From Fundamentals to Applications*. Springer, n.d.

[51] K. Worden. Rayleigh and lamb waves - basic principles. *Strain*, 37:167–172, 2001.

[52] N. Yue, Z. S. Khodaei, and M. H. Aliabadi. An innovative secondary bonding of sensors to composite structures for shm application. *Key Eng Mater*, 774:516–522,, 2018.

[53] J.E. Michaels, S.J. Lee, A.J. Croxford, and P.D. Wilcox. Chirp excitation of ultrasonic guided waves. *Ultrasonics*, 53:265–270, 2013.

[54] K.J.C.J. Lissenden, I. Solodov, and Y. Ohara. *Springer Series in Measurement Science and Technology: Measurement of Nonlinear Ultrasonic Characteristics*. Springer, 2021.

[55] J. Chen, C.L. Hu, F. Kong, and J.G. Mao. High-performance second-harmonic-generation (shg) materials: New developments and new strategies. *Accounts of Chemical Research*, 54:2775–2783, 2021.

[56] J.-Y. Kim, L.J. Jacobs, J. Qu, and J.W. Littles. Experimental characterization of fatigue damage in a nickel-base superalloy using nonlinear ultrasonic waves. *Journal of the Acoustical Society of America*, 120:1266–1273, 2006.

[57] M. Hong, Z. Su, Q. Wang, L. Cheng, and X. Qing. Modeling nonlinearities of ultrasonic waves for fatigue damage characterization: Theory, simulation, and experimental validation. *Ultrasonics*, 54:770–778, 2014.

[58] W.J.N. De Lima and M.F. Hamilton. Finite-amplitude waves in isotropic elastic plates. *Journal of Sound and Vibration*, 265:819–839, 2003.

[59] Yongtak Kim, Hyung Jin Lim, and Hoon Sohn. Nonlinear ultrasonic modulation based failure warning for aluminum plates subject to fatigue loading. *International Journal of Fatigue*, 114:130–137, 2018.

[60] R.B. Thompson, O. Buck, and D.O. Thompson. Higher harmonics of finite amplitude ultrasonic waves in solids. *Journal of the Acoustical Society of America*, 59:1087–1094, 1976.

[61] G. Gutiérrez-Vargas, A. Ruiz, J.Y. Kim, and L.J. Jacobs. Characterization of thermal embrittlement in 2507 super duplex stainless steel using nonlinear acoustic effects. *NDT & E International*, 94:101–108, 2018.

[62] K.H. Matlack, J.Y. Kim, L.J. Jacobs, and J. Qu. Review of second harmonic generation measurement techniques for material state determination in metals. *Journal of Nondestructive Evaluation*, 34:1–23, 2014.

[63] S.-J. Bang, D.-G. Song, and K.-Y. Jhang. Comparisons of second- and third-order ultrasonic nonlinearity parameters measured using through-transmission and pulse-echo methods. *NDT & E International*, 133:102757, 2023.

[64] J. Kim, D.G. Song, and K.Y. Jhang. Absolute measurement and relative measurement of ultrasonic nonlinear parameters. *Research in Nondestructive Evaluation*, 28:211–225, 2017.

[65] C. Pruell, J.Y. Kim, J. Qu, and L.J. Jacobs. Evaluation of plasticity driven material damage using lamb waves. *Applied Physics Letters*, 91:231911, 2007.

[66] Y. Liu, V.K. Chillara, and C.J. Lissenden. On selection of primary modes for generation of strong internally resonant second harmonics in plate. *J Sound Vib.*, 332(19):4517–4528,, 2013.

[67] C. Bermes, J.Y. Kim, J. Qu, and L.J. Jacobs. Nonlinear lamb waves for the detection of material nonlinearity. *Mechanical Systems and Signal Processing*, 22:638–646, 2008.

[68] A. Srivastava and F. Lanza di Scalea. On the existence of antisymmetric or symmetric lamb waves at nonlinear higher harmonics. *Journal of Sound and Vibration*, 323:932–943, 2009.

[69] M.F. Müller, J.-Y. Kim, J. Qu, and L.J. Jacobs. Characteristics of second harmonic generation of lamb waves in nonlinear elastic plates. *Journal of the Acoustical Society of America*, 127:2141–2152, 2010.

[70] N. Matsuda and S. Biwa. Phase and group velocity matching for cumulative harmonic generation in lamb waves. *Journal of Applied Physics*, 109, 2011.

[71] V.K. Chillara and C.J. Lissenden. Interaction of guided wave modes in isotropic weakly nonlinear elastic plates: Higher harmonic generation. *Journal of Applied Physics*, 111, 2012.

[72] Y. Lu and J.E. Michaels. Feature extraction and sensor fusion for ultrasonic structural health monitoring under changing environmental conditions. *IEEE Sensors Journal*, 9:1462–1471, 2009.

[73] S. Talaei, F. Khoshnoudian, and S. Talaei. A new damage index using frf data, 2d-pca method and pattern recognition techniques. *International Journal of Structural Stability and Dynamics*, 2016.

[74] C. Zang and M. Imregun. Structural damage detection using artificial neural networks and measured frf data reduced via principal component projection. *Journal of Sound and Vibration*, 242:813–827, 2001.

[75] K.H. Padil, N. Bakhary, M. Abdulkareem, J. Li, and H. Hao. Non-probabilistic method to consider uncertainties in frequency response function for vibration-based damage detection using artificial neural network. *Journal of Sound and Vibration*, 467:115069, 2020.

[76] V Meruane. Online sequential extreme learning machine for vibration-based damage assessment using transmissibility data. *J Comput Civil Eng*, 30(3):04015042, 2016.

[77] Ayisha Nayyar, Ummul Baneen, Syed Abbas Zilqurnain Naqvi, and Muhammad Ahsan. Detection and localization of multiple small damages in beam. *Adv Mech Eng*, 13(1):1–14, 2021.

[78] R.P. Bandara, T.H.T. Chan, and D.P. Thambiratnam. Frequency response function based damage identification using principal component analysis and pattern recognition technique. *Engineering Structures*, 66:116–128, 2014.

[79] Rosette Niyirora, Wei Ji, Elyse Masengesho, Jean Munyaneza, Ferdinand Niyonyungu, and Ritha Nyirandayisabye. Intelligent damage diagnosis in bridges using vibration-based monitoring approaches and machine learning: A systematic review. *Results in Engineering*, 16:100761, 2022.

[80] W. Fan and P. Qiao. Vibration-based damage identification methods: A review and comparative study. *Structural Health Monitoring*, 10(1):83–111, 2011.

[81] P. Gudmundson. Eigenfrequency changes of structures due to cracks, notches or other geometrical changes. *Journal of the Mechanics and Physics of Solids*, 30:339–353, 1982.

[82] R. Y. Liang, J. L. Hu, and F. Choy. Theoretical study of crack-induced eigenfrequency changes on beam structures. *Journal of Engineering Mechanics-ASCE*, 118:384–396, 1992.

[83] A. Morassi. Crack-induced changes in eigenparameters of beam structures. *Journal of Engineering Mechanics-ASCE*, 119:1798–1803, 1993.

[84] D. G. Kasper, D. C. Swanson, and K. M. Reichard. Higher-frequency wavenumber shift and frequency shift in a cracked, vibrating beam. *Journal of Sound and Vibration*, 312:1–18, 2008.

[85] Alireza Arabha, Farhad Daneshjoo, and Hamid Reza Ahmadi. Multiple damage detection in complex bridges based on strain energy extracted from single point measurement. *Frontiers of Structural and Civil Engineering*, 14(3):722–730, 2020.

[86] Z. Shang, L. Sun, Y. Xia, and W. Zhang. Vibration-based damage detection for bridges by deep convolutional denoising autoencoder. *Structural Health Monitoring*, 20(4):1880–1903, 2021.

[87] Shuqing Wang and Mingqiang Xu. Modal strain energy-based structural damage identification: A review and comparative study. *Structural Engineering International*, 29(2):234–248, 2019.

[88] Z. X. Tan, D. P. Thambiratnam, T. H. T. Chan, M. Gordan, and H. Abdul Razak. Damage detection in steel-concrete composite bridge using vibration characteristics and artificial neural network. *Structure and Infrastructure Engineering*, 16(9):1247–1261, 2020.

[89] Z. X. Tan, D. P. Thambiratnam, T. H. T. Chan, and H. Abdul Razak. Detecting damage in steel beams using modal strain energy based damage index and artificial neural network. *Engineering Failure Analysis*, 79:253–262, 2017.

[90] A. K. Pandey and M. Biswas. Damage detection in structures using changes in flexibility. *Journal of Sound and Vibration*, 169:3–17, 1994.

[91] W. R. Wickramasinghe, D. P. Thambiratnam, and T. H. T. Chan. Damage detection in a suspension bridge using modal flexibility method. *Engineering Failure Analysis*, 107:104194, 2020.

[92] A. C. Altunışık, F. Y. Okur, S. Karaca, and V. Kahya. Vibration-based damage detection in beam structures with multiple cracks: Modal curvature vs. modal flexibility methods. *Nondestructive Testing and Evaluation*, pages 1–21, 2018.

[93] S. Lei, K. Mao, L. Li, W. Xiao, and B. Li. Sensitivity analysis of modal assurance criteria of damped systems. *Journal of Vibration and Control*, 2015.

[94] Yaozong Ma, Qian Zou, and Longlin Wang. Supporting condition evaluation method of cable-stayed bridges based on modal assurance criterion. In *IOP Conference Series: Earth and Environmental Science*, volume 719, page 032059. IOP Publishing, 2021.

[95] Szymon Greś, Michael Döhler, and Laurent Mevel. Uncertainty quantification of the modal assurance criterion in operational modal analysis. *Mechanical Systems and Signal Processing*, 152:107457, 2021.

[96] J. Ciambella, A. Pau, and F. Vestroni. Modal curvature-based damage localization in weakly damaged continuous beams. *Mechanical Systems and Signal Processing*, 121:171–182, 2019.

[97] J. Sirohi and I. Chopra. Fundamental behavior of piezoceramic sheet actuators. *Journal of Intelligent Material Systems and Structures*, 11(1):47–61, 2000.

[98] C. Liang, F. P. Sun, and C. A. Rogers. Coupled electro-mechanical analysis of adaptive material systems—determination of the actuator power consumption and system energy transfer. *Journal of Intelligent Material Systems and Structures*, 8(4):335–343, 1997.

[99] J. S. Knopp, J. C. Aldrin, and K. V. Jata. Computational methods in eddy current crack detection at fastener sites in multi-layer structures. *Nondestruct Test Eval*, 24:103–20, 2009.

[100] Ling Zhang and Bo Zhang. A geometrical representation of mcculloch-pitts neural model and its applications. *IEEE Transactions on Neural Networks*, 10(4):939–945, July 1999.

[101] Yuko Munakata and Jason Pfaffly. Hebbian learning and development. *Developmental Science*, 7(2):141–148, 2004.

[102] Derek A. Pisner and David M. Schnyer. Chapter 6 - support vector machine. In *Machine Learning: Methods and Applications to Brain Disorders*, pages 101–121. Academic Press, 2020.

[103] Y. Pan, Y. Wang, P. Zhou, Y. Yan, and D. Guo. Activation functions selection for bp neural network model of ground surface roughness. *J Intell Manuf*, 31:1825–1836, 2020.

[104] Jiuxiang Gu, Zhenhua Wang, Jason Kuen, Lianyuan Ma, Amir Shahroudy, Bing Shuai, Ting Liu, Xingxing Wang, Gang Wang, Jianfei Cai, and Tsuhan Chen. Recent advances in convolutional neural networks. *Pattern Recognition*, 77:354–377, May 2018.

[105] Hessam Amanollah, Arghavan Asghari, Mohammadreza Mashayekhi, and Seyed Mehdi Zahrai. Damage detection of structures based on wavelet analysis using improved alexnet. *Structures*, 56:105019, October 2023.

[106] Haroon Malik, Ammar Alzarrad, and Elhadi Shakshuki. Payload assisted unmanned aerial vehicle structural health monitoring (uavshm) for active damage detection. *Procedia Computer Science*, 210:78–85, 2022.

[107] X. Qing, Y. Liao, Y. Wang, B. Chen, F. Zhang, and Y. Wang. Machine learning based quantitative damage monitoring of composite structure. *Structural Health Monitoring*, 13(2):167–202, 2022.

[108] G. Toh and J. Park. Review of vibration-based structural health monitoring using deep learning. *Applied Sciences*, 10(5):1680, 2020.

[109] F. Ricci, E. Monaco, N. D. Boffa, L. Maio, and V. Memmolo. Guided waves for structural health monitoring in composites: A review and implementation strategies. *Progress in Aerospace Sciences*, 129:100790, 2022.

[110] I. N. Giannakeas, Z. Sharif Khodaei, and M. H. Aliabadi. An up-scaling temperature compensation framework for guided wave–based structural health monitoring in large composite structures. *Structural Health Monitoring*, 22(2):777–798, 2023.

[111] F. Lambinet and Z. Sharif Khodaei. Measurement platform for structural health monitoring application of large scale structures. *Measurement*, 190:110675, February 2022.

[112] Y. Pan, Y. Qiao, Y. Wang, X. Liu, and P. Zhou. Real-time prediction of grinding surface roughness based on multi-sensor signal fusion. *The International Journal of Advanced Manufacturing Technology*, 127:5847–5861, 2023.

[113] N Yue and M H Aliabadi. A scalable data-driven approach to temperature baseline reconstruction for guided wave structural health monitoring of anisotropic carbon-fiber-reinforced polymer structures. *Struct Health Monit*, 19(5):1487–1506, 2020.

[114] Y Lu and J E Michaels. A methodology for structural health monitoring with diffuse ultrasonic waves in the presence of temperature variations. *Ultrasonics*, 43(10):717–731, 2005.

[115] A J Croxford, J Moll, P D Wilcox, and J E Michaels. Efficient temperature compensation strategies for guided wave structural health monitoring. *Ultrasonics*, 50:517–528, 2010.

[116] J E Michaels and T E Michaels. Detection of structural damage from the local temporal coherence of diffuse ultrasonic signals. *IEEE Trans Ultrason Ferroelectr Freq Control*, 52(10):1769–1782, 2005.

[117] G Liu, Y Xiao, H Zhang, and G Ren. Baseline signal reconstruction for temperature compensation in lamb wave-based damage detection. *Sensors*, 16(8):1273, 2016.

[118] C R Farrar and G H James. System identification from ambient vibration measurements on a bridge. *J Sound Vib*, 205(1):1–18, 1997.

[119] R D Adams and J Coppendale. Measurement of the elastic moduli of structural adhesives by a resonant bar technique. In *Journal of Mechanical Engineering Science*, volume 18, pages 149–158, 1976.

[120] O S Salawu. Detection of structural damage through changes in frequency: a review. *Eng Struct*, 19(9):718–723, 1997.

[121] R Zhao, R Yan, Z Chen, K Mao, P Wang, and R X Gao. Deep learning and its applications to machine health monitoring. *Mech Syst Signal Pro*, 115:213–237, 2019.

[122] W Zhang, C Li, G Peng, Y Chen, and Z Zhang. A deep convolutional neural network with new training methods for bearing fault diagnosis under noisy environment and different working load. *Mech Syst Signal Pro*, 100:439–453, 2018.

[123] A. Khan, D. K. Ko, S. C. Lim, and H. S. Kim. Structural vibration-based classification and prediction of delamination in smart composite laminates using deep learning neural network. *Composites Part B: Engineering*, 161:586–594, 2019.

[124] G. Minak, R. Palazzetti, I. Trendafilova, and A. Zucchelli. Localization of a delamination and estimation of its length in a composite laminate beam by the vshm and pattern recognition methods. *Mechanics of Composite Materials*, 46(4):387–394, 2010.

[125] P. Castellini and G. Marco Revel. Experimental technique for structural diagnostic based on laser vibrometry and neural networks. *Shock and Vibration*, 7(6):381–397, 2000.

[126] Sahar Hassani, Mohsen Mousavi, and Amir H. Gandomi. Structural health monitoring in composite structures: A comprehensive review. *Sensors*, 22(1):153, 2022.

[127] B T Wang and C C Wang. Feasibility analysis of using piezoceramic transducers for cantilever beam modal testing. *Smart Mater Struct*, 6:106–113, 1997.

[128] F Zonzini, M M Malatesta, D Bogomolov, N Testoni, A Marzani, and L De Marchi. Vibration-based shm with upscalable and low-cost sensor networks. *IEEE Trans Instrum Meas*, 69(10):7990–7998, 2020.

[129] T J Johnson, R L Brown, D E Adams, and M Schiefer. Distributed structural health monitoring with a smart sensor array. *Mech Syst Signal Pro*, 18(3):555–572, 2004.

[130] T J Johnson and D E Adams. Transmissibility as a differential indicator of structural damage. In *Proceedings of the 6th International Workshop on Structural Health Monitoring*, pages 47907–1077, 2002.

[131] C Devriendt and P Guillaume. The use of transmissibility measurements in output-only modal analysis. *Mech Syst Signal Pro*, 21(7):2689–2696, 2007.

[132] W J Yan and W X Ren. An enhanced power spectral density transmissibility (epsdt) approach for operational modal analysis: Theoretical and experimental investigation. *Eng Struct*, 102:108–119, 2015.

[133] W J Yan and W X Ren. Operational modal parameter identification from power spectrum density transmissibility. *Comput-Aided Civ Inf*, 27(3):202–217, 2012.

[134] D D Mandal and S Banerjee. Identification of breathing type disbonds in stiffened panels using non-linear lamb waves and built-in circular pwt array. *Mech Syst Signal Pr*, 117:33–51, 2019.

[135] W J Yan, D Chronopoulos, K V Yuen, and Y C Zhu. Structural anomaly detection based on probabilistic distance measures of transmissibility function and statistical threshold selection scheme. *Mech Syst Signal Pr*, 162:108009, 2022.

[136] N M M Maia, J M M Silva, and A M R Ribeiro. The transmissibility concept in multi-degree-of-freedom systems. *Mech Syst Signal Process*, 15(1):129–137, 2001.

[137] V Meruane. Model updating using antiresonant frequencies identified from transmissibility functions. *J Sound Vib*, 332(4):807–820, 2013.

[138] D García and D Tcherniak. An experimental study on the data-driven structural health monitoring of large wind turbine blades using a single accelerometer and actuator. *Mech Syst Signal Pr*, 127:102–119, 2019.

[139] Francisco de Sá Rodrigues, Ilias N. Giannakeas, Zahra Sharif Khodaei, and Ferri M.H. Aliabadi. Probability based damage detection on a composite fuselage panel based on large data set of guided wave signals. *NDT and E Int*, 139:102924, 2023.

[140] F. Ren, I.N. Giannakeas, Z. Sharif Khodaei, and M.H.F. Aliabadi. The temperature effects on embedded pzt signals in structural health monitoring for composite structures with different thicknesses. *NDT and E Int*, 141:102988, 2024.

[141] F. Ren, I.N. Giannakeas, Z. Sharif Khodaei, and M.H.F. Aliabadi. Theoretical and experimental investigation of guided wave temperature compensation for composite structures with different thicknesses. *Mech Syst Signal Process*, 200:110594, 2023.

[142] E. Garcia-Macias and F. Ubertini. Real-time bayesian damage identification enabled by sparse pce-kriging meta-modelling for continuous shm of large-scale civil engineering structures. *Journal of Building Engineering*, 59:105004, 2022.

[143] M. Mishra, P.B. Lourenco, and G. V. Ramana. Structural health monitoring of civil engineering structures by using the internet of things: A review. *Journal of Building Engineering*, 48:103954, 2022.

[144] M. Martinez-Luengo, A. Kolios, and L. Wang. Structural health monitoring of offshore wind turbines: A review through the statistical pattern recognition paradigm. *Renewable and Sustainable Energy Reviews*, 64:91–105, 2016.

[145] M. Khazaee, P. Derian, and A. Mouraud. A comprehensive study on structural health monitoring (shm) of wind turbine blades by instrumenting tower using machine learning methods. *Renew Energy*, 199:1568–1579, 2022.

[146] M. Steczek, P. Chudzik, and A. Szelag. Combination of she- and shm-pwm techniques for vsi dc-link current harmonics control in railway applications. *IEEE Transactions on Industrial Electronics*, 64:7666–7678, 2017.

[147] I. Ahmad and F.U. Khan. Multi-mode vibration based electromagnetic type micro power generator for structural health monitoring of bridges. *Sens Actuators A Phys*, 275:154–161, 2018.

[148] I.N. Giannakeas, F. Mazaheri, O. Bacarreza, Z. Sharif Khodaei, and F.M.H. Aliabadi. Probabilistic residual strength assessment of smart composite aircraft panels using guided waves. *Reliab Eng Syst Saf*, 237:109338, 2023.

[149] P.S. Tua, S.T. Quek, and Q. Wang. Detection of cracks in plates using piezo-actuated lamb waves. *Smart Mater Struct*, 13:643–660, 2004.

[150] P. Kudela, W. Ostachowicz, and A. Zak. Damage detection in composite plates with embedded pzt transducers. *Mech Syst Signal Process*, 22:1327–1335, 2008.

[151] C. Ramadas, K. Balasubramaniam, M. Joshi, and C.V. Krishnamurthy. Interaction of guided lamb waves with an asymmetrically located delamination in a laminated composite plate. *Smart Mater Struct*, 19:065009, 2010.

[152] P. Kudela, M. Radzieński, and W. Ostachowicz. Identification of cracks in thin-walled structures by means of wavenumber filtering. *Mech Syst Signal Process*, 50–51:456–466, 2015.

[153] H. Liu and Y. Zhang. Deep learning based crack damage detection technique for thin plate structures using guided lamb wave signals. *Smart Mater Struct*, 29:015032, 2019.

[154] J. He, X. Guan, T. Peng, Y. Liu, A. Saxena, J. Celaya, and K. Goebel. A multi-feature integration method for fatigue crack detection and crack length estimation in riveted lap joints using lamb waves. *Smart Mater Struct*, 22:105007, 2013.

[155] A. Mardanshahi, V. Nasir, S. Kazemirad, and M.M. Shokrieh. Detection and classification of matrix cracking in laminated composites using guided wave propagation and artificial neural networks. *Compos Struct*, 246:112403, 2020.

[156] N. Yue and M.H. Aliabadi. Hierarchical approach for uncertainty quantification and reliability assessment of guided wave-based structural health monitoring. *Struct Health Monit*, 20:2274–2299, 2021.

[157] C. Yeung and C.T. Ng. Nonlinear guided wave mixing in pipes for detection of material nonlinearity. *J Sound Vib*, 485:115541, 2020.

[158] S. Sampath, J. Jang, and H. Sohn. Ultrasonic lamb wave mixing based fatigue crack detection using a deep learning model and higher-order spectral analysis. *Int J Fatigue*, 163:107028, 2022.

[159] T. Maruyama, T. Saitoh, and S. Hirose. Numerical study on sub-harmonic generation due to interior and surface breaking cracks with contact boundary conditions using time-domain boundary element method. *Int J Solids Struct*, 126–127:74–89, 2017.

[160] M. Zhang, L. Xiao, W. Qu, and Y. Lu. Damage detection of fatigue cracks under nonlinear boundary condition using subharmonic resonance. *Ultrasonics*, 77:152–159, 2017.

[161] N. Rauter, R. Lammering, and T. Kuhnrich. On the detection of fatigue damage in composites by use of second harmonic guided waves. *Compos Struct*, 152:247–258, 2016.

[162] Y. Yang, C.T. Ng, A. Kotousov, H. Sohn, and H.J. Lim. Second harmonic generation at fatigue cracks by low-frequency lamb waves: Experimental and numerical studies. *Mech Syst Signal Process*, 99:760–773, 2018.

[163] G. Zhao, M. Jiang, W. Li, Y. Luo, Q. Sui, and L. Jia. Early fatigue damage evaluation based on nonlinear lamb wave third-harmonic phase velocity matching. *Int J Fatigue*, 167, 2023.

[164] G. Zhao, M. Jiang, Y. Luo, and Q. Sui. Third harmonic approximate phase velocity matching nonlinear early fatigue damage detection. *Measurement*, 189:110518, 2022.

[165] H. Yun, R. Rayhana, S. Pant, M. Genest, and Z. Liu. Nonlinear ultrasonic testing and data analytics for damage characterization: A review. *Measurement*, 186:110155, 2021.

[166] Z. Zhang, M. He, A. Liu, H. K. Singh, K. R. Ramakrishnan, and D. Hui. Vibration-based assessment of delaminations in frp composite plates. *Composites Part B: Engineering*, 144:254–266, 2018.

[167] C. Zhang, A.A. Mousavi, S.F. Masri, G. Gholipour, K. Yan, and X. Li. Vibration feature extraction using signal processing techniques for structural health monitoring: A review. *Mech Syst Signal Process*, 177:109175, 2022.

[168] M. Zhuang. Reliability and life assessment of engineering structures with the boundary element method. *Reliab Eng Syst Saf*, 237:103721, 2024.

[169] E28.04. Standard test methods for tension testing of metallic materials. *ASTM E8/E8M-22*, 2022.

[170] J.R. Cahoon, W.H. Broughton, and A.R. Kutzak. The determination of yield strength from hardness measurements. *Metallurgical Transactions*, 2:1979–1983, 1971.

[171] Subir Patra, Hossain Ahmed, Mohammadsadegh Saadatzi, and Sourav Banerjee. Evidence of dissipative and growing nonlinearity in lamb waves due to stress-relaxation and material degradation in composites. *Ultrasonics*, 96:224–231, 2019.

[172] Y. Pan, Z. Sharif Khodaei, and M.H.F. Aliabadi. A robust hybrid method for damage detection under varying environmental conditions. *Struct Health Monit*, 20:2274–2299, 2021.

[173] M. Arunachalam, S.A. Arunkumar, P. Sampath, A. Haiyum, and Y. Khakhar. A sensitivity study on inertance frequency response function through non-parametric variability approach. *SAE Technical Papers*, 2017-March:0445, 2017.

[174] M. Han, J.K. Kim, J.H. Park, W. Kim, S.W. Kang, S.H. Kong, and D. Jung. Sensitivity and frequency-response improvement of a thermal convection–based accelerometer. *Sensors*, 17:1765, 2017.

[175] J.M. Le Floch, C. Murphy, J.G. Hartnett, V. Madrangeas, J. Krupka, D. Cros, and M.E. Tobar. Frequency-temperature sensitivity reduction with optimized microwave bragg resonators. *J Appl Phys*, 121:067521, 2017.

[176] J.C. Dodson and D.J. Inman. Thermal sensitivity of lamb waves for structural health monitoring applications. *Ultrasonics*, 53:677–685, 2013.

[177] O. Putkis, R.P. Dalton, and A.J. Croxford. The influence of temperature variations on ultrasonic guided waves in anisotropic cfrp plates. *Ultrasonics*, 60:109–116, 2015.

[178] F. Lanza di Scalea and S. Salamone. Temperature effects in ultrasonic lamb wave structural health monitoring systems. *J Acoust Soc Am*, 124:161–174, 2008.

[179] J. Zhao, J. Wu, X. Chen, and R. Zeng. Effect of temperature on ultrasonic nonlinear parameters of carbonated concrete. *Materials*, 15:8797, 2022.

[180] V.K. Chillara, H. Cho, M. Hasanian, and C.J. Lissenden. Effect of load and temperature changes on nonlinear ultrasonic measurements: Implications for shm. *IWSHM Proceedings*, 2:783–790, 2015.

[181] M. Li and J. He. Effect of high temperature on ultrasonic velocity in graphite. *Diam Relat Mater*, 116:108368, 2021.

[182] Z. Wu, X. P. Qing, and F. K. Chang. Damage detection for composite laminate plates with a distributed hybrid pzt/fbg sensor network. *J Intell Mater Syst Struct.*, 20(9):1069–1077,, 2009.

[183] W. Ostachowicz, P. Kudela, P. Malinowski, and T. Wandowski. Damage localisation in plate-like structures based on pzt sensors. *Mech Syst Signal Process.*, 23(6):1805–1829,, 2009.

[184] Y. L. Koh, W. K. Chiu, and N. Rajic. Effects of local stiffness changes and delamination on lamb wave transmission using surface-mounted piezoelectric transducers. *Compos Struct.*, 57(1-4):437–443,, 2002.

[185] J. Chen, S. Yuan, and X. Jin. On-line prognosis of fatigue cracking via a regularized particle filter and guided wave monitoring. *Mech Syst Signal Process.*, 131:1–17,, 2019.

[186] B. Masserey and P. Fromme. Fatigue crack growth monitoring using high-frequency guided waves. *Struct Health Monit.*, 12(5-6):484–493,, 2013.

[187] L. Qiu, S. Yuan, Q. Bao, H. Mei, and Y. Ren. Crack propagation monitoring in a full-scale aircraft fatigue test based on guided wave-gaussian mixture model. *Smart Mater Struct.*, 25:055048,, 2016.

[188] H. J. Lim, Y. Kim, G. Koo, S. Yang, H. Sohn, I. H. Bae, and et al. Development and field application of a nonlinear ultrasonic modulation technique for fatigue crack detection without reference data from an intact condition. *Smart Mater Struct.*, 25:095055,, 2016.

[189] R. Wang, Q. Wu, F. Yu, Y. Okabe, and K. Xiong. Nonlinear ultrasonic detection for evaluating fatigue crack in metal plate. *Struct Health Monit.*, 18:869–881,, 2019.

[190] N. Zhao, L. Huo, and G. Song. A nonlinear ultrasonic method for real-time bolt looseness monitoring using pzt transducer-enabled vibro-acoustic modulation. *J Intell Mater Syst Struct.*, 31(3):364–376,, 2020.

[191] D. Donskoy, A. Sutin, and A. Ekimov. Nonlinear acoustic interaction on contact interfaces and its use for nondestructive testing. *NDT and E Int.*, 34(4):231–238,, 2001.

[192] C. S. Park, J. W. Kim, S. Cho, and D. C. Seo. A high resolution approach for nonlinear sub-harmonic imaging. *NDT and E Int.*, 79:114–122,, 2016.

[193] J. Jang and H. Sohn. Online remaining fatigue life estimation of curved steel connection using nonlinear ultrasonic modulation. *Int J Fatigue.*, 170:107566,, 2023.

[194] Y. Yang, C. T. Ng, and A. Kotousov. Second-order harmonic generation of lamb wave in prestressed plates. *J Sound Vib.*, 460:10,, 2019.

[195] F. Aymerich and W.J. Staszewski. Experimental study of impact-damage detection in composite laminates using a cross-modulation vibro-acoustic technique. *Struct Health Monit*, 9:6, 2010.

[196] L. Xu, S. Yuan, J. Chen, and Y. Ren. Guided wave-convolutional neural network based fatigue crack diagnosis of aircraft structures. *Sensors.*, 19(16), 2019.

[197] J. Chen, S. Yuan, C. Sbarufatti, and X. Jin. Dual crack growth prognosis by using a mixture proposal particle filter and on-line crack monitoring. *Reliab Eng Syst Saf.*, 215:107758,, 2021.

[198] Y. Zhu, X. Zeng, M. Deng, K. Han, and D. Gao. Mode selection of nonlinear lamb wave based on approximate phase velocity matching. *NDT and E Int.*, 102:295–303,, 2019.

[199] G. Pitarresi, M. Ricotta, and G. Meneghetti. Investigation of the crack tip stress field in a stainless steel sent specimen by means of thermoelastic stress analysis. *Procedia Structural Integrity*, 18:330–346, 2019.

[200] A. A. Griffith. The phenomena of rupture and flow in solids. *Philosophical Transactions of the Royal Society of London. Series A, Containing Papers of a Mathematical or Physical Character*, 221(582–593):163–198, 1921.

[201] S. Deng, H. Li, G. Piero, M. Fierro, and M. Meo. Residual fatigue life estimation using a nonlinear ultrasound modulation method. *Smart Mater Struct*, 24:025040, 2015.

[202] L. Yan and J. K. Fan. In-situ sem study of fatigue crack initiation and propagation behavior in 2524 aluminum alloy. *Mater Des.*, 110:592–601,, 2016.

[203] C. Yue, S. Dong, L. Weng, Y. Wang, and L. Zhao. Environmental resistance and fatigue behaviors of epoxy/nano-boron nitride thermally conductive structural film adhesive toughened by polyphenoxy. *Polymers (Basel)*, 13:325,, 2021.

[204] S. Wang, S. Tang, C. He, and Q. Wang. Cyclic deformation and fatigue failure mechanisms of thermoplastic polyurethane in high cycle fatigue. *Polymers*, 15:899,, 2023.

[205] V. V. S. Jaya Rao, Elankumaran Kannan, Raghu V. Prakash, and Krishnan Balasubramaniam. Fatigue damage characterization using surface acoustic wave nonlinearity in aluminum alloy AA7175-T7351. *J Appl Phys.*, 104:12,, 2008.

[206] M. Chai, X. Hou, Z. Zhang, and Q. Duan. Identification and prediction of fatigue crack growth under different stress ratios using acoustic emission data. *Int J Fatigue.*, 160:106860,, 2022.

[207] W. Kim, G. Lee, H. Son, H. Choi, and B.D. Youn. Estimation of fatigue crack initiation and growth in engineering product development using a digital twin approach. *Reliab Eng Syst Saf*, 226:108721, 2022.

[208] P. Paris and F. Erdogan. A critical analysis of crack propagation laws. *Journal of Basic Engineering*, 85:528–533, 1963.

[209] H.J. Lim and H. Sohn. Online fatigue crack prognosis using nonlinear ultrasonic modulation. *Struct Health Monit*, 18:1889–1902, 2019.

[210] A.M. Alshoaibi and Y.A. Fageehi. Finite element simulation of a crack growth in the presence of a hole in the vicinity of the crack trajectory. *Materials*, 15:363, 2022.

[211] H. Li, J. Li, and H. Yuan. A review of the extended finite element method on macrocrack and microcrack growth simulations. *Theor Appl Fract Mec*, 97:236–249, 2018.

[212] M. Zhuang, L. Morse, Z. Sharif Khodaei, and M.H. Aliabadi. Reliability analysis of fatigue crack growth in shallow shell structures using the dual boundary element method. *Theor Appl Fract Mec*, 131:104403, 2024.

[213] M. Zhuang, L. Morse, Z. Sharif Khodaei, and M.H. Aliabadi. Statistical inference of the equivalent initial flaw size distribution for an anisotropic material with the dual boundary element method. *Int J Fatigue*, 158:106702, 2022.

[214] S. Mohanty, S. Das, A. Chattopadhyay, and P. Peralta. Gaussian process time series model for life prognosis of metallic structures. *J Intell Mat Syst Str*, 20:1889–1902, 2009.

[215] X. Long, M. Yu, W. Liao, and C. Jiang. A deep learning-based fatigue crack growth rate measurement method using mobile phones. *Int J Fatigue*, 167:107327, 2022.

[216] S. Chawla and A. Gionisy. K-means: A unified approach to clustering and outlier detection. *Proc West Mark Ed Assoc Conf*, pages 189–197, 2013.

[217] D. Xu, Y. Wang, Y. Meng, and Z. Zhang. An improved data anomaly detection method based on isolation forest. *Proceedings - 2017 10th International Symposium on Computational Intelligence and Design, ISCID 2017*, 2:287–291, 2018.

[218] Yong Yu, Xiaosheng Si, Changhua Hu, and Jianxun Zhang. A review of recurrent neural networks: Lstm cells and network architectures. *Neural Computation*, 31(7):1235–1270, 2019.

[219] G.E. Karniadakis, I.G. Kevrekidis, L. Lu, P. Perdikaris, S. Wang, and L. Yang. Physics-informed machine learning. *Nature Reviews Physics*, 3:422–440, 2021.

[220] S. Cai, Z. Mao, Z. Wang, M. Yin, and G.E. Karniadakis. Physics-informed neural networks (pinns) for fluid mechanics: a review. *Acta Mechanica Sinica*, 37:1727–1738, 2021.

[221] B. Huang and J. Wang. Applications of physics-informed neural networks in power systems - a review. *IEEE Transactions on Power Systems*, 38:572–588, 2023.

[222] Y. Chen, Y. Xu, L. Yang, and M. Hu. General real-time three-dimensional multi-aircraft conflict resolution method using multi-agent reinforcement learning. *Transp Res Part C Emerg Technol*, 157:104367, 2023.

[223] J. Chen and Y. Liu. Probabilistic physics-guided machine learning for fatigue data analysis. *Expert Syst Appl*, 168:114316, 2021.

[224] R.G. Nascimento and F.A.C. Viana. Cumulative damage modeling with recurrent neural networks. *AIAA Journal*, 2020.

[225] T. Asrav and E. Aydin. Physics-informed recurrent neural networks and hyper-parameter optimization for dynamic process systems. *Comput Chem Eng*, 173:108195, 2023.

[226] C. Garbin, X. Zhu, and O. Marques. Dropout vs. batch normalization: an empirical study of their impact to deep learning. *Multimed Tools Appl*, 79:12777–12815, 2020.

[227] D. Singh and B. Singh. Investigating the impact of data normalization on classification performance. *Appl Soft Comput*, 97:105524, 2020.